Inaugural–Dissertation

zur

Erlangung der Doktorwürde

der

Naturwissenschaftlich–Mathematischen
Gesamtfakultät

der

Ruprecht–Karls–Universität
Heidelberg

vorgelegt von
Dipl.-Phys. Frank-Peter Schilling
aus Hanau

Diffractive Jet Production in Deep-Inelastic e^+p Collisions at HERA

Dissertation
submitted to the
Combined Faculties for Natural Sciences and Mathematics
of the Ruperto-Carola University of
Heidelberg, Germany
for the degree of a
Doctor of Natural Sciences (Dr. rer. nat.)

Diffractive Jet Production in Deep-Inelastic e^+p Collisions at HERA

presented by
Dipl.-Phys. Frank-Peter Schilling
born in Hanau, Germany

Heidelberg, February 15th, 2001

Referees: Prof. Dr. Franz Eisele
Prof. Dr. Otto Nachtmann

Abstract

Diffractive Jet Production in Deep-Inelastic e^+p Collisions at HERA – A measurement is presented of dijet and 3-jet cross sections in low-$|t|$ diffractive deep-inelastic scattering interactions of the type $ep \rightarrow eXY$, where the system X is separated by a large rapidity gap from a low-mass baryonic system Y. Data taken with the H1 detector at HERA, corresponding to an integrated luminosity of 18.0 pb^{-1}, are used to measure hadron level single and double differential cross sections for $4 < Q^2 < 80$ GeV^2, $x_{I\!P} < 0.05$ and $p_{T,jet} > 4$ GeV. The energy flow not attributed to jets is investigated. Viewed in terms of the diffractive scattering of partonic fluctuations of the photon, the data require the dominance of $q\overline{q}g$ over $q\overline{q}$ states. The measurements are consistent with a factorising diffractive exchange with an intercept close to 1.2 and tightly constrain the dominating diffractive gluon distribution. Soft colour neutralisation models in their present form cannot simultaneously reproduce the shapes and the normalisations of the differential cross sections. Models based on 2-gluon exchange are able to reproduce the shapes of the cross sections at low $x_{I\!P}$ values.

Zusammenfassung

Diffraktive Jet-Produktion in tief-inelastischer e^+p Streuung bei HERA – Es wird eine Messung von 2- und 3-Jet-Wirkungsquerschnitten in diffraktiver tief-inelastischer Streuung für Ereignisse des Typs $ep \rightarrow eXY$ bei kleinen $|t|$ vorgestellt. Das System X ist durch eine große Rapiditätslücke von einem baryonischen System Y kleiner Masse getrennt. Aus Daten, die mit dem H1-Detektor bei HERA aufgezeichnet wurden und einer integrierten Luminosität von 18.0 pb^{-1} entsprechen, werden einfach- und doppelt-differentielle Wirkungsquerschnitte auf Hadron-Niveau im kinematischen Bereich $4 < Q^2 < 80$ GeV^2, $x_{I\!P} < 0.05$ und $p_{T,jet} > 4$ GeV bestimmt. Der Energiefluß außerhalb der Jets wird untersucht. Im Proton-Ruhesystem gesehen verlangen die Daten eine Dominanz von $q\overline{q}g$- über $q\overline{q}$-Fluktuationen des Photons. Die gemessenen Wirkungsquerschnitte sind konsistent mit einem faktorisierenden diffraktiven Austausch mit einem *Intercept* nahe bei 1.2 und schränken die dominierende diffraktive Gluondichte stark ein. Gegenwärtige Modelle weicher Farb-Neutralisation können die Form und Normierung der differentiellen Wirkungsquerschnitte nicht gleichzeitig beschreiben. Auf 2-Gluon-Austausch basierende Modelle sind in der Lage, die Form der Wirkungsquerschnitte bei kleinen Werten von $x_{I\!P}$ zu reproduzieren.

Table of Contents

Introduction

According to our present understanding of the fundamental particles and their interactions, all matter is made up of point-like particles, the quarks and leptons. In the **Standard Model of particle physics**, these interact via the exchange of gauge bosons. The electromagnetic and weak forces are mediated by the massless photon and the massive $W^{\pm}$ and Z^0 bosons respectively. Gravity is up to now not included in the standard model.

The scope of this thesis is the strong interaction. In the Standard Model, the theory of strong interactions is **Quantum Chromodynamics (QCD)**, a non-Abelian quantum field theory. In QCD, the strong force is mediated by gluons which couple to colour charge. The non-Abelian structure of QCD is reflected by the gluon self-coupling. The value of the strong coupling constant α_s depends on the scale μ^2 of the interaction. For large enough μ^2, the value of α_s is much smaller than unity, so that *perturbative* QCD can be applied. However, for the bulk of interactions where hadrons are involved, the scale of the interaction, usually provided by the momentum transfer, is small, so that α_s is large and perturbation theory cannot be applied.

In a special class of such soft hadronic interactions at high energies, only vacuum quantum numbers are exchanged. These **colour singlet exchange** events are interpreted as being due to **diffractive scattering**. Experimentally, such interactions are characterised by a large *rapidity gap* in the hadronic final state without particle production. The underlying dynamics of the colourless exchange in terms of QCD are not yet precisely known, although the exchange is expected to be driven by gluons. Phenomenological models to describe diffractive scattering range from approaches where a pseudo-particle called *pomeron* is introduced to 2-gluon exchange calculations.

The observation of rapidity gap events in deep-inelastic scattering (DIS) at the **electron-proton collider HERA** [1] has generated considerable renewed interest in understanding diffraction in terms of Quantum Chromodynamics. The advantage of investigating diffractive interactions in DIS is that the colourless exchange can be studied using a point-like, highly virtual photon probe, similarly to proton structure measurements in non-diffractive DIS. This offers the chance to illuminate the underlying dynamics of diffractive DIS in terms of QCD.

In addition to studying inclusive diffractive scattering at HERA [2–5], it is particularly interesting to focus on those hadronic final states where additional hard scales are introduced. Examples are the production of heavy quarks, in which the quark

mass provides the hard scale, and **high transverse momentum jet production**. Such topologies are promising candidates for which the diffractive cross section may be calculable using perturbation theory, in contrast to inclusive diffraction. High transverse momentum (p_T) jet final states in diffraction are studied in $p\overline{p}$ collisions [6–9] as well as at HERA [10,11].

This thesis is concerned with **diffractive jet production in DIS**. A high statistics measurement of dijet and a first measurement of 3-jet production in colour singlet exchange DIS events are presented, which were performed using the H1 detector at HERA. Compared with a previous measurement [11], the integrated luminosity is increased by one order of magnitude. The kinematic range is extended towards lower photon virtualities and jet transverse momenta. The available amount of data allows for the first time to measure double-differential diffractive jet cross sections, which enable tests of Regge and QCD factorisation hypotheses. In addition, restricted phase space regions can be explored where calculations based on 2-gluon exchange are expected to be applicable. Diffractive jet production is also highly sensitive to the role of gluons in diffraction, in contrast to more inclusive measurements where it can only be inferred indirectly from scaling violations.

For **the analysis** presented here, DIS events are selected where the proton (or a low-mass proton excitation) loses only a small fraction of its incoming momentum and escapes undetected through the beam pipe. Separated from this system by a large rapidity region devoid of hadronic activity, the photon dissociation system X is well contained within the central part of the detector. In the analysis, the two cases where there are either at least two or exactly three high p_T jets contained in X are considered. The measured distributions are corrected to hadron level cross sections. The systematic uncertainties are determined. The hadronic final state of the events which is not contained in the jets is also investigated. The predictions of various QCD inspired phenomenological models and calculations are confronted with the data.

Preliminary results of this analysis have been reported in [12–14]. The final results are published in [15].

Structure of the Thesis

The theoretical foundations are outlined in chapter 1, where the first part is concerned with deep-inelastic scattering and QCD. The second part gives an overview of diffractive scattering, starting with the concepts of Regge phenomenology and then turning to diffractive DIS, where the relevant phenomenological models are reviewed. Previous H1 results are summarised in chapter 2. Chapter 3 describes the simulation of events using Monte Carlo generators. An overview of the HERA collider and the H1 experiment is given in chapter 4. Data selection and cross section measurement are explained in chapters 5 and 6. The measured cross sections are presented, interpreted and compared to the model predictions in chapter 7. In the appendix, additional model comparisons are presented and recent results from the Tevatron $p\overline{p}$ collider are discussed.

Chapter 1

Theoretical Overview

In this chapter, the theoretical foundations for the measurement of jet production cross sections in diffractive deep-inelastic scattering at HERA are reviewed. In the first part (section 1.1), the kinematics of deep-inelastic scattering (DIS) at HERA are explained and the theory of Quantum Chromodynamics (QCD) is introduced. In the second part (section 1.2), an overview of diffraction in hadron-hadron interactions and in deep-inelastic scattering at HERA is given. The currently available phenomenological models and QCD calculations which attempt to describe diffractive DIS at HERA including jet-production are reviewed. The theoretical aspects are discussed here only to an extent which is necessary for the motivation of the analysis and the interpretation of the data.

1.1 Deep-Inelastic Scattering and QCD

The basics of deep-inelastic scattering (DIS) and QCD are reviewed in this section. After the kinematics of DIS have been introduced, the DIS cross section is interpreted in terms of the parton model and its refinement using perturbative QCD. The basic properties of the theory of QCD are outlined. The DGLAP and BFKL approximations are discussed. The kinematics of leading order QCD processes in DIS are explained. The concept of resolved virtual photons as an approximation to higher order QCD diagrams is introduced. For a detailed review of DIS and QCD, see e.g. [16].

1.1.1 Kinematics of Deep-Inelastic Scattering

In Fig. 1.1, the kinematics of deep-inelastic electron-proton scattering are visualised. The beam electron interacts with a parton from the proton by the exchange of a virtual gauge boson. In neutral current (NC) scattering, a γ^* or Z^0 boson is exchanged. In the case of charged current (CC) scattering, a $W^\pm$ boson is exchanged, which leads to an electron-neutrino in the final state. If the 4-vectors of the incoming and outgoing lepton are denoted k and k' and q is the boson 4-vector, the negative squared invariant mass of the exchanged virtual boson is given by

$$Q^2 = -q^2 = (k - k')^2 \ . \tag{1.1}$$
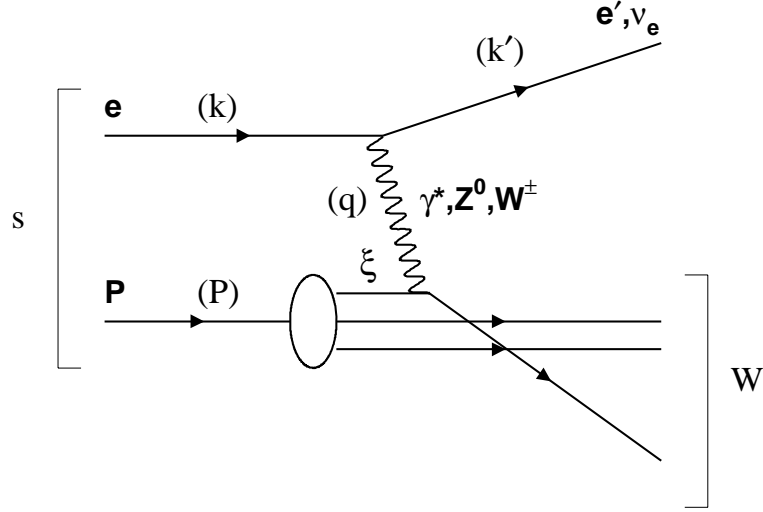
Figure 1.1: The kinematics of deep-inelastic electron-proton scattering. The electron (with 4-vector k) interacts with the proton (P) via the exchange of a virtual gauge boson (q), which scatters off a parton in the proton with longitudinal momentum fraction ξ.

Values of Q^2 above ~ 4 GeV^2 correspond to the regime of deep-inelastic scattering. If the photon is almost real ($Q^2 \simeq 0$), the process is usually referred to as *photoproduction*. It is convenient to introduce the two dimensionless quantities x and y:

$$x = \frac{-q^2}{2P \cdot q} \;\; (0 \le x \le 1) \; ; \qquad y = \frac{P \cdot q}{P \cdot k} \;\; (0 \le y \le 1) \; , \tag{1.2}$$

where P denotes the 4-vector of the proton. The squared invariant masses of the electron-proton and photon-proton systems s and W^2 are given by[1]:

$$s = (k + P)^2 \simeq Q^2/xy \simeq 4E_e E_p \; ; \qquad W^2 = (q + P)^2 \simeq ys - Q^2 \; . \tag{1.3}$$

1.1.2 DIS Cross Section and Parton Model

The analysis presented in this thesis is only concerned with neutral current (NC) interactions. The deep-inelastic scattering cross section can then be expressed as the sum of the contributions from γ^* and Z^0 exchange and an interference term:

$$\sigma_{NC} = \sigma(\gamma^*) + \sigma(Z^0) + \sigma(\gamma^* Z^0) \; . \tag{1.4}$$

The large mass of the Z^0 boson ($M_{Z^0} = 91.1882 \pm 0.0022$ GeV [17]) suppresses the contribution from Z^0 exchange and the interference term at low values of Q^2 according to the ratios of the propagator terms:

$$\frac{\sigma(Z^0)}{\sigma(\gamma^*)} \sim \left(\frac{Q^2}{Q^2 + M_{Z^0}^2} \right)^2 \; ; \qquad \frac{\sigma(\gamma^* Z^0)}{\sigma(\gamma^*)} \sim \frac{Q^2}{Q^2 + M_{Z^0}^2} \; . \tag{1.5}$$

---

[1]Particle masses have been neglected.

Since in the analysis presented here deep-inelastic scattering events for $Q^2 < 80$ GeV^2 are studied, the contributions from Z^0 exchange and $Z^0 \gamma^*$-interference can safely be neglected. The cross section, expressed in terms of the two variables x and Q^2, can then be written as:

$$\frac{\mathrm{d}^2\sigma(x,Q^2)}{\mathrm{d}x\ \mathrm{d}Q^2} = \frac{4\pi\alpha^2}{xQ^4}\left[\left(1 - y + \frac{y^2}{2}\right)F_2(x,Q^2) - \frac{y^2}{2}F_L(x,Q^2)\right] . \tag{1.6}$$

Here, α is the electromagnetic coupling. $F_2(x,Q^2)$ denotes the proton structure function. Because the cross section consists of two contributions from the scattering of transversely and longitudinally polarised photons, the longitudinal structure function $F_L(x,Q^2)$ is introduced. F_2 corresponds to the sum of longitudinal and transverse photon polarisation contributions, whereas F_L corresponds to longitudinal polarisation only. The ratio of the longitudinal to transverse photon cross sections $R(x,Q^2)$ is given by

$$R(x,Q^2) = \frac{\sigma_L}{\sigma_T} = \frac{F_L(x,Q^2)}{F_2(x,Q^2) - F_L(x,Q^2)} , \tag{1.7}$$

The DIS cross section can then be re-expressed as:

$$\frac{\mathrm{d}^2\sigma(x,Q^2)}{\mathrm{d}x\ \mathrm{d}Q^2} = \frac{4\pi\alpha^2}{xQ^4}\left[1 - y + \left(\frac{1}{1+R}\right)\frac{y^2}{2}\right]F_2(x,Q^2) . \tag{1.8}$$

In the kinematic region of not too large y, contributions from longitudinal photon exchange can be neglected ($R = 0$) and Eq. 1.8 reduces to

$$\frac{\mathrm{d}^2\sigma(x,Q^2)}{\mathrm{d}x\ \mathrm{d}Q^2} = \frac{4\pi\alpha^2}{xQ^4}\left(1 - y + \frac{y^2}{2}\right)F_2(x,Q^2) . \tag{1.9}$$

The Parton Model

When the first deep-inelastic scattering experiments were performed at SLAC [18], a *scaling* behaviour of the proton structure function was observed: $F_2(x,Q^2)$ was found to be approximately independent of Q^2 for $1 < Q^2 < 10$ GeV^2. Bjorken [19] predicted that F_2 should only depend on x in the limit $Q^2 \to \infty$. The quark-parton model, invented by Feynman [20] to explain the scaling behaviour, is based on two assumptions:

- The hadron taking part in the scattering process is made of point-like constituents (partons or *quarks*, as introduced by Gell-Mann [21]), among which the hadron momentum is distributed.

- At large Q^2, the quarks interact as free particles inside the hadron. At the short time scale $\mathcal{O}(1/\sqrt{Q^2})$ of the interaction, the photon sees a frozen state of non-interacting quarks. The cross section can thus be expressed as an incoherent sum of elastic photon-parton scattering processes.

In the parton model, the dimensionless quantity x (Eq. 1.2) corresponds to the momentum fraction ξ of the struck quark (neglecting the quark mass). In consequence, the structure function F_2 can be expressed as:

$$F_2(x,Q^2) \to F_2(x) = \sum_i e_i^2 x f_i(x) . \tag{1.10}$$

Here, the sum runs over the constituent quarks, e_i is the electric charge of quark i and $f_i(x)$ is the momentum distribution or *parton density* function in the proton. If quarks and anti-quarks were the only constituents of the proton, their momentum sum should satisfy unity. Measurements however yield $\sum_i \int_0^1 x[q(x) + \bar{q}(x)]\, dx \simeq 0.5$. The missing momentum is carried by gluons.

1.1.3 Quantum Chromodynamics

With more and more precise structure function measurements, *scaling violations*, i.e. a dependence of F_2 on Q^2, are observed at x values lower and higher than those accessed by the first SLAC measurements. Fig 1.2 shows high precision measurements of $F_2(x, Q^2)$ over 5 orders of magnitude in Q^2 and a range in x between $3.2 \cdot 10^{-5}$ and 0.65. F_2 exhibits a dependence on the resolution power Q^2 of the photon probe. These *scaling violations* can be explained within Quantum Chromodynamics (QCD): The quarks in the proton can radiate gluons, which themselves may split into $q\bar{q}$ pairs.

QCD is a non-Abelian gauge theory which is invariant under the $SU(3)$ *colour* transformation. 'Colour' corresponds to an additional degree of freedom which represents the charge of the strong interaction. The colour charge is carried by quarks and gluons. Quarks appear in *red*, *green* or *blue* colour. The massless gauge bosons of the theory are the eight bi-coloured gluons. The gluon self-coupling is a reflection of the non-Abelian structure of QCD.

Renormalisation and Factorisation

Renormalisation   To calculate QCD cross sections, integrations have to be performed over the entire phase space of real and virtual quarks and gluons. These integrals turn out to be divergent. A scheme called *regularisation* is therefore defined to leave out the divergent parts of the integrals. The calculated cross sections then depend on the energy scale μ_r^2 used in the regularisation. This dependence is compensated by defining an effective coupling constant α_s, in which the divergent contributions are absorbed (*renormalisation*). The coupling constant is defined by the renormalisation scheme used and depends on the *renormalisation scale μ_r^2*. The requirement that the calculated cross sections should be independent of μ_r^2 leads to the renormalisation group equation (RGE), a perturbative expansion in α_s which describes the dependence of α_s on μ_r^2. When calculating up to $\mathcal{O}(\alpha_s)$, the solution is:

$$\alpha_s(\mu_r^2) = \frac{12\pi}{(33 - 2n_f)\ln(\mu_r^2/\Lambda_{QCD}^2)} \ . \tag{1.11}$$

Here, Λ_{QCD} is a free parameter which has to be determined experimentally and n_f is the number of quarks with mass less than μ_r. The current world average value of α_s at the Z^0 mass is $\alpha_s(\mu_r = M_Z) = 0.1185 \pm 0.0020$ [17]. Consequences of the scale dependence of the strong coupling constant are

- **Asymptotic freedom:** If μ_r^2 is large, the coupling α_s is small and cross sections for specific processes are calculable as a perturbative expansion in α_s. In this limit, quarks can be treated as free particles.
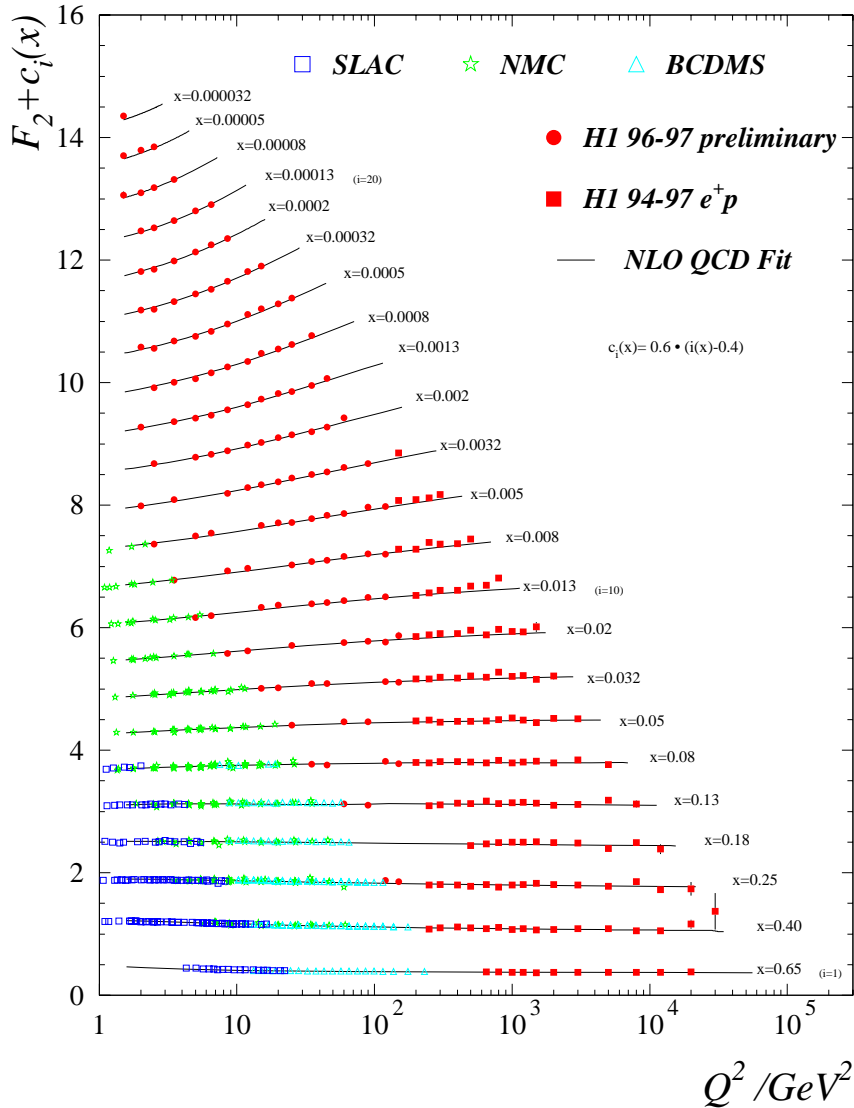
FIGURE 1.2: Experimental data on the proton structure function $F_2(x, Q^2)$, shown as a function of Q^2 for different x values. For display purposes, a factor $c_i(x) = 0.6 \cdot (i(x) - 0.4)$ is added to the F_2 values, where $i(x)$ is the integer bin number in x. Shown are measurements of the H1 collaboration at HERA [22] and earlier results from the NMC and BCDMS fixed target experiments [23] (figure from [22]).

- **Infrared slavery:** At small values of μ_r^2, corresponding to large distances, the coupling strength α_s gets large and perturbation theory is no longer applicable. Quarks are confined in hadrons and non-perturbative methods have to be applied.

Factorisation The theorem of *hard scattering factorisation in QCD* states that the short-range, perturbatively calculable aspects of a physical process can be separated from the long-range aspects, for which perturbation theory is not applicable. As an application
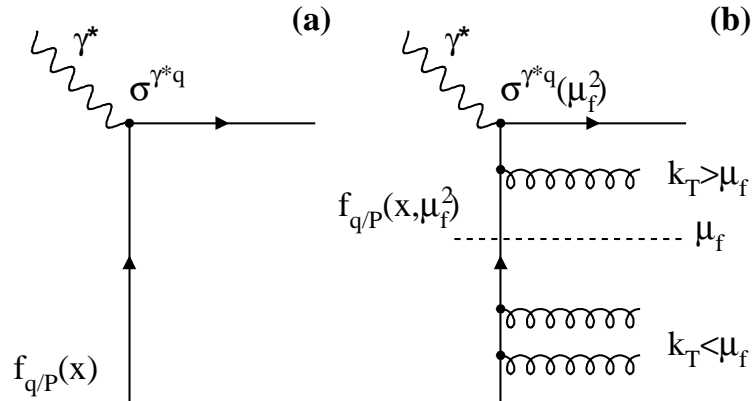
FIGURE 1.3: Hard scattering factorisation in QCD. Diagrams for photon-quark scattering *(a)* in lowest order and *(b)* in higher orders of α_s are shown. By a redefinition of the quark distribution function $f_{q/P}$, all soft gluon emissions with transverse momentum $k_T < \mu_f$ are absorbed into the quark density (k_T is the gluon transverse momentum with respect to the proton). This introduces a dependence on the factorisation scale μ_f into both the quark density $f_{q/P}(x, \mu_f^2)$ and the partonic cross section $\sigma^{\gamma^* q}(\mu_f^2)$ of the process.

of this theorem, the proton structure function, F_2 can be expressed as:

$$F_2(x, Q^2) = \sum_{i=q,g} \int_x^1 d\xi \; f_i(\xi, \mu_r^2, \mu_f^2, \alpha_s) \cdot C_i^V \left(\frac{x}{\xi}, \frac{Q^2}{\mu_r^2}, \mu_f^2, \alpha_s \right) \; . \qquad (1.12)$$

Here, μ_f^2 is the *factorisation scale*, the C_i^V are *coefficient functions* and the f_i are the parton distribution functions. The factorisation scale μ_f^2 defines the energy scale above which the process is calculated within perturbative QCD (Fig. 1.3). The resulting coefficient functions C_i^V depend on the parton flavour i and on the exchanged boson V, but *not* on the type of hadron. They are therefore process independent. The physics below the factorisation scale is absorbed into the quark and gluon distribution functions f_i, which are dependent on the hadron which takes part in the interaction.

Because the coefficient functions have been calculated completely so far only up to $\mathcal{O}(\alpha_s^2)$ for the inclusive ep cross section, the calculated cross sections as well as the parton distribution functions exhibit dependences on the choices of the renormalisation and factorisation scales.

1.1.4 Evolution of Parton Distributions

The parton distributions $f_i(x, Q^2)$ have not been calculable so far from first principles in QCD. However, for sufficiently large values of Q^2 (i.e. small α_s) it is possible to predict the evolution of the parton distributions using perturbative calculations. There, approximations of QCD are commonly used in which different choices of the region of phase space taken into account are made. In the perturbative expansion terms containing powers of $\alpha_s \ln(Q^2/Q_0^2)$, $\alpha_s \ln(1/x)$ and mixed terms of the form $\alpha_s \ln(Q^2/Q_0^2) \ln(1/x)$
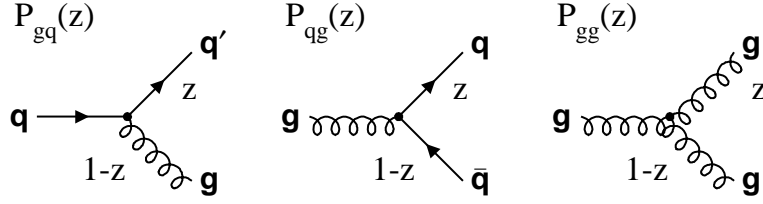
FIGURE 1.4: Feynman diagrams for the $\mathcal{O}(\alpha_s)$ splitting functions. From left to right, the processes $q \to q'g$, $g \to q\bar{q}$ and $g \to gg$ are shown, corresponding to the splitting functions $P_{gq}(z)$ $(P_{qq}(1-z))$, $P_{qg}(z)$ and $P_{gg}(z)$.

appear. The two main approximations which are made are reflected by the DGLAP and the BFKL approaches:

The DGLAP Evolution Equations

In the DGLAP (Dokshitzer, Gribov, Lipatov, Altarelli, Parisi) [24] scheme, only contributions in the perturbative expansion proportional to leading powers of $\alpha_s \ln(Q^2/Q_0^2)$ are taken into account. Terms proportional to leading powers of $\alpha_s \ln(1/x)$ are neglected. Obviously, this is a reasonable approximation for large Q^2 and not too small values of x. The evolution of the quark and gluon distributions $q_i(x, Q^2)$ and $g(x, Q^2)$ is then given by the DGLAP equations:

$$\frac{\mathrm{d}q_i(x,Q^2)}{\mathrm{d}\ln Q^2} = \frac{\alpha_s}{2\pi} \int_x^1 \frac{\mathrm{d}z}{z} \left[q_i(z,Q^2)P_{qq}\left(\frac{x}{z}\right) + g(z,Q^2)P_{qg}\left(\frac{x}{z}\right) \right] ; \qquad (1.13)$$

$$\frac{\mathrm{d}g(x,Q^2)}{\mathrm{d}\ln Q^2} = \frac{\alpha_s}{2\pi} \int_x^1 \frac{\mathrm{d}z}{z} \left[\sum_i q_i(z,Q^2)P_{gq}\left(\frac{x}{z}\right) + g(z,Q^2)P_{gg}\left(\frac{x}{z}\right) \right] . \qquad (1.14)$$

The index i runs over the quark and anti-quarks flavours. The $P_{ij}(z)$ denote the *splitting functions*. They give the probability for parton branchings $q \to qg$, $g \to q\bar{q}$ and $g \to gg$ of a mother parton j, where a daughter parton i is emitted with fractional momentum $(1-z)$ and the mother parton retains the fraction z of its momentum (see Fig. 1.4). The splitting functions are perturbatively calculable. In leading order ($\mathcal{O}(\alpha_s)$), they are given by[2]:

$$P_{qq}(z) = P_{gq}(1-z) = \frac{4}{3} \left[\frac{1+z^2}{(1-z)_+} \right] + 2 \cdot \delta(1-z) ; \qquad (1.15)$$

$$P_{qg}(z) = \frac{1}{2} \left(z^2 + (1-z)^2 \right) ; \qquad (1.16)$$

$$P_{gg}(z) = 6 \left[\frac{z}{(1-z)_+} + \frac{1-z}{z} + z(1-z) \right] + \left(11 - \frac{n_f}{3} \right) \cdot \delta(1-z) . \qquad (1.17)$$

_____

[2]The '+' subscript indicates that the collinear singularities at $z = 1$ are regularised by: $\int_0^1 dz \frac{f(z)}{(1-z)_+} := \int_0^1 dz \frac{f(z)-f(1)}{1-z}$.
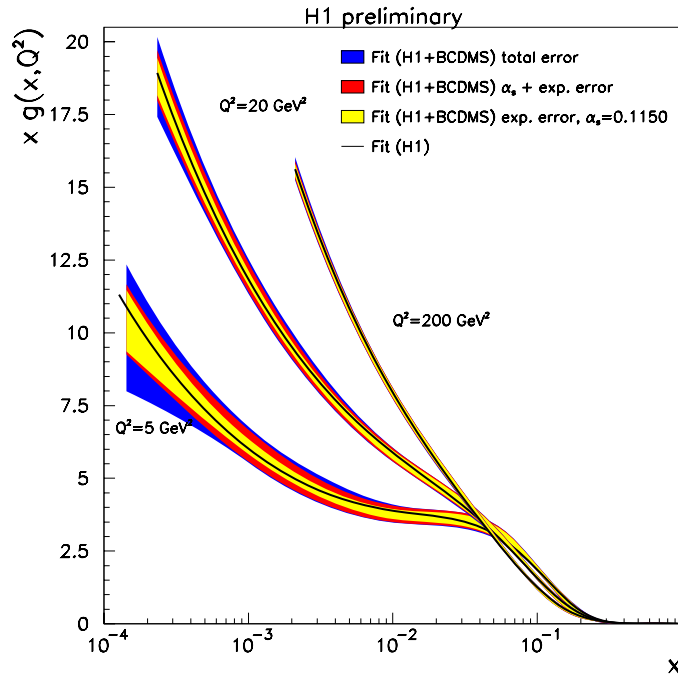
FIGURE 1.5: The gluon distribution in the proton as obtained from an NLO DGLAP fit to $F_2(x, Q^2)$ data from H1 and BCDMS [25]. The gluon distribution is shown for different values of $Q^2 = 5, 20, 200$ GeV^2. The fit was done for $\alpha_s(M_Z) = 0.115$ and $Q_0^2 = 4$ GeV^2. The meaning of the error bands is explained in the legend.

Using this formalism, the parton distributions f_i can be evaluated for any value of Q^2 if they are given at the starting scale Q_0^2 of the QCD evolution. In a 'DGLAP QCD fit', parton distributions can be extracted from measured structure function data by parameterising the parton densities $f_i^{\{a_j\}}(x, Q_0^2)$ at Q_0^2. The free parameters $\{a_j\}$ are determined from a fit in which the parton distributions evolve according to the DGLAP equations. As an example, Fig. 1.5 shows the gluon distribution in the proton for different values of Q^2, as extracted from a NLO DGLAP QCD analysis of $F_2(x, Q^2)$ data [25]. The gluon distribution shows a global increase with increasing resolution power Q^2 and a strong rise towards low x values.

The evolution of parton distributions can be visualised by a *ladder diagram* of parton emissions as shown in Fig. 1.6. In the DGLAP scheme or 'leading $\log(Q^2)$' approximation, only those configurations are summed up which fulfil:

- Strong ordering of transverse momenta $k_{T,i}$: $k_{T,i}^2 \ll k_{T,i+1}^2 \ll \ldots \ll Q^2$;

- Ordering of longitudinal momenta x_i: $x_i > x_{i+1} > \ldots > x$.

As mentioned before, the DGLAP approach neglects terms proportional to powers of $\alpha_s \ln(1/x)$ in the perturbative expansion. However the kinematic region which can be accessed at HERA extends to very low x values down to 10^{-5}. In the region of low x, the
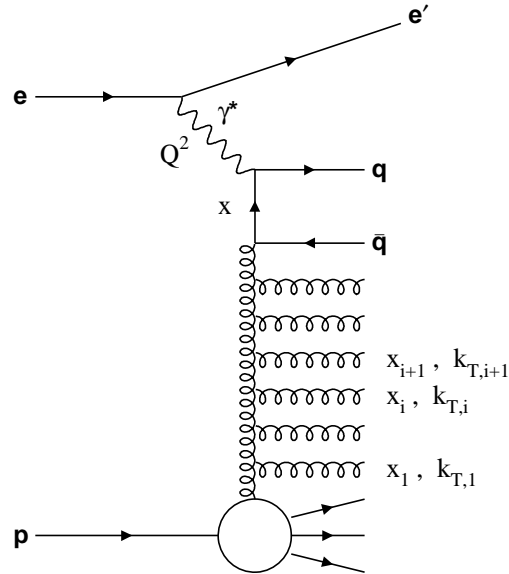
FIGURE 1.6: Ladder diagram of the QCD parton evolution. The longitudinal and transverse momenta of the emitted gluons are labelled x_i and $k_{T,i}$.

$\alpha_s \ln(1/x)$ terms should eventually become important. This forms the basis of the second approach:

The BFKL Equation

The BFKL (Balitzky, Fadin, Kuraev, Lipatov) [26] approximation sums up contributions proportional to leading powers of $\alpha_s \ln(1/x)$ in the perturbative expansion, which become important at very low x. In this approximation, the gluon ladder as shown in Fig. 1.6 need not be ordered in k_T. As a consequence, the appropriate gluon distribution is not integrated over k_T. Instead, an *unintegrated gluon distribution* $\mathcal{F}(x, k_T^2)$ is defined, which is related to the conventional gluon distribution by

$$xg(x, Q^2) = \int^{Q^2} \frac{\mathrm{d}k_T^2}{k_T^2} \, \mathcal{F}(x, k_T^2) \; . \tag{1.18}$$

The BFKL equation describes the $\ln(1/x)$ evolution of $\mathcal{F}(x, k_T^2)$:

$$\frac{\mathrm{d}\mathcal{F}(x, k_T^2)}{\mathrm{d}\ln(1/x)} = \int \mathrm{d}k'^2_T \; K(k_T^2, k'^2_T) \, \mathcal{F}(x, k'^2_T) = K \otimes \mathcal{F} = \lambda \mathcal{F} \; . \tag{1.19}$$

The solution of the BFKL equation is controlled by the largest eigenvalue λ of the kernel K. Up to leading order in $\ln(1/x)$ and for fixed α_s, a steep power law is obtained for the gluon distribution:

$$xg(x, Q^2) \sim f(Q^2) \cdot x^{-\lambda} \; ; \qquad \lambda = \alpha_s \frac{12 \cdot \ln 2}{\pi} \simeq 0.4 \dots 0.5 \; . \tag{1.20}$$
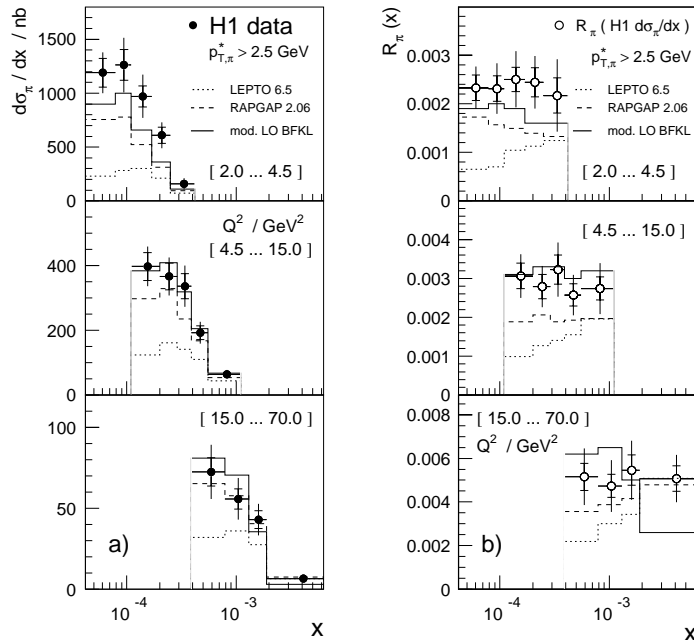
FIGURE 1.7: (a) The forward π^0 meson production cross section ($p_{T,\pi}^* > 2.5$ GeV) as a function of x in three bins of Q^2 as measured by H1 [28]. The QCD models RAPGAP (direct and resolved virtual photon contributions, see section 1.1.6) and LEPTO (only direct γ^* contributions) as well as a leading order BFKL calculation are compared to the data. (b) The rate of forward π^0 production in DIS, obtained by dividing the data points from (a) by the inclusive DIS cross section.

It is noted that the inclusion of a running α_s and next-to-leading order contributions have a strong effect on λ [27]. The BFKL approximation takes the following gluon ladder diagrams into account:

- No ordering of transverse momenta $k_{T,i}$ ('random walk');

- Strong ordering of longitudinal momenta x_i: $x_i \gg x_{i+1} \gg \ldots \gg x$.

Because there is no lower bound on $k_{T,i}$ in the BFKL approximation, a cut-off parameter k_0^2 has to be introduced in the calculations. The resulting cross sections therefore depend on the value of k_0^2.

There is no conclusive evidence so far for a breakdown of the DGLAP QCD approximation even at the lowest accessible values of x at HERA (see Fig. 1.2). It may however well be possible that BFKL effects *are* present in the data but the DGLAP approach is flexible enough to accommodate for this by adjustment of the parton distributions. It is more promising to look for BFKL effects in the final state, especially very close to the proton direction. Fig. 1.7 shows a measurement of the cross section for the production of high p_T π^0 mesons close to the proton direction in DIS events [28, 29]. Models with a DGLAP-based strong k_T ordering clearly fail to reproduce the observed cross sections. On the other hand, a model based on a leading order BFKL calculation is roughly in agreement with the data.
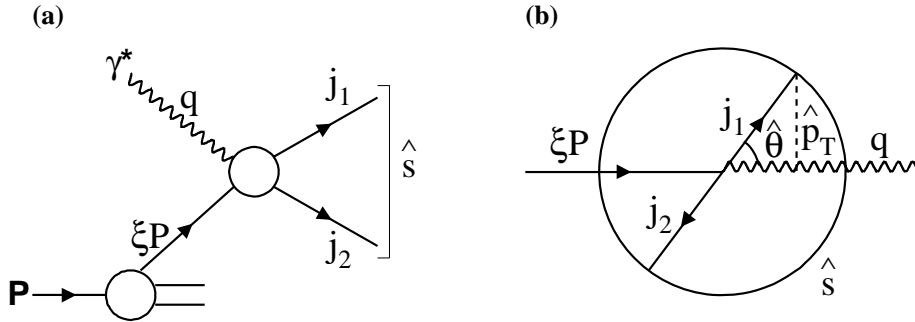
FIGURE 1.8: Kinematics of leading order QCD processes in deep-inelastic scattering, viewed *(a)* in the proton infinite momentum frame and *(b)* in the centre-of-mass frame of the final state partons. A parton from the proton with longitudinal momentum ξP interacts with the virtual photon γ^*, producing two final state partons j_1 and j_2. The centre-of-mass energy squared of the hard interaction is $\hat{s}$. In the centre-of-mass frame, the two final state partons are emitted back-to-back with polar angle $\hat{\theta}$ and corresponding transverse momentum $\hat{p}_T$.

1.1.5 Leading Order QCD Processes

At fixed order α_s^n, a finite number of diagrams contribute to the deep-inelastic lepton-proton cross section. These diagrams have been explicitly calculated without approximations up to $\mathcal{O}(\alpha_s^2)$ or *next-to-leading order* QCD by now. In leading order QCD ($\mathcal{O}(\alpha_s)$), diagrams with one QCD vertex are summed, which results in a second parton in the final state emerging from the hard partonic scattering.

Kinematics

The kinematics of these $2 \rightarrow 2$ processes are visualised in Fig. 1.8. A parton from the proton with longitudinal momentum $\xi \cdot P$ interacts with the virtual photon (q). Two final state partons with 4-momenta j_1 and j_2 are produced. From 4-momentum conservation, the relation

$$\hat{s} = (q + \xi P)^2 = (j_1 + j_2)^2 \tag{1.21}$$

follows. $\hat{s}$ denotes the squared centre-of-mass energy of the hard scattering process. A relation between the parton momentum fraction ξ and the Bjorken-x variable follows which is different from the quark parton model:

$$\xi = x \left(1 + \frac{\hat{s}}{Q^2} \right) \ . \tag{1.22}$$

In the centre-of-mass frame of the hard interaction, the two final state partons are back-to-back in the azimuthal and polar angles $\hat{\theta}$ and $\hat{\phi}$. The dependences on $\hat{\theta}$ and $\hat{\phi}$ are given by the matrix element of the hard scattering. If the transverse momentum of the outgoing partons is denoted $\hat{p}_T$, the following relation holds between $\hat{p}_T$, $\hat{s}$ and $\hat{\theta}$ (neglecting parton
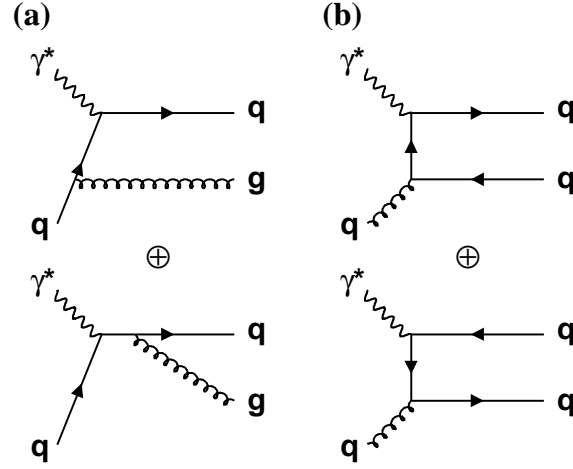
Figure 1.9: The leading order QCD diagrams in DIS. *(a)* The QCD-Compton (QCDC) process. The struck quark emits a gluon before or after the interaction with the virtual photon. *(b)* Boson-Gluon-Fusion (BGF). The virtual photon annihilates with a gluon from the proton. A $q\bar{q}$ pair is produced.

masses):

$$\hat{p}_T = \frac{\sqrt{\hat{s}}}{2} \sin(\hat{\theta}) \ . \tag{1.23}$$

Order α_s Processes

At $\mathcal{O}(\alpha_s)$, the following diagrams have to be included in the calculation of the DIS cross section in addition to the bare quark parton model (QPM) process (see Fig. 1.9):

- **QCD-Compton Scattering (QCDC):** The struck quark from the proton radiates a gluon before or after the interaction with the virtual photon;

- **Boson-Gluon-Fusion (BGF):** The virtual photon annihilates with a gluon from the proton, whereby producing a quark-antiquark pair.

In both cases a QCD vertex proportional to α_s is introduced. The dynamics of the $2 \to 2$ process $ab \to cd$ are conveniently expressed in terms of the *Mandelstam variables* $\hat{s}$, $\hat{t}$ and $\hat{u}$:

$$\hat{s} = (a+b)^2 = (c+d)^2 \ ; \qquad \hat{t} = (a-c)^2 \ ; \qquad \hat{u} = (a-d)^2 \ . \tag{1.24}$$

The transversely polarised photon-parton cross sections for the QCD-Compton and Boson-Gluon-Fusion processes are then given by:

$$\frac{d\hat{\sigma}_T(\gamma^* q \to qg)}{d\hat{t}} = \frac{8\pi e_i^2 \alpha \alpha_s}{3(\hat{s}+Q^2)^2} \left[-\frac{\hat{t}}{\hat{s}} - \frac{\hat{s}}{\hat{t}} + \frac{2\hat{u}Q^2}{\hat{s}\hat{t}} - \frac{2\hat{u}Q^2}{(\hat{s}+Q^2)^2} \right] \quad \text{(QCDC)} \ ; \tag{1.25}$$

$$\frac{d\hat{\sigma}_T(\gamma^* g \to q\bar{g})}{d\hat{t}} = \frac{\pi e_i^2 \alpha \alpha_s}{(\hat{s}+Q^2)^2} \left[\frac{\hat{u}}{\hat{t}} + \frac{\hat{t}}{\hat{u}} - \frac{2\hat{s}Q^2}{\hat{t}\hat{u}} + \frac{4\hat{s}Q^2}{(\hat{s}+Q^2)^2} \right] \quad \text{(BGF)} \ . \tag{1.26}$$
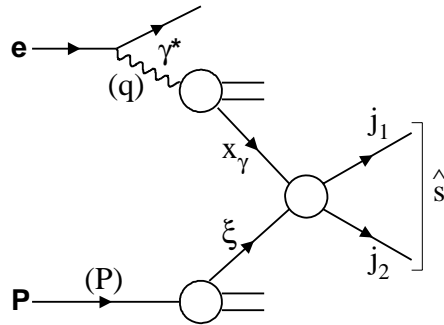
Figure 1.10: Kinematics of a $2 \to 2$ hard scattering process in DIS where the virtual photon is resolved. A parton from the photon with momentum fraction x_γ interacts with a parton from the proton, producing two final state partons j_1 and j_2.

Quark masses have been neglected. It is important to note that in leading order QCD, in contrast to the QPM process, a direct sensitivity to the gluon distribution $g(x, Q^2)$ arises from the BGF diagram.

1.1.6 Virtual Photon Structure

In deep-inelastic scattering, the photon interacts as a point-like particle because of its high virtuality Q^2. By contrast, real photons ($Q^2 \simeq 0$) can fluctuate into long-lived hadronic systems which can be considered in terms of photon structure functions. For a review of real photon structure, see [30]. There are several approaches for the modelling of the transition region of a few GeV^2 in Q^2, which is covered by the HERA experiments and also by the analysis presented in this thesis.

Kinematics

The kinematics of resolved photon deep-inelastic scattering events are visualised in Fig. 1.10. If the photon is resolved, only a fraction x_γ of the photon momentum q enters the hard scattering process. If the 4-vector of the parton from the photon entering the hard scattering is labelled u, then

$$x_\gamma = \frac{P \cdot u}{P \cdot q} \ . \tag{1.27}$$

Direct photon events satisfy $x_\gamma \equiv 1$ by definition. Events where the photon is resolved have $x_\gamma < 1$. The squared centre-of-mass energy of the hard interaction $\hat{s}$ and the proton momentum fraction ξ of the parton which enters the hard interaction are given by:

$$\hat{s} = (\xi P + x_\gamma q)^2 = (j_1 + j_2)^2 \ ; \qquad \xi = x x_\gamma \left(1 + \frac{\hat{s}}{x_\gamma^2 Q^2} \right) \ . \tag{1.28}$$

Applying hard scattering factorisation also to the photon, the cross section can, by analogy to hadron-hadron scattering, be expressed as the product of the photon and proton parton

densities and the hard scattering cross section $\hat{\sigma}$:

$$\frac{\mathrm{d}^5\sigma}{\mathrm{d}y\ \mathrm{d}x_\gamma\ \mathrm{d}\xi\ \mathrm{d}\cos\hat{\theta}\ \mathrm{d}Q^2} = \frac{1}{32\pi s}\ \frac{f_{\gamma/\mathrm{e}}(y,Q^2)}{y}\ \sum_{ij}\ \frac{f_i^{\gamma^*}(x_\gamma,\mu_f^2,Q^2)}{x_\gamma}\ \frac{f_j^P(\xi,\mu_f^2)}{\xi}\ \hat{\sigma}(\cos\hat{\theta})\ ,$$

$$(1.29)$$

where $f_{\gamma/\mathrm{e}}(y,Q^2)$ denotes the flux of transversely polarised photons. Longitudinal photon exchange is neglected here. The $f_i^{\gamma^*}$ and f_j^P are the parton densities of the virtual photon and the proton. Usually, p_T^2 or $Q^2 + p_T^2$ is chosen for the factorisation scale μ_f^2, where p_T is the transverse momentum of the final state partons. The physical picture is that for the region $p_T^2 > Q^2$ the structure of the photon can be resolved.

Two popular models for the parton distributions of the virtual photon originate from Schuler and Sjöstrand and from Drees and Godbole:

Schuler and Sjöstrand Model

This approach (also called 'SaS') [31] assumes that the parton distributions of the virtual photon correspond to those of the real photon but are suppressed with increasing Q^2, parameterised by a factor of the form $(k^2/(k^2 + Q^2))^2$. The parton density functions of the virtual photon can then be expressed as

$$
\begin{aligned}
f_i^{\gamma^*}(x_\gamma,\mu_f^2,Q^2) \ = \ & \sum_V \frac{4\pi\alpha}{f_V^2}\left(\frac{m_V^2}{m_V^2+Q^2}\right)^2 p_i^V(x_\gamma,\mu_f^2,\mu_0^2) + \\
+ \ & \frac{\alpha}{2\pi}\sum_q 2e_q^2 \int_{\mu_0^2}^{\mu_f^2}\frac{\mathrm{d}k^2}{k^2}\left(\frac{k^2}{k^2+Q^2}\right)^2 p_i^{q\bar{q}}(x_\gamma,\mu_f^2,k^2)\ .
\end{aligned}
$$

$$(1.30)$$

The parton distributions are decomposed into a non-perturbative component modeled by *vector meson dominance* (VMD) p_i^V and an *anomalous* perturbative component $p_i^{q\bar{q}}$. The VMD component parameterises the non-perturbative fluctuations of the photon to vector mesons $(\rho^0,\ \omega,\ \Phi,\ ...)$ with experimentally determined couplings f_V^2. The anomalous component is given by the perturbatively treatable $q\bar{q}$ virtual photon fluctuation. The scale μ_0^2 represents the border between the non-perturbative and perturbative regimes. There are four models, SAS-1M, SAS-2M, SAS-1D and SAS-2D which differ in their choice of factorisation scheme (DIS (D) or $\overline{\mathrm{MS}}$ (M) [32]) and the scale at which the evolution is started (0.6 or 2.0 GeV indicated by the 1 or 2 in the name, respectively).

Drees and Godbole Model

The model by Drees and Godbole (abbreviated by 'DG') [33] starts with real photon parton densities [35] and suppresses them by a factor $\mathcal{L}$ which depends on Q^2, p_T^2 and a free parameter ω which controls the onset of the suppression:

$$\mathcal{L}(Q^2,p_T^2,\omega^2) = \ln\frac{p_T^2+\omega^2}{Q^2+\omega^2}\ \bigg/ \ln\frac{p_T^2+\omega^2}{\omega^2}\ \ .$$

$$(1.31)$$
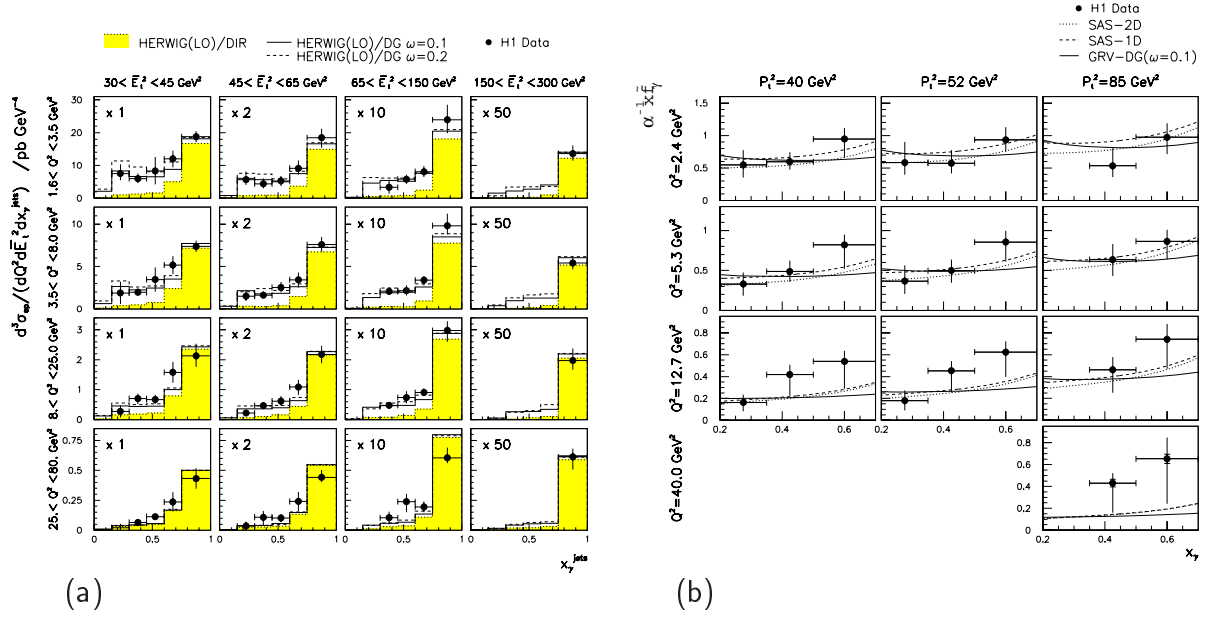
FIGURE 1.11: (a) Triple differential dijet cross section $\mathrm{d}^3\sigma_{ep} \,/\, \mathrm{d}Q^2 \mathrm{d}p_T^2 \mathrm{d}x_\gamma^{jets}$ as measured by H1 [36]. The shaded areas represent a QCD prediction based on direct photon contributions only. The solid and dashed lines correspond to QCD predictions where direct and resolved photon contributions according to the DG model are added. (b) Effective parton density of the virtual photon $f_{eff}^{\gamma^*}$, multiplied by x_γ/α_s, in bins of Q^2 and p_T^2 [36]. Also shown are predictions based on the SaS and DG models.

Quark densities in the real photon are suppressed by $\mathcal{L}$ and the gluon densities by $\mathcal{L}^2$. This ansatz [34] is designed to interpolate smoothly between the leading-logarithmic part of the real photon parton densities, $\sim \ln(p_T^2/\Lambda_{QCD}^2)$, and the asymptotic domain, $p_T^2 \gg Q^2 \gg \Lambda_{QCD}^2$, where the photon density functions are predicted by perturbative QCD to behave as $\sim \ln(p_T^2/Q^2)$.

Comparison with Data

Fig. 1.11a presents a measurement of the triple-differential dijet cross section

$$\mathrm{d}^3\sigma_{ep} \,/\, (\mathrm{d}Q^2 \; \mathrm{d}p_T^2 \; \mathrm{d}x_\gamma^{jets}) \tag{1.32}$$

at low Q^2 [36]. In the region of small Q^2 and $p_T^2 > Q^2$, a leading order QCD prediction with direct photon contributions only is not able to describe the data at low values of x_γ. A much improved description is achieved if a model is used which includes resolved photon contributions as well. The data were used to extract an effective parton density

$$f_{eff}^{\gamma^*} = \sum_i (q_i^{\gamma^*} + \bar{q}_i^{\gamma^*}) + \tfrac{9}{4} g^{\gamma^*} \tag{1.33}$$

of the virtual photon, which is in broad agreement with the DG and SaS models, as shown in Fig. 1.11b.

$y, Q^2 \rightarrow$

$\bar{q}$

$x_\gamma f(x_\gamma, \mu^2, Q^2)$ γ - DGLAP

$x_\gamma, \mu^2 \rightarrow$

q

$\hat{t} \rightarrow$

g

$qg \rightarrow qg$
hard scattering

$x_p f(x_p, \mu^2)$ p - DGLAP

p
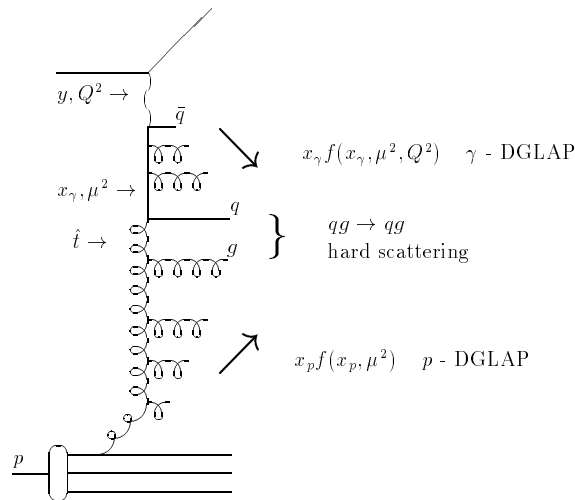
Figure 1.12: Ladder diagram for a resolved virtual photon event in DIS. At the proton as well as the photon sides, QCD evolution according to the DGLAP formalism is assumed. The hard $2 \rightarrow 2$ scattering takes place somewhere in the middle of the ladder where k_T is largest. This leads to non-ordered k_T across the whole ladder (figure from [37]).

Resolved virtual Photons and non-ordered k_T

A ladder diagram for a resolved virtual photon process is shown in Fig. 1.12. For not too small values of the scale μ^2, the parton distributions of the proton and the photon each evolve according to the DGLAP scheme, with strongly ordered $k_{T,i}$ increasing from both ends of the ladder until the hard $2 \rightarrow 2$ scattering process is reached at the largest k_T values. This corresponds to a situation where the strong k_T ordering of the DGLAP approximation is no longer valid across the whole ladder. In this way, the resolved virtual photon approach has a certain similarity to the BFKL approximation, where also the $k_{T,i}$ need not be ordered.

1.2   Diffractive Scattering

In this section, an overview of diffraction in soft hadron interactions and in deep-inelastic scattering is given. For recent reviews of diffractive scattering, see e.g. [38–40]. Hadronic diffraction in general is first introduced following the historical developments in the pre-QCD era. The kinematics of diffractive scattering at HERA and diffractive jet production are then introduced. The modern phenomenological models which try to explain diffractive DIS at HERA, including diffractive jet production, are reviewed.

1.2.1   Diffraction in Soft Hadron Interactions

When studying hadron-hadron collisions, the cross section for hard interaction processes is relatively small, of the order of a few nb. For the hard interaction case, due to the
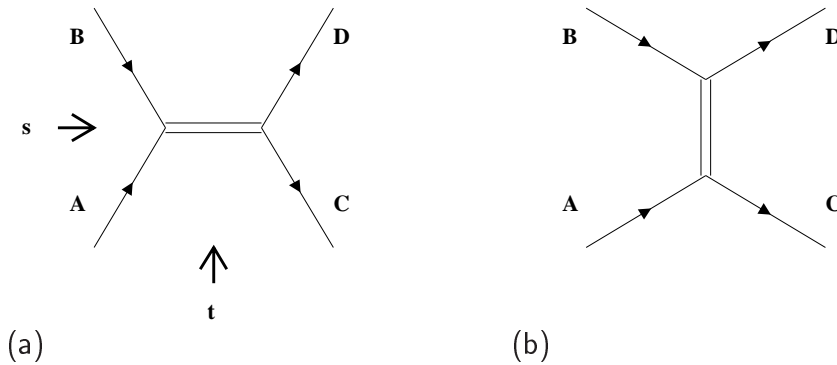
FIGURE 1.13: Generic *(a)* *s*- and *(b)* *t*-channel two-body interactions of the type $A + B \longrightarrow C + D$. The two processes are related by the crossing relations.

hard scale which is provided by the transverse momentum of the produced particles, the value of α_s (see Eq. 1.11) is small and QCD perturbation theory, as described in the previous sections, can be applied. However, the bulk of the interactions is *soft*, with low momentum transfer. α_s is then large and the perturbative expansion in QCD does not converge. Thus, perturbative QCD can not be applied for these interactions.

Regge Phenomenology

Historically, Regge phenomenology was introduced in the beginning of the 1960's [41], the pre-QCD era, to describe soft hadron-hadron interactions at high energy by the *t*-channel exchange of mesons. It is still used as a tool to model soft interactions and elastic scattering, where perturbative QCD cannot be used. In the *S-matrix* prescription, the $2 \to 2$ process $A + B \longrightarrow C + D$ is characterised by the amplitude S

$$S(s, t) = I + iT(s, t) , \tag{1.34}$$

where I is the unit matrix and T is the transition amplitude. S and T are expressed in terms of the Mandelstam variables s and t. In the *s-channel* process (see Fig. 1.13), A and B annihilate to an intermediate state which then decays into C and D. In the *t-channel* reaction, A and B scatter by the exchange of some state. Both types of interactions are related by the crossing relation

$$T_{AB \to CD}(s, t) = T_{A\bar{C} \to \bar{B}D}(t, s) . \tag{1.35}$$

The simplest scattering amplitude to consider is that for the exchange of the lightest meson, the pion, as in the *one pion exchange* (OPE) model [42]. The scattering amplitude contains a propagator of the form:

$$T(s, t) \sim \frac{1}{m_\pi^2 - t} . \tag{1.36}$$

For a *t*-channel exchange, $t < 0$, which leads to a pole at $t = m_\pi^2$ in the unphysical region of $t > 0$, corresponding to a resonance in the *s*-channel.
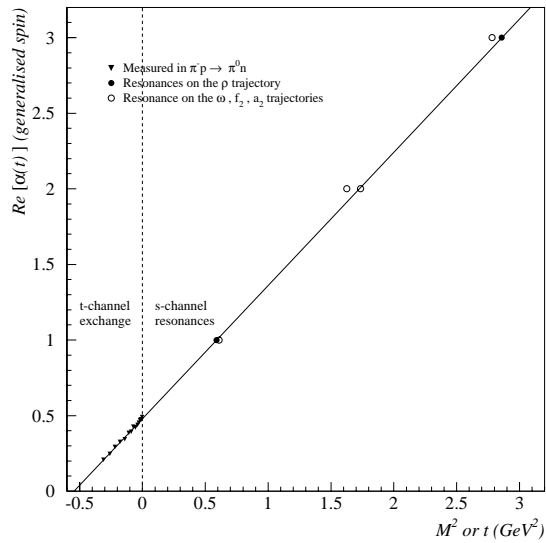
FIGURE 1.14: The leading meson trajectory (comprising the ρ, f, ω and a trajectories; also called *reggeon*) in the $(m^2 = t, J)$ plane. At positive t, it fits through the corresponding s-channel meson resonances. The extrapolation to negative t is in agreement with a measurement of the t-channel charge exchange reaction $\pi^- p \to \pi^0 n$ [43].

To obtain a more accurate and complete description of hadronic cross section amplitudes, it is necessary to sum up contributions from all possible exchanges with the appropriate quantum numbers. It was observed in experiment that groups of mesons with the same quantum numbers but different angular momenta J lie on approximate straight lines in the (m^2, J) plane, where m is the meson mass. In Regge phenomenology, a generalised complex angular momentum $\alpha(t)$ is introduced: $J = \mathrm{Re}\ \alpha(t)$. The dependence of α on t (Fig. 1.14) is parameterised linearly in terms of a *Regge trajectory*:

$$\alpha(t) = \alpha(0) + \alpha' t \; . \tag{1.37}$$

$\alpha(0)$ and α' denote the intercept and the slope of the trajectory. In the asymptotic high-energy, small scattering angle limit $s \to \infty$, $t/s \to 0$, the leading contribution to the elastic scattering amplitude for the scattering of two hadrons a and b is then given by

$$T(s, t) \sim \beta_a(t) \left(\frac{s}{s_0} \right)^{\alpha(t)} \beta_b(t) \; , \tag{1.38}$$

where $\beta_a(t)$ and $\beta_b(t)$ (related to the hadronic *form factors*) describe the dependence on the species of the incoming hadron and s_0 defines a hadronic scale relative to which s must be large (usually $s_0 \simeq 1$ GeV^2). The differential cross section for the elastic t-channel scattering process is then:

$$\frac{\mathrm{d}\sigma}{\mathrm{d}t} \sim \frac{1}{s^2} |T(s, t)|^2 = (\beta_a(t)\beta_b(t))^2 \left(\frac{s}{s_0} \right)^{2\alpha(t)-2} \; . \tag{1.39}$$

Via the optical theorem, the elastic amplitude for $t = 0$ (forward scattering) is related to the total cross section:

$$\sigma_{tot}(s) = \frac{1}{s}\text{Im } T(s, t = 0) \sim \beta_a(0)\beta_b(0)s^{\alpha(0)-1} \; . \tag{1.40}$$

Inserting Eq. 1.37 into Eq. 1.39 and parameterising $\beta(t)$ as $e^{b't}$ yields (for small t):

$$\frac{\mathrm{d}\sigma}{\mathrm{d}t} \sim (\beta_a(t)\beta_b(t))^2 \left(\frac{s}{s_0}\right)^{2\alpha(t)-2} = \frac{\mathrm{d}\sigma}{\mathrm{d}t}\bigg|_{(t=0)} e^{Bt} \; , \tag{1.41}$$

where B is the *slope parameter*

$$B = b_{0,a} + b_{0,b} + 2\alpha'\ln\left(\frac{s}{s_0}\right) \; . \tag{1.42}$$

The energy independent terms $b_{0,a}$ and $b_{0,b}$ arise from the approximate exponential t dependence of the hadron form factors $\beta_{a,b}(t)$. For the proton, a value of $b_{0,p} = 4 \ldots 6 \text{ GeV}^{-2}$ is required by experimental data, which is consistent with the often quoted value for the proton radius $R_p \simeq 1$ fm. The increase of B with centre-of-mass energy s which leads to a steepening of the exponential decrease of the elastic cross section is commonly called *shrinkage*.

The Pomeron Trajectory

Experimentally, total and elastic hadronic cross sections decrease with s up to $\sqrt{s} \simeq 10$ GeV (Fig. 1.15). At higher energies, a rise of the cross sections with s is observed, in contradiction to the fact that the trajectories of all known meson families have $\alpha(0) < 0.6$, which results in a monotonously falling cross section (Eq. 1.40). To resolve this, a new trajectory, the *pomeron*, was introduced by Gribov [46] and named after the Russian theoretician Y. Pomeranchuk. It has since been parameterised as [47]

$$\alpha_{I\!P}(t) = 1.08 + 0.25t \tag{1.43}$$

to accommodate the rise of σ_{tot} with s. Since it mediates elastic scattering, the pomeron carries vacuum quantum numbers ($C = P = +1$).

The postulated $C = P = -1$ partner of the pomeron is called *odderon* [48]. It could manifest itself via a non-vanishing difference of the pp and $p\overline{p}$ total cross sections at very high energies. The odderon may also be observable in exclusive pseudoscalar meson production at HERA [49].

Processes involving pomeron exchange are referred to as *diffractive*, because the t dependence of the elastic process at fixed s is similar to the classical diffraction pattern from the scattering of light off an opaque sphere.

The combination of the meson and pomeron trajectories gives a good parameterisation of hadron-hadron and photon-hadron high-energy interactions at low momentum transfer
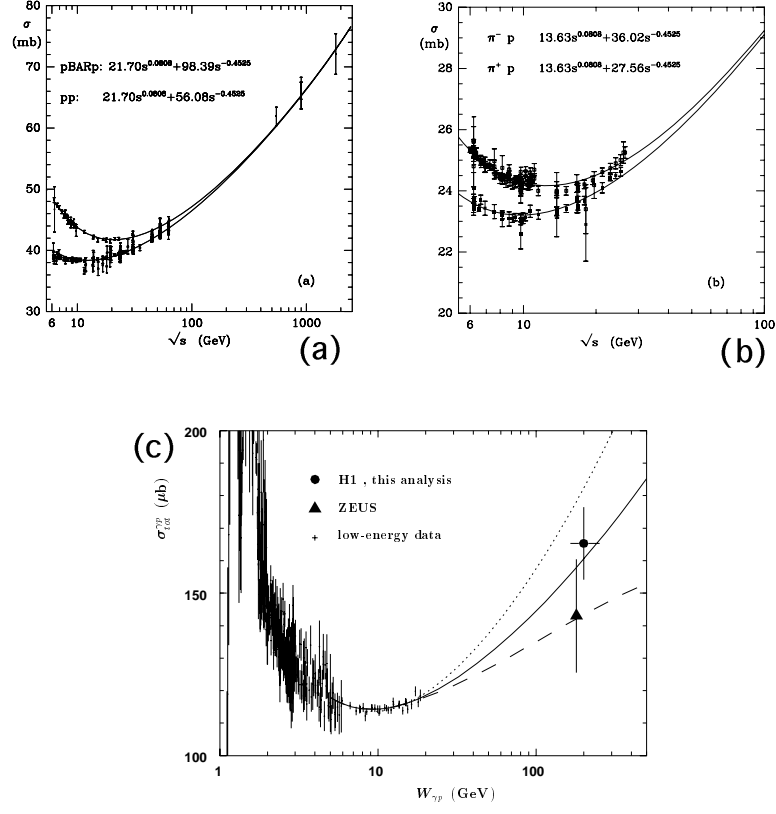
FIGURE 1.15: Total hadron-hadron and photon-hadron cross sections. Shown are *(a)* proton-proton [44], *(b)* pion-proton [44] and *(c)* photon-proton [45] cross sections as a function of the centre-of-mass energy $\sqrt{s}$ or W.

(Fig. 1.15). In [44], a variety of total cross sections, namely for pp, $\overline{p}p$, $\pi^{\pm}p$, $K^{\pm}p$, γp and other processes, were fitted to

$$\sigma_{tot}(s) = C_{I\!P}s^{\alpha_{I\!P}(0)-1} + C_{I\!R}s^{\alpha_{I\!R}(0)-1} . \qquad (1.44)$$

The normalisation parameters $C_{I\!P}$ and $C_{I\!R}$ depend on the specific type of interaction. All considered hadronic cross sections are well described simultaneously for

$$\alpha_{I\!P}(0) = 1.0808 ; \qquad \alpha_{I\!R}(0) = 0.5475 . \qquad (1.45)$$

The parameterisation of total hadronic cross sections at high energies where the energy dependence is given by $s^{\alpha_{I\!P}(0)-1}$ with $\alpha_{I\!P}(0) \simeq 1.08$ is usually referred to as the 'soft pomeron', since it parameterises low momentum transfer cross sections.

'Hard' Pomerons

Recent experimental observations have shown that the energy dependences of some diffractive processes are stronger than those expected from the soft pomeron. In this context,

the term 'hard pomeron' is frequently used. One example is the elastic photoproduction of J/Ψ mesons [50, 51], which requires a pomeron intercept of around 1.2.

Another case is the x dependence of the structure function $F_2(x, Q^2)$. F_2 is related to the total photon-proton cross section by

$$\sigma^{\gamma p} = \frac{4\pi^2 \alpha}{Q^2} F_2(x, Q^2) \bigg|_{Q^2=0} . \tag{1.46}$$

If the x dependence of $F_2(x, Q^2)$ at fixed Q^2 is assumed to follow a simple power behaviour, the power λ can be considered in terms of an effective pomeron intercept according to

$$F_2(x, Q^2) \sim f(Q^2)\, x^{-\lambda} = f(Q^2) \left(\frac{1}{x}\right)^{\alpha(0)-1} \iff \sigma^{\gamma p}(W^2) \sim \left(W^2\right)^{\lambda} = \left(W^2\right)^{\alpha(0)-1} . \tag{1.47}$$

The precise F_2 data from HERA [25] have shown a clear dependence of the effective intercept $\alpha_{I\!P}(0)$ on Q^2, reaching values much larger than the soft pomeron intercept as Q^2 gets large. The general pattern is that the pomeron intercept becomes larger than that of the soft pomeron wherever hard scales such as Q^2 or the charm quark mass are present.

In the following, two parameterisations of 'hard pomerons' are briefly introduced which are relevant for deep-inelastic electron-proton scattering.

Leading Order BFKL Pomeron The power law $x^{-\lambda}$ which is obtained for the gluon distribution in the LO BFKL [26] approximation (Eq. 1.20) can be interpreted as a perturbative QCD 'BFKL pomeron' with intercept $\alpha_{I\!P}^{BFKL}(0) = 1 + \lambda^{LO}$, where $\lambda^{LO} = 0.4 \ldots 0.5$. If the (large) NLO corrections to the BFKL equation are taken into account [27, 52] the intercept of the NLO BFKL pomeron is determined as $\alpha_{I\!P}^{NLO\ BFKL}(0) \simeq 1.17$.

Hard Donnachie-Landshoff Pomeron Donnachie and Landshoff [53] performed fits to $F_2(x, Q^2)$ data for $x < 0.07$ and $Q^2 < 10$ GeV^2, where in addition to the intercepts of the pomeron and reggeon trajectories a third term of the form $x^{1-\alpha_{I\!P}^{hard}(0)}$ is included, which is called 'hard pomeron'. The result of the fit, which also gives a good description of J/Ψ data [50], is $\alpha_{I\!P}^{hard}(0) = 1.42 \pm 0.05$.

Inelastic Diffraction in γp Interactions

Diffraction is not only relevant for elastic and total hadronic cross sections. It also exists in inelastic processes, where one or both of the hadrons *dissociate* into an unbound state in a high-mass continuum. This is observed not only in hadron-hadron collisions, but also in photon-hadron interactions as studied at the HERA *ep* collider. In γp scattering, there are four principle types of diffractive processes (see Fig. 1.16): The photon can fluctuate into a vector meson with the quantum numbers of the photon ($J^{PC} = 1^{--}$), where the proton either stays intact (*elastic vector meson production*) or dissociates into a system Y of (small) mass M_Y (*proton dissociative vector meson production*). The photon can also dissociate into a high-mass system X with mass M_X. Also in this case,
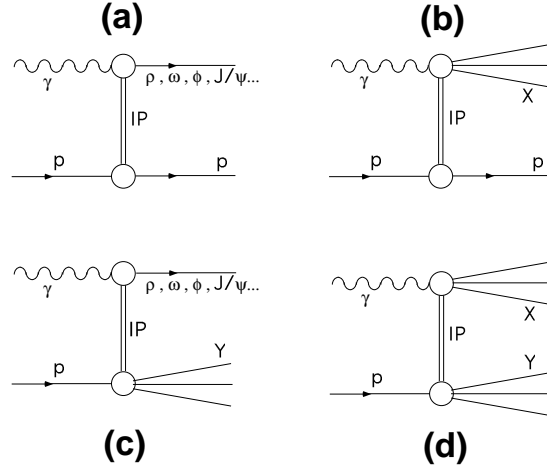
Figure 1.16: The four principal diffractive processes in photon-proton interactions: *(a)* Elastic vector meson production, *(b)* proton elastic photon dissociation, *(c)* proton dissociative vector meson production and *(d)* double dissociation.

the proton can either stay intact or dissociate into a Y system.

In the analysis presented in this thesis, diffractive photon-proton interactions are studied where the photon dissociates into a high-mass system X. The proton either stays intact or dissociates into a very low-mass system Y (Figs. 1.16b,d).

1.2.2 Diffraction in Deep-Inelastic Scattering

Diffractive events were also observed in deep-inelastic ep scattering (DIS) at the HERA ep collider [1]. In approximately 10% of all DIS events, there is no hadronic final state activity observed in the region of the outgoing proton. Such activity is normally produced by the remnant of the proton or the colour flow from the proton debris to the struck quark. This signature is attributed to a diffractive exchange between the photon and the proton.

Kinematics

The kinematics of diffractive DIS at HERA are visualised in Fig. 1.17. The electron couples to a virtual photon γ^* which interacts with the proton by a colourless exchange, producing two final state systems X and Y of the dissociating photon and proton, respectively. The definitions of the DIS kinematical variables as introduced in section 1.1.1 remain valid also in diffractive DIS. In addition, several new variables are introduced. If the 4-vectors of the X and Y systems are denoted p_X and p_Y, the masses are given by:

$$M_X = p_X^2 \; ; \qquad M_Y = p_Y^2 \; . \tag{1.48}$$

In the case where M_X and M_Y are small compared with W, the systems are separated by a large rapidity gap. The longitudinal momentum fraction of the colourless exchange
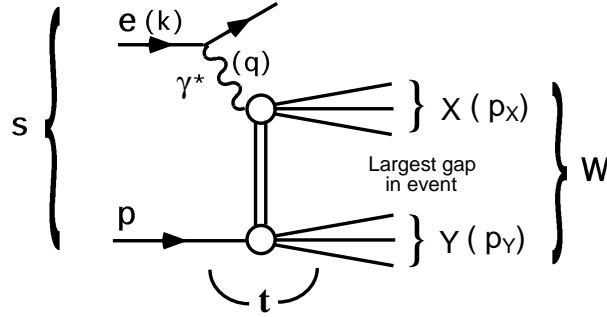
FIGURE 1.17: The kinematics of diffractive DIS. The electron couples to a virtual photon γ^* which interacts with the proton by a colourless exchange, producing two final state systems X and Y. If the masses of X and Y are small compared with W, the two systems are separated by a large rapidity gap.

with respect to the proton $x_{I\!P}$ and the squared 4-momentum transferred at the proton vertex t are then defined by:

$$x_{I\!P} = \frac{q \cdot (P - p_Y)}{q \cdot P} \; ; \qquad t = (P - p_Y)^2 \; . \tag{1.49}$$

In addition, the quantity β is defined as

$$\beta = \frac{x}{x_{I\!P}} = \frac{-q^2}{2q \cdot (P - p_Y)} \; . \tag{1.50}$$

In an interpretation in which partonic structure is ascribed to the colourless exchange, β is the longitudinal momentum fraction of the exchange that is carried by the struck quark, in analogy to x in the case of inclusive scattering.

The Diffractive Structure Function

As for the case of *inclusive* DIS, i.e. without the requirement of a rapidity gap, the cross section for diffractive DIS can be expressed in terms of a structure function, the so-called *diffractive structure function F_2^D*. In the most general case, the diffractive cross section depends on five variables[3]:

$$\frac{\mathrm{d}^5 \sigma_{ep \to eXY}}{\mathrm{d}x_{I\!P} \, \mathrm{d}\beta \, \mathrm{d}Q^2 \, \mathrm{d}M_Y \, \mathrm{d}t} = \frac{4\pi\alpha^2}{\beta Q^4} \left(1 - y + \frac{y^2}{2(1 + R^{D(5)})} \right) \; F_2^{D(5)}(\beta, Q^2, x_{I\!P}, M_Y, t) \; . \tag{1.51}$$

$R^D = \sigma_L^D / \sigma_T^D$ is the ratio of the diffractive longitudinal to transverse photon cross sections. In the analysis presented in this thesis, contributions from longitudinal photon exchange are neglected.

---

[3]Dependences on azimuthal angles are not considered here.
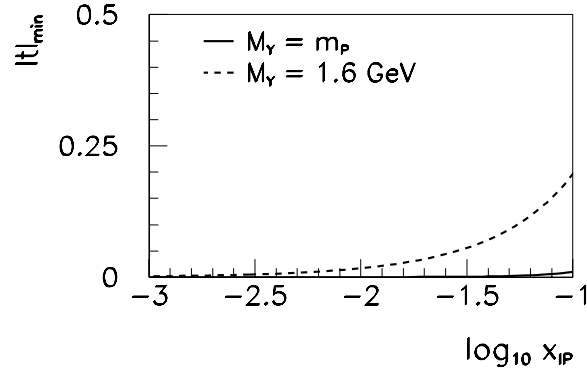
FIGURE 1.18: Dependence of $|t|_{min}$ on $x_{I\!P}$. The minimum kinematically allowed value of $|t|$ is shown as a function of $\log x_{I\!P}$ for $M_Y = m_P$ and $M_Y = 1.6$ GeV.

If the outgoing dissociating proton system Y is not detected and escapes through the beam pipe, t and M_Y are not measured and hence are integrated over implicitly. The data are then interpreted in terms of the triple-differential structure function $F_2^{D(3)}$:

$$\frac{\mathrm{d}^3 \sigma_{ep \to eXY}}{\mathrm{d}x_{I\!P}\, \mathrm{d}\beta\, \mathrm{d}Q^2} = \frac{4\pi\alpha^2}{\beta Q^4}\left(1 - y + \frac{y^2}{2}\right)\, F_2^{D(3)}(\beta, Q^2, x_{I\!P})\ , \tag{1.52}$$

with

$$F_2^{D(3)}(\beta, Q^2, x_{I\!P}) = \int_{m_P}^{M_{Y,max}} \mathrm{d}M_Y \int_{t_{max}}^{t_{min}} \mathrm{d}t\ F_2^{D(5)}(\beta, Q^2, x_{I\!P}, M_Y, t)\ . \tag{1.53}$$

$M_{Y,max}$ and t_{max} are the upper and lower[4] bounds for M_Y and t, respectively. t_{min} is the lowest kinematically allowed value of $|t|$ and is approximately given by:

$$t_{min} \simeq m_P^2 x_{I\!P} - \frac{M_Y^2 x_{I\!P}}{1 - x_{I\!P}}\ . \tag{1.54}$$

The dependence of $|t_{min}|$ on $x_{I\!P}$ and M_Y in the ranges relevant for the analysis presented here is shown in Fig. 1.18. t_{min} only becomes significantly different from zero if M_Y and $x_{I\!P}$ are close to their upper limits.

1.2.3 The Proton Rest Frame and Diffractive Jet Production

Viewing DIS at low x in the proton rest frame, the virtual photon splits into a $q\bar{q}$ pair well before the interaction with the proton (Fig. 1.19a). The $q\bar{q}$ state may then scatter elastically with the proton. The production of high p_T final states by the diffractive $q\bar{q}$ scattering process is heavily suppressed [55] and the invariant masses M_X produced are typically small. It is thus expected that for large values of M_X or p_T, $\mathcal{O}(\alpha_s)$ contributions

---

[4]Note that $t < 0$ for t channel reactions.

Proton rest frame   **Proton infinite momentum frame**

(a)   **(b)**
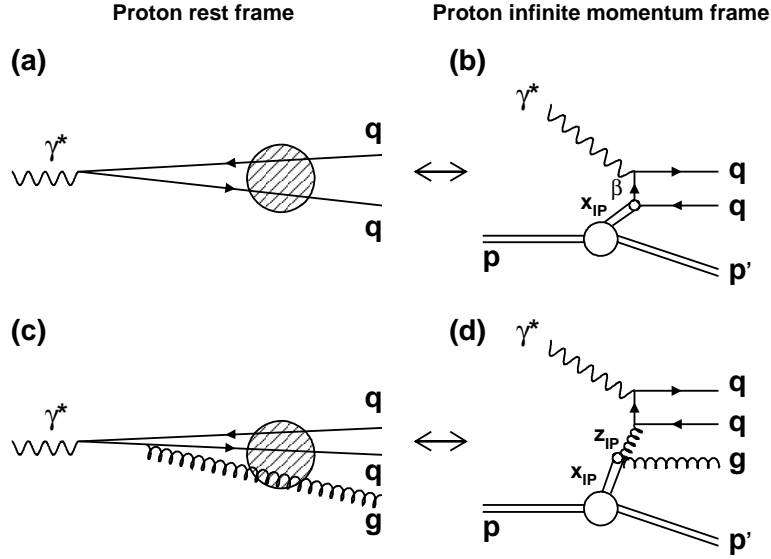
FIGURE 1.19: Diffractive scattering in the proton rest frame and the proton infinite momentum frame. In the proton rest frame, the virtual photon dissociates into a $q\bar{q}$ state (a), scattering off the proton by colour singlet (e.g. 2-gluon) exchange. In the infinite momentum frame, this can be related to diffractive quark scattering (b). The emission of an additional gluon forms an incoming $q\bar{q}g$ state (c). If the gluon is the lowest p_T parton, this contribution can be related to diffractive Boson-Gluon-Fusion (d) (figure after [54]).

due to the radiation of an extra gluon become important [56,57]. The result is an incoming $q\bar{q}g$ system (Fig. 1.19c).

In the proton infinite momentum frame, the lowest order (i.e. $\mathcal{O}(\alpha_s^0)$) contribution to the diffractive cross section is the diffractive quark scattering diagram (Fig. 1.19b). The $\mathcal{O}(\alpha_s)$ contributions are diffractive Boson-Gluon-Fusion (BGF) and QCD-Compton (QCDC) scattering. Unlike inclusive diffractive scattering, diffractive jet production is directly sensitive to the diffractive gluon distribution due to the direct coupling to the gluon in the case of the BGF diagram (Fig. 1.19d).

There is a correspondence between the proton rest frame and the infinite momentum frame pictures, which is discussed here in the context of the leading $\log(Q^2)$ approximation. Diffractive $q\bar{q}$ scattering (Fig. 1.19a) can be related to the diffractive quark scattering diagram (Fig. 1.19b). If the gluon is the lowest p_T parton, diffractive $q\bar{q}g$ scattering (Fig. 1.19c) can be related to diffractive BGF (Fig. 1.19d). If the q or $\bar{q}$ is the lowest p_T parton, the process corresponds to diffractive QCDC scattering (not shown). In the case of 2-gluon exchange (section 1.2.7), additional diagrams have to be taken into account in Fig. 1.19b,d where the two gluons couple to different partons.

Because of the non-zero invariant mass squared $\hat{s}$ of the two highest p_T partons emerging from the hard interaction in the $\mathcal{O}(\alpha_s)$ case, a new variable $z_{I\!P}$ is introduced:

$$z_{I\!P} = \beta \cdot \left(1 + \frac{\hat{s}}{Q^2}\right) \; . \tag{1.55}$$

Similarly to β for the case of the lowest order diagram, $z_{I\!\!P}$ corresponds to the longitudinal momentum fraction of the exchange which takes part in the hard interaction.

1.2.4   Diffractive Parton Distributions

In the leading $\log(Q^2)$ approximation, the cross section for the diffractive process $\gamma^* p \rightarrow p'X$ can be written in terms of convolutions of universal partonic cross sections $\hat{\sigma}^{\gamma^* i}$ with diffractive parton distributions f_i^D, representing probability distributions for a parton i in the proton under the additional constraint that the proton remains intact with particular values of $x_{I\!\!P}$ and t: Thus, at leading twist[5],

$$\frac{\mathrm{d}^2 \sigma(x, Q^2, x_{I\!\!P}, t)^{\gamma^* p \rightarrow p'X}}{\mathrm{d}x_{I\!\!P}\,\mathrm{d}t} \;=\; \sum_i \int_x^{x_{I\!\!P}} \mathrm{d}\xi\; \hat{\sigma}^{\gamma^* i}(x, Q^2, \xi)\; f_i^D(\xi, Q^2, x_{I\!\!P}, t)\;. \qquad (1.56)$$

This hard scattering factorisation formula for diffractive DIS holds for large enough Q^2 and fixed x, $x_{I\!\!P}$ and t. This ansatz was first introduced in [58] and applied to hard diffraction in [59]. The proof of Eq. 1.56 for inclusive diffractive lepton-hadron scattering was given in [60] in the framework of a scalar model and in [61] for full QCD. The diffractive parton distributions are not known from first principles, though they should obey the DGLAP [24] evolution equations.

Recently, there have been attempts to calculate the diffractive parton distributions at a starting scale μ_0^2 for QCD evolution under certain assumptions. In [62], the proton is replaced by a small-size pair of heavy quarks, such that perturbation theory can be applied. A different approach is the semiclassical model by Buchmüller, Gehrmann and Hebecker [54], based on the opposite extreme of a very large hadron. In spite of the different assumptions, the two approaches give rather similar results for the diffractive parton distributions. The parton distributions follow the same general behaviour at the endpoints $z = 0, 1$ and the gluon distribution is much larger than the quark distribution. The endpoint behaviour of the gluon distribution is given by:

$$\lim_{z \rightarrow 0} g^D(z) \sim z^{-1}\;; \qquad \lim_{z \rightarrow 1} g^D(z) \sim (1-z)^2\;. \qquad (1.57)$$

In Fig. 1.20, the diffractive parton distributions and the resulting diffractive structure function F_2^D as obtained from the model in [62] are shown.

1.2.5   Resolved Pomeron Model

The application of Regge phenomenology of soft hadronic high energy interactions to the concept of diffractive parton distributions leads to the Ingelman-Schlein model of a 'resolved pomeron' with a partonic structure [63] invariant under changes in $x_{I\!\!P}$ and t. The diffractive parton distributions then factorise into a flux factor $f_{I\!\!P/p}$ and pomeron parton distributions $f_i^{I\!\!P}$:

$$f_i^D(x, Q^2, x_{I\!\!P}, t) \;=\; f_{I\!\!P/p}(x_{I\!\!P}, t) \cdot f_i^{I\!\!P}(\beta = x/x_{I\!\!P}, Q^2)\;. \qquad (1.58)$$

---

[5]'Leading twist' means that non-leading powers of Q are neglected.
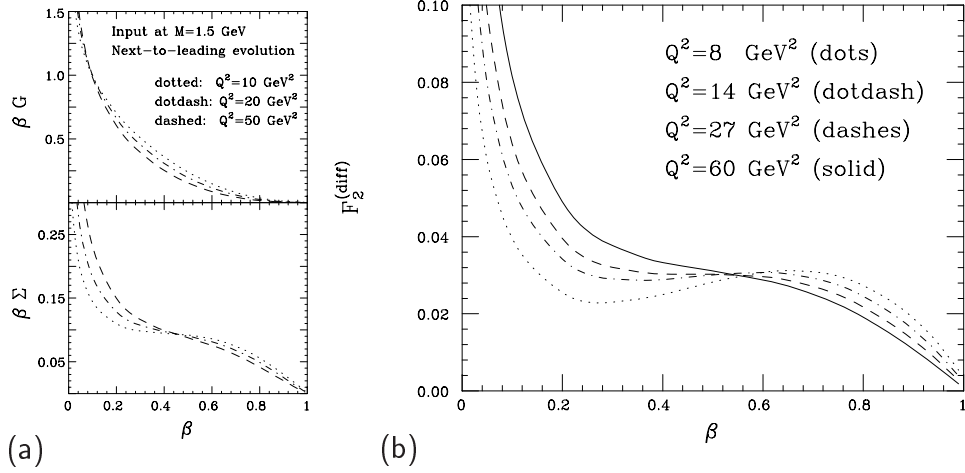
FIGURE 1.20: Parameterisations of diffractive parton distributions and the diffractive structure function F_2^D from [62]. (a) The diffractive gluon (top) and quark singlet (bottom) distributions are shown for different values of the scale Q^2. (b) The corresponding diffractive structure function F_2^D as a function of β for different Q^2.

The universal flux factor describes the probability of finding a pomeron in the proton as a function of $x_{I\!P}$ and t. The pomeron parton distributions are usually expressed in terms of $\beta = x/x_{I\!P}$. Equivalently, the diffractive structure function $F_2^{D(4)}(x_{I\!P}, t, \beta, Q^2)$ factorises:

$$F_2^{D(4)}(x_{I\!P}, t, \beta, Q^2) = f_{I\!P/p}(x_{I\!P}, t) \cdot F_2^{I\!P}(\beta, Q^2) \ . \tag{1.59}$$

Here, $F_2^{I\!P}(\beta, Q^2)$ denotes the pomeron structure function which is, by analogy to $F_2(x, Q^2)$, related to the pomeron parton distributions and obeys the usual DGLAP QCD evolution equations:

$$F_2^{I\!P}(\beta, Q^2) = \sum_i e_i^2 \ \beta \ q_i^{I\!P}(\beta, Q^2) \ . \tag{1.60}$$

In the following, two parameterisations of the resolved pomeron model are presented which will be confronted with the measured diffractive jet cross sections in chapter 7.

The H1 parameterisation

The H1 collaboration has interpreted their measurements of the inclusive diffractive structure function $F_2^{D(3)}$ in terms of a resolved pomeron model [3] (Fig. 1.21). At the largest $x_{I\!P}$ studied, it was necessary to consider more generally contributions from sub-leading reggeon exchanges as well as the pomeron, such that (neglecting possible interference terms)

$$F_2^{D(4)}(x_{I\!P}, t, \beta, Q^2) = f_{I\!P/p}(x_{I\!P}, t) \cdot F_2^{I\!P}(\beta, Q^2) \ + \ f_{I\!R/p}(x_{I\!P}, t) \cdot F_2^{I\!R}(\beta, Q^2) \ . \tag{1.61}$$

The flux factors for the pomeron and reggeon exchanges were parameterised in a Regge-inspired form:

$$f_{\{I\!P, I\!R\}/p}(x_{I\!P}, t) = C_{\{I\!P, I\!R\}} \ \left(\frac{1}{x_{I\!P}}\right)^{2\alpha_{\{I\!P, I\!R\}}(t)-1} e^{b_{\{I\!P, I\!R\}} t} \ , \tag{1.62}$$

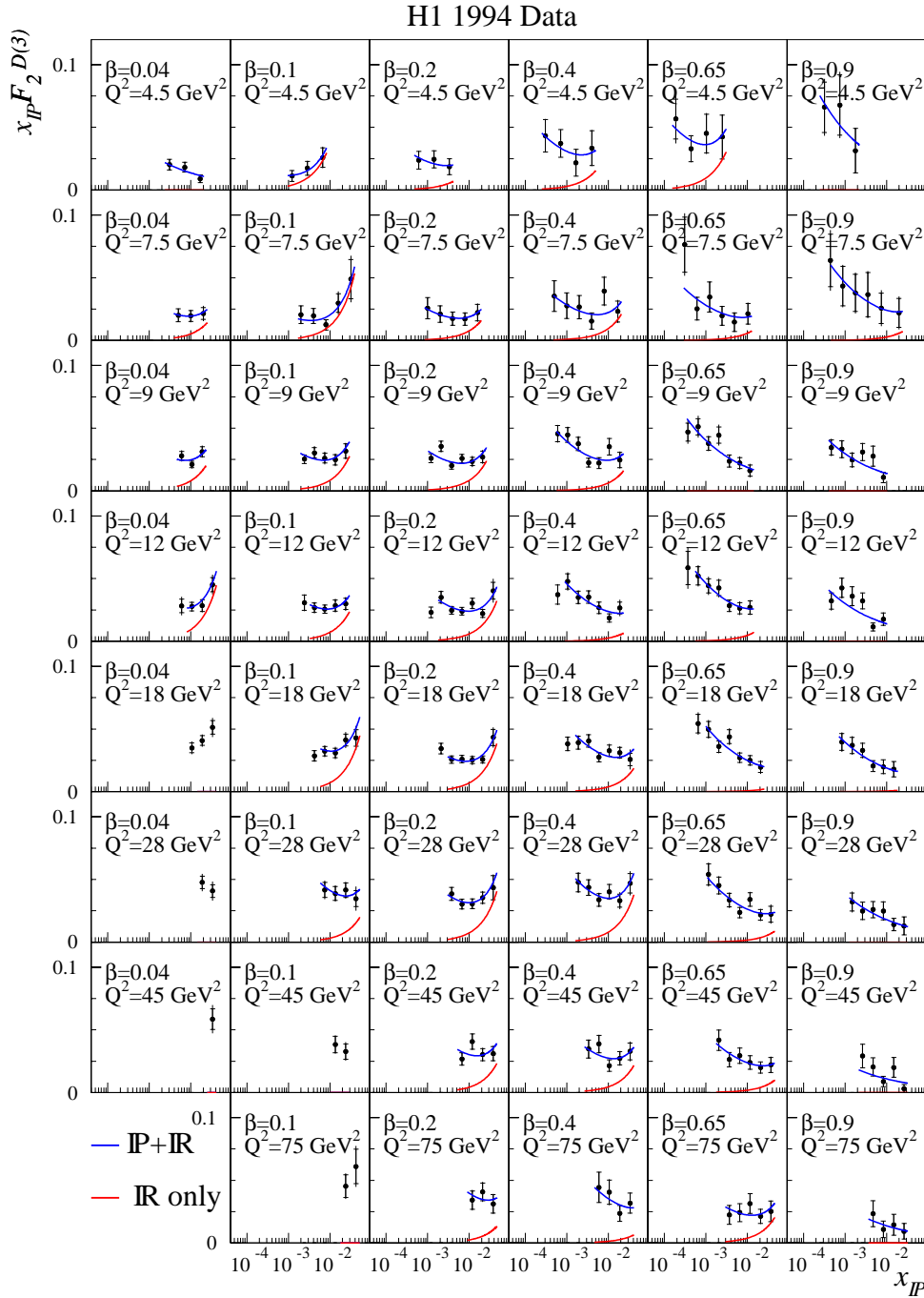Figure 1.21: The measurement in [3] of the diffractive structure function, plotted as $x_{I\!P} F_2^{D(3)}(x_{I\!P}, \beta, Q^2)$. Overlaid is the result of a Regge parameterisation of the data, where the reggeon contribution only *(lower lines)* and the sum of pomeron and reggeon contributions *(upper lines)* are shown.

with

$$\alpha_{\{I\!\!P,I\!\!R\}}(t) = \alpha_{\{I\!\!P,I\!\!R\}}(0) + \alpha'_{\{I\!\!P,I\!\!R\}} t \ . \tag{1.63}$$

From fits in which the parton densities evolve according to the DGLAP equations, parameterisations of the pomeron quark and gluon distributions and values for $\alpha_{I\!\!P}(0)$ and $\alpha_{I\!\!R}(0)$ were obtained. The resulting value of

$$\alpha_{I\!\!P}(0) = 1.203 \pm 0.020 \ (\text{stat.}) \pm 0.013 \ (\text{syst.}) \pm 0.030 \ (\text{model}) \tag{1.64}$$

is significantly higher than that obtained from soft hadronic interactions, where $\alpha_{I\!\!P}(0) \simeq 1.08$ [44,64] (see section 1.2.1).

For the pomeron parton densities, it was assumed that the pomeron is an iso-singlet and self charge-conjugate. A light quark singlet density

$$q_i^{I\!\!P}(z) = u(z) + d(z) + s(z) + \bar{u}(z) + \bar{d}(z) + \bar{s}(z) \tag{1.65}$$

and a gluon density $g^{I\!\!P}(z)$ were parameterised at the starting scale $\mu_0^2 = 3 \text{ GeV}^2$. The DGLAP QCD evolution was performed at leading order. The parton densities extracted for the pomeron, shown in Fig. 1.22, are dominated by gluons, which carry $80 - 90\%$ of the exchanged momentum throughout the measured Q^2 range. The two solutions of the fit, labelled 'fit 2' and 'fit 3', differ mainly in the shape of the gluon distribution at large z. This is a reflection of the uncertainties related to extracting the gluon distribution in an indirect way from the scaling violations. At large $z = \beta$, the gluon distribution is not well constrained because $F_2^{D(3)}$ data with $\beta > 0.65$ were excluded from the fits. The 'fit 3' parameterisation ($\chi^2/\text{ndf} = 176/156$) is preferred by the data with respect to 'fit 2' ($\chi^2/\text{ndf} = 187/156$). Pomeron parton distributions where only quarks contribute at the starting scale of the QCD evolution (e.g. 'fit 1' in [3]) fail to reproduce the observed scaling violations of $F_2^{I\!\!P}(\beta, Q^2)$.

The ACTW parameterisation

Alvero, Collins, Terron and Whitmore [65] have performed combined fits to inclusive diffractive structure function measurements by the H1 [3] and ZEUS [4,66] collaborations and to diffractive jet production in photoproduction as measured by ZEUS [67]. A parameterisation of the pomeron flux factor is used in which dependences on t are neglected:

$$f_{I\!\!P/p}(x_{I\!\!P}) = C \left(\frac{1}{x_{I\!\!P}} \right)^{2\alpha_{I\!\!P} - 1} \ . \tag{1.66}$$

Because only data with low $x_{I\!\!P}$ values were included in the fits, sub-leading reggeon exchanges are not taken into account. A series of fits were made where the pomeron parton distributions were evolved in NLO, using the $\overline{MS}$ scheme [32], from a starting scale $\mu_0^2 = 4 \text{ GeV}^2$. The best fit is labelled 'D', in which the value of the pomeron intercept is set to $\alpha_{I\!\!P}(0) = 1.19$.

It should be noted that there are indications [11] that the the diffractive photoproduction cross section at HERA is suppressed if the photon is resolved, possibly due to
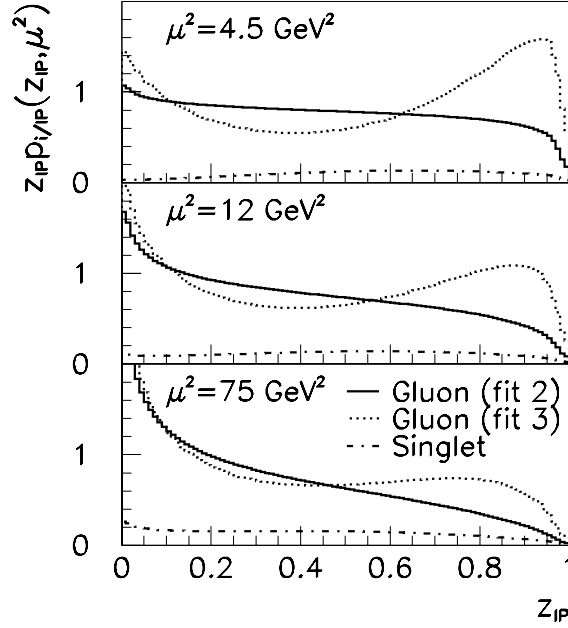
FIGURE 1.22: Pomeron parton densities, extracted from a leading order DGLAP QCD analysis of $F_2^{D(3)}(x_{I\!P}, \beta, Q^2)$ [3]. Shown are two parameterisations ('H1 fit 2' and 'H1 fit 3') of the quark singlet and gluon distributions, evaluated at three values of the scale μ^2. The quark singlet distributions are very similar for the two fits and therefore not plotted separately. The distributions are normalised such that the pomeron flux $f_{I\!P/p}(x_{I\!P} = 0.003, t = 0)$ is unity.

secondary interactions which destroy the rapidity gap. This effect was not taken into account in the ACTW fits, where the pomeron gluon distribution is mainly constrained by the photoproduction jet data.

1.2.6   Soft Colour Neutralisation

An alternative approach to diffractive DIS is given by soft colour neutralisation models, which naturally lead to very similar properties of inclusive and diffractive DIS final states.

Soft Colour Interactions

In the Soft Colour Interaction (SCI) model by Edin, Ingelman and Rathsman [68], the hard interaction in diffractive DIS is treated identically to that in inclusive DIS. Diffraction occurs through soft colour rearrangements between the outgoing partons, leaving their momentum configuration unchanged. If two colour singlet systems are produced by such a mechanism, the hadronic final state can exhibit a large rapidity gap (Fig. 1.23). In the original SCI model, diffractive final states are produced using only one additional free parameter, the universal colour rearrangement probability P_0, which is fixed by a fit to $F_2^{D(3)}$.
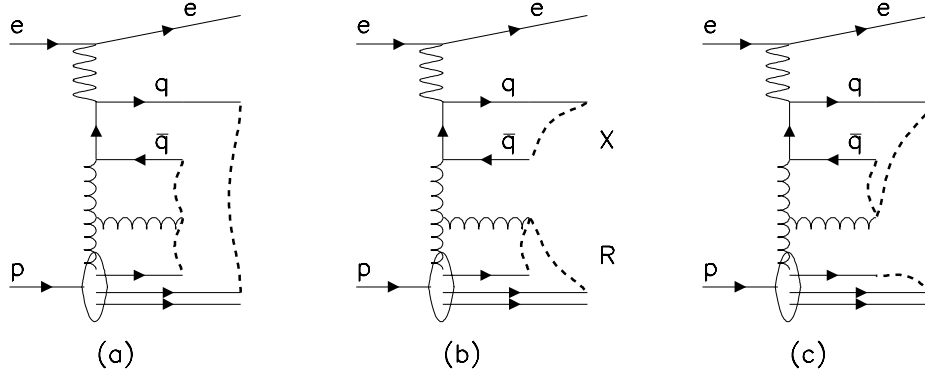
FIGURE 1.23: The Soft Colour Interaction (SCI) model for diffractive DIS [68]. *(a)* In deep-inelastic scattering, colour strings *(dashed lines)* are spanned between the final state partons and the proton remnant. *(b,c)* Soft colour interactions can lead to rearrangements of the colour strings and hence to colour singlet configurations in the final state.

The model has been refined recently [69]. In the Lund string model [70], the so-called *area law* ensures that large-size string configurations are exponentially suppressed. Here, the area of a string spanned between two partons is defined as

$$A_{ij} = (p_i + p_j)^2 - (m_i + m_j)^2 \; = \; 2(p_i p_j - m_i m_j) \; . \tag{1.67}$$

For the production of rapidity gaps by Soft Colour Interactions, a *generalised area law* is introduced in [69] which makes the colour rearrangement probability proportional to the normalised difference in the generalised areas of the string configurations before and after the rearrangement. The probability can thus be written as:

$$P_{ij} = R_0(1 - \exp(-b\Delta A_{ij})) \; , \tag{1.68}$$

where R_0 and b are free parameters which are determined by fits to $F_2^{D(3)}$ data.

Semiclassical Model

Another approach is the semiclassical model by Buchmüller, Gehrmann and Hebecker [54], a non-perturbative model which was already mentioned in section 1.2.4. Viewed in the proton rest frame, $q\bar{q}$ and $q\bar{q}g$ fluctuations of the virtual photon scatter off a superposition of soft colour fields associated with the proton. Those configurations which emerge in a net colour singlet configuration contribute to the diffractive cross section [57]. The calculation is performed under the assumption of a very large hadron. The gluonic fields encountered by the partonic probe in distant regions of the target are uncorrelated (see Fig. 1.24).

The result is formulated as a parameterisation of t-integrated diffractive parton distributions f_i^D [71], which are shown in Fig. 1.25. An $x_{I\!\!P}$ or energy dependence is put into the model which reflects the assumption that with increasing energy of the $q\bar{q}$ or $q\bar{q}g$
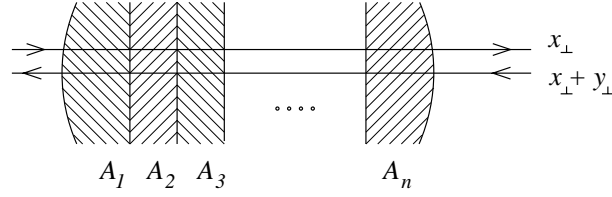
FIGURE 1.24: Semiclassical model [54]. A colour dipole is travelling through a large hadron, interacting with uncorrelated gluonic colour fields A_i. $x_\perp$ and $y_\perp$ are transverse coordinates.
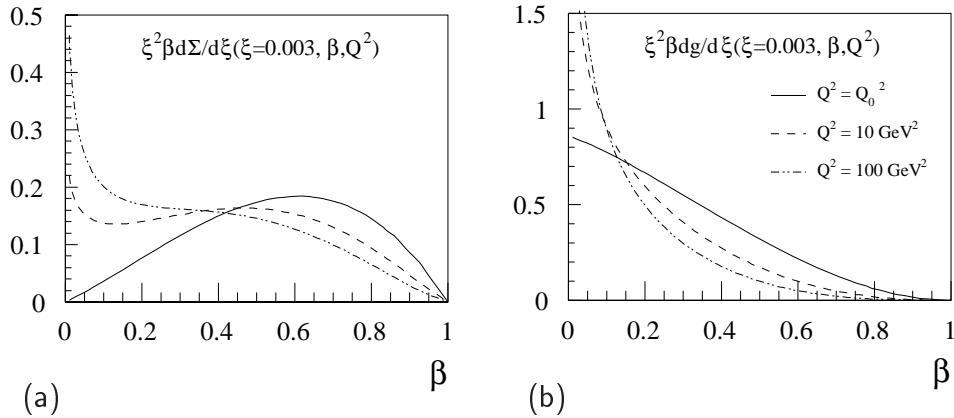
FIGURE 1.25: The diffractive quark singlet *(a)* and gluon *(b)* distributions in the semi-classical model [54], multiplied by $\xi^2 \equiv x_{I\!P}^2$ and evaluated at $\xi^2 \equiv x_{I\!P}^2 = 0.003$.

probe, more and more modes of the gluonic proton field are 'seen' by the probe. This is parameterised as a soft logarithmic increase of the cross section with energy:

$$\frac{\mathrm{d}f_i^D(x_{I\!P}, \beta, Q^2)}{\mathrm{d}x_{I\!P}} \sim (L - \ln x_{I\!P})^2 f_i^D(\beta, Q^2) \ . \tag{1.69}$$

It is noted here that, although Regge factorisation is not implied in the model, Eq. 1.69 demonstrates that the cross section is formulated in a way that the $x_{I\!P}$ dependence is factorising.

The four free parameters of the model (including L) are determined from a combined fit to the inclusive and diffractive structure functions F_2 and F_2^D at x ($x_{I\!P}$) values below 0.01. A detailed description of the model can also be found in [38].

1.2.7 Colour Dipole and 2-Gluon Exchange Models

In the proton rest frame, diffractive DIS is often treated by considering the $q\bar{q}$ and $q\bar{q}g$ photon fluctuations (Fig. 1.26) as (effective) colour dipoles. The diffractive $\gamma^* p$ cross section can be factorised into an effective photon dipole wave function $|\Psi|^2$ and the squared
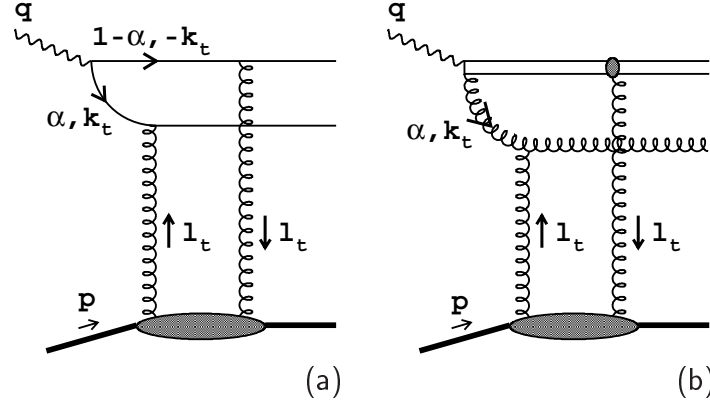
Figure 1.26: Dipole picture of diffractive $q\bar{q}$ (a) and $q\bar{q}g$ (b) electroproduction, mediated by the exchange of two gluons with transverse momenta $\pm\mathbf{l}_t$. The photon is viewed as dissociating into either a quark dipole or an effective gluon dipole, made up of a gluon and a compact $q\bar{q}$ pair (figure from [72]).

'dipole cross section' $\hat{\sigma}^2$ for the scattering of these dipoles off the proton [73, 74]:

$$\left.\frac{\mathrm{d}\sigma^{\gamma^*p}_{T,L}}{\mathrm{d}t}\right|_{t=0} \sim \int \mathrm{d}^2\mathbf{r} \int_0^1 \mathrm{d}\alpha |\Psi_{T,L}(\alpha,\mathbf{r})|^2 \, \hat{\sigma}^2(r^2, x, ...) \ . \tag{1.70}$$

Here, the subscripts T and L denote transverse and longitudinal photon polarisation, $\mathbf{r}$ is the relative transverse separation between the quarks and α, $(1-\alpha)$ are the momentum fractions of the quark and the antiquark.

Many properties of the diffractive final state, for instance the gross features of the diffractive β distribution, can be deduced from a knowledge of the partonic wave functions $\Psi_{T,L}(\alpha,\mathbf{r})$ of the photon alone.

Effective Photon Dipole Wave Functions

The wave functions for the $q\bar{q}$ fluctuation of a transversely polarised photon with helicity $\lambda_\gamma = +1$, expressed in terms of the transverse momentum $\mathbf{k}_t$ instead of the transverse separation $\mathbf{r}$, are given by (see [72] and references therein):

$$\begin{aligned}
\Psi^{+-}_{T,q\bar{q}}(\alpha,\mathbf{k}_t) &= \frac{\sqrt{2}e_q\alpha \, (\mathbf{k}_t \cdot \varepsilon_{\lambda_\gamma=1})}{k_t^2 + \alpha(1-\alpha)Q^2}, \\
\Psi^{-+}_{T,q\bar{q}}(\alpha,\mathbf{k}_t) &= -\frac{\sqrt{2}e_q(1-\alpha) \, (\mathbf{k}_t \cdot \varepsilon_{\lambda_\gamma=1})}{k_t^2 + \alpha(1-\alpha)Q^2} \ .
\end{aligned} \tag{1.71}$$

The wave function indices $\Psi^{\lambda\lambda'}$ denote the helicities of the quark (λ) and the antiquark (λ'). e_q is the quark electrical charge and ε is the polarisation vector. The longitudinal wave functions are

$$\Psi^{+-}_{L,q\bar{q}}(\alpha,\mathbf{k}_t) = \Psi^{-+}_{L,q\bar{q}}(\alpha,\mathbf{k}_t) = \frac{2e_q\alpha(1-\alpha)Q}{k_t^2 + \alpha(1-\alpha)Q^2} \ . \tag{1.72}$$

For the $q\bar{q}g$ photon wave function, the situation is more complicated. One possibility is to apply the leading $\log(Q^2)$ approximation, which is equivalent to a strong ordering of transverse momenta (section 1.1.4). Then, in the limit of large Q^2 and small $k_{T,g} \ll Q$, $\alpha_g \ll 1$, the small separation between the large k_T quark-antiquark pair leads to a combination of their colour structures into an effective gluon which forms, together with the small transverse momentum gluon $g(\alpha_g, k_{T,g})$, an effective gluon dipole. In this approximation [75], the effective wave function for transversely polarised photons can be written as

$$\Psi_{q\bar{q}g} \;\; = \;\; \frac{1}{\sqrt{\alpha Q^2}} \; \frac{k_t^2 (\varepsilon_1 \cdot \varepsilon_2) \; - \; 2(\mathbf{k}_t \cdot \varepsilon_1)(\mathbf{k}_t \cdot \varepsilon_2)}{k_t^2 + \alpha Q^2} \; , \tag{1.73}$$

where $\varepsilon_{1,2}$ are the polarisation vectors of the $q\bar{q}$ and g forming the gluon dipole. Since $\alpha \ll 1$, $(1 - \alpha)$ was replaced by 1.

In a recent QCD motivated parameterisation by Bartels, Ellis, Kowalski and Wüsthoff [76], longitudinally and transversely polarised $q\bar{q}$ states dominate at high and medium values of β respectively. The $q\bar{q}g$ state originating from transversely polarised photons is dominant at low β (high M_X), although it is a higher order contribution which is suppressed by α_s. The β-dependences of the different components, as obtained from the dipole wave functions, are given by

$$\sigma_{T,q\bar{q}} \sim \beta(1 - \beta) \; ; \qquad \sigma_{T,q\bar{q}g} \sim (1 - \beta)^\gamma \; ; \qquad \sigma_{L,q\bar{q}} \sim \beta^3 (1 - 2\beta)^2 \tag{1.74}$$

and to first approximation do not depend on the dipole cross section. The resulting decomposition of the diffractive structure function F_2^D in terms of these contributions is illustrated in Fig. 1.27, where a value of $\gamma \simeq 4$ was used, in agreement with a fit to $F_2^{D(3)}$ data.

The dipole cross section

Investigating diffractive final states with varying transverse momenta k_t probes the dipole cross section as a function of the dipole size. Large size, low k_t configurations interact with the proton similarly to soft hadron-hadron scattering. Small size, high k_t dipole configurations lead to hard scales which encourage a perturbative QCD treatment of the dipole cross section. The precise dynamics of the dipole cross section are not known a priori. However, the simplest realisation of a net colour singlet exchange at the parton level is a pair of gluons with cancelling colour charges [77]. To ensure gauge invariance, all possible couplings of the two t-channel gluons to the quark or effective-gluon dipole have to be considered.

In this picture, the dipole cross section in Eq. 1.70 can be related to the unintegrated gluon distribution $\mathcal{F}(x, l_t^2)$ [26] in the proton [73, 74]:

$$\hat{\sigma}(x, \mathbf{r}) \sim \int \frac{d^2 \mathbf{l}_t}{l_t^2} \left[1 - e^{i\mathbf{r} \cdot \mathbf{l}} \right] \alpha_s(l_t^2) \mathcal{F}(x, l_t^2) \; . \tag{1.75}$$
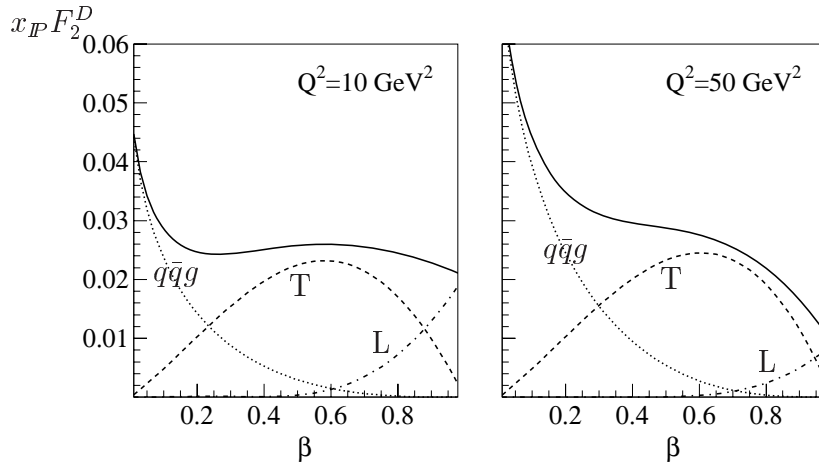
FIGURE 1.27: Decomposition of the diffractive structure function in the dipole picture of [72], shown as $x_{I\!P}F_2^D$ as a function of β for two values of Q^2. The dashed and dashed-dotted lines labelled 'T' and 'L' represent the contribution from transversely and longitudinally polarised $q\bar{q}$ states, respectively, whereas the dotted line corresponds to the contribution from transversely polarised $q\bar{q}g$ states. The upper solid line is the sum of the three contributions.

$\mathbf{l}_t$ denotes the transverse momentum of the t-channel gluon (Fig. 1.26). The diffractive cross section is then proportional to the unintegrated gluon distribution squared.

In the following, two recent models based on the ideas of dipole cross sections and 2-gluon exchange are introduced. Other colour dipole approaches can be found in [56,78,79], for example.

Saturation Model by Golec-Biernat and Wüsthoff

The dipole approach has been employed in the 'saturation' model by Golec-Biernat and Wüsthoff [80]. Here, an ansatz for the dipole cross section is made which interpolates between the perturbative and non-perturbative regions of σ^{γ^*p}. It is mainly a model for inclusive DIS which can also predict the diffractive cross section.

The idea behind the model is to describe the transition between large and small values of Q^2 in inclusive DIS at low x, i.e. the transition between the perturbative QCD regime where the proton structure is parameterised in terms of parton distributions evolving with Q^2 and the non-perturbative regime of vanishing Q^2, usually assessed in terms of Regge phenomenology. *Saturation* in this context means that the strong rise of the cross section towards lower x is damped because the parton density in the proton becomes so high that recombination effects limit a further growth. The nucleon then appears to be *black*. The following ansatz for the dipole cross section is made:

$$\hat{\sigma}(x, r^2) = \sigma_0 \left[1 - \exp\left(-\frac{r^2}{4R_0^2(x)} \right) \right] \; . \tag{1.76}$$

Low-x saturation of $\hat{\sigma}$ is introduced via an x-dependent radius $R_0(x)$:

$$R_0(x) = \frac{1}{\text{GeV}} \left(\frac{x}{x_0} \right)^{\lambda/2} . \tag{1.77}$$

$2R_0$ corresponds approximately to the mean parton separation. Convoluting $\hat{\sigma}$ with the effective dipole wave functions leads to a cross section behaviour which shows Bjorken scaling behaviour for large Q^2 and goes to a constant for $Q^2 = 0$. The relation between $\hat{\sigma}$ and $\mathcal{F}$ is given by

$$\alpha_s \mathcal{F}(x, l_t^2) = \frac{3\sigma_0}{4\pi^2} R_0^2(x) \, l_t^2 \, e^{-R_0^2(x)l_t^2} . \tag{1.78}$$

If Eq. 1.78 is inserted into Eq. 1.75, Eq. 1.76 can be reproduced. This model is able to give a reasonable description of $F_2(x, Q^2)$ at low x, which determines the three free parameters (x_0, λ and σ_0). The parameterised dipole cross section can be re-expressed in terms of the unintegrated gluon density $\mathcal{F}(x, l_t^2)$. Integrating $\mathcal{F}(x, l_t^2)$ at large Q^2 leads back to the ordinary gluon distribution:

$$xg(x, Q^2) \sim (\alpha_s R_0^2(x))^{-1} \sim x^{-\lambda} , \tag{1.79}$$

which shows a plain scaling behaviour because Q^2 evolution is not included in the model. The fit to $F_2(x, Q^2)$ yields $\lambda = 0.228$, higher than the soft pomeron value of 0.08 (see section 1.2.1).

The dipole cross section as parameterised from the fit to the inclusive $F_2(x, Q^2)$ can be used to predict the diffractive cross section at $t = 0$. If an additional free parameter $B = 6.0 \text{ GeV}^{-2}$ is introduced to describe the t dependence as e^{Bt}, the diffractive structure function $F_2^{D(3)}$ is successfully described in this model. The model predicts a constant ratio of the diffractive to the inclusive cross sections. It is important to note that the calculation of the $q\bar{q}g$ cross section using Eq. 1.73 is made under the assumption of strong k_T ordering of the final state partons (leading $\log(Q^2)$ approximation), corresponding to $k_T^{(g)} \ll k_T^{(q,\bar{q})}$.

Model by Bartels et al. (BJLW)

Cross sections for diffractive $q\bar{q}$ and $q\bar{q}g$ production by 2-gluon exchange have been calculated by Bartels, Ewerz, Lotter and Wüsthoff ($q\bar{q}$) [81] and by Bartels, Jung, Kyrieleis and Wüsthoff ($q\bar{q}g$) [82]. In this model, the cross section for a particular diffractive DIS final state consisting of (only) high p_T jets is calculated employing perturbative QCD techniques. It can then be explored how far this approach can be extrapolated into the soft region.

The calculation of the $q\bar{q}g$ final state is performed in a more general way than the leading $\log(Q^2)$ approach which has been employed in the saturation model. To be specific, also contributions where the transverse momentum of the gluon is comparable or larger than those of the quark or antiquark are included in the calculation of the cross section. The calculation is performed in the leading $\log(1/\beta)$, $\log(1/x_{I\!P})$ approximation, retaining all powers of (k_T^2/Q^2), and applies to the region

$$Q^2 \ll M_X^2 \ll W^2 , \tag{1.80}$$

corresponding to $\beta, x_{I\!\!P} \ll 1$. The requirement to be fulfilled in order to apply perturbation theory is that all partons have sufficiently high k_T:

$$k_{T,q}^2, k_{T,\bar{q}}^2, k_{T,g}^2 \gg Q_0^2 \; , \tag{1.81}$$

where Q_0^2 is a typical hadronic scale. The result of the calculation is

$$\frac{\mathrm{d}\sigma}{\mathrm{d}M_X^2 \; \mathrm{d}^2\mathbf{k}_1 \; \mathrm{d}^2\mathbf{k}_2 \; \mathrm{d}t}\bigg|_{t=0} = K \cdot M_{il} M_{il}^* \; , \tag{1.82}$$

where K represents kinematic factors, $\mathbf{k}_1$ and $\mathbf{k}_2$ are the transverse momenta of the quark and the gluon respectively and the matrix element M is given by

$$M_{il} = \int_{\mathbf{l}_{t,min}^2} \frac{\mathrm{d}^2\mathbf{l}_t}{\pi \mathbf{l}_t^2} \; \alpha_s \; \mathcal{F}(x_{I\!\!P}, \mathbf{l}_t^2) \; T_{il} \; . \tag{1.83}$$

$\mathbf{l}_t$ is the t channel gluon transverse momentum. T_{il} represents the $q\bar{q}g$ component of the photon wave function:

$$
\begin{aligned}
T_{il} = & \left(\frac{\mathbf{l}_t + \mathbf{k}_1 + \mathbf{k}_2}{D(\mathbf{l}_t + \mathbf{k}_1 + \mathbf{k}_2)} + \frac{\mathbf{k}_1 + \mathbf{k}_2}{D(\mathbf{k}_1 + \mathbf{k}_2)} - \frac{\mathbf{k}_1 - \mathbf{l}_t}{D(\mathbf{k}_1 - \mathbf{l}_t)} - \frac{\mathbf{k}_1}{D(\mathbf{k}_1)} \right)_i \\
& \left(\frac{\mathbf{l}_t + \mathbf{k}_2}{(\mathbf{l}_t + \mathbf{k}_2)^2} - \frac{\mathbf{k}_2}{\mathbf{k}_2^2} \right)_l \hspace{4cm} + (\mathbf{l}_t \to -\mathbf{l}_t) \; ,
\end{aligned}
\tag{1.84}
$$

with

$$D(\mathbf{k}) = \alpha(1 - \alpha)Q^2 + \mathbf{k}^2 \; . \tag{1.85}$$

The derivative of the next-to-leading order (NLO) GRV [83] gluon parameterisation is used for $\mathcal{F}(x, l_t^2)$. The infrared cut-off $\mathbf{l}_{t,min}^2$ for the t channel gluon transverse momentum is tuned to reproduce the GRV parameterisation. The calculations require all outgoing partons to have high p_T (Eq. 1.81) and are thus not suited to describe $F_2^{D(3)}$. The minimum value

$$k_{2,min} \equiv p_{T,g}^{\mathrm{cut}} \tag{1.86}$$

for the final state gluon transverse momentum is a free parameter. As for the saturation model, the calculation yields predictions at $t = 0$. The extension to finite t is performed using the Donnachie-Landshoff elastic proton form factor [84]. The sum of the $q\bar{q}$ and $q\bar{q}g$ contributions in this model is hereafter referred to as 'BJLW'.

Chapter 2

Previous H1 Results on Diffractive Final States

In this chapter, previous results on diffractive final states in DIS which were obtained within the H1 collaboration are presented. Here, the focus is on high-p_T jet or heavy quark production, where a hard scale in addition to Q^2 is provided. Other H1 results on diffractive final states can be found in [85].

2.1   Diffractive Dijet Production

The first measurement of diffractive dijet production in DIS [11] was based on data taken in 1994, corresponding to an integrated luminosity of 2.0 pb^{-1}. The basic selection cuts were $7.5 < Q^2 < 80$ GeV^2, $0.1 < y < 0.7$, $x_{I\!\!P} < 0.05$ and $p_{T,jet} > 5$ GeV. 55 events were selected and thus the measurement was clearly statistically limited. Differential cross sections (Fig. 2.1) were measured as functions of the transverse momentum of the jets $p_{T,jet}$ and of $z_{I\!\!P}^{jets}$, a hadron level estimator for the momentum fraction of the colourless exchange which enters the hard process (Eq. 1.55).

The data were compared with the resolved pomeron model according to the H1 parameterisation (see section 1.2.5). Even with the limited statistics available at that time, the conclusion could be drawn that in such a model pomeron parton distributions which contain only quarks at the starting scale of the QCD evolution ('fit 1') fail to accommodate the observed dijet rate, consistent with what was observed in the QCD analysis of $F_2^{D(3)}$. The $z_{I\!\!P}^{jets}$ distribution was also compared with the BJLW 2-gluon exchange model (section 1.2.7). At that time, only the calculation of the $q\overline{q}$ cross section [81] was available, shown in Fig. 2.1b as the hatched area. The conclusion was that this contribution alone is not able to describe the dijet rate.
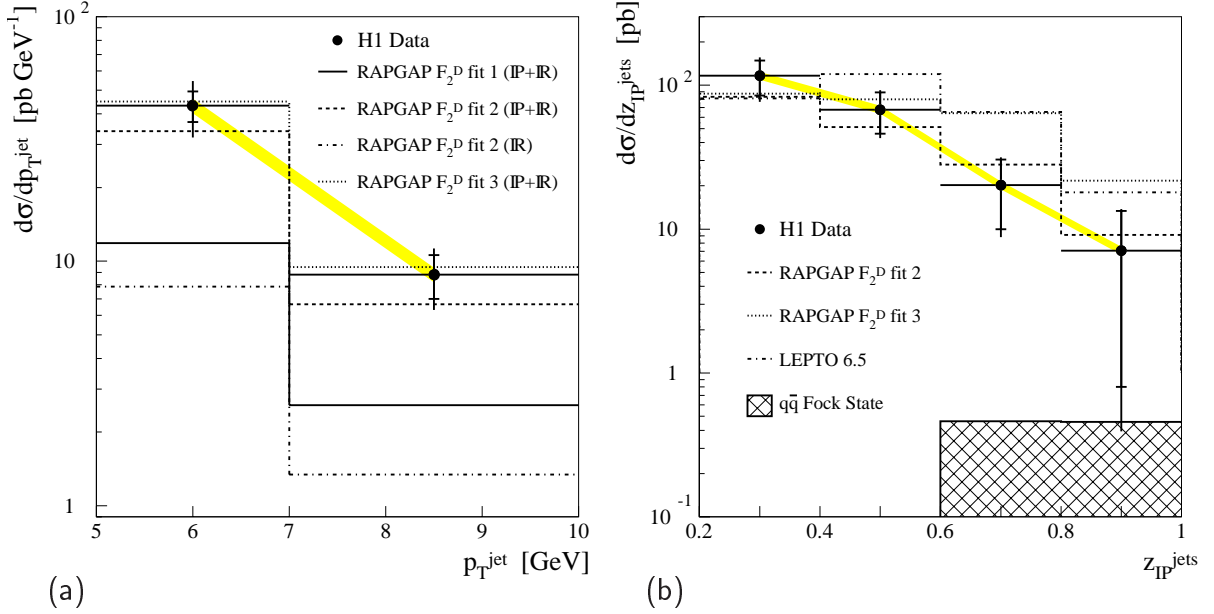
41

FIGURE 2.1: First results on diffractive dijet production in DIS from H1 [11]. Shown are differential cross sections as functions of *(a)* the transverse momentum of the jets p_T^{jet} and *(b)* $z_{I\!P}^{jets}$, an estimator for the fraction of the colourless exchange momentum entering the hard interaction. The model predictions which are shown are explained in the text.

2.2   Diffractive D^* Meson Production

H1 has measured the diffractive production of D^* mesons [86–88] via the decay

$$D^{*+} \rightarrow D^0 \ \pi_{slow}^+ \rightarrow (K^- \ \pi^+) \ \pi_{slow}^+ \qquad (\text{and charge conjugate}) . \qquad (2.1)$$

The kinematic range of the measurement is $2 < Q^2 < 100$ GeV^2, $0.05 < y < 0.7$, $x_{I\!P} < 0.04$, $p_T(D^*) > 2.0$ GeV and $|\eta(D^*)| < 1.5$. The data, which were taken in 1995-97, correspond to an integrated luminosity of 21 pb^{-1}. As for the jets, the analysis was statistically limited since a total number of 38 ± 10 events were selected.

Fig. 2.2 shows the extracted differential cross sections as functions of p_T^* (the transverse momentum of the D^* in the γ^*p-CMS), $x_{I\!P}$, β and $z_{I\!P}^{obs}$, an estimator for the fraction of the colourless exchange momentum entering the hard interaction (Eq. 1.55). Here, the conclusions are different from those obtained in the first analysis of dijet production (see last section): The resolved pomeron model based on the H1 fits to $F_2^{D(3)}$ overestimates the cross sections by a factor of three, although the shapes are reproduced. The BJLW model, taking only the $q\bar{q}$ contribution into account [81], is in agreement with the data at high values of β, $z_{I\!P}^{obs}$ and low values of p_T^* and $x_{I\!P}$.

The conflicting conclusions which can be drawn from the dijet and the D^* meson cross sections call for an improvement in the statistical precision of the data in both
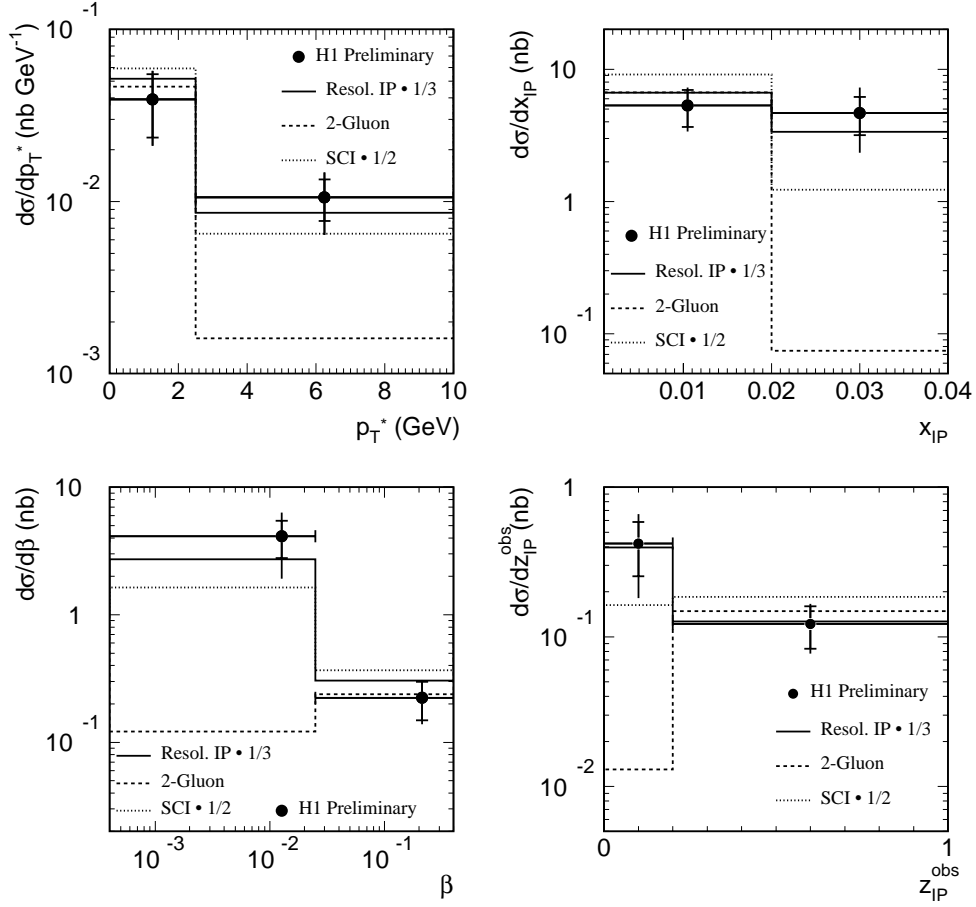
FIGURE 2.2: Results on the production of D^* mesons in diffractive DIS from H1 [86]. Shown are differential cross sections as functions of p_T^* (the transverse momentum of the D^* in the $\gamma^* p$-CMS), $x_{I\!P}$, β and $z_{I\!P}^{obs}$, an estimator for the fraction of the colourless exchange momentum entering the hard interaction. The model predictions which are shown are explained in the text.

measurements, which may then either confirm this discrepancy or reveal that it originates from a statistical fluctuation.

Chapter 3

Monte Carlo Simulation

The use of so-called *Monte Carlo* programs is essential for several aspects of data analysis and interpretation in a high energy physics experiment:

- They are used to correct the measured data for the limited efficiencies, acceptances and resolutions which are unavoidable in a real world detector. In the terminology of high energy physics, the measured distributions of *detector level* observables are corrected by use of Monte Carlo programs to the *hadron level*, that is the final state of the event after hadronisation and subsequent fast decays.

- They are also used to compare the obtained cross sections to the predictions of phenomenological models or QCD calculations.

The techniques employed in Monte Carlo generators are reviewed and a model independent definition of diffraction at the hadron level is introduced. The simulation of events for the purpose of this analysis is explained.

3.1   Techniques

In this section, the main concepts of the technical implementation of the physics processes into Monte Carlo generators are introduced. The general structure of these programs is visualised in Fig. 3.1.

Matrix Elements

In fixed order $(\alpha_s)^n$ perturbation theory, all diagrams to order n, including the virtual corrections from loop diagrams, are calculated and summed to obtain a prediction of the partonic cross section. Up to now, the matrix elements up to the order $(\alpha_s)^2$ are available (NLO QCD). In the analysis presented here, only $(\alpha_s)^1$ matrix element calculations (LO QCD) are used. This is due to the fact that so far no NLO QCD Monte Carlo programs are available which are able to generate colour singlet DIS events. The leading order QCD matrix elements are those for the Boson-Gluon-Fusion (BGF) and QCD-Compton (QCDC) diagrams as explained in section 1.1.5, including the corresponding virtual corrections. A lower cut-off in the transverse momentum p_T of the outgoing partons has to
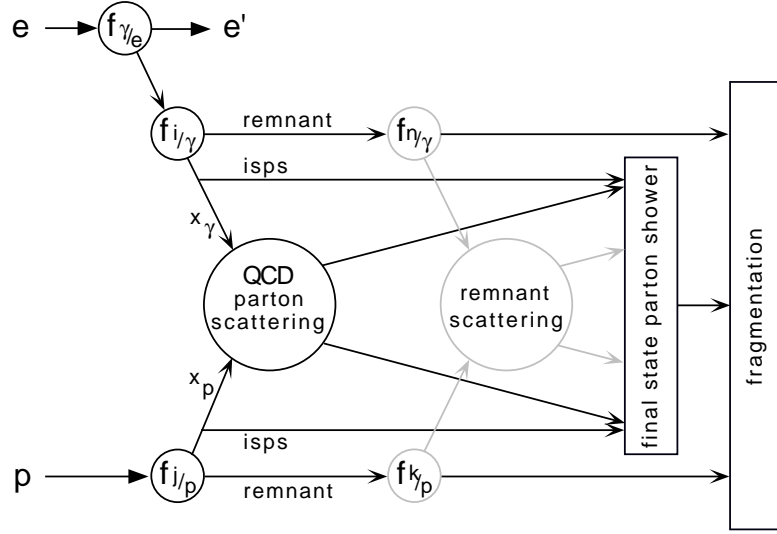
FIGURE 3.1: General structure of a Monte Carlo generator for lepton-proton scattering. 'isps' stands for initial state parton showers (figure from [30]).
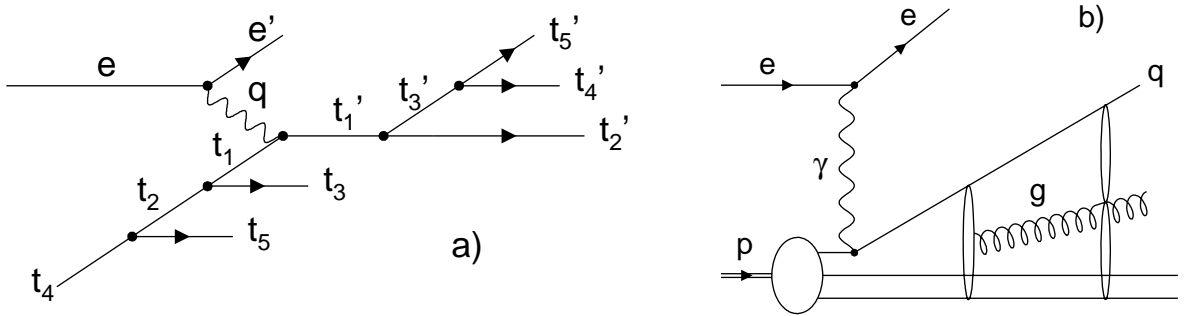
FIGURE 3.2: Parton cascades in deep-inelastic scattering: *(a)* Leading $\log Q^2$ initial and final state parton showers (MEPS). *(b)* The colour dipole approach (CDM).

be introduced for light quark production (*uds*) because of a collinear divergence of the matrix element at $p_T = 0$. It is important to consider observables that do not depend on the value of the cut-off, for instance by studying final states with $p_T \gg p_T^{cut}$. In the case of heavy quark production (e.g. *c*) a cut-off is not needed because of the scale set by the large quark mass.

Parton Cascades

As already said, complete fixed order $(\alpha_s)^n$ calculations are not available so far for $n > 2$. However, with the *parton shower* ansatz [89], higher order effects can be approximated in arbitrarily high order α_s, but only in the leading $\log Q^2$ approximation (see Fig. 3.2a). The struck quark in deep-inelastic scattering can emit partons before and/or after the hard scattering vertex, which initiate the *initial state* and *final state* parton showers, respectively. As a consequence of the leading $\log Q^2$ approximation, the parton cascade
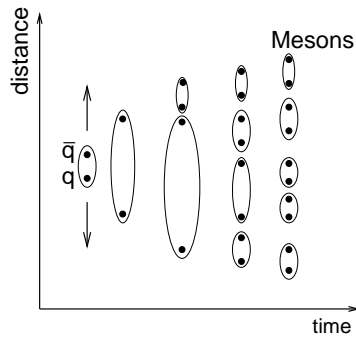
Figure 3.3: Hadronisation in the Lund string model. A colour string spanned between pairs of quarks successively splits up by creating new $q\bar{q}$ pairs.

is strongly ordered in k_T. The parton branchings are based upon the DGLAP splitting functions.

An alternative modelling to parton showers is provided by the *colour dipole* approach (CDM)[1] [90]. Here, the parton cascade is not divided into an initial and a final state (see Fig. 3.2b). All parton radiation is described starting from a colour dipole formed between the struck quark and the proton remnant. Subsequent gluon radiation emerges from dipoles spanned between the newly created and the original colour charges. The process is iterated until the available energy has been used up. The Boson-Gluon-Fusion (BGF) process is not included in this scheme and is thus inserted manually. The parton emissions are not ordered in k_T. Because of this feature, the colour dipole approach creates final states which are expected to be similar to BFKL topologies.

Hadronisation

The most commonly used model to describe the transition from partons to the observable hadrons is the *Lund string model* as introduced in [70]. It starts by stretching a string-like (i.e. constant energy per unit length) colour field between the two separating partons of a $q\bar{q}$ pair (see Fig, 3.3). In DIS, a string is also stretched to the proton remnant. When the energy stored in the string is large enough, the string breaks up by creating a new $q\bar{q}$ pair, forming new string pieces. The process is iterated until the available energy is used up. The resulting string fragments are combined into mesons and baryons. Gluons are realized as kinks in the string.

An alternative hadronisation model, provided by the so-called *cluster fragmentation model* [91], exists but is not used in this thesis.

---

[1]'Colour dipole approach' as an approximation of higher order QCD effects is not to be confused with the 'Colour dipole models' introduced in section 1.2.7.
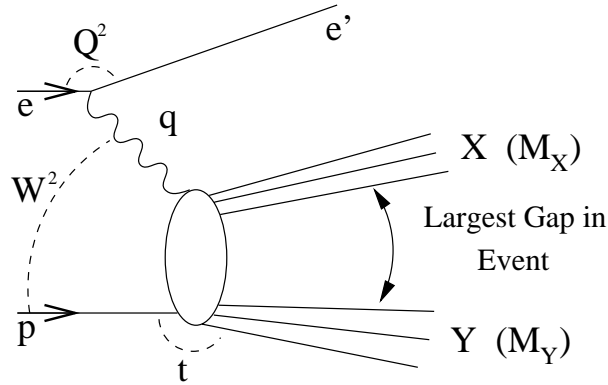
FIGURE 3.4: Model independent definition of diffraction in DIS. The two systems X and Y are separated by the largest rapidity gap between the final state hadrons.

3.2   Model Independent Definition of Diffraction

In measurements of events containing a large rapidity gap, the definition of a *diffractive* hadron level cross section should be used which does not depend on the specific model for generating diffractive events which is implemented in the Monte Carlo simulation.

The definition which is usually employed in diffractive analyses within the H1 experiment complies with this requirement. It is based on the decomposition of the hadronic final state into two distinct topological systems, labelled X and Y (Fig. 3.4). The two systems are separated by the largest gap in rapidity between the final state hadrons in the photon-proton centre-of-mass frame. The system closest to the direction of the proton is labelled Y. From these systems X and Y the hadron level quantities $x_{I\!P}$, M_Y and t are computed from the 4-momenta p_X and p_Y by

$$x_{I\!P} = \frac{q \cdot (P - p_Y)}{q \cdot P} \; ; \qquad M_Y = p_Y^2 \; ; \qquad t = (P - p_Y)^2 \qquad (3.1)$$

for every simulated event, where q and P denote the photon and proton 4-vectors. By making cuts on these quantities which require small $x_{I\!P}$, $M_Y = m_P$ or small and t depending on the analysis, a hadron level cross section for diffractive events can be defined model-independently because the procedure is well defined, irrespective of the underlying physics model in the Monte Carlo generator.

3.3   Detector Level Event Simulation

In this section, it is explained how the sample of Monte Carlo events is obtained which has been fed through the full H1 detector simulation and reconstruction. This sample will be used for correcting the data to the hadron level. It is noted that for this purpose, although the physics model which is used for the simulation is explained in detail, it is in principle irrelevant which specific model has been used, as long as a good description of all aspects of the data is achieved.

Two samples of simulated Monte Carlo events are used for the correction of the data to the hadron level (and for detector level comparisons). In one sample, colour singlet exchange events are simulated. In the other, standard deep-inelastic scattering is simulated. The two samples are mixed together such that the colour singlet exchange sample is used to model the region

$$x_{I\!P} < 0.2 \; ; \qquad M_Y = m_P \; ; \qquad \text{all } |t| \; . \tag{3.2}$$

The standard DIS sample is used for

$$x_{I\!P} > 0.2 \qquad \text{or} \qquad M_Y > 5 \text{ GeV} \; . \tag{3.3}$$

Details of the simulation of the two event samples are given below. The region of phase space which corresponds to

$$m_P < M_Y < 5 \text{ GeV} \; , \tag{3.4}$$

which is not covered by two samples mentioned above, is treated separately for technical reasons (see section 6.4.5).

Colour Singlet Exchange Events ('RG-DIF' Sample)

The Monte Carlo generator used to generate colour singlet exchange events is RAPGAP, version 2.08/06 [92]. Events are generated according to a resolved (partonic) pomeron model, as described in section 1.2.5. Contributions from pomeron and reggeon exchanges are included neglecting any possible interference effects. The parameterisations of the pomeron and reggeon flux factors and parton distributions are taken from the H1 analysis of $F_2^{D(3)}$ [3]. The pomeron and reggeon trajectories and slope parameters are $\alpha_{I\!P}(t) = 1.20 + 0.26t$, $b_{I\!P} = 4.6 \text{ GeV}^{-2}$, $\alpha_{I\!R}(t) = 0.50 + 0.90t$ and $b_{I\!R} = 2.0 \text{ GeV}^{-2}$. The pomeron parton distributions are the 'flat gluon' (or 'fit 2') parameterisations extracted from the leading order QCD fits to F_2^D. Those of the meson are taken from fits to pion data [93].

The renormalisation and factorisation scales are set to $\mu^2 = Q^2 + p_T^2$, where p_T is the transverse momentum of the partons emerging from the hard scattering. The parton distributions are convoluted with hard scattering matrix elements to leading order in QCD. Intrinsic transverse momentum of the partons in the pomeron [94] is not included. Charm quarks are produced in the *massive scheme* via Boson-Gluon-Fusion. For the production of light quarks, a lower cut-off $p_T^2 > 9.0 \text{ GeV}^2$ is introduced in the $\mathcal{O}(\alpha_s)$ QCD matrix elements to avoid divergences. Higher order QCD diagrams are approximated with parton showers in the leading $\log(Q^2)$ approximation (MEPS) [89] or the colour dipole approach [90] as implemented in ARIADNE [95]. Hadronisation is simulated using the Lund string model in JETSET [96]. QED radiative effects are taken into account via an interface to the HERACLES program [97].

A contribution of events where the virtual photon γ^* is assigned an internal partonic structure is also simulated (section 1.1.6). The resolved virtual photon is parameterised according to the SaS-2D [31] set of photon parton densities, which has been found to give a reasonable description of inclusive dijet production at low Q^2 in a previous H1

analysis [36].

For the simulation of pomeron exchange, a total of 2.4M events were generated, which correspond to an integrated luminosity of 120 pb^{-1}. Before the events were fed through the CPU-time consuming full detector simulation and reconstruction, a *preselection* was applied in order to reduce the number of events without a loss of information. This was achieved by selecting only those events where at least one jet is found at the hadron level with $p_{T,jet} > 3$ GeV. Events not passing this selection do not belong to the hadron level cross section definition, nor are they generally selected on detector level. The preselection reduces the event sample to 360K events. Because the detector simulation had to be performed according to the year in which the data were taken, the events were split into two samples which were then simulated for 1996 and 1997 running conditions separately.

For the simulation of reggeon exchange, 4M events were generated (corresponding to 77 pb^{-1}), out of which 460K survived the preselection. Finally, 200K resolved virtual photon events (93 pb^{-1}) were generated, out of which 80K were kept. The sum of all three contributions is hereafter referred to as 'RG-DIF'.

Inclusive DIS Events ('RG-DIS' Sample)

Inclusive DIS events are simulated by RAPGAP as well. The proton structure function is parameterised according to [83]. The parton distributions are convoluted with leading order QCD matrix elements. $\mu^2 = Q^2 + p_T^2$ was chosen as the renormalisation and factorisation scale. Higher order QCD diagrams are approximated by parton showers (MEPS) and hadronisation is performed according to the Lund string model. QED radiative effects are taken into account via HERACLES [97].

A sample of 1.2M events was used for this analysis, corresponding to an integrated luminosity of 24.2 pb^{-1}. This sample is hereafter referred to as 'RG-DIS'.

3.4 Simulation of Model Predictions

Monte Carlo generators are also used to compare the measured hadron level cross sections with the predictions of the phenomenological models and QCD calculations described in sections 1.2.4 to 1.2.7. For this purpose, the time consuming detector simulation is not required. Therefore, high statistics event samples can be generated. For each of the different model predictions or parameterisations which are compared with the data, several million events have been generated, corresponding to integrated luminosities which are typically one order of magnitude larger than the data. A very convenient technical framework to obtain the predicted cross sections is provided by the HZTOOL [98] package, which has been used for this purpose.

All of the predictions are made to leading order of QCD. Unless otherwise stated, higher order QCD effects are approximated by initial and final state parton showers.

RAPGAP is used to obtain the predictions of the resolved pomeron model with different pomeron intercept values and parton distributions. It also contains implementations of the saturation, semiclassical and BJLW models. Both versions of the Soft Colour Interactions (SCI) model are implemented in the LEPTO $6.5.2\beta$ generator [99].

Chapter 4

Experimental Setup

In this chapter, the *ep* collider HERA[1] at the DESY[2] laboratory in Hamburg is introduced. The H1 detector at HERA, which was used to measure the data which are analysed in this thesis, is described.

4.1 The HERA Collider

The HERA collider [100] is located at the DESY laboratory in Hamburg, Germany, and operates since 1992. It is the first and, so far, the only accelerator in which different particle species, electrons (or positrons) and protons, are accelerated in two storage rings and brought into collision. The HERA tunnel has a circumference of 6.3 km. The final energy of the electron ring is $E_e = 27.5$ GeV. The proton beam energy was increased from $E_p = 820$ GeV to $E_p = 920$ GeV in 1998. The available centre-of-mass energy E_{CM} for *ep* collisions is thus

$$E_{CM} = \sqrt{s} \simeq \sqrt{4E_e E_p} \simeq 320 \text{ GeV} \qquad \text{(for } E_p = 920 \text{ GeV)} . \qquad (4.1)$$

The electron ring is equipped with dipole magnets with a field strength of 0.17 T. The proton ring consists of super-conducting dipole magnets which are cooled with liquid Helium and operated at 4.7 T. The proton energy is limited by this field strength, whereas the electron energy is limited by the available RF power because of the losses due to Synchrotron radiation.

Fig. 4.1 shows a view of the HERA accelerator complex, consisting of the main HERA ring and the pre-accelerators. Proton injection starts by accelerating negatively charged hydrogen-ions in the linear accelerator H-LINAC. After stripping off the electrons from the ions, the protons are accelerated in the DESY-III and PETRA rings to an energy of 40 GeV. They are then transferred to HERA and brought to their final energy. Electrons or positrons are initially accelerated in the e-LINAC, brought to 12 GeV energy in the DESY-II and PETRA rings and are then transferred to HERA for acceleration to their final energy.

---

[1] Hadron-Elektron Ring Anlage.
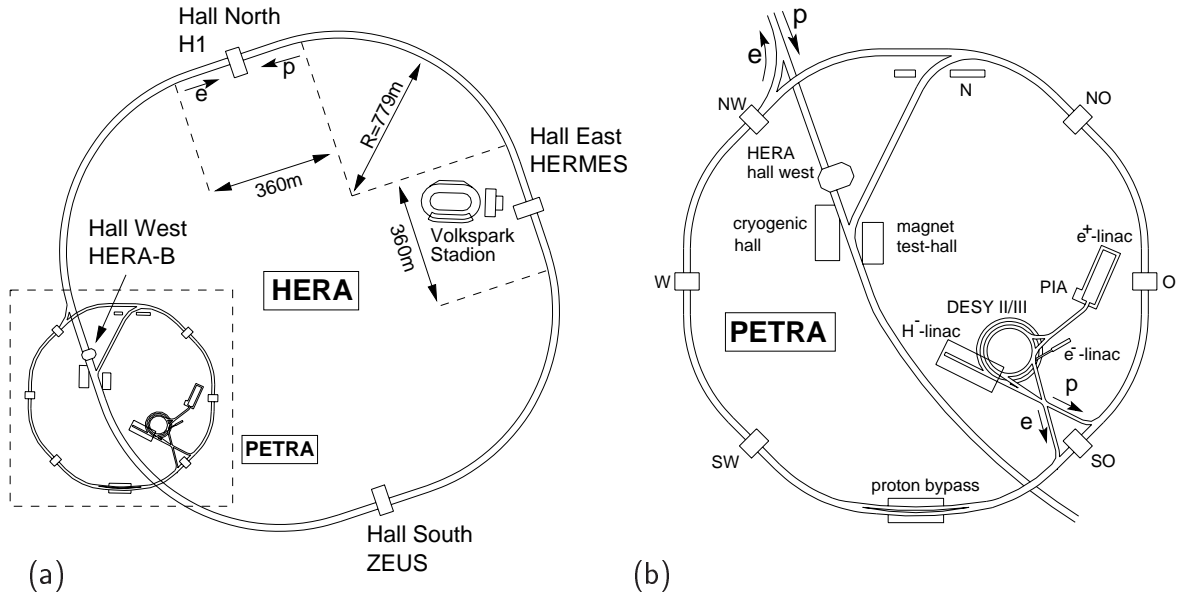[2] Deutsches Elektronen-Synchrotron.

Figure 4.1: Schematic overview of the HERA accelerator complex at DESY. Figure *(b)* is an enlargement of the area indicated by the dashed rectangle in *(a)*.

In HERA, electrons and protons are structured in $210 - 220$ *bunches* of 10^{10} to 10^{11} particles each. From these bunches approximately 175 are *colliding bunches*. The rest are so-called *pilot bunches* which do not collide with bunches from the other beam. The bunch crossing frequency ν_{BC} and time interval t_{BC} are given by the bunch structure:

$$\nu_{BC} \simeq 10.4 \text{ MHz} ; \qquad t_{BC} = 96 \text{ ns} . \tag{4.2}$$

By the year 2000, the peak electron and proton currents routinely reached values up to $I_e = 50$ mA and $I_p = 110$ mA, resulting in a peak luminosity of up to

$$\mathcal{L} = 1.5 \cdot 10^{31} \text{ cm}^{-2}\text{s}^{-1} , \tag{4.3}$$

in agreement with the design value.

The two counter-rotating beams are brought into collision at two interaction regions (north and south). There, the H1 and ZEUS experiments were built around the interaction regions to study *ep* collisions. In the east and west areas, the two fixed target experiments HERMES and HERA-B are located. The HERMES experiment, operating since 1995, measures collisions of the polarised electron beam with a polarised gas target (H_2, D, He) in order to measure the spin structure of nucleons. The HERA-B detector, completely installed since 2000, uses the proton beam in fixed target mode by inserting tungsten wire targets into the beam halo. The experiment aims at measurements of CP-violation in the system of the neutral *b*-mesons $B_0/\overline{B_0}$.

In September 2000, HERA operation was stopped to undertake a major upgrade of both HERA and the colliding beam experiments H1 and ZEUS. The goal is to increase the delivered specific luminosity by a factor of 4 to 5 by inserting super-conducting quadrupole magnets close to the H1 and ZEUS interaction regions. The detectors also undergo major upgrade programmes. Luminosity operation will be resumed in the summer of 2001.

4.2   The H1 Experiment

The H1 experiment is a multi-purpose apparatus to study ep collisions. It is described in detail in [101]. It has an almost 4π calorimetric and tracking coverage in order to measure the complete final state of ep interactions. Because of the non-equal beam energies, the detector is asymmetric with respect to the beam axis. The granularity of the calorimeters for example is much finer in the region of the outgoing proton.

Fig. 4.2 shows an isometric view of the detector. The dimensions of the detector, which has a total weight of about 2800 tons, are approximately 12x10x15 m. Electrons enter from the left, protons from the right side into the interaction region. The H1 coordinate system is defined such that the positive z-axis points along the proton beam direction. The nominal interaction point is at $z = 0$. The x-axis points towards the centre of the HERA ring, the y-axis points upwards. A spherical coordinate system is often used where the polar and azimuthal angles θ and ϕ are defined in the (y, z) and (x, y) planes respectively such that $\theta = 0^\mathrm{o}$ corresponds to the positive z direction and $\phi = 0^\mathrm{o}$ points along the x-direction. For ultra-relativistic particles, the *pseudo-rapidity* η is often used instead of θ:

$$\eta = -\ln\tan\frac{\theta}{2} \ . \tag{4.4}$$

It corresponds for massless particles to the *rapidity* y:

$$y = \frac{1}{2}\ln\frac{E + p_Z}{E - p_Z} \ . \tag{4.5}$$

A convenient feature of η and y is that they transform linearly under Lorentz boosts along the z axis. The consequence is that (pseudo-) rapidity differences Δy ($\Delta\eta$) are invariant under such boosts. The region of the outgoing proton ($z > 0$, $\eta > 0$, $\theta < 90^\mathrm{o}$) is often referred to as the *forward* region, whereas the direction of outgoing lepton ($z < 0$, $\eta < 0$, $\theta > 90^\mathrm{o}$) is called the *backward* region.

The H1 detector is a complex arrangement of many different components. The general design follows the established scheme for collider detectors in high-energy physics: The interaction point is surrounded by a tracking system in which the trajectories of charged particles, bent due to a magnetic field, are measured. The tracking system is surrounded by electromagnetic and hadronic calorimeters. The outermost part of the detector is formed by the muon system. In the following, the focus will be on those detector components which are relevant for the analysis presented in this thesis.

4.2.1   Tracking

The tracking system of H1 covers the angular range $5^\mathrm{o} < \theta < 178^\mathrm{o}$ with full azimuthal coverage (Fig. 4.3). It is subdivided into several parts: The central tracking system covers the region $15^\mathrm{o} < \theta < 165^\mathrm{o}$ and consists of concentrical drift and proportional chambers. The forward tracker, which is similarly composed, covers $5^\mathrm{o} < \theta < 25^\mathrm{o}$. The backward region $155^\mathrm{o} < \theta < 178^\mathrm{o}$ is covered by the backward drift chamber (BDC). Very close to the interaction point, the central and backward silicon tracking detectors CST [102] and BST [103] are installed. They are however not used for this analysis.

HERA Experiment H1

y

θ   Φ

z   x

p

15

14

9

10

9 6

5

4

12

2 1

15

3

9

13

9

9

11

8

7

e

1	Beam pipe and magnets	9	Muon chambers
2	Central tracking detectors	10	Instrumented Iron yoke
3	Forward tracking detectors	11	Forward muon toroid
4	Electromagnetic LAr calorimeter	12	SPACAL and BDC
5	Hadronic LAr calorimeter	13	PLUG calorimeter
6	Super-conducting coil	14	Concrete shielding
7	Compensating magnet	15	LAr cryostat
8	Liquid Helium supply		

Figure 4.2: An isometric view of the H1 Detector at HERA.

Central Tracking System

Fig. 4.4 shows a radial view of the central tracking system. It comprises two large concentric drift chambers (CJC1 and CJC2) with a length of 2.2 m. The drift cells are inclined by about 30° with respect to the radial direction. CJC1 (CJC2) consists of 30 (60) cells with 24 (32) sense wires, strung parallel to the z axis. The space-point resolution in (r, ϕ) is 170 μm, in z it is 2.2 cm (from measuring the charge at both ends of the wire). A

FIGURE 4.3: A side view of the H1 tracking system including the central, forward and backward tracking devices.

homogeneous solenoidal magnetic field of 1.15 T is provided by a super-conducting coil of 6 m diameter which is located beyond the main calorimeter to minimise dead material losses.

The resolution in z is much improved by two additional inner (CIZ) and outer (COZ) z-chambers with wires perpendicular to the beam axis, located inside and outside of CJC1. CIZ and COZ are divided into 15 and 24 drift cells respectively with 4 sense wires per cell. They achie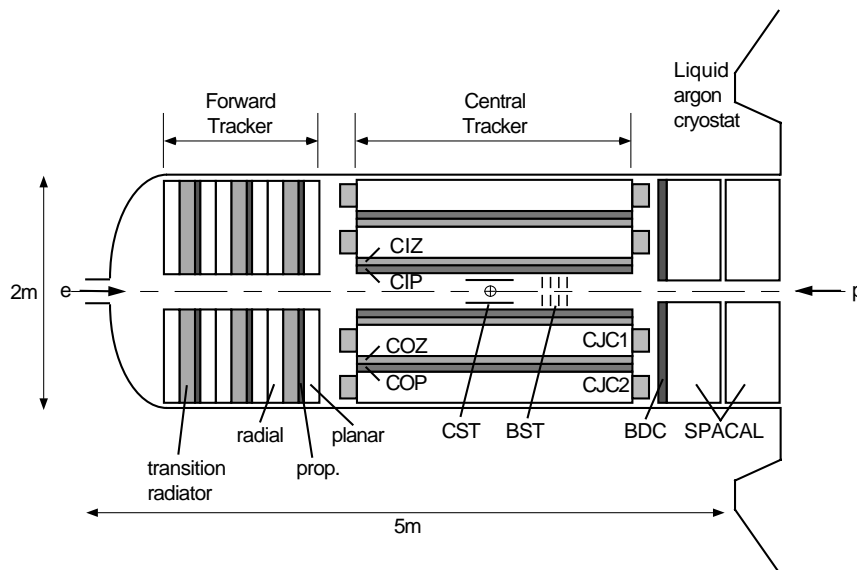ve a z resolution of 260 μm. The combination of the z-chambers with CJC1 and CJC2 leads to a tracking resolution of $\sigma(p)/p < 0.01 \cdot p/\text{GeV}$.

The central tracking system is completed by two multi-wire proportional chambers (MWPC's). The central inner proportional chamber (CIP), located inside of the CIZ, and the central outer proportional chamber (COP), sitting between COZ and CJC2, deliver fast timing signals with a resolution of 21 ns, better than the bunch crossing time. They also provide moderately accurate space points for tracking information which is used for the first level trigger. The segmentation of CIP and COP in (ϕ, z) is $(8, 60)$ and $(16, 18)$ respectively.

Forward Tracking

The forward tracking system consists of three identical super-modules aligned along the z-axis. Each super-module contains a planar and a radial drift chamber, a proportional chamber and a transition radiator (see Fig. 4.3). In this analysis, only the forward multi-wire proportional chambers (FPC) with a timing resolution of 20 ns are used to provide, together with CIP and COP, a fast trigger on tracks pointing towards the nominal interaction point.
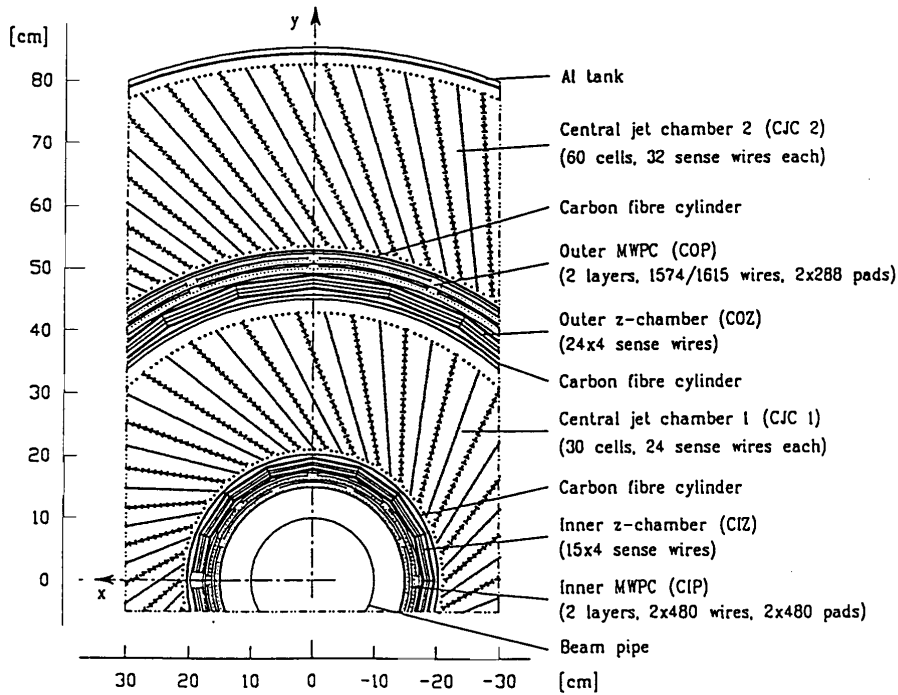
Figure 4.4: A radial view of the central tracking system, comprising the central drift chambers CJC1 and CJC2, the z chambers CIZ and COZ and the proportional chambers CIP and COP.

Backward Tracking

Tracking information in the backward region is provided by the backward drift chamber (BDC) [104], which was installed in H1 as part of a major detector upgrade in 1995. Its main purpose is to measure the direction of the scattered lepton in the angular range $155^\circ < \theta < 178^\circ$. The design of the BDC (Fig. 4.5) is optimised with respect to a maximum resolution in the polar angle θ, which is important for the determination of the event kinematics (Q^2, x) from the scattered lepton in DIS events.

The sense wires are strung perpendicular to the beam axis, forming octagons in ϕ, so that the drift direction in the cells is radial, which optimises polar angle resolution. The BDC consists of four double layers of 32 drift cells each. Each double layer is rotated with respect to the previous one by 11.25°, avoiding insensitive regions at the octant boundaries and giving the possibility to resolve ambiguities in the ϕ measurement. The drift cells in a double layer are shifted half a cell width in r, which resolves the left-right ambiguity. At small radii, the drift cells are smaller compared to large radii because of the larger rate of background particles which are produced at smaller distances from the beam pipe. Each of the $8 \cdot 8 = 64$ octants consists of 16 small and 16 large drift cells with a drift radius of 0.5 and 1.5 cm respectively. In total, the BDC thus contains 2048 signal channels.

The precision to which the polar angle of the scattered electron is measured in the BDC with additional information on the event vertex position has been shown to exceed
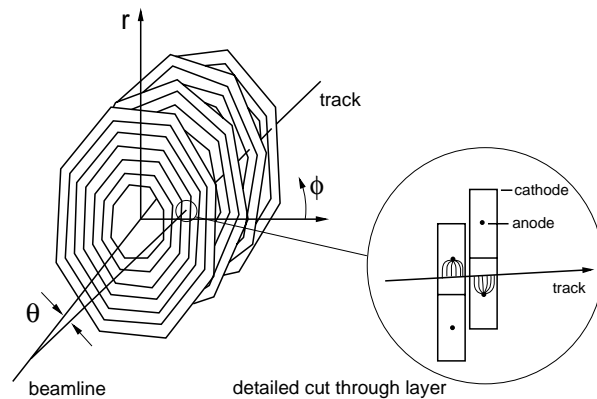
FIGURE 4.5: Schematic overview of the design of the backward drift chamber (BDC).

0.7 mrad [105]. The BDC is also successfully used as a preshower detector. The scattered electron loses energy because of the material it has to pass before reaching the backward calorimeter. Using the deposited charge in the BDC the resolution of the reconstructed electron energy can be improved [106].

4.2.2 Calorimetry

The H1 detector comprises four calorimeters: The liquid Argon calorimeter (LAr), the backward 'spaghetti' calorimeter SPACAL, the so-called 'tail catcher' (TC) (the iron magnet return yoke instrumented with streamer chambers) and the PLUG calorimeter around the forward beam pipe.

The PLUG and TC calorimeters are not used for this analysis. The calibration of the PLUG is not well understood and for the events under study, the hadronic final state energies are not large enough to allow for significant leakage from the LAr into the tail catcher.

The LAr Calorimeter

The LAr sampling calorimeter provides energy measurement in the polar angular range $4^{\circ} < \theta < 154^{\circ}$ and in full azimuthal coverage. The main advantages of the liquid Argon technique are good stability, homogeneity of the response, ease of calibration and fine granularity which can be achieved. The LAr is located in a cryostat inside the solenoid coil to minimise the amount of dead material in front of the calorimeter. It is segmented along the z axis into eight wheels (see Fig. 4.6). Each wheel itself is segmented in ϕ into eight octants and is divided into an inner electromagnetic (e.m.) and an outer hadronic (had.) section (with exception of the 'BBE' wheel, which has only an e.m. section). The total number of readout channels is about $45,000$.

The e.m. part consists of 2.4mm thick lead absorber plates with 2.35mm liquid Argon as active material, leading to a thickness of 20 to 30 radiation lengths. The had. section consists of 19mm stainless steel absorber plates with a double gap of 2.4mm LAr. The energy resolution for electrons has been determined as $\sigma_{e.m.}(E)/E \simeq 11\%/\sqrt{E/\mathrm{GeV}} \oplus 0.01$,
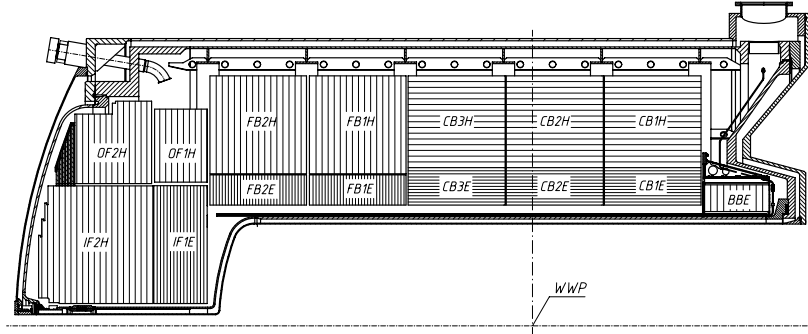
Figure 4.6: A side view of the LAr calorimeter. Only the upper half of the calorimeter is drawn. The location of the nominal interaction point is labeled 'WWP'.

for hadrons is is $\sigma_{had.}(E)/E \simeq 50\%/\sqrt{E/\text{GeV}} \oplus 0.02$, as obtained from test beam measurements. The total depth of the calorimeter corresponds to 5 to 8 hadronic interaction lengths.

The LAr calorimeter is non-compensating, i.e. the response to hadrons is about 30% smaller than that to electrons of the same energy. This is corrected off-line by a weighting technique. The absolute hadronic energy scale (for typical hadronic energies which are studied in this thesis) is known to 4% from studies of the transverse momentum balance between the scattered lepton and the hadronic final state in DIS events.

The SPACAL Calorimeter

Calorimetric information in the backward region is provided by a scintillating fibre 'spaghetti' calorimeter with lead absorbers (SPACAL) [107]. It covers the polar angular region $155^{\circ} < \theta < 178^{\circ}$ and is mainly used together with the BDC for measuring the scattered lepton in low Q^2 DIS events ($1 < Q^2 < 150$ GeV^2).

Incident particles develop into a shower in the lead, which causes the fibres to scintillate. The light is then collected by photo-multipliers. The SPACAL is split into an inner electromagnetic and an outer hadronic part (see Fig. 4.7), in total corresponding to 2 hadronic interaction lengths. The e.m. part is 28 radiation lengths deep, so that for a 27.5 GeV electron the energy leakage is negligible. The small cell size of $(40.5 \text{ mm})^2$ is well matched to the Molière radius of 25.5 mm, ensuring good electron-pion separation and position resolution. The cell size in the hadronic section is $(119 \text{ mm})^2$. In total 1328 channels are read out with a time resolution of 1 ns. This excellent timing information is used to provide time-of-flight information for energy depositions in the SPACAL. In the electromagnetic section, energies can be measured with a resolution of $\sigma(E)/E = ((7.1 \pm 0.2)\%/\sqrt{E/\text{GeV}}) \oplus (1.0 \pm 0.1)\%$, as obtained in test beam measurements. The absolute energy scale was determined as 0.3% for electrons with 27.5 GeV, 2.0% at low energies and following a linear extrapolation inbetween [108]. In the hadronic section, energies are measured with a resolution of $\sigma(E)/E \simeq 30\%/\sqrt{E/\text{GeV}}$ and the energy scale is known to 7%.
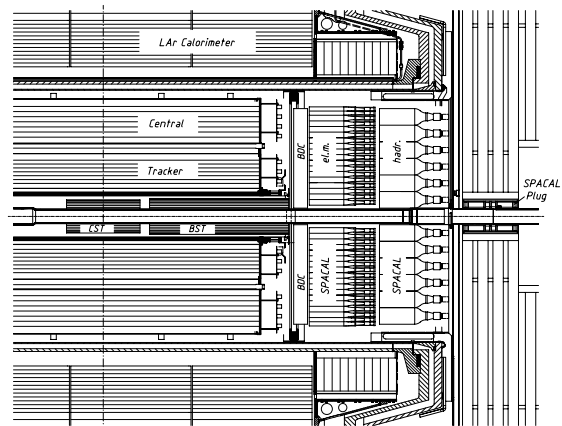
Figure 4.7: Side view of the backward region of the H1 detector. The positions of the electromagnetic and hadronic sections of the SPACAL calorimeter and of the BDC are shown.

4.2.3   Forward Detectors

The forward part of the LAr calorimeter ends at a pseudorapidity value of $\eta = 3.4$. In order to select events with a rapidity gap, two additional sub-detectors are used which enlarge the coverage for hadronic activity to values of the pseudorapidity of up to $\eta \simeq 7.5$. These are the forward muon detector (FMD) and the proton remnant tagger (PRT).

The Forward Muon Detector

The forward muon detector (FMD) is situated beyond the return yoke for the magnetic field. Its design purpose is to trigger on and to measure muons in the forward region of H1. The detector is shown in Fig. 4.8a. The angular coverage is $3^{\circ} < \theta < 17^{\circ}$, $3.7 > \eta > 1.9$. The FMD consists of six double layers of drift chambers, four with wires strung tangentially around the beam pipe to measure θ and two with wires strung radially to measure ϕ. The double layer structure resolves the left-right ambiguity.

Three double layers are situated on either side of a toroidal magnet, designed to bend the muons to allow momentum measurement in the range $5 < p < 100$ GeV. A charged particle produces a pair of hits in a double layer. The hit pairs in the six double layers are linked to produce full tracks.

Because of secondary scattering with the beam pipe, the FMD has an indirect sensitivity to particle production at pseudorapidity values larger than its direct coverage of $\eta < 3.7$. This is employed for the selection of diffractive events.

The Proton Remnant Tagger

The proton remnant tagger (PRT) is located at $z = +24$ m in the forward direction inside the HERA tunnel. It consists of seven scintillators arranged around and between the proton and electron beam pipes as visualised in Fig. 4.8b. Each scintillator comprises
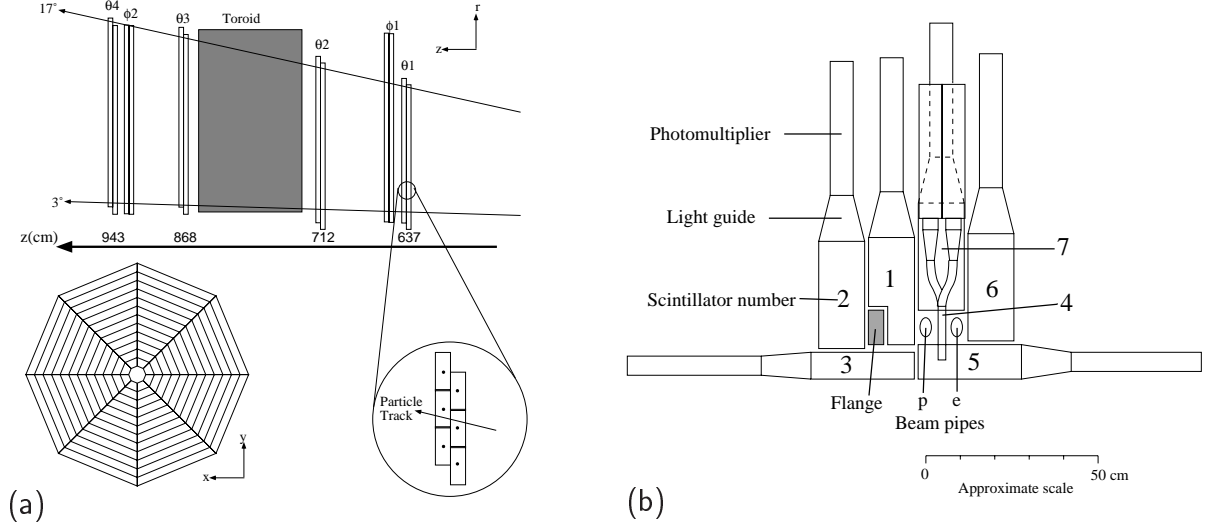
FIGURE 4.8: Illustrations of *(a)* the forward muon detector (FMD) and *(b)* the proton remnant tagger (PRT).

two sheets of plastic scintillator with separate photo-multipliers and pulse-height discriminators. Signals are only considered if they are within the time window expected from an ep interaction. The PRT is sensitive to particles produced in the pseudorapidity range $6 < \eta < 7.5$.

4.2.4   Luminosity Measurement and Time-of-Flight System

An essential ingredient for a cross section measurement is the precise determination of the integrated luminosity to which the accumulated data correspond. This is commonly done by measuring the rate of events of a reaction with a well known cross section. In H1, the Bethe-Heitler process $ep \rightarrow ep\gamma$ is used for this purpose.

Fig. 4.9 shows the layout of the luminosity system. The two principal components are the electron tagger (ET), installed close to the electron beam pipe at $z = -33.4$ m, and the photon detector (PD) at $z = -102.9$ m, next to the proton beam pipe. Both are hodoscopes of total absorption crystal Cerenkow counters which have high radiation resistance and good energy, spatial and time resolution. Scattered electrons are deflected by a set of low-β quadrupoles before they leave the beam pipe at $z = -27.3$ m through an exit window and hit the ET. The photons leave the proton beam pipe at the point where it bents upwards at $z = -92.3$ m and then reach the PD, which is shielded from synchrotron radiation by a Pb filter / water Cerenkow veto counter combination. The ET and PD devices are mounted on movable platforms which are retracted during beam injection in order to reduce radiation damage.   Two different methods are used to determine the luminosity:

- **Coincidence method:** The simultaneous detection of electron and photon is required.
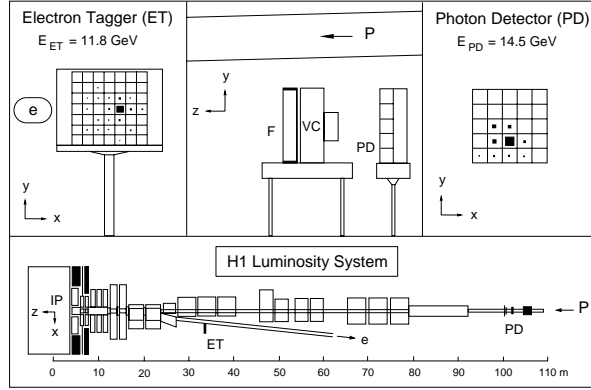
Figure 4.9: An overview of the luminosity measurement system.

- **Photon method:** The number of Bethe-Heitler events N_{BH} with a photon energy E_γ above the threshold E_{min} is counted. The luminosity is then obtained by:

$$\mathcal{L} = \frac{N_{BH}^{ep}(E_\gamma > E_{min})}{\sigma_{BH}(E_\gamma > E_{min})} = \frac{\frac{\sum_i (W_i^{tot}(E_{min}) - W_i^{bgr}(E_{min}))}{\epsilon_{trig}(E_{min})} \left(1 - \delta_{n\gamma}(\mathcal{L}, E_{min})\right)}{\sigma_{BH}(E_{min}) \cdot A_\gamma(\Theta_x, \Theta_y)} , \qquad (4.6)$$

where σ_{BH} is the Bethe-Heitler cross section, W_i denotes the total and background number of events in part i of the data and $A_\gamma(\Theta_x, \Theta_y)$ is the correction for the limited acceptance of the PD which depends on the lepton beam tilt (Θ_x, Θ_y). $\delta_{n\gamma}(\mathcal{L}, E_{min})$ corrects for the *pile-up* effect in the PD, i.e. the detection of more than one photon in a single bunch crossing, which depends on the luminosity and on E_{min}.

In the off-line analysis, the photon method is used. After all corrections are applied, the systematic uncertainty in the luminosity measurement is 2%. Fig. 4.10 shows the integrated luminosity delivered by HERA and accumulated by H1. It is shown for each year since 1992 as a function of the day within the year. In each consecutive year, the performance of HERA increased. By the end of the year 2000, each colliding beam experiment had more than 100 pb^{-1} of luminosity available on tape for physics analysis.

The Time-of-Flight System

The time-of-flight (ToF) system rejects background originating from beam interactions with residual gas atoms. Based on a precise knowledge of the timing structure of the beams provided by the HERA clock, time windows are set corresponding to the position of the counters which reflect the amount of time a particle from an *ep* interaction needs to reach the counter. Time-of-flight counters are installed in the forward (FToF) and backward (BToF) regions of H1. In addition, unused space in the PLUG calorimeter is instrumented to provide a PLUG ToF (PToF) system. Finally, a double wall of scintillators, known as *veto wall*, is positioned at $-8.1 < z < -6.5$ m. Time-of-flight information is also provided by the SPACAL calorimeter, as mentioned in section 4.2.2.
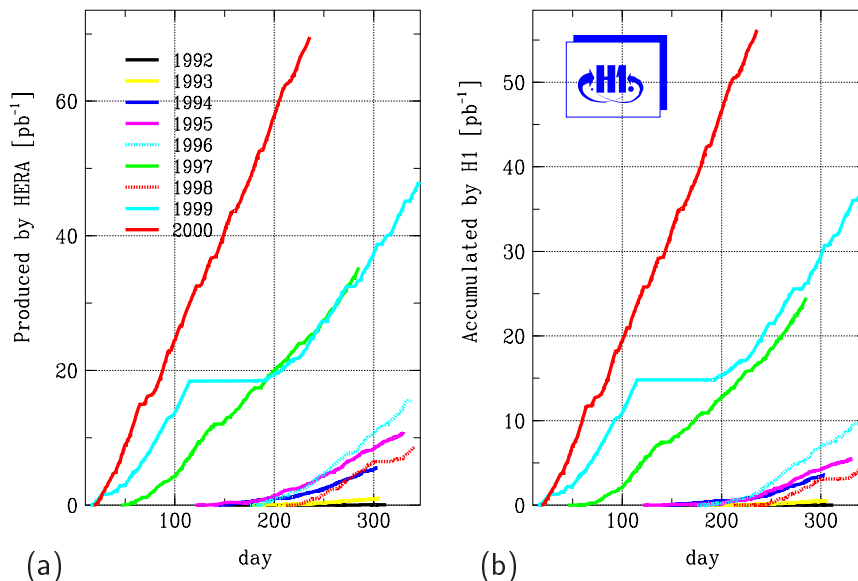
Figure 4.10: Summary plot of the integrated luminosity *(a)* delivered by HERA and *(b)* accumulated by H1 for the years since 1992. The accumulated integrated luminosity is shown as a function of the day within the year.

4.2.5   Trigger and Data Acquisition

The purpose of the trigger system is to select ep interactions of physics interest and to reject background. The H1 experiment is equipped with a multi-level (L1-L5) trigger system.

The first level trigger (L1) is a dead-time free system which provides a decision whether to keep an event or not within 2.5 μs. Because of the bunch crossing time of 96 ns a pipeline system is employed to store the full event information until the L1 decision is reached. An event is kept if one of 128 L1 sub-triggers (S0-S127) has fired. These sub-triggers are logical combinations of *trigger elements*, signals provided by individual detector components. An overview of the trigger elements which are most important for the analysis presented in this thesis is given in the next section.

The second level trigger (L2) provides the opportunity to verify the L1 decision by employing more sophisticated algorithms which contain for example neural nets or are sensitive to certain event topologies. The L2 decision is available after 20 μs. In this analysis, no L2 condition is used.

If L2 decides to keep the event, the complete event information is read out and transferred directly to the fourth-level trigger (L4). The L3 trigger is currently not implemented. L4 is a software filter farm with approximately 30 parallel processors, each running a reduced version of the H1 reconstruction software and processing one event at a time. Because the full event information is available now, the remaining number of background events can be further suppressed. The computing power of the L4 farm allows for a rate of events being processed of approximately 45 Hz.

In order to make maximum use of this bandwidth, a flexible scheme of *prescaling* is

applied on the L1 trigger level. Each of the sub-triggers is assigned a prescale factor. A prescale of 10 for example means that only one out of 10 events which fire this sub-trigger is kept, the remaining 9 events are rejected on L1. The reason is that the full bandwidth should not be occupied by triggers with a high rate which are typically soft physics (e.g. very low Q^2). The prescales are adjusted regularly during a fill because the relatively low electron beam lifetime of 10h leads to a fast change of the L1 trigger rates with time during a fill. Until 1997, there were 4 *trigger phases* with predefined prescales for the L1 triggers. Phase 1 was used at the beginning of a fill when the currents (i.e. trigger rates) were highest. During the fill, phases 2 to 4 were selected by the shift crew to accommodate more and more decreasing currents. Since 1998, there is an automatic scheme for adjusting the prescales according to physics demands in such a way that the L4 target rate of 45 Hz is optimally made use of. Events which pass the L4 filtering are written to tape with a rate of approximately 8 Hz and stored permanently.

The last level L5 is performed off-line. The events are fully reconstructed and classified according to criteria provided by the H1 physics working groups. Non-classified events are rejected. Out of the events rejected by L4 and L5, 1% each is still kept for monitoring purposes in a separate file.

The data are taken in separate *runs* of events in which ideally the conditions do not change. Whenever the setup of the experiment changes, such as changes of the trigger setup, the prescales or the availability of subsystems, a new run is started. A run comprises typically a few 10k events.

4.2.6   L1 Trigger Elements

The following L1 trigger elements (see previous section) are most relevant for the analysis presented in this thesis:

SPACAL IET Trigger

The purpose of the *inclusive electron trigger* (IET) of the SPACAL is to trigger on candidates for the scattered electron in low Q^2 deep-inelastic scattering events. The IET is built from 4x4 analogue energy sums over neighbouring electromagnetic cells, which are read out in the time-of-flight window for *ep* interactions. The energy sums are performed in overlapping sliding windows to avoid inefficiencies. They are compared to three programmable thresholds. Additionally, each IET threshold is divided into two regions: The inner region (CIET), a rectangular region close to the beam pipe with the approximate coordinates

$$-17 < x < -9 \text{ cm} ; \qquad -9 < y < 17 \text{ cm} , \qquad (4.7)$$

and the outer region, comprising the rest of the SPACAL. The reason for this distinction is that the inner region suffers from a large beam-induced background, called the *hot spot*. The definition of the IET trigger elements and thresholds is given in Tab. 4.1.

Inner region	Outer region	Threshold energy
SPCLe_IET_CEN_1	SPCLe_IET>0	$E_{thres} = 0.5$ GeV
SPCLe_IET_CEN_2	SPCLe_IET>1	$E_{thres} = 2.0$ GeV
SPCLe_IET_CEN_3	SPCLe_IET>2	$E_{thres} = 6.5$ GeV

Table 4.1: Definition of the IET trigger elements.
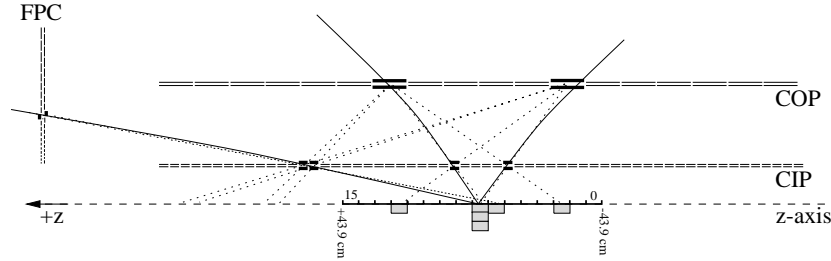
Figure 4.11: Visualisation of the z-vertex trigger.

Z-Vertex Trigger

By requiring a reconstructed vertex in the nominal interaction region, the majority of non-ep induced background can be rejected. The *z-vertex trigger* uses fast signals from the MWPC layers of the CIP and COP combined with information form the planar MWPC of the first super-module of the forward tracker. The *z-vertex histogram* (Fig. 4.11) is filled with the z coordinates at $r = 0$ of *rays*, straight-line coincidences in the rz-plane of MWPC hits. in ϕ, there is a 16-fold segmentation. In the histogram, the bin with the largest number of entries, above the relatively flat background from wrongly identified rays, is expected to correspond to the interaction vertex of the ep collision. The `zVtx_sig` trigger element is set when a large or significant peak above background is found in the interaction region.

CJC Track Trigger

The CJC trigger is responsible for triggering events containing high transverse momentum tracks. It employs 10 of the 56 wire layers in CJC1 and CJC2 and compares the digitised hits to a total of 10000 predefined masks. In this analysis, two trigger elements with a different p_T threshold are used, as defined in Tab. 4.2. Track candidates with a *distance of closest approach* (dca) of less than 2 cm to the origin in the $r\phi$-plane are accepted.

4.2.7 Detector Simulation and Reconstruction

Monte Carlo generators (chapter 3) produce as output a list of 4-vectors containing the initial particles produced in the ep collision and the subsequent decay products according to the used fragmentation and hadronisation schemes.

Name	Definition
DCRPh_Ta	at least 1 track with $400 < p_T < 800$ MeV
DCRPh_THig	at least 1 track with $p_T > 800$ MeV

TABLE 4.2: Definition of the CJC trigger elements used in the analysis.

Detector Simulation

In order to compare the Monte Carlo events with the measured data and to estimate the detector corrections, the generated events can be subjected to a full simulation of the H1 detector. The simulation is contained in the H1SIM [109] program, which is based on the GEANT [110] detector simulation package. In H1SIM, the details of the geometrical acceptance and intrinsic resolution of the detector components as well as the distribution of instrumented and uninstrumented material are implemented, so that the detector response to the generated particles can be calculated.

Reconstruction

After the detector simulation, the events are subjected to the same reconstruction software as the actual data. The reconstruction code is contained within the (H1REC) [111] program. Here, particle trajectories (*tracks*) are reconstructed from hits in the tracking detectors, for example.

Chapter 5

Data Selection

In this chapter, the selection of diffractive deep-inelastic scattering events with at least two or exactly three high-p_T jets is described. The selection can be divided into different tasks. After the general selection requirements, for example on the operational status of the detector, the selection of deep-inelastic scattering (DIS) events by identifying the scattered electron in the SPACAL calorimeter is described. Then, the reconstruction of the hadronic final state and the selection of events with two or more jets using a jet algorithm is explained. After the selection of diffractive events based on requirements on the absence of activity in the outgoing proton region has been presented, the chapter ends with a discussion of the trigger efficiency for the selected events.

5.1   Basic Event Selection

In the analysis presented here, data taken with the H1 detector in the years 1996 and 1997 are analysed. In this period, HERA collided $E_p = 820$ GeV protons with $E_e = 27.5$ GeV positrons[1].

Trigger Phases and Run Ranges

Only events recorded when the L1 trigger phases 2 to 4 were active are considered for the analysis. Phase 1 is used at the beginning of the fill when the detector is typically not yet fully operational.

A period at the beginning of the 1996 data taking was excluded from the analysis because of frequently changing definitions of the trigger elements and L1 triggers, caused by high backgrounds in the inner part of the SPACAL, the so-called *hot spot*. The basic run-ranges used in the analysis are given in Tab. 5.1.

Detector Status

Only events are selected where all components of the detector which are relevant for the analysis were fully operational. This is achieved by:

---

[1]From now on, 'electron' will be used as a generic term for both electrons and positrons throughout this thesis.

Year	Run range
1996	158094 – 171156
1997	177921 – 201519

Table 5.1: Run ranges of the data used in the analysis.

- The individual runs are classified as *good*, *medium* and *poor*, according to the operational status of the detector. For the analysis, only runs classified as *good* or *medium* are used.

- On an event-by-event basis, the operational status of the H1 components used in the analysis is checked. This comprises information on the status of the low and high voltage power supply, the subdetector readout status and other status information. The status of the following systems is monitored: CJC, CIZ, SPACAL, BDC, LAr, TOF, PRT, FMD and the luminosity system.

- A set of runs where a problem was identified, either concerning a relevant detector component or the data taking, is not used for the analysis. In part, the information used was provided by [112].

After these selections, the analysed data sample corresponds to a total integrated luminosity of

$$\mathcal{L} = 17.96 \pm 0.36 \text{ pb}^{-1} \, , \tag{5.1}$$

out of which ~ 5 pb^{-1} were recorded in 1996 and ~ 13 pb^{-1} in 1997. The luminosity values are obtained using the *photon method*, as described in section 4.2.4.

5.2 Selection of DIS Events

In this section, the selection performed to obtain a clean sample of deep-inelastic scattering events with Q^2 values in the range 4 to 80 GeV^2 is presented. This sample then serves as the basis for the further selection of large rapidity gap events containing jets.

Reconstructed Event Vertex

The selection requires that there is an event vertex reconstructed by the tracking system, to which at least one track is pointing. The z coordinate of the vertex is required to lie within

$$-35 < z_{vtx} < +35 \text{ cm} \, , \tag{5.2}$$

corresponding to a region of approximately $\pm 3\sigma$ within the nominal interaction point at $z = 0$ (Fig. 5.1a). This cut ensures the selection of ep collision events and rejects background from beam-gas or beam-wall interactions.

The z-vertex distribution implemented in the Monte Carlo simulations show slight shifts in the peak position and the width of the distribution with respect to the data.
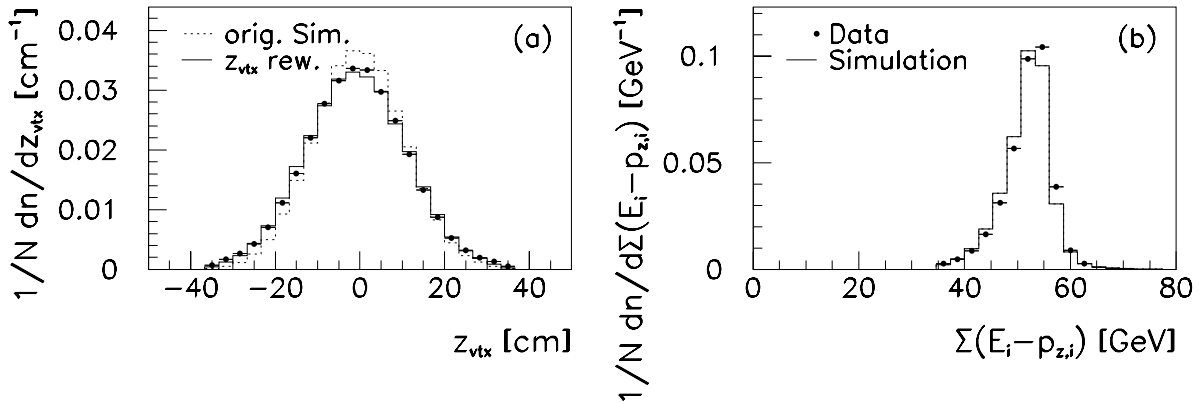
FIGURE 5.1: Distributions of (a) z_{vtx} and (b) $\sum_i(E_i - p_{Z,i})$, shown for data and the Monte Carlo simulation. In (a), the effect of reweighting the z_{vtx} distribution in the simulation to that observed in the data is also shown. All distributions have been normalised to unit area.

Because the z coordinate of the vertex is important for reconstructing the polar angle of the scattered electron, the z-vertex distribution in the simulations is reweighted to that observed in the data (Fig. 5.1a). The applied weight is formed by the ratio of two Gaussians fitted to the distributions in the data and the simulations.

Containment of the Event

For each event, the quantity $\sum_i(E_i - p_{Z,i})$ can be calculated, where i runs over every final state object reconstructed in the detector, including the scattered electron. If all final state particles of an ep collision were detected and perfectly measured, $\sum_i(E_i - p_{Z,i}) = 2E_e \simeq 55$ GeV would be satisfied because of energy and longitudinal momentum conservation. The distribution of this quantity for data and simulation is shown in Fig. 5.1b. The distribution is smeared around the nominal value because of the finite resolution and acceptance of the detector. A cut

$$\sum_i(E_i - p_{Z,i}) > 35 \text{ GeV} \tag{5.3}$$

is applied for the selection of DIS events for two reasons:

- In the case of a photoproduction ($Q^2 \simeq 0$) event, where the scattered electron escapes undetected through the beam pipe, a final state hadron can fake an electron candidate in the SPACAL. The undetected electron leads to a reconstructed $\sum_i(E_i - p_{Z,i})$ which is significantly lower than 55 GeV. Due to the cut, this photoproduction background is significantly reduced.

- In the case of interactions with initial state QED radiation, the photon radiated from the electron can escape through the beam pipe, which detoriates the reconstruction of the event kinematics. These events are also suppressed by the cut.

Year	Reason	Coordinates (in [cm])	
1996	dead cell	$-25.0 < x < -20.5$	$-37.5 < y < -33.0$
	broken HV	$8.1 < x < 24.5$	$-8.1 < y < 8.1$
1997	dead cell	$-48.0 < x < -46.1$	$-28.0 < y < -25.0$
	dead cell	$-16.3 < x < -12.5$	$-21.0 < y < -16.0$
	dead cell	$-31.5 < x < -25.5$	$33.1 < y < 39.1$
	dead cell	$27.0 < x < 38.1$	$-38.0 < y < -27.0$
	broken HV	$22.3 < x < 42.5$	$-42.5 < y < -22.3$

TABLE 5.2: Regions in the SPACAL excluded from the analysis. 'broken HV' means that the high voltage power supply of the corresponding region was not working properly.

Fiducial Region for Electron Candidates

The scattered electron in low Q^2 DIS events is identified in the SPACAL together with the BDC by a series of selection cuts. The candidate for the scattered electron is the electromagnetic SPACAL cluster with the highest energy in the event.

A fiducial region is defined in the SPACAL in order to ensure a high quality selection of electron candidates with high efficiency. Due to high background levels, the innermost region of the SPACAL is excluded by requiring the distance between the electromagnetic cluster and the beam pipe d_{cl-bp} to satisfy

$$d_{cl-bp} > 9.0 \text{ cm} .\qquad(5.4)$$

In addition, only electron candidates with a reconstructed polar angle θ'_e within

$$156^\circ < \theta'_e < 176^\circ\qquad(5.5)$$

are considered. The lower boundary is motivated by the outer acceptance of the SPACAL, the inner boundary is matched to the lower analysis cut in Q^2 which is applied (see below). Finally, a number of rectangular regions in the SPACAL are cut out because of dead or inefficient cells or because of problems with the high voltage power supply (see Fig. 5.2a). A list of these regions is found in Tab. 5.2.

Cuts on the Electron Candidate

A series of cuts is applied on the electron candidate in order to select DIS events and reject background. The energy E'_e of the cluster forming the electron candidate has to satisfy

$$E'_e > 8.0 \text{ GeV} .\qquad(5.6)$$

Towards lower values, the background from photoproduction events with a misidentified hadron in the SPACAL increases strongly.

The radius of the cluster r_{cl} (Fig. 5.3a) is required to satisfy

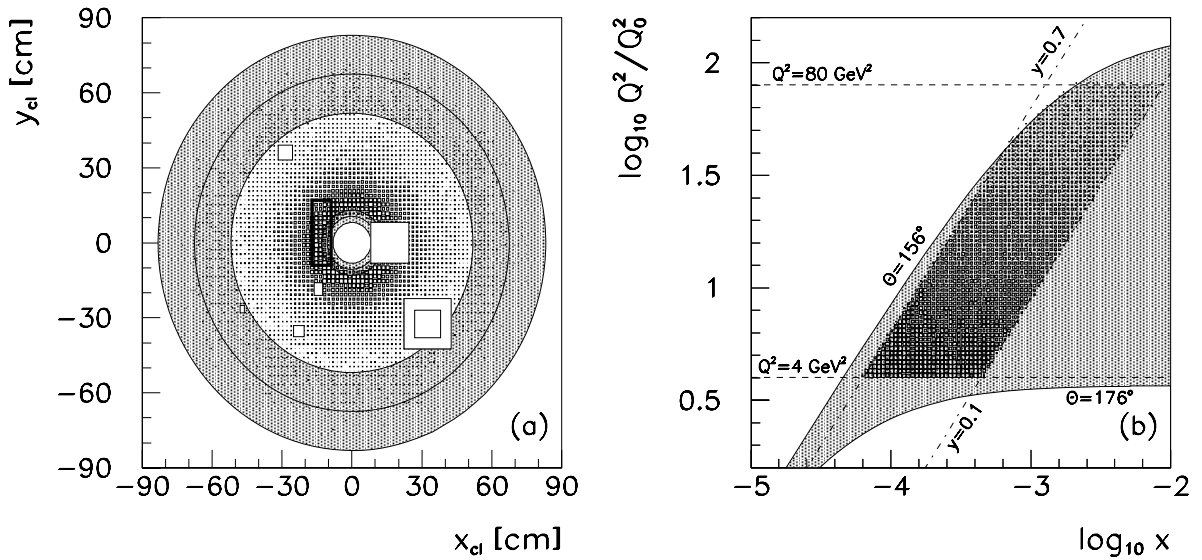$$r_{cl} < 3.5 \text{ cm} ,\qquad(5.7)$$

FIGURE 5.2: *(a)* The fiducial acceptance of the SPACAL, shown as a function of the x- and y-position of the cluster centre of gravity. The inner and outer shaded areas with three concentric rings each correspond to $\theta'_e = 176^\circ$ and $\theta'_e = 156^\circ$, with a z_{vtx}-position of 0 (central rings) or ± 35 cm (inner and outer rings). The thick rectangle corresponds to the acceptance of the inner SPACAL IET trigger (CIET, see section 4.2.6). The white boxes visualise the regions discarded from the event selection as described in Tab. 5.2. The distribution of the scattered electrons for selected DIS events is symbolised by the small boxes. *(b)* The kinematic plane $(\log x, \log Q^2/Q_0^2)$, where $Q_0^2 = 1$ GeV^2. The shaded area corresponds to the acceptance of the SPACAL $(156^\circ < \theta'_e < 176^\circ)$. Also drawn are the isolines for $Q^2 = 4$ GeV^2 and 80 GeV^2 and for $y = 0.1$ and 0.7. The distribution of DIS events is represented by the small boxes.

because the transverse dispersion within in a calorimeter is larger for hadronic than for electromagnetic showers. The cut thus rejects photoproduction background. In the Monte Carlo simulation, the electron cluster radius is typically underestimated by approximately 5%, which is corrected before applying the cut.

Because of the 28 radiation lengths of the electromagnetic part of the SPACAL, showers of electrons with energies up to 27.5 GeV should be fully contained. Therefore, any activity in the hadronic section of the SPACAL behind the electron candidate is a sign of a hadron faking an electron. To quantify this, a variable E_{had} is defined by summing up the hadronic energy within a cone with 4° opening angle with respect to the direction of the electron candidate (Fig. 5.3b). E_{had} is required to satisfy

$$E_{had} < 0.5 \text{ GeV} . \tag{5.8}$$

Furthermore, at small scattering angles of the electron (corresponding to low Q^2), leakage into the beam pipe has to be avoided to ensure a good energy measurement. For this purpose, the summed energy E_{veto} (Fig. 5.3c) in the 4 cells of the *veto layer* of the
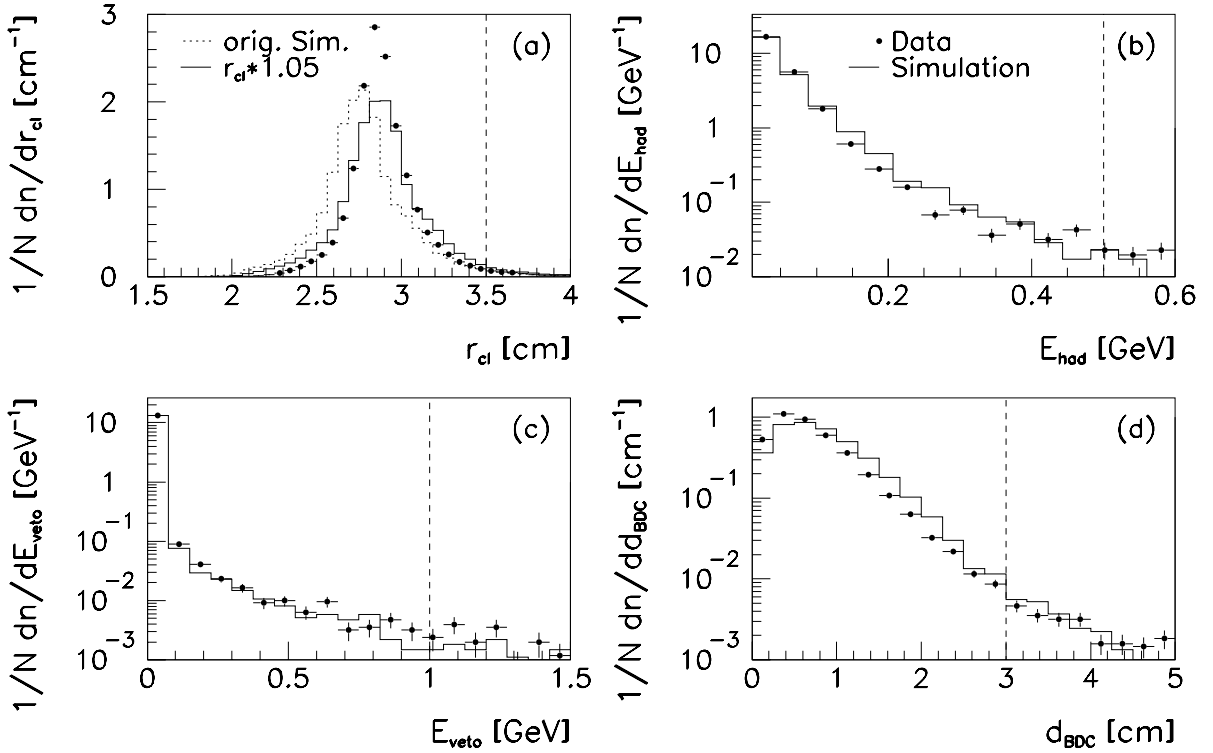
FIGURE 5.3: Distributions of variables used for the selection of the scattered electron for data *(points)* and Monte Carlo simulation *(histograms)*. Shown are *(a)* the cluster radius r_{cl}, *(b)* the hadronic energy behind the electron candidate E_{had}, *(c)* the energy in the SPACAL veto layer E_{veto} and *(d)* the radial distance of the closest BDC track from the cluster centre of gravity. In *(a)*, the effect of increasing the simulated cluster radius by 5% is shown. The dashed vertical lines indicate the cut values. All distributions have been scaled to unit area.

SPACAL, directly adjacent to the beam pipe, is required to satisfy

$$E_{veto} < 1.0 \text{ GeV} . \tag{5.9}$$

The measurement of the electromagnetic cluster in the SPACAL is complemented by tracking information provided by the BDC. Clusters from neutral hadrons such as π^0's would not produce a track in the BDC. For this reason, the distance d_{BDC} between the SPACAL cluster centre of gravity and the closest track in the BDC (Fig. 5.3d) should fulfil

$$d_{BDC} < 3.0 \text{ cm} . \tag{5.10}$$

A summary of these cuts can be found in Tab. 5.3.

Cut	Explanation
$E'_e > 8.0$ GeV	Cluster energy
$r_{cl} < 3.5$ cm	Cluster radius
$E_{had} < 0.5$ GeV	Hadronic energy behind e.m. cluster
$E_{veto} < 1.0$ GeV	Energy in veto layer
$d_{BDC} < 3.0$ cm	Distance to closest BDC track

TABLE 5.3: Cuts on the electron candidate in the SPACAL. The cuts are explained in the text.

Kinematic Reconstruction of the DIS Variables

The kinematics of a DIS event are given by the Q^2,x, y and W^2 variables, as introduced in section 1.1.1. From these quantities, only two are independent. In this analysis, Q^2 and y are chosen for the characterisation and selection of DIS events. x does not have a well-defined interpretation in the case of diffraction. W^2 is closely related to y (Eq. 1.3). In the H1 detector, the scattered electron as well as the hadronic final state formed by the electron-proton interaction are well measured. The DIS kinematics can therefore be determined either from the electron only (*electron method*), from the hadrons only (*hadron method*) or from a combination of both.

In this analysis, the electron method is used. Q^2 and y are reconstructed from the polar angle θ'_e and the energy E'_e of the scattered electron by

$$Q^2 = 4E_e E'_e \cos^2\left(\frac{\theta'_e}{2}\right) \ ; \qquad y = 1 - \frac{E'_e}{E_e}\sin^2\left(\frac{\theta'_e}{2}\right) \ . \qquad (5.11)$$

The quality of the reconstruction of Q^2 and y is visualised in Fig. 5.4. Q^2 is reconstructed with a resolution of 5.9%. The y measurement suffers mostly from initial state QED radiation, where a photon radiated before the interaction escapes through the beam pipe, which leads to a wrong assumption on E_e. y is then reconstructed too large. The following cuts on Q^2 and y are applied for the final selection of DIS events:

$$4 < Q^2 < 80 \text{ GeV}^2 \ ; \qquad 0.1 < y < 0.7 \ . \qquad (5.12)$$

The lower limit in Q^2 results from the intention to stay in the region of deep-inelastic scattering. The upper limit is chosen because, although the acceptance of the SPACAL extends to $Q^2 = 150$ GeV^2, the highest Q^2 region is only sparsely populated with events in the final selection and the acceptance is reduced because of the cut $\theta'_e > 156°$ (see Fig. 5.2b). The upper limit in y corresponds roughly to the cut $E'_e > 8$ GeV. The lower limit is motivated by the fact that due to the selection of diffractive events as explained in section 5.5, events with lower y values are suppressed. In addition, the resolution in y when using the electron method is degrading below $y = 0.1$. The distribution of the selected events in the ($\log x$,$\log Q^2/Q_0^2$) plane ($Q_0^2 = 1$ GeV^2) is visualised in Fig. 5.2b. After all cuts have been applied, approximately 1,900,000 events remain for further analysis.
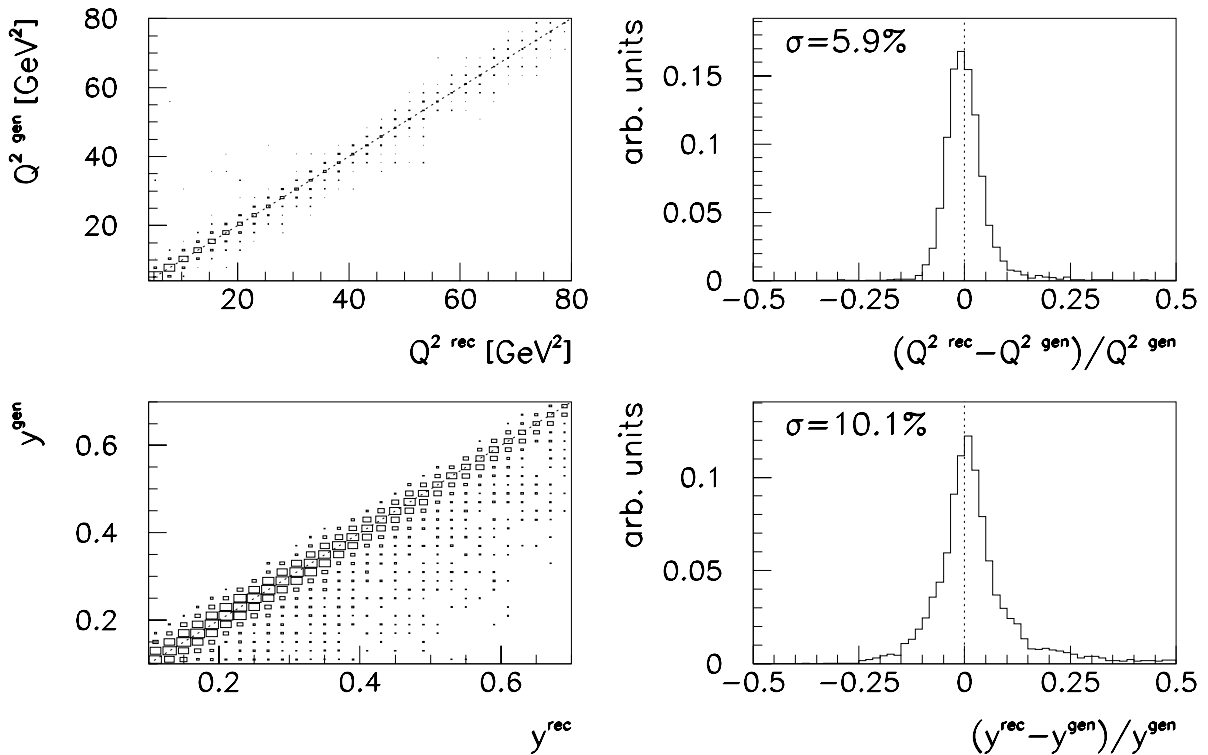
FIGURE 5.4: The reconstruction of Q^2 *(top)* and y *(bottom)*, as obtained from the simulation.

5.3 Hadronic Final State Reconstruction

In this section, the reconstruction of the hadronic final state of the events, formed by the interaction of the virtual photon with the proton, is described and the understanding of the calibration of the measured hadronic energies is presented.

The hadronic final state is reconstructed by combining calorimetric with tracking information. Associations of neighbouring calorimeter cells, called *clusters*, in the LAr and SPACAL calorimeters are considered for the analysis. If only this information was used for the reconstruction of the hadronic final state, the measured energies would be typically measured too low because of two reasons:

- Because of dead material in front of the calorimeter, particles originating from the event vertex typically lose energy before they reach the calorimeter;

- To reduce the sensitivity to (electronic) noise, cuts are applied to reject low energetic isolated energy depositions in the calorimeter.

To compensate for these effects, tracking information is used in addition:

5.3.1   Combination of Clusters and Tracks

In [113], an algorithm was developed which combines calorimeter and tracking information whilst carefully avoiding double counting. For this procedure, only tracks reconstructed in the central tracking system (CJC) are considered. The transverse momentum of the selected tracks has to satisfy

$$p_{T,track} < 2.0 \text{ GeV} . \qquad (5.13)$$

This cut takes into account that the momentum measurement of charged hadrons degenerates towards higher momentum. On the other hand, these highly energetic hadrons are well measured in the calorimeter. The selected clusters and tracks are combined by the following procedure:

1. The selected tracks are extrapolated into the calorimeter.

2. For each track, the energies of clusters within a cone around the extrapolated impact point in the calorimeter are summed up. The cone radius is 25 cm (50 cm) in the electromagnetic (hadronic) sections of the calorimeter.

3. The clusters in the cone are sorted in ascending distance with respect to the impact point.

4. The clusters are removed one by one until the difference of the track energy E_{track} and the energy sum of the removed clusters $\sum_i E_{cluster,i}$ is less than the energy resolution in σ_E in the cone:

$$|E_{track} - \sum_i E_{cluster,i}| < \sigma_E . \qquad (5.14)$$

5. If removing a cluster would lead to a total removed cluster energy which is bigger than the track energy:

$$\sum_i E_{cluster,i} > E_{track} + \sigma_E , \qquad (5.15)$$

   the cluster is kept and its energy is rescaled accordingly.

The combined objects are then formed by the remaining clusters and the tracks. This procedure leads to an improved reconstruction of the hadronic final state with respect to using calorimeter information only. It also results in a reduced systematic uncertainty originating from the hadronic energy calibration of the calorimeter.

Transverse Momentum Balance

Fig. 5.5 shows the distribution of the ratio $p_{T,had}/p_{T,e}$, which ideally would satisfy unity because of transverse momentum conservation. $p_{T,had}$ is determined from the summed 4-vectors of all hadronic final state particles by

$$p_{T,had} = \sqrt{(\sum_i p_{x,i})^2 + (\sum_i p_{y,i})^2} . \qquad (5.16)$$
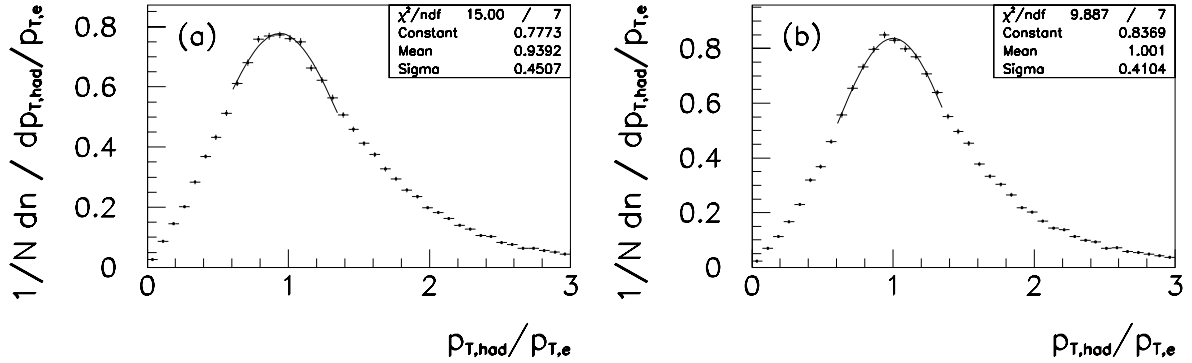
FIGURE 5.5: The ratio $p_{T,had}/p_{T,e}$ for data. Shown are distributions where the hadronic final state was reconstructed (*a*) from calorimeter clusters only or (*b*) from combining clusters and tracks. The distributions have been scaled to unit area. For the fits, only the region around the peak value has been used, due to the non-Gaussian behaviour of the distributions away from the peak.

The mean and width of the measured distribution is mainly given by the hadronic final state reconstruction, since the electron p_T is well measured from $p_{T,e} = E'_e \cdot \sin \theta'_e$. If only clusters are used, the distribution peaks at 0.94, indicating that a fraction of the hadronic final state is typically not reconstructed (Fig. 5.5a). If combined objects are used, the distribution peaks at 1 and also has a smaller width (Fig. 5.5b).

5.3.2 Calibration of Hadronic Energies

A good knowledge of the calibration of the hadronic final state energies is crucial for an analysis of jet production. A tool to study the consistency of the hadronic calibrations between the data and the simulation used to correct the data is provided by the double ratio

$$R_{cal} = \frac{(p_{T,had}/p_{T,e})_{Data}}{(p_{T,had}/p_{T,e})_{MC}} \; . \tag{5.17}$$

In Fig. 5.6, this quantity is studied as a function of the hadronic final state polar angle γ_{had}, calculated from

$$\tan \left(\frac{\gamma_{had}}{2} \right) = \frac{E_{had} - p_{Z,had}}{p_{T,had}} \; . \tag{5.18}$$

By looking at different values of γ_{had}, the calibration can be checked locally in different regions of the detector. The relative calibrations of the individual LAr wheels (see section 4.2.2) for example may differ with respect to each other. The observed double ratio shows a flat behaviour in γ_{had} and is consistent with unity within $\pm 4\%$, the quoted uncertainty in the knowledge of the absolute hadronic energy scale of the LAr calorimeter.
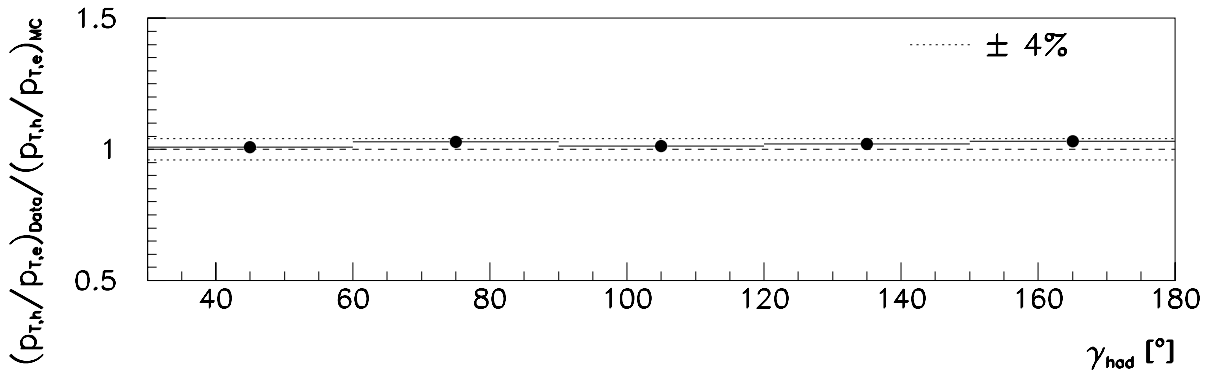
FIGURE 5.6: Double ratio of the p_T-balances for data and simulation as a function of γ_{had}, the polar angle of the hadronic final state. The dotted lines correspond to the quoted 4% uncertainty in the knowledge of the absolute hadronic energy scale of the LAr calorimeter.

5.4   Selection of Jet Events

In the following, the selection of events where the hadronic final state contains either two or exactly three jets with transverse momentum of at least 4 GeV with respect to the $\gamma^* p$ collision axis is described.

High transverse momentum partons which emerge from a hard scattering process are not observable directly. They fragment into collimated sprays of hadrons, which are commonly called *jets*. A jet retains, to a certain degree, information on the 3-momentum of the initial hard parton. Jets are experimentally identified by the use of so-called *jet algorithms*. From an analysis of the properties of reconstructed jets, the dynamics of the underlying hard partonic process can be inferred.

5.4.1   Jet Algorithm

In this analysis, jets are reconstructed with the CDF cone jet algorithm [114]. It uses a cone with fixed radius

$$R_{cone} = \sqrt{(\Delta\eta)^2 + (\Delta\phi)^2} \tag{5.19}$$

in (η,ϕ) space to define the jets. The algorithm works as follows:

1. First, a list of hadronic final state objects above a fixed threshold transverse energy $E_{T,ini}$, to be used as seeds for the jet finder, is created.

2. From these seeds, jets are formed by grouping together all objects within a radius R_{cone} around the seed.

3. For each jet, a new jet-axis is calculated from the E_T-weighted mean in η and ϕ of all objects in the jet:

$$\eta_{jet} = \sum_i \frac{E_{T,i}\ \eta_i}{E_{T,i}}\ ; \qquad \phi_{jet} = \sum_i \frac{E_{T,i}\ \phi_i}{E_{T,i}}\ . \qquad (5.20)$$

4. Steps 2 and 3 are iterated until the list of jets remains unchanged.

5. The energy and momentum of each jet are calculated from the massless 4-vectors $(E_i, \mathbf{p}_i)$ of the objects in the jet cone by

$$E_{jet} = \sum_i E_i\ ; \qquad p_{\{x,y,z\},jet} = \sum_i p_{\{x,y,z\},i}\ . \qquad (5.21)$$

Then, the jet quantities used in the analysis, namely $p_{T,jet} = E_{T,jet}$ (jets are treated as being massless), η_{jet} and ϕ_{jet}, are calculated.

6. All jets with transverse momentum $p_{T,jet} > p_{T,jet}^{min}$ form the output of the algorithm.

Treatment of overlapping Jets

For multi-jet events, it is important to properly handle cases where two jets overlap. This can happen if a final state parton radiates a gluon under a small emission angle. This gluon then could form a jet which overlaps with the jet of the mother parton. Such configurations are treated as follows:

- In the case where one jet is completely contained within another one, the contained jet is simply removed from the list of jets.

- If there is a partial overlap between two jets with transverse energies $E_{T,1}^{jet}$ and $E_{T,2}^{jet}$, where $E_{T,1}^{jet} > E_{T,2}^{jet}$, the *overlap fraction* ϵ_{ov} is computed by

$$\epsilon_{ov} = \frac{\sum_i E_{T,i}}{E_{T,2}^{jet}}\ , \qquad (5.22)$$

where i runs over all objects contained in both jets. If ϵ_{ov} is above a cutoff, which is typically set to 0.75, the two jets are combined.

5.4.2 Jet Selection

The objects used as input for the jet algorithm are the combined objects as defined in section 5.3.1.

Boost into the γ^*p frame

The jet algorithm is applied after boosting the objects into the γ^*p centre-of-mass frame, defined by

$$q + p = l - l' + p = 0\ , \qquad (5.23)$$

where l (l') is the 4-vector of the incoming (outgoing) electron, q (p) is the photon (proton) 4-vector. The reason to go into this frame is that because of the conservation of transverse momentum, the p_T of the scattered electron is balanced by the hadronic final state. This 'artificial' transverse momentum is however not relevant for the study of QCD dynamics. What counts is the transverse momentum with respect to the photon-proton collision axis. Therefore, the boost to the γ^*p frame is performed.

With respect to diffraction, it is noted that the γ^*p frame differs from the rest frame of the photon dissociation system X, defined by $q + x_{I\!\!P}P = 0$ (see section 6.1.1), only by a Lorentz boost along the z axis. The consequence is that transverse momenta are equal in both frames.

Jet Selection

The parameters that are used to run the jet algorithm are

$$R_{cone} = 1.0 \; ; \qquad E_{T,ini} = 0.15 \text{ GeV} \; ; \qquad \epsilon_{\text{ov}} = 0.75 \; . \tag{5.24}$$

The transverse momentum of the selected jets is required to satisfy[2]

$$p^*_{T,jet} > 4.0 \text{ GeV} \; . \tag{5.25}$$

The jets are required to lie within

$$-1.0 < \eta_{jet} < 2.2 \; . \tag{5.26}$$

in the laboratory frame, to ensure good containment within the LAr calorimeter. Events with either at least two or exactly three jets are considered in the analysis:

$$N_{jets} \geq 2 \qquad \text{or} \qquad N_{jets} = 3 \; . \tag{5.27}$$

In Fig. 5.7, correlations between jets found on hadron level and on detector level are shown for events with two or more jets. Jets on the different levels are matched by minimising the distance in (η^*, ϕ^*). A good spatial correlation between hadron level and reconstructed jets is observed. The resolution in $p^*_{T,jet}$ is found to be 17.8%. The correlation between the hadron level jets and the partons emerging from the $2 \rightarrow 2$ leading order QCD processes BGF and QCDC (section 1.1.5) is studied in Fig. 5.8, which shows that a good correlation exists between partons and jets. The pseudorapidities of the hadron level jets are on average slightly shifted towards the forward direction with respect to the partons, which is caused by hadronisation effects.

---

[2]Quantities in the γ^*p frame are labelled with a star '*'.
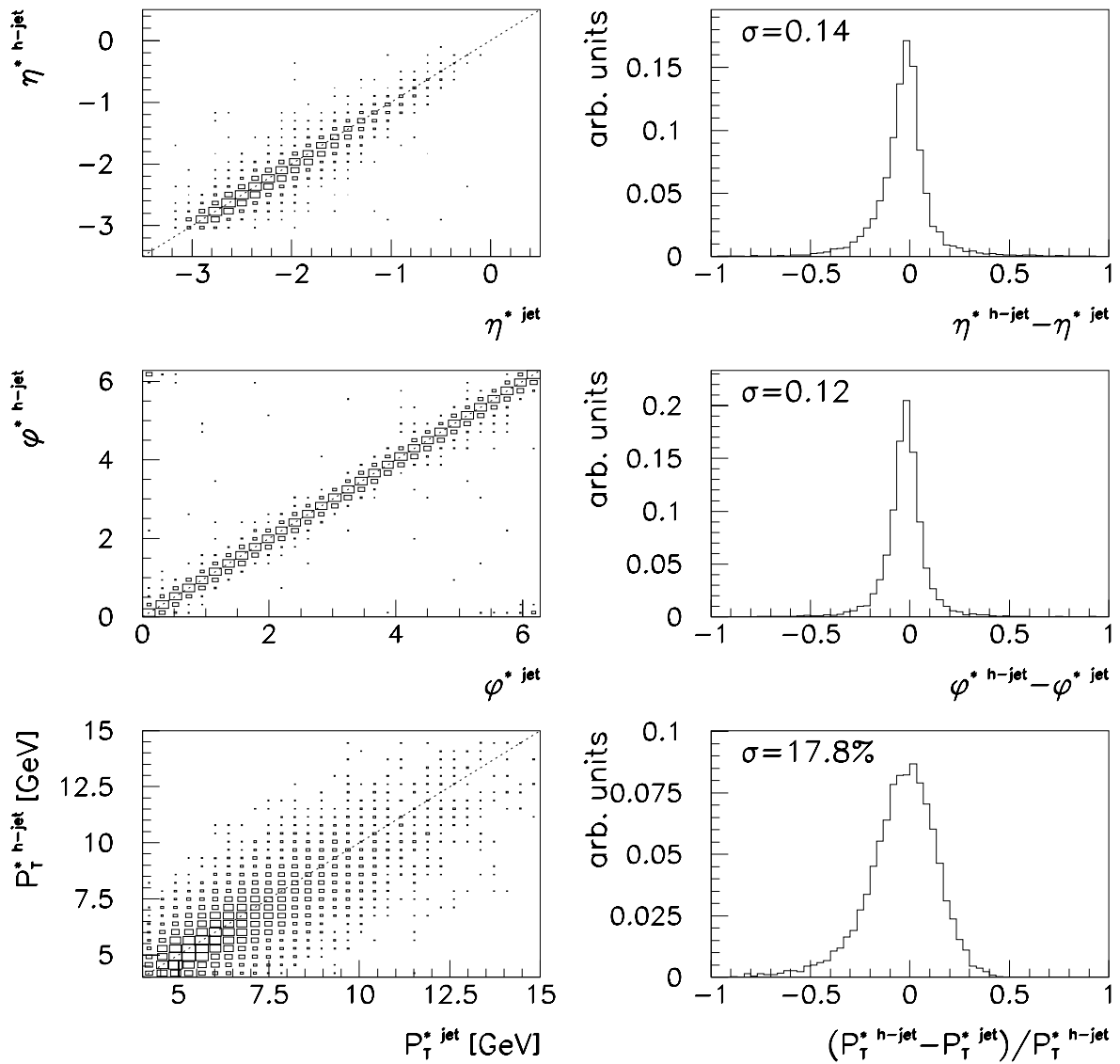
FIGURE 5.7: Correlations between hadron level *('h-jet')* and detector level *('jet')* jets for dijet events. Jets are matched by minimising the distance in (η^*, ϕ^*). Shown are correlations for η^*_{jet} *(top)*, ϕ^*_{jet} *(middle)* and $p^*_{T,jet}$ *(bottom)*.

FIGURE 5.8: Correlations between the hard partons emerging from the $2 \to 2$ BGF and QCDC processes *('parton')* and hadron level jets *('h-jet')*. Partons and jets are matched by minimising the distance in (η^*, ϕ^*). Shown are correlations for η^* *(top)*, ϕ^* *(middle)* and p_T^* *(bottom)*.

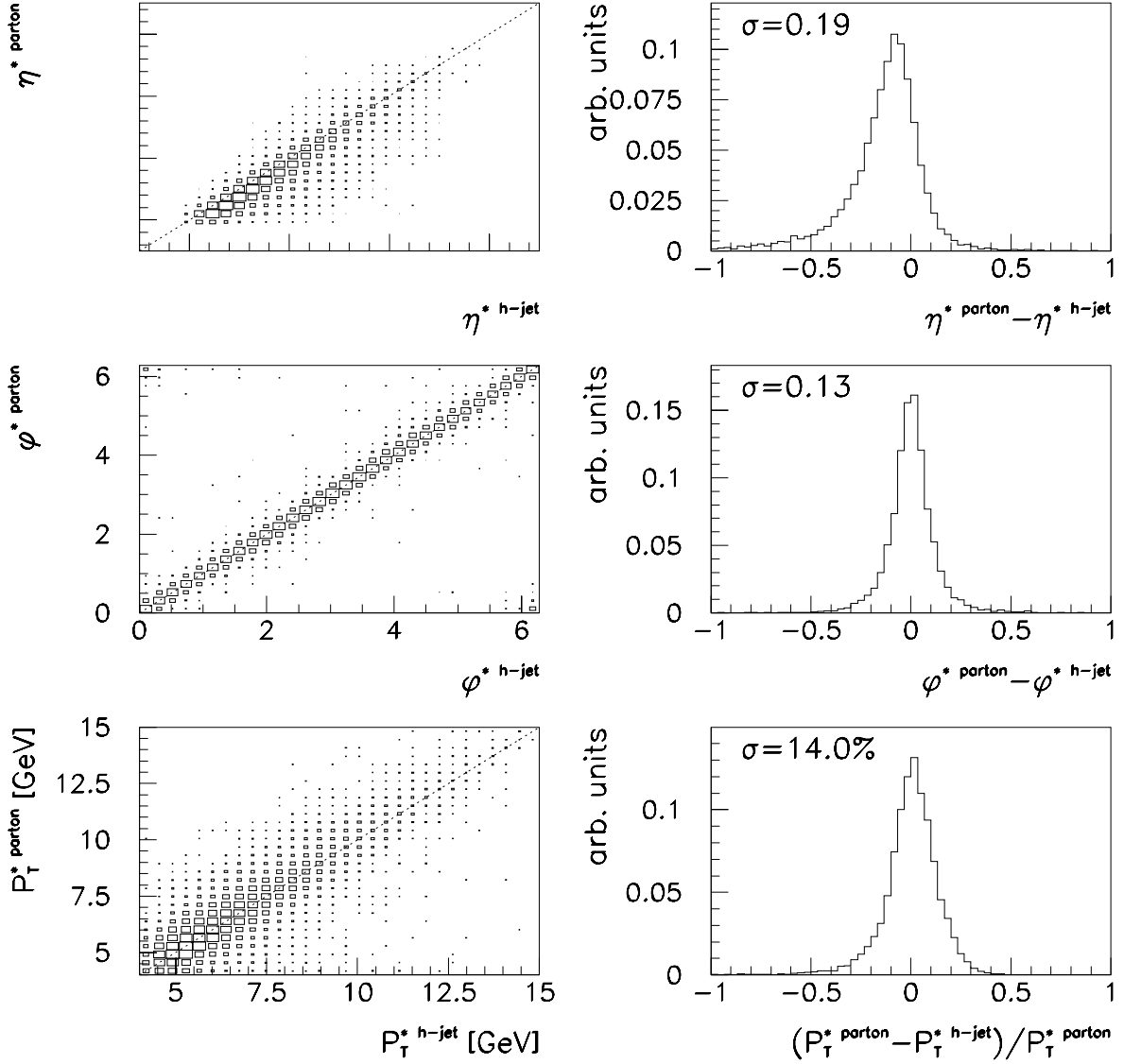# 5.5   Selection of Diffractive Events

Diffractive events are selected by the requirement of a large rapidity gap without hadronic final state particle production between the outgoing proton direction and the hadronic final state system, which is contained well within the central part of the detector. For this purpose, the forward detectors FMD and PRT (see section 4.2.3) are used together with the most forward part of the LAr calorimeter.

5.5.1   Energy Flow in the Forward LAr Calorimeter

As said in section 4.2, the LAr calorimeter covers pseudorapidity values up to $\eta = 3.4$. A quantity η_{max} is reconstructed, which is defined as the pseudorapidity of the most forward LAr cluster with $E_{\text{Cluster}} > 400$ MeV. The energy threshold is introduced to reduce the sensitivity to low-energy noise in the calorimeter. To select diffractive events, a cut

$$\eta_{max} < 3.2 \tag{5.28}$$

is applied. In principle, diffractive events can be rejected due to electronic noise (corresponding to energies above 400 MeV) in the calorimeter. This effect exists but the resulting efficiency loss for diffractive events is correctly taken into account in the Monte Carlo simulations. The random noise in the LAr is monitored over regular periods of the data and incorporated into the detector simulation automatically.

5.5.2   Activity in the FMD Detector

The FMD covers the pseudorapidity range $1.9 < \eta < 3.7$ directly. It is however also sensitive to particle production at larger η values because of secondary scattering with the beam pipe and collimators which shield the central part of the detector from synchrotron radiation induced from the electron beam. Out of the six layers of the FMD, only the three layers in front of the toroid magnet, when viewed from the interaction point, are used to select diffractive events. The post-toroid layers are suffering from high background rates due to synchrotron radiation. A cut is made on N_{FMD}, the sum of reconstructed hit pairs in the three pre-toroid FMD layers:

$$N_{FMD} \leq 1 \ . \tag{5.29}$$

Because there is some amount of random noise in these layers, N_{FMD} is not required to be exactly zero. By doing so, one would reject too much diffractive events due to noise.

Noise in the FMD detector

Even if one hit pair in the FMD is allowed, there is still a fraction of diffractive events rejected because of two or more noise hit pairs. It has to be taken care that the losses due to noise are correctly taken into account in the calculation of the cross sections, since they are not included in the standard detector simulation. To determine the noise in the FMD, samples of *random trigger* events are analysed which were taken during the same run ranges as the selected data.
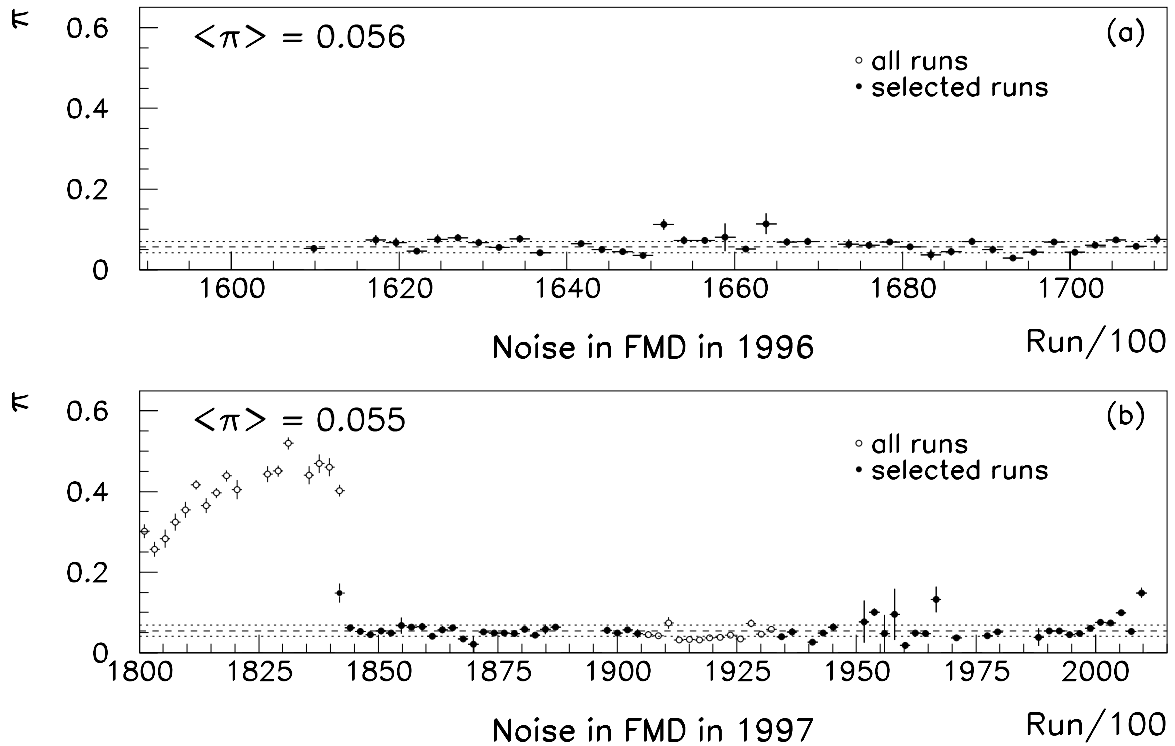
FIGURE 5.9: Random noise in the FMD detector. Shown is π, the fraction of random trigger events with $N_{FMD} > 1$, $\eta_{max} < 3.2$ as a function of the run number, divided by 100, for the *(a)* 1996 and *(b)* 1997 data taking periods. The period with $\pi > 0.25$ at the beginning of the 1997 data taking is excluded from the analysis because of a readout problem with the FMD. The dashed lines correspond to the mean values of π, the dotted lines visualise the assumed uncertainty of 25%.

In order to investigate the time dependence of the noise, the effect is studied as a function of the run number. In Fig. 5.9, the fraction of random trigger events satisfying

$$N_{FMD} > 1 \; ; \qquad \eta_{max} < 3.2 \tag{5.30}$$

is shown as a function of the run number for 1996 and 1997. The additional cut on the absence of activity in the forward part of the LAr ($\eta_{max} < 3.2$) is made to avoid double counting of events which have noise in the FMD *and* in the LAr. The efficiency loss due to such events is already taken into account by the LAr noise simulation. As can be seen in Fig. 5.9, the noise fraction π is stable within a level of 25% (indicated by the dotted lines) with an averaged value of

$$\langle \pi \rangle = 5.5\% \pm 1.4\% \tag{5.31}$$

At the beginning of 1997, a set of runs had to be discarded from the analysis because of a readout problem with the FMD detector, which can also be seen from Fig. 5.9.
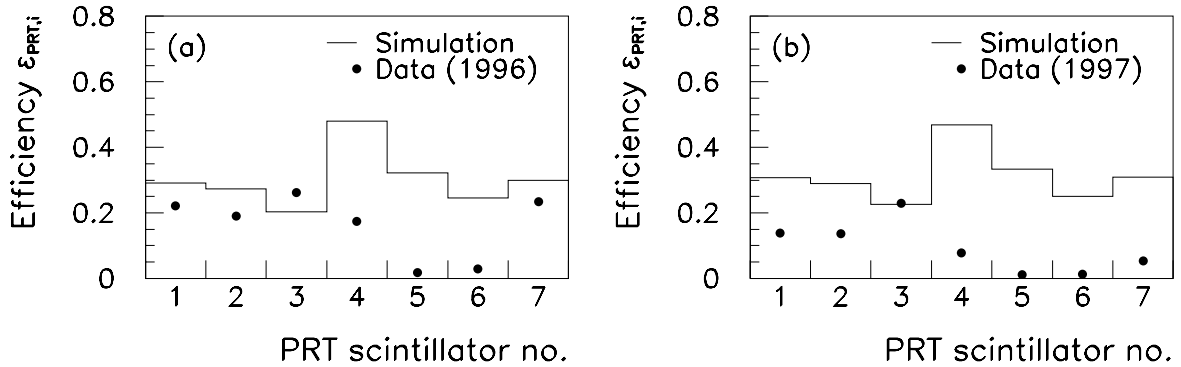
FIGURE 5.10: Efficiency of the PRT detector. The individual efficiencies $\epsilon_{PRT,i}$ for each of the 7 scintillators are shown for data *(points)* and simulation *(histograms)* for the *(a)* 1996 and *(b)* 1997 running periods.

5.5.3 Activity in the PRT Detector

The PRT, covering approximately the pseudorapidity interval $6.0 < \eta < 7.5$, is sensitive to hadronic activity very close to the outgoing proton beam, typically originating from the proton remnant. To select diffractive events, it is required that N_{PRT}, the sum of hits in the seven scintillators of the PRT, is equal to zero:

$$N_{PRT} = 0 \ . \tag{5.32}$$

The amount of random noise in the PRT scintillators is found to be negligible.

Efficiency of the PRT Detector

The efficiencies of the PRT scintillators are not well described by the Monte Carlo simulations used to correct the data. This is mainly due to a rapid aging of the scintillators, because they are exposed to a high rate environment close to the proton beam. It is thus necessary to estimate the actual efficiencies from the data and then to correct the Monte Carlo simulation.

Fig. 5.10 shows the efficiencies $\epsilon_{PRT,i}$ of the individual scintillators of the PRT for data and simulation (standard DIS) for the 1996 and 1997 running periods. The efficiencies have been derived by evaluating the fraction of events where the individual PRT scintillator fired for events with activity in the forward part of the LAr calorimeter and in the FMD:

$$\epsilon_{PRT,i} = \frac{N_{PRT,i}}{N_{all}} \left(\eta_{max} > 3.2; N_{FMD} > 1 \right) \ . \tag{5.33}$$

One observes that the measured efficiencies are typically much smaller than the simulated values. Furthermore, whereas for the simulations the efficiencies are very similar between 1996 and 1997, they are significantly lower on average in 1997 compared with 1996 in

the data. The efficiencies in the simulation are reduced by the ratio of the measured to the simulated efficiencies. The obtained correction factors for 1996 and 1997 are listed in Tab. 5.4.

Year	PRT scintillator no.							Overall factor
	1	2	3	4	5	6	7	
1996	0.782	0.703	1.000	0.397	0.071	0.151	0.813	0.850
1997	0.460	0.517	1.000	0.191	0.086	0.095	0.216	0.770

TABLE 5.4: Correction factors for the PRT efficiencies.

The efficiency for scintillator number 3 is left unchanged because in this case, the measured efficiency is bigger than the simulated value. If these correction factors are applied to the simulation, there is still a significant discrepancy in the observed distribution of PRT hits if simulation and data are compared. This suggests that the simulation the showering of particles in the material surrounding the PRT is not perfect or that the primary particle multiplicities are too large. The result are correlations between hits in different scintillators which are overestimated in the simulation. Therefore, an overall reduction of the probability to measure activity in any of the scintillators is applied on top of the recalibration for each year, as given in the rightmost column of Tab. 5.4. The efficiency of the PRT was also investigated in detail in [87], where identical values for the correction factors were obtained for corresponding running periods.

5.5.4 The $x_{I\!P}$ Variable

The quantity $x_{I\!P}$, as introduced in section 1.2.2, measures the longitudinal momentum fraction of the colourless exchange with respect to the proton (Eq. 1.49). $x_{I\!P}$ is reconstructed from Q^2, W and the invariant mass M_X of the hadronic final state by:

$$x_{I\!P} = \frac{Q^2 + M_X^2 - t}{Q^2 + W^2 - m_P^2} \simeq \frac{Q^2 + M_X^2}{Q^2 + W^2} \ . \tag{5.34}$$

For the kinematic range under study, t (which is not measured) and m_P can be neglected. M_X is calculated from the 4-vectors of the hadronic final state particles:

$$M_X^2 = \left(\sum_i E_i\right)^2 - \left(\sum_i p_{x,i}\right)^2 - \left(\sum_i p_{y,i}\right)^2 - \left(\sum_i p_{z,i}\right)^2 \ . \tag{5.35}$$

The reconstruction of M_X and $\log x_{I\!P}$ is visualised in Fig. 5.11.

Events with a large rapidity gap in the final state, as selected by the above mentioned cuts on η_{max}, N_{FMD} and N_{PRT}, have $x_{I\!P}$ values up to 0.2. In order to select events in the region of $x_{I\!P}$ where the cross section is dominated by diffractive exchange and remaining background from non-diffractive DIS is small, an additional cut
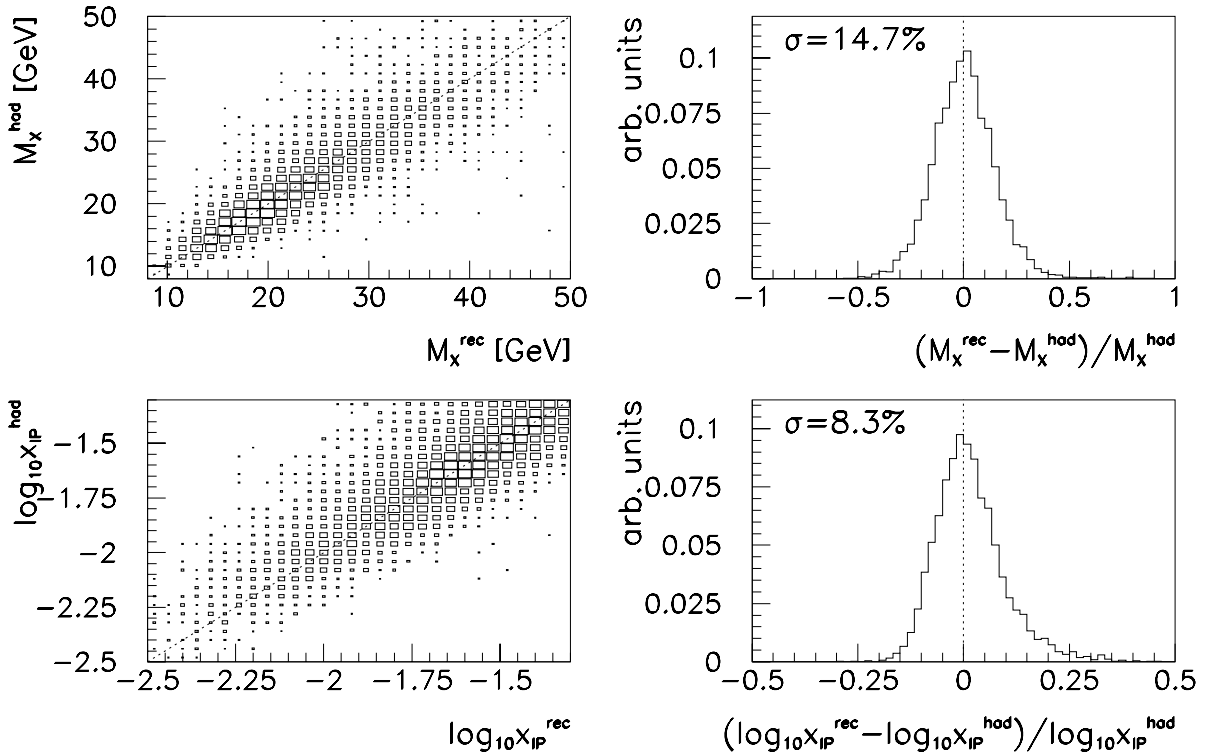
$$x_{I\!P} < 0.05 \tag{5.36}$$

is applied.

FIGURE 5.11: Reconstruction of M_X and $\log x_{I\!P}$. Correlations between the hadron level and reconstructed level values of the hadronic final state invariant mass M_X *(top)* and of $\log x_{I\!P}$ *(bottom)* are shown.

5.5.5   Summary of the Diffractive Selection

A summary of the cuts which are applied to select diffractive events is given in Tab. 5.5.

Diffractive Cuts
$\eta_{max} < 3.2$
$N_{FMD} \leq 1$
$N_{PRT} = 0$
$x_{I\!P} < 0.05$

TABLE 5.5: Summary of the diffractive cuts.

In Fig. 5.12, the distributions of η_{max}, $\log x_{I\!P}$, N_{FMD} and N_{PRT} are shown for data and the sum of the diffractive and inclusive DIS Monte Carlo simulations, mixed together as described in 3.3. The relative normalisations of the simulations are adjusted individually to match the data. The distributions are well described by the simulations. The contribution of diffractive events dominates at low η_{max}, low $x_{I\!P}$ and at zero N_{FMD}, N_{PRT} values. The excess of events at low η_{max} values over the standard DIS simulation is characteristic for diffractive events at HERA [1].
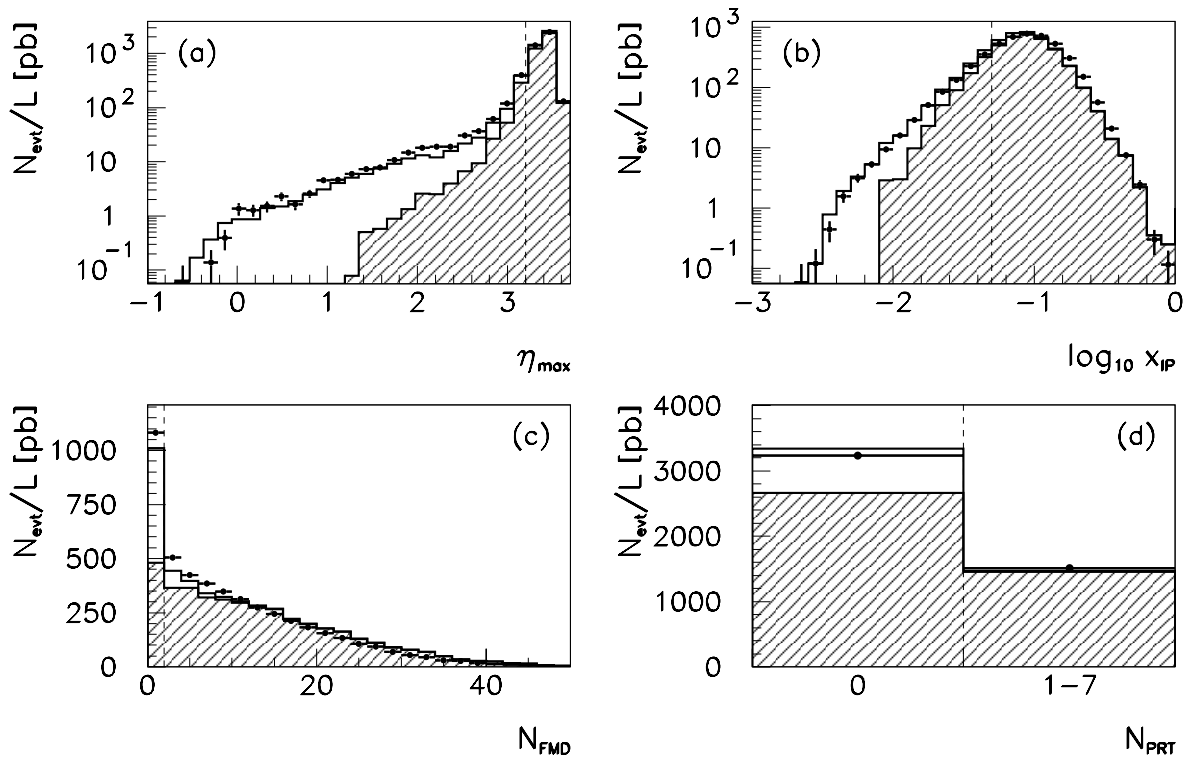
FIGURE 5.12: Distributions of *(a)* η_{max}, *(b)* $\log x_{I\!\!P}$, *(c)* N_{FMD} and *(d)* N_{PRT}. Shown are DIS data with at least two jets *(points)* and the Monte Carlo simulation *(histograms)*. The simulation is the sum of the inclusive ('RG-DIS') and the diffractive ('RG-DIF') DIS Monte Carlo event samples, mixed together as explained in section 3.3. The contribution of the inclusive DIS simulation is represented by the hatched areas. The cut values are indicated by the dashed vertical lines.

5.6 Trigger Selection and Trigger Efficiency

In order to measure cross sections, it is mandatory to require at least one level-one subtrigger with a well-known trigger efficiency for the selected events. Only then it is possible to fully determine the selection efficiency and thus to obtain a measurement of the cross section. In order to make maximum use of the available luminosity, a subtrigger has to be chosen which triggers on as much of the selected events as possible. This requires (a) a high efficiency for the given event signature and (b) a low prescale value of the trigger.

For an analysis of jet production at low Q^2 as presented in this thesis, a trigger which combines a trigger element based on an electromagnetic cluster in the SPACAL (the electron candidate) in conjunction with a high p_T track signal in the central tracker (with a high efficiency for jet events) is optimal. The use of a trigger solely based on the scattered electron, for which the efficiency is basically 100% (see below) is sub-optimal because the high rate of such a trigger for the region of Q^2 under study leads to a significant amount of prescaling, which in turn reduces the effective luminosity for that trigger.

Year	Run range	Trigger	Comment
1996	$158094 - 163254$	$S2(\text{l})$	
	$163255 - 171156$	$S2(\text{h})$	track p_T threshold increased
1997	$177921 - 193432$	$S2(\text{h})$	
	$193433 - 200444$	$S61$	IET threshold increased
	$200445 - 201519$	$S0$	no track requirement (min. bias)

Trigger	Definition
$S2(\text{l})$	`(SPCLe_IET_CEN_2 || SPCLe_IET>1) && (DCRPh_Ta && Zvtx_Sig)`
$S2(\text{h})$	`(SPCLe_IET_CEN_2 || SPCLe_IET>1) && (DCRPh_THig && Zvtx_Sig)`
$S61$	`(SPCLe_IET_CEN_3 || SPCLe_IET>2) && (DCRPh_THig && Zvtx_Sig)`
$S0$	`(SPCLe_IET_CEN_2 || SPCLe_IET>1)`
	(`&&` = 'and' ; `||` = 'or')

TABLE 5.6: Compilation of the subtriggers used in the analysis. The upper table comprises the data taking periods, the used subtriggers and comments explaining the changes in the trigger definition. In the lower table, the definitions of the individual subtriggers are given. Included are just the main trigger conditions.

The basic subtrigger chosen for the analysis is $S2$, which is formed by a logical combination of the SPACAL IET trigger (including the inner 'CIET' region) in conjunction with the CJC and z-vertex trigger elements (see section 4.2.6).

Trigger History

At the beginning of the data taking period under study (1996), the definition of $S2$ (Tab. 5.6) included the SPACAL IET trigger element (including the CIET region) with a medium energy threshold (`SPCLe_IET_CEN_2 || SPCLe_IET>1`), the DCRPh trigger element with the lower p_T threshold for the track candidate (`DCRPh_Ta`) and the z-vertex trigger element (`Zvtx_Sig`). Starting from run 163255, the track trigger element was replaced by `DCRPh_THig`, which has a higher p_T threshold. This however does not significantly reduce the efficiency of the trigger for the selected events. At the beginning of the 1997 data taking, the definition of $S2$ was the same as for the second part of 1996. Starting with run 193433, the definition of $S2$ was copied 1:1 to $S61$, with the exception that the IET trigger energy threshold was increased to the high value (`SPCLe_IET_CEN_3 || SPCLe_IET>2`). Finally, at the end of 1997 during the so-called *minimum bias*[3] run, subtrigger $S0$ was used for the analysis. This subtrigger comprised no track requirement and the medium IET energy threshold.

Prescales

The chosen subtriggers have a prescale of 1 for most of the corresponding running periods. There is a small fraction of runs where the trigger used had a prescale > 1. In such cases,

---

[3]'Minimum bias' stands for a trigger setup where the available data taking bandwidth is distributed mainly to triggers with a very high rate (e.g. very low Q^2) which are downscaled otherwise.

the corresponding events are counted with a weight equal to the prescale. Runs where the prescale of the used subtrigger is very high are excluded from the analysis.

Trigger Efficiency

In general, the efficiency of the SPACAL IET trigger for electrons with $E'_e > 8$ GeV, as considered in this analysis, is very close to 100%. The total trigger efficiency is thus basically given by the efficiencies of the tracking-based trigger elements (`DCRPh` and `Zvtx_Sig`). There are two ways to determine the trigger efficiency for the data sample under study:

The first possibility is simply to make use of the simulation of the trigger in the Monte Carlo. The strategy would then be to require that the corresponding subtrigger fired in the data as well as in the Monte Carlo simulation which is later used to correct the data. This strategy however has to rely on the correct parameterisation of the efficiency in the simulation, which is not necessarily the case. An alternative approach is to determine the trigger efficiency from the data itself, and then to correct the data for the inefficiency. Then, the trigger simulation is not needed for the determination of the cross sections. The second approach has been employed for this analysis.

The efficiency of a given trigger for the selected sample of events can be determined by using an independent subtrigger which is called *monitor trigger*. 'Independent' means that the studied trigger and the monitor trigger have no trigger elements in common. The trigger efficiency is then given by

$$\epsilon_{trig.} = \frac{N_{mon.+trig.}}{N_{mon.}} \ , \tag{5.37}$$

where $N_{mon.}$ is the number of events where the monitor trigger fired and $N_{mon.+trig.}$ is the number of events where the monitor trigger and the trigger under study both fired. In this analysis, the efficiencies of the SPACAL-based (ϵ_{el}) and the tracking-based (ϵ_{tr}) components of the trigger are determined individually. The combined trigger efficiency is then

$$\epsilon_{trig.} = \epsilon_{el} \cdot \epsilon_{tr} \ . \tag{5.38}$$

The monitor triggers used are

- Subtriggers $S67$, $S75$ and $S77$ for the determination of ϵ_{el}. These triggers are based on energy deposits in the LAr calorimeter.

- Subtrigger $S0$ for the determination of ϵ_{tr}. $S0$ is based on SPACAL information only.

The value of ϵ_{el} is generally above 99%, except at the lowest electron energies between 8 and 11 GeV. In addition, for two subsamples of the 1997 data the IET efficiency was reduced in certain regions of the SPACAL because of hardware problems with the trigger. These effects have been taken into account in the efficiency calculations. The tracking efficiency, given mainly by the `DCRPh` and `Zvtx_Sig` trigger elements, is typically between 80 and 90%. It is slightly reduced from run 163255 because of the increased `DCRPh` p_T threshold. ϵ_{tr} has been parameterised 2-dimensionally as a function of the pseudorapidities
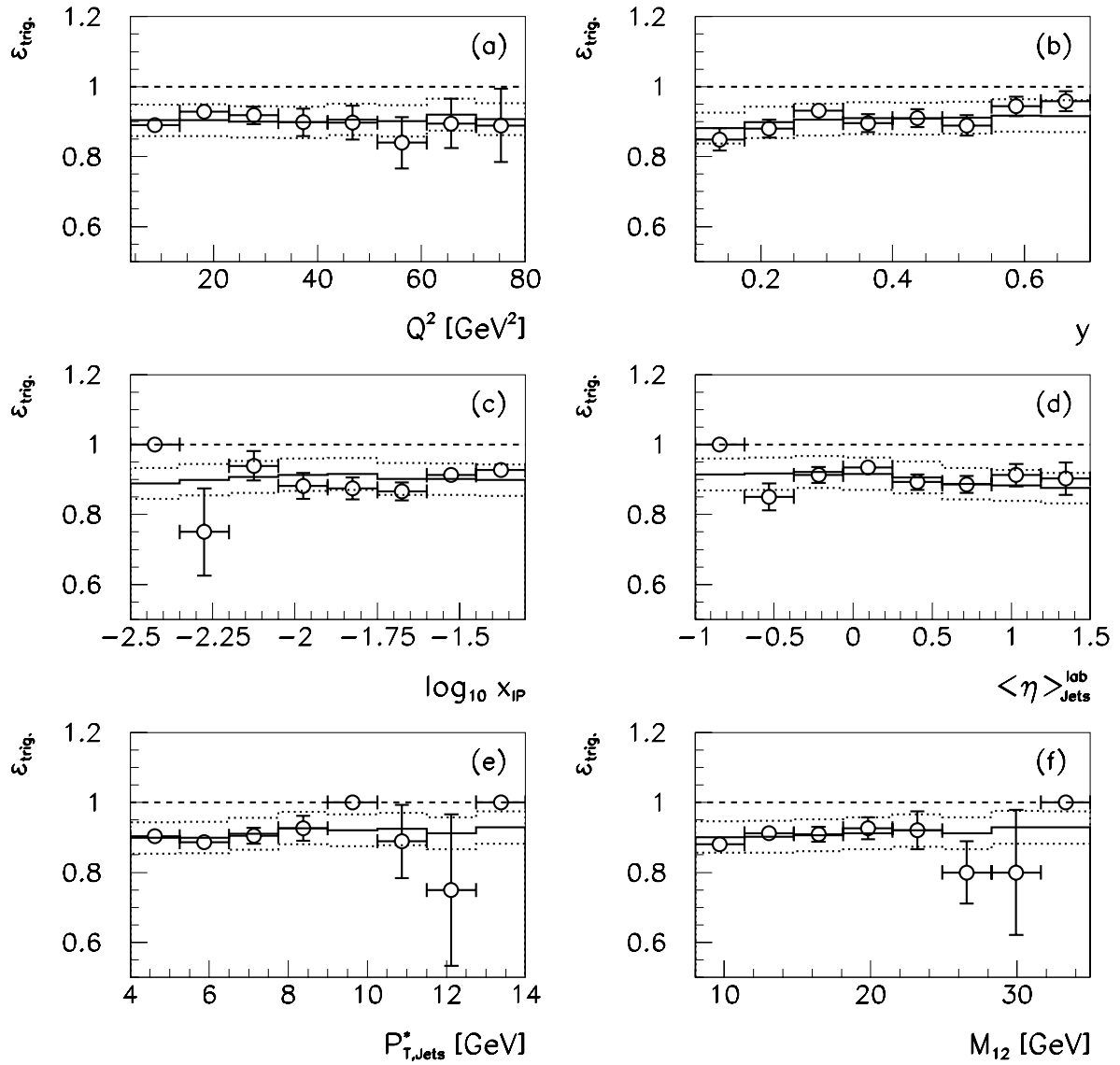
FIGURE 5.13: Trigger efficiency for diffractive dijet events. Shown is the total trigger efficiency for the selected data sample *(open circles)* as a function of *(a)* Q^2, *(b)* y, *(c)* $\log x_{I\!P}$, *(d)* the average dijet pseudorapidity in the laboratory frame $\langle \eta \rangle_{jets}^{lab}$, *(e)* the average transverse momentum $p_{T,jets}^*$ and *(f)* the dijet invariant mass M_{12}. Also shown is the 2-dimensional parameterisation of the trigger efficiency *(solid lines)* together with the assumed $\pm 5\%$ uncertainty *(dotted lines)*.
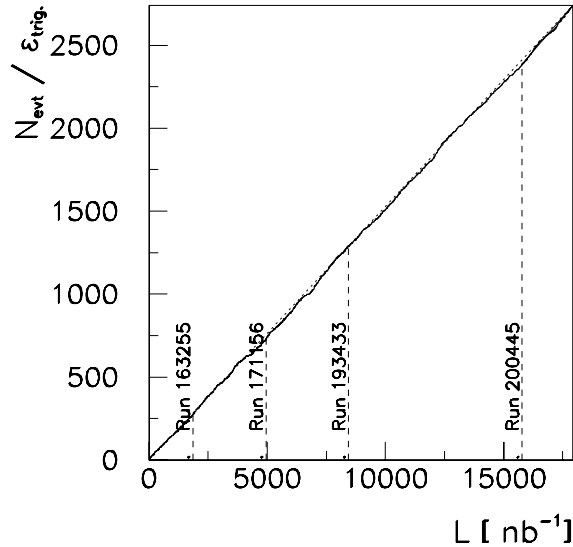
FIGURE 5.14: Number of accumulated events, divided by the trigger efficiency, plotted as a function of the accumulated integrated luminosity. The dashed vertical lines indicate where the trigger used for the analysis or its definition changed.

and transverse momenta of the jets. The main features of this parameterisation are that ϵ_{tr} is increasing with p_T and decreasing towards large η values because jets with $\eta > 1.5$ are not contained within the full acceptance of the central tracking system. Starting from run 200445 (the minimum bias running period), there is no inefficiency originating from a tracking requirement and the total trigger efficiency is given by ϵ_{el}.

Fig. 5.13 presents the overall trigger efficiency for the complete 1996 and 1997 sample of selected diffractive dijet events. The points represent the measured values of the total trigger efficiency. The solid lines correspond to the above mentioned parameterisation of $\epsilon_{trig.}$. The upper and lower dotted lines represent a $\pm 5\%$ uncertainty in the trigger efficiency, which is included into the systematic uncertainty of the cross section measurements.

The trigger efficiency for the 3-jet sample cannot be determined from monitor triggers because of a lack of statistics. It is parameterised in the same way as the dijet efficiency. It is noted here that the diffractive dijet trigger efficiency was cross checked with the much larger sample of inclusive dijet events with jet pseudorapidities and transverse momenta in a similar range but without a rapidity gap.

Stability of the Selection

Fig. 5.14 shows the number of accumulated events, divided by the trigger efficiency, as a function of the accumulated integrated luminosity. Significant deviations from the expected straight line are not observed and reassure that the trigger efficiencies for the different running periods with varying trigger setups have been taken into account consistently.
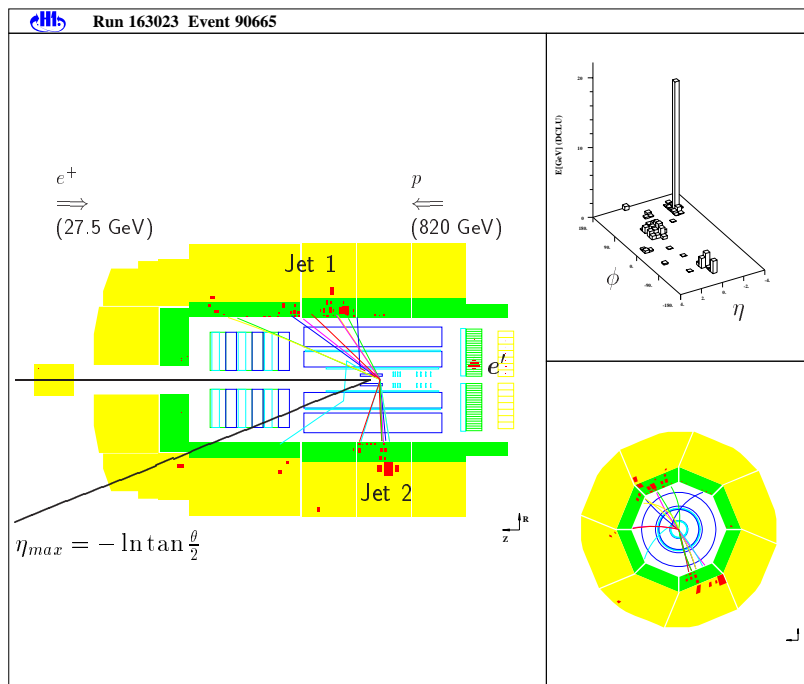
Figure 5.15: Graphical representation of a selected diffractive DIS dijet event. *(left)* rz-view: Protons enter the detector from the right, electrons (positrons) from the left. The scattered electron is measured in the SPACAL. There are no energy deposits in the forward part of the LAr calorimeter. Two jets are measured in the calorimeter together with the central tracking system. *(right top)* Distribution of the deposited energy in the calorimeter as a function of η and ϕ. The large peak corresponds to the electron. *(right bottom)* $r\phi$-view: The back-to-back structure of the two jets is visible. The picture has been created using the LOOK [115] program.

5.7   Summary

Diffractive deep-inelastic scattering events with at least two or exactly three jets have been selected from data taken in the years 1996 to 1997. After all cuts have been applied, the numbers of selected events for the kinematic range mainly given by $4 < Q^2 < 80$ GeV^2, $0.1 < y < 0.7$, $x_{I\!P} < 0.05$ and $p^*_{T,jet} > 4$ GeV are

$$N_{\mathrm{Dijet}} = 2506 \; ; \qquad N_{3-\mathrm{Jet}} = 130 \; . \tag{5.39}$$

The data correspond to an integrated luminosity of

$$\mathcal{L} = 17.96 \pm 0.36 \text{ pb}^{-1} \; . \tag{5.40}$$

A graphical representation of one of the selected dijet events is shown for illustration in Fig. 5.15.

Chapter 6

Cross Section Measurement

The following chapter describes the measurement of the differential hadron level cross sections for diffractive dijet and 3-jet production in DIS . After the chosen observables have been introduced, the measured data are compared with the Monte Carlo simulations which are used to correct the data. The definition of the cross sections at the hadron level is explained. Then, the corrections which are applied to the data to obtain the cross sections are reviewed in detail. The chapter ends with a study of the systematic uncertainties in the measurements.

6.1 Definition of the Observables

In this section, the chosen observables to study diffractive dijet and 3-jet production are presented. The distributions of these observables are corrected to the hadron level.

6.1.1 Dijet Cross Sections

The dijet cross sections are measured differentially in the following observables:

Basic event properties

The following observables represent fundamental quantities for diffractive deep-inelastic scattering:

- The photon virtuality Q^2;

- The photon-proton centre-of-mass energy W;

- The invariant mass of the photon dissociation system M_X;

Q^2 is well reconstructed from the polar angle and energy measurements of the scattered electron (Fig. 5.4). The quality of the W measurement can be inferred indirectly from the y reconstruction, which is also shown in Fig. 5.4, if one bears in mind the relation between W and y given by $W^2 = ys - Q^2$. The reconstruction of M_X was already presented in Fig. 5.11.

Jet Observables

The properties of the dijet system are studied in terms of the jet transverse momentum in the $\gamma^* p$ frame $p^*_{T,jet}$ and the jet pseudorapidity in the laboratory frame η^{lab}_{jet}. For each event, average values for the two highest p_T jets are constructed:

- The average transverse momentum of the jets, defined as

$$p^*_{T,jets} = \frac{1}{2} \left(p^*_{T,jet\ 1} + p^*_{T,jet\ 2} \right) \ ; \tag{6.1}$$

- The average pseudorapidity of the jets, defined as

$$\langle \eta \rangle^{lab}_{jets} = \frac{1}{2} \left(\eta^{lab}_{jet\ 1} + \eta^{lab}_{jet\ 2} \right) \ . \tag{6.2}$$

The reconstruction of the jet pseudorapidities and transverse momenta with respect to the hadron level was shown in Fig. 5.7. The good correlation between the hadron level jets and the partons emerging from the hard scattering process was demonstrated in Fig. 5.8. A good correlation between partons and jets is important in order to infer the underlying dynamics of the process under study.

Observables related to Diffraction

The following observables are suited to interpret the data in the context of diffraction:

- The longitudinal momentum fraction $x_{I\!P}$ of the proton which is carried by the colourless exchange. The dependence on $x_{I\!P}$ is essentially a measure of the energy dependence of the cross section. For the reconstruction of $x_{I\!P}$ see Fig. 5.11. The correlation between the hadron level value of $x_{I\!P}$, as calculated from the X system, and the 'true' generated value of $x_{I\!P}$ is essentially perfect (not shown).

- The β variable, which is calculated from

$$\beta = \frac{Q^2}{Q^2 + M_X^2 - t} \simeq \frac{Q^2}{Q^2 + M_X^2} \ . \tag{6.3}$$

  In a partonic interpretation, β corresponds to the momentum fraction of the colourless exchange which is carried by the struck quark which couples to the virtual photon. Inclusive measurements of the diffractive structure function are typically expressed as a function of β.

- The momentum fraction $z^{(jets)}_{I\!P}$ of the colourless exchange which enters the hard interaction, calculated from

$$z^{(jets)}_{I\!P} = \frac{Q^2 + M_{12}^2}{Q^2 + M_X^2} \ , \tag{6.4}$$

  where M_{12} is the invariant dijet mass, calculated from the massless jet 4-vectors. In loose terms, $z^{(jets)}_{I\!P}$ measures the fraction of the energy of the X system which is
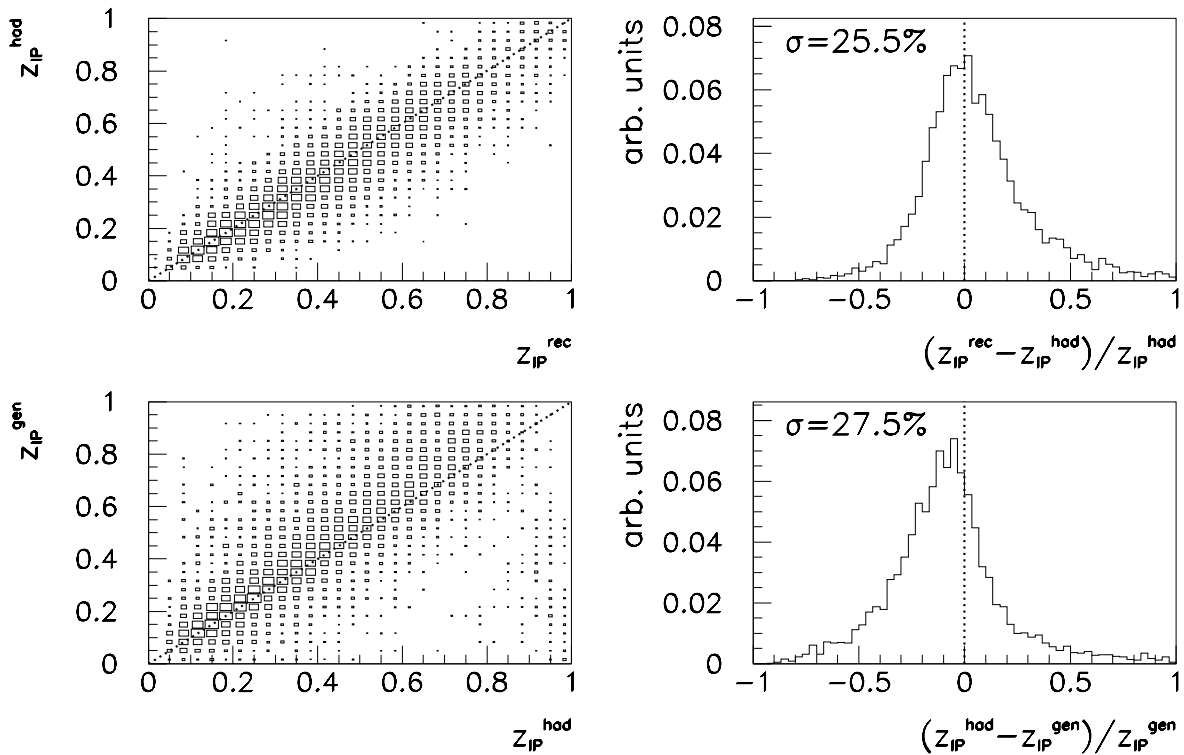
FIGURE 6.1: Reconstruction of the $z_{I\!P}^{(jets)}$ variable. Shown are correlations between *(top)* the hadron level (labelled '$z_{I\!P}^{had}$') and detector level (labelled '$z_{I\!P}^{rec}$') values and *(bottom)* between the generated (labelled '$z_{I\!P}^{gen}$') and the hadron level values of $z_{I\!P}^{(jets)}$.

contained in the two highest p_T jets. In the context of a resolved partonic pomeron model (section 1.2.5), $z_{I\!P}^{(jets)}$ is an estimator for the longitudinal momentum fraction of the parton in the pomeron which enters the hard scattering.

The $z_{I\!P}^{(jets)}$ variable is reconstructed on detector level with respect to the hadron level with a precision of approximately 25%, as shown in Fig. 6.1(top). There is also a good correlation between the hadron level value of $z_{I\!P}^{(jets)}$ and the true generated value of $z_{I\!P}$ (Eq. 1.55), as can be seen in Fig. 6.1(bottom). A small contribution from events generated at small but reconstructed on hadron level at large values of $z_{I\!P}$, which is observed in the lower right corner of Fig. 6.1(bottom left) originates from events where a pair of charm quarks ($c\bar{c}$) is produced via the Boson-Gluon-Fusion (BGF) diagram.

In order to test factorisation properties and scale dependence effects in the data, the following two-dimensional distributions are studied:

- In order to test Regge factorisation, i.e. the factorisation of the cross section into a term which only depends on $x_{I\!P}$ (integrating over t) and a second term which

depends on Q^2, $p^*_{T,jets}$, $z^{(jets)}_{I\!P}$ etc. but *not* on $x_{I\!P}$, the $z_{I\!P}$ distribution is measured in four intervals of $x_{I\!P}$. For the special case of a resolved pomeron model (section 1.2.5), the term depending only on $x_{I\!P}$ corresponds to the t-integrated pomeron flux factor $f_{I\!P/p}(x_{I\!P})$, the other term is proportional to the pomeron parton distributions $f^{I\!P}_i(z, \mu^2)$, probed at a parton momentum fraction $z = z^{(jets)}_{I\!P}$ and evaluated at the factorisation scale μ^2.

- To test the dependence of the cross section on the factorisation and renormalisation scale μ^2, the $z^{(jets)}_{I\!P}$ distribution is measured in four intervals of μ^2, set to $Q^2 + p^2_T$, the sum of the two hard scales in the process. The dependence on this particular choice of scale is investigated in chapter 7 and appendix A. In the context of diffractive or pomeron parton distributions, the evolution of the parton distributions with scale can be investigated.

Resolved Virtual Photon Contributions

In order to investigate the possible presence of a contribution from events where the virtual photon is resolved, the following observable is studied:

- $x^{(jets)}_\gamma$, an estimator for the photon momentum fraction x_γ which enters the hard interaction. For the definition of x_γ see Eq. 1.27. As in the case of real photoproduction analyses at HERA [116], $x^{(jets)}_\gamma$ is calculated from the ratio of the summed $E - p_Z$ of the two jets to the total $E - p_Z$ of the X system:

$$x^{(jets)}_\gamma = \frac{\sum_i (E_i - p_{Z,i})_{jets}}{\sum_i (E_i - p_{Z,i})_X} \ . \tag{6.5}$$

$x^{(jets)}_\gamma$ correlates well with the parton level and is reconstructed with a resolution of approximately 12% relative to the hadron level definition, if direct and resolved photon contributions are combined. For the resolved photon contribution only, the corresponding correlations are shown in Fig. 6.2.

Hadronic activity outside the Jets

The intention behind a study of the hadronic activity outside of the two highest p_T jets is to discriminate between different models for diffractive jet production. In the proton rest frame picture, diffractively scattered $q\overline{q}$ photon fluctuations cannot produce additional hadronic energy outside the two jet cones (neglecting jet resolution and higher order QCD effects). By contrast, $q\overline{q}g$ states would lead to a significant energy beyond the two highest p_T jets. Another aspect is that the resolved pomeron model implies the presence of a soft non-collimated pomeron remnant, whereas in the BJLW model for $q\overline{q}g$ production by 2-gluon exchange all three partons are required to have high transverse momentum. Furthermore, the possible presence of resolved virtual photon contributions in the data can also be investigated by studying the energy flow outside the jets.
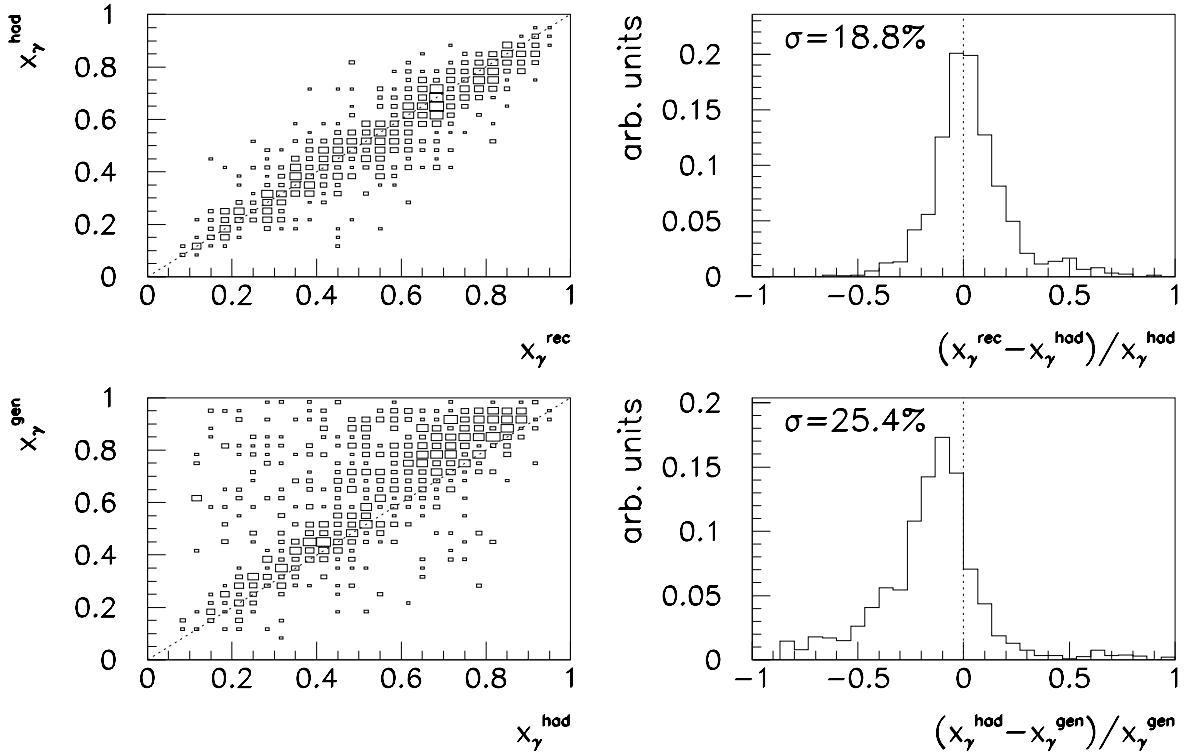
FIGURE 6.2: Reconstruction of the $x_\gamma^{(jets)}$ variable. Shown are correlations *(top)* between the hadron level (labelled 'x_γ^{had}') and detector level (labelled 'x_γ^{rec}') values and *(bottom)* between the generated value x_γ^{gen} and the hadron level estimator for $x_\gamma^{(jets)}$. In both cases, only simulated events where the virtual photon is resolved have been included in the plots.

It is desirable to investigate these questions in the rest frame of the X system, which is also called the $\gamma^* I\!\!P$ centre-of-mass system (Fig. 6.3). It is defined by:

$$q + x_{I\!\!P}P = 0 \ , \tag{6.6}$$

where q (P) are the photon (proton) 4-vectors. Quantities in that frame are labelled with a dagger '†'. The $z^\dagger = 0$ plane defines two hemispheres: The $z^\dagger < 0$, $\eta^\dagger < 0$ hemisphere corresponds to the photon direction, whereas the $z^\dagger > 0$, $\eta^\dagger > 0$ hemisphere corresponds to the 'pomeron' direction. In this context, the term 'pomeron' is only used synonymously with the colourless exchange, not implying the context of a certain physical model. The following observables are studied:

- $E_{rem}^{(\gamma)}$, the energy sum of all hadronic final state particles of the X system not contained in the two highest p_T jets and located in the photon hemisphere ($z^\dagger < 0$) of the $\gamma^* I\!\!P$ centre-of-mass frame:

$$E_{rem}^{(\gamma)} = \sum_i E_i^\dagger \quad (p_{z,i}^\dagger < 0; \ i \notin \text{Jets } 1, 2) \ . \tag{6.7}$$
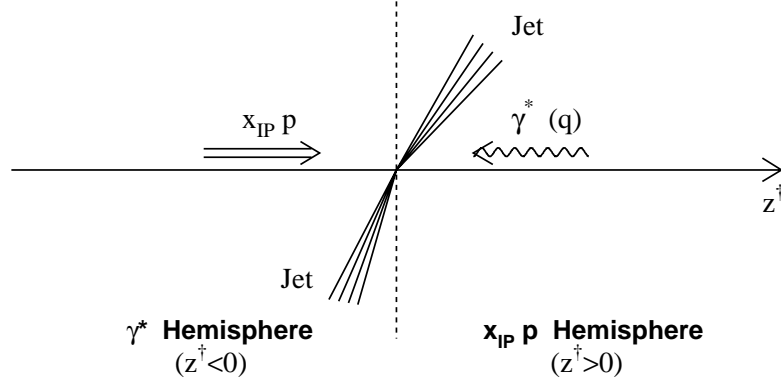
FIGURE 6.3: Visualisation of the $\gamma^* I\!\!P$ centre-of-mass system. This frame corresponds to the rest frame of the X system and is defined by $q + x_{I\!\!P}P = 0$. The $z^\dagger > 0$, $\eta^\dagger > 0$ hemisphere corresponds to the pomeron direction, whereas the $z^\dagger < 0$, $\eta^\dagger < 0$ hemisphere corresponds to the photon direction.

Similarly to $x_\gamma^{(jets)}$, this observable is used to investigate the presence of resolved photon contributions, since a possible *photon remnant* would lead to an increased energy flow in the photon hemisphere.

- $p_{T,rem}^{(I\!\!P)}$, the transverse momentum of the summed final state hadrons of the X system not contained in the two highest p_T jets and located in the pomeron hemisphere ($z^\dagger > 0$) of the $\gamma^* I\!\!P$ centre-of-mass frame:

$$p_{T,rem}^{(I\!\!P)} = \sqrt{(\sum_i p_{x,i}^\dagger)^2 + (\sum_i p_{y,i}^\dagger)^2} \quad (p_{z,i}^\dagger > 0; \ i \notin \text{Jets } 1, 2) \ . \qquad (6.8)$$

This observable is designed to discriminate between models with a soft pomeron remnant (e.g. the resolved pomeron model and the saturation model) and those with a third high-p_T parton (BJLW model).

For the quality of the reconstruction of the two observables, see Fig. 6.4.

6.1.2   3-Jet Cross Sections

The cross sections for diffractive 3-jet production in DIS are measured differentially in the following observables:

- The 3-jet invariant mass M_{123}, calculated from the massless jet 4-vectors.

- The $z_{I\!\!P}^{(3\ jets)}$ observable, calculated from:

$$z_{I\!\!P}^{(3\ jets)} = \frac{Q^2 + M_{123}^2}{Q^2 + M_X^2} \ . \qquad (6.9)$$

This quantity corresponds, by analogy to the definition of $z_{I\!\!P}^{(jets)}$ in the case of dijet production, to the fraction of the colourless exchange momentum which enters the hard scattering process. It can also be viewed as a measure of the fraction of the hadronic final state energy of the X system which is contained in the three jets.
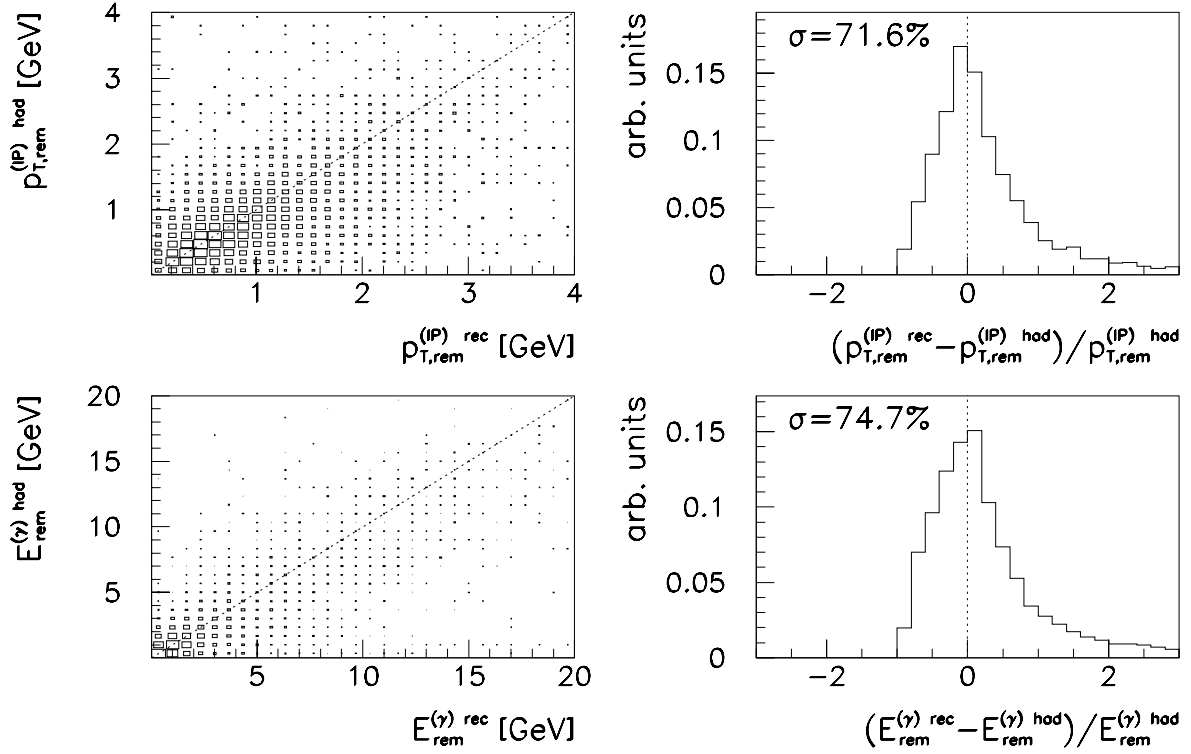
FIGURE 6.4: Reconstruction of *(top)* $E_{rem}^{(\gamma)}$ and *(bottom)* $p_{T,rem}^{(I\!P)}$. Shown are correlations between the hadron level and detector level quantities.

6.2 Comparison Data – Simulation

For the unfolding of the data from effects of limited detector acceptances, resolutions and efficiencies, it is essential that the Monte Carlo simulation which is used for the unfolding gives an adequate representation of these effects. Confidence that this is actually the case can be obtained by comparing all relevant kinematic distributions of the measured events with the simulation. If a good agreement is found between data and simulation, the unfolding procedure can be expected to give reliable results.

Deviations observed in the distributions of the simulated with respect to the measured events have to be taken into account in the estimation of the systematic errors on the unfolded cross sections. In addition, it will have to be investigated how the corrections depend on the specific physical model which is implemented in the Monte Carlo generator used to simulate the events. This *model dependence* of the corrections has to be incorporated into the systematic error.

6.2.1   Diffractive Dijet Events

In Figs. 6.5 and 6.6, the measured diffractive dijet events (data points with statistical error bars) are compared with the prediction of the Monte Carlo simulations (solid histograms) which are used to correct the data to the hadron level. For each measurement interval, the number of observed events in the data has been divided by the integrated luminosity. Losses due to trigger inefficiency are corrected for (see section 5.6). The Monte Carlo simulation corresponds to the sum of the simulated colour singlet exchange (RG-DIF) and standard DIS (RG-DIS) events, mixed together as explained in section 3.3. For the simulation of colour singlet exchange events, direct and resolved virtual photon contributions are included. The contribution from the standard DIS simulation (RG-DIS) is indicated (dotted histograms). The simulations have been scaled to the data.

In general, the simulations give a very good description of the properties of the dijet events. In Fig. 6.5d, the distribution of events as a function of the logarithm of the (Bjorken-) x variable is shown. Due to the selection of events where the scattered electron is detected in the SPACAL (see section 5.2), the range in x is approximately 10^{-4} to 10^{-2}. In this low-x regime, the contribution from valence quarks in the proton is negligible and the gluon distribution is much larger than the quark distribution.

Fig. 6.6b shows that the distribution of the average pseudorapidity $\langle \eta \rangle_{Jets}^{lab}$ of the jets is not perfectly described by the simulations. The measured jets tend to lie more forward on average compared with the simulations. This discrepancy is taken into account when the systematic error on the cross sections which originates from the model dependence of the corrections is evaluated.

The $\left| \cos \Theta_{Jets}^* \right|$ distribution is shown in Fig. 6.6d. This quantity relates to the pseudorapidity difference of the two jets via

$$\left| \cos \Theta_{Jets}^* \right| \;=\; \left| \tanh \left(\tfrac{1}{2} \left(\eta_{Jet\,1}^* - \eta_{Jet\,2}^* \right) \right) \right| \tag{6.10}$$

Θ^* corresponds to the polar angle $\hat{\theta}$ in the parton-parton rest frame, as defined in section 1.1.5, because rapidity differences are invariant under longitudinal Lorentz-boosts. The dependence on Θ^* is, apart from acceptance effects (the cuts in $p_{T,jet}^*$ and η_{jet}^{lab}) which limit the accessible range of Θ^*, given by the matrix element of the underlying hard scattering process. A good agreement with the simulation is observed, where 2-jet events are dominantly produced via the leading order QCD matrix elements.

The dependence on $\Delta\Phi_{Jets}^*$, the azimuthal angular difference between the two jets, is presented in Fig. 6.6e. The distribution is peaked at a value of 180°, corresponding to the *back-to-back* configuration. The smearing towards smaller values of $\Delta\Phi_{Jets}^*$ is slightly more pronounced in the data with respect to the simulations. Deviations from the picture of a two-parton final state with an ideal back-to-back configuration may originate from higher order QCD or hadronisation effects.

In Fig. 6.6f, the data are presented as a function of $p_{T,Jets}^{*\,2}/Q^2$, the ratio of the squared dijet transverse momentum to the photon virtuality. Due to the selection of events with $Q^2 > 4$ GeV^2 and $p_{T,Jet}^{*\,2} > 16$ GeV^2, the relation

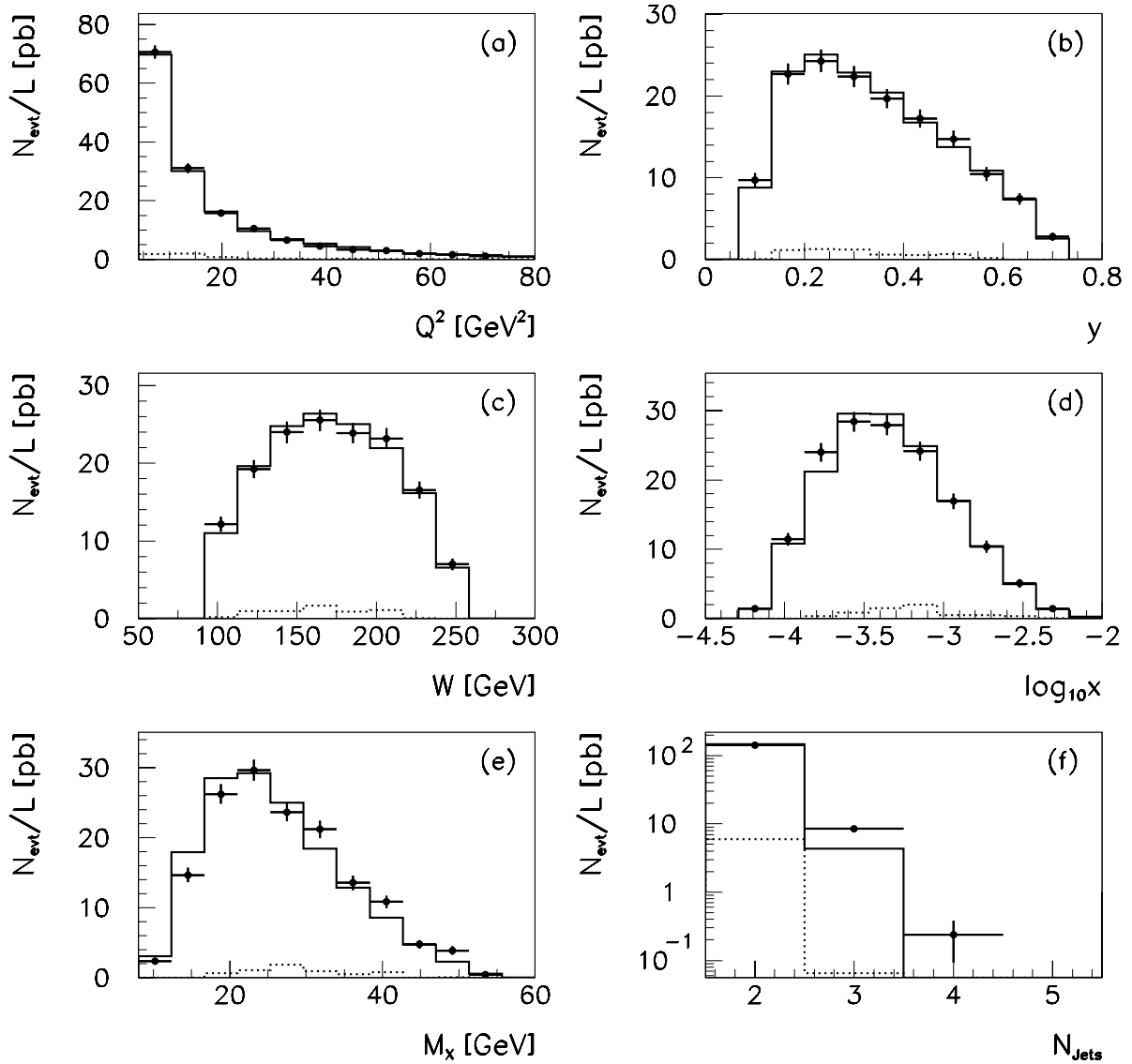$$p_{T,Jets}^{*\,2}/Q^2 \gg 1 \tag{6.11}$$

FIGURE 6.5: Comparison of the diffractive dijet data *(data points)* with the Monte Carlo simulation *(solid histograms)*. Shown are distributions for *(a)* the photon virtuality Q^2, *(b)* y, *(c)* the $\gamma^* p$ invariant mass W, *(d)* $\log x$, *(e)* the invariant mass M_X of the photon dissociation system and *(f)* the number of jets N_{Jets}. The Monte Carlo simulation is the sum of the colour singlet exchange and the inclusive DIS samples, as explained in the text. The contribution from the inclusive DIS simulation alone is also shown *(dotted histograms)*. The simulations have been scaled to the data, which are divided by the integrated luminosity and corrected for trigger inefficiency.
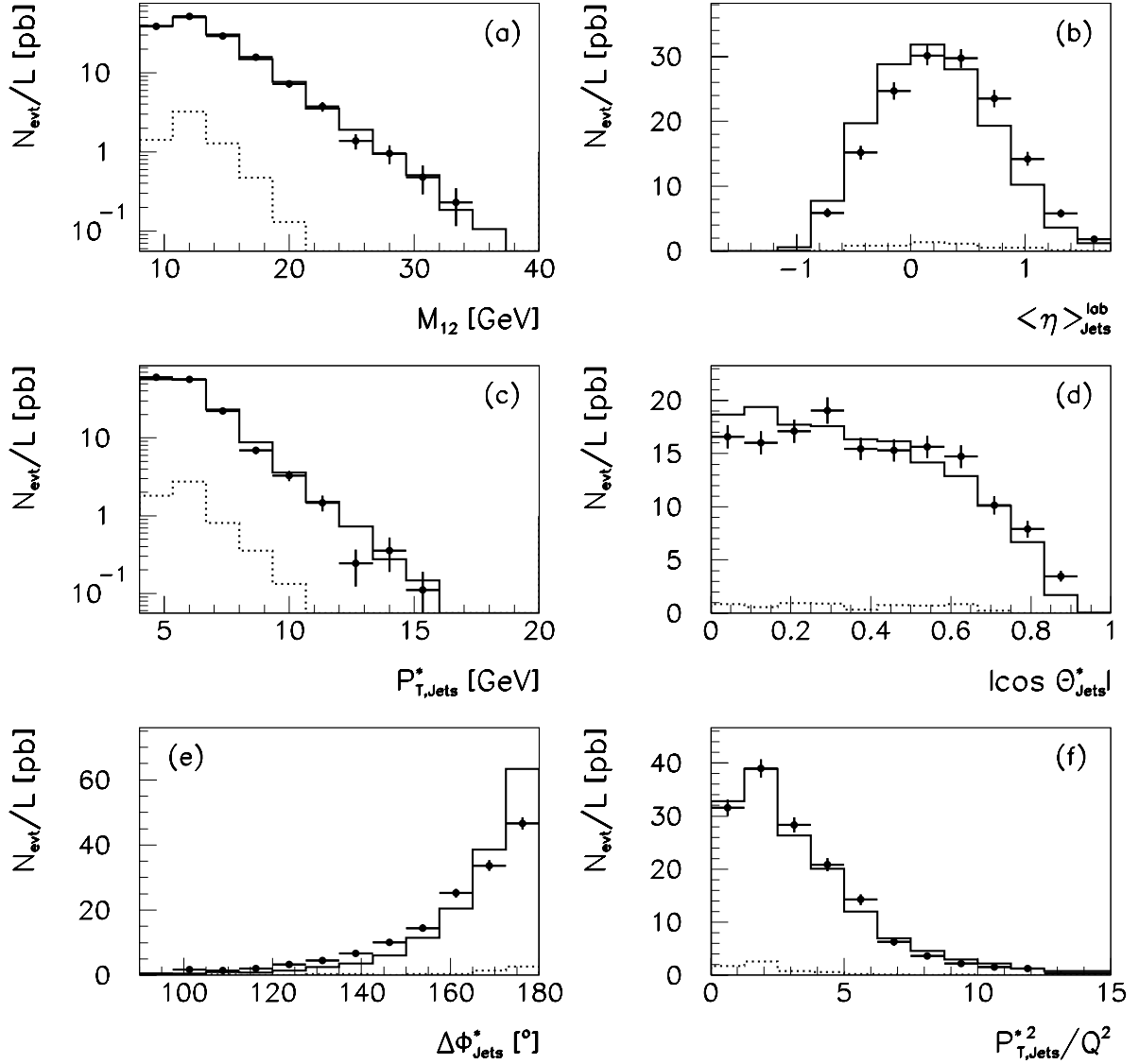
FIGURE 6.6: Comparison of the dijet data *(data points)* with the Monte Carlo simulation *(solid histograms)* (continued). Shown are distributions for *(a)* the dijet invariant mass M_{12}, *(b,c)* the average jet pseudorapidity and transverse momentum variables $\langle \eta \rangle_{Jets}^{lab}$ and $p_{T,Jets}^*$. Also shown is *(d)* the $|\cos \Theta^*|$ distribution, *(e)* the difference in azimuthal angle between the jets $\Delta \Phi_{Jets}^*$ and *(f)* the ratio $p_{T,Jets}^{*\,2}/Q^2$.

holds for most of the events. Q^2 and $p_{T,Jet}^{*\,2}$ act as the two hard scales for the process under study.

6.2.2 Diffractive 3-Jet Events

In Fig. 6.7, distributions of kinematic variables for the selected 3-jet events are shown. As for the dijet sample, the 3-jet distributions are compared with the simulations of colour singlet exchange (RG-DIF) and standard DIS (R(RG-DIS) events, mixed together as described in section 3.3.

Taking into account the limited statistical precision of the 3-jet data, also this data sample is well described by the simulations that are used to correct the data.

6.2.3 Energy Flow around the Jets

Fig. 6.8 shows the transverse energy flow around the jet axes for the dijet sample. For the jet profiles in η^* and ϕ^*, only transverse energies within one unit in azimuth and pseudorapidity are included in the plots respectively. The jet profiles for backward and forward jets are shown separately in Figs. 6.8a,c and b,d. The data exhibit a clear back-to-back dijet structure in azimuth. The energy flow is well described by the Monte Carlo simulation that is used to correct the data (solid lines). As said in section 3.3, the simulation includes a contribution from resolved virtual photons. The contribution from direct photons alone is indicated by the dotted histograms. It underestimates the energy flow backward of the jets, corresponding to the photon hemisphere.

6.3 Definition of the Hadron Level Cross Sections

In this section, the definition of the phase space for diffractive dijet and 3-jet production hadron level cross sections in deep-inelastic scattering is given. Two aspects are relevant here: The first is that the phase space must not contain regions where nothing can be measured because of detector acceptance or limited statistics. Secondly, the phase space has to be defined such that the corrections which have to be applied to the measured data in order to unfold them to the hadron level are small. Large acceptance corrections lead to large systematic errors on the extracted cross sections.

Phase Space for DIS Events

The data are corrected to a phase space for deep-inelastic scattering (DIS) events which is given solely in terms of the kinematic variables Q^2 and y:

$$4 < Q^2 < 80 \text{ GeV}^2 \; ; \qquad 0.1 < y < 0.7 \; . \tag{6.12}$$

No detector related cuts, e.g. on the polar angle θ_e' of the scattered electron, are made for the definition of the cross sections at the hadron level.
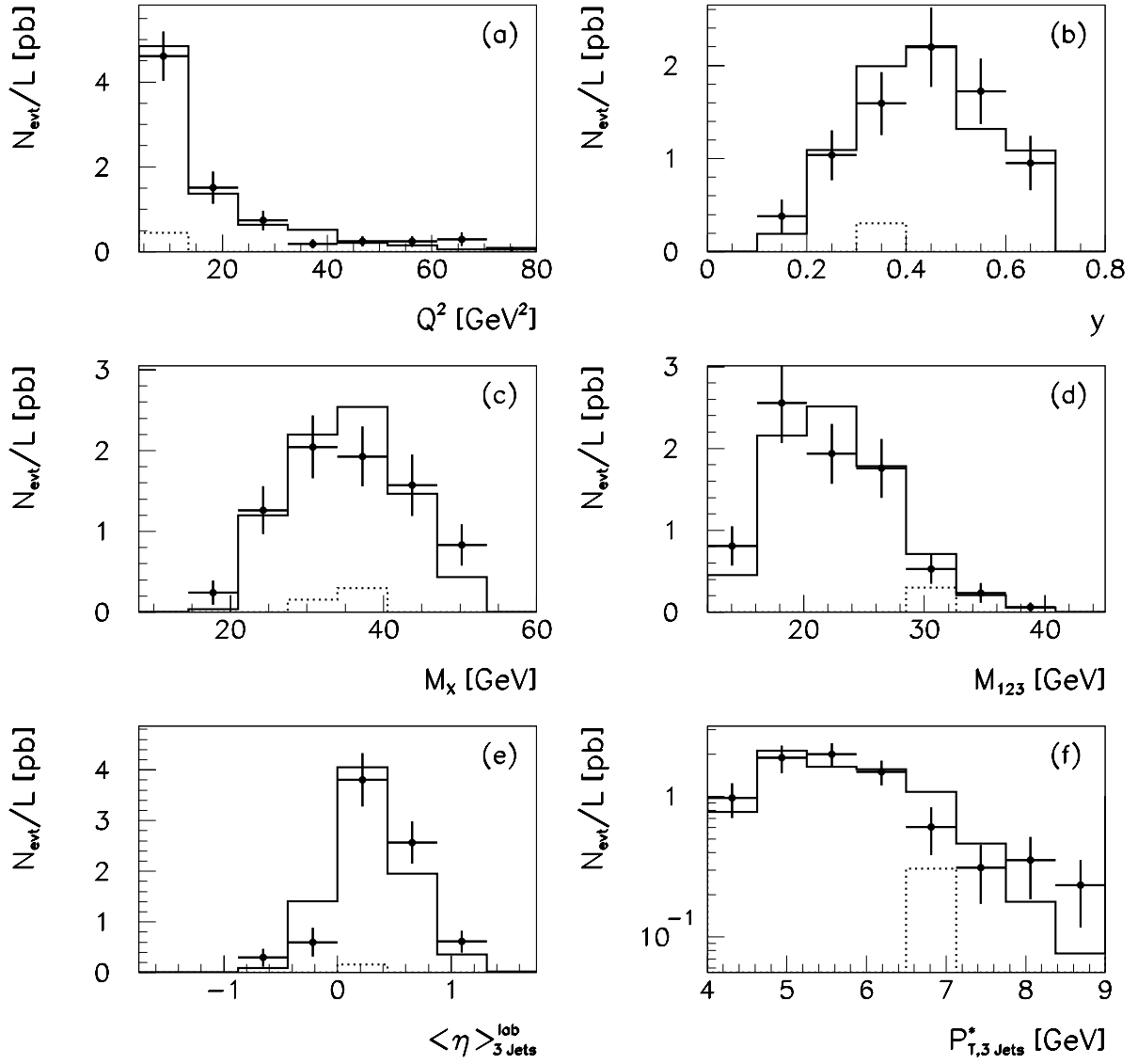
FIGURE 6.7: Comparison of the selected 3-jet events *(data points)* with the Monte Carlo simulation *(solid histograms)*, as explained in the text. Shown are distributions for *(a)* Q^2, *(b)* y, *(c)* M_X, *(d)* the three-jet invariant mass M_{123} and *(e,f)* the mean pseudorapidity and transverse momentum of the three jets, $\langle \eta \rangle_{3\ Jets}^{lab}$ and $p_{T,3\ Jets}^*$.
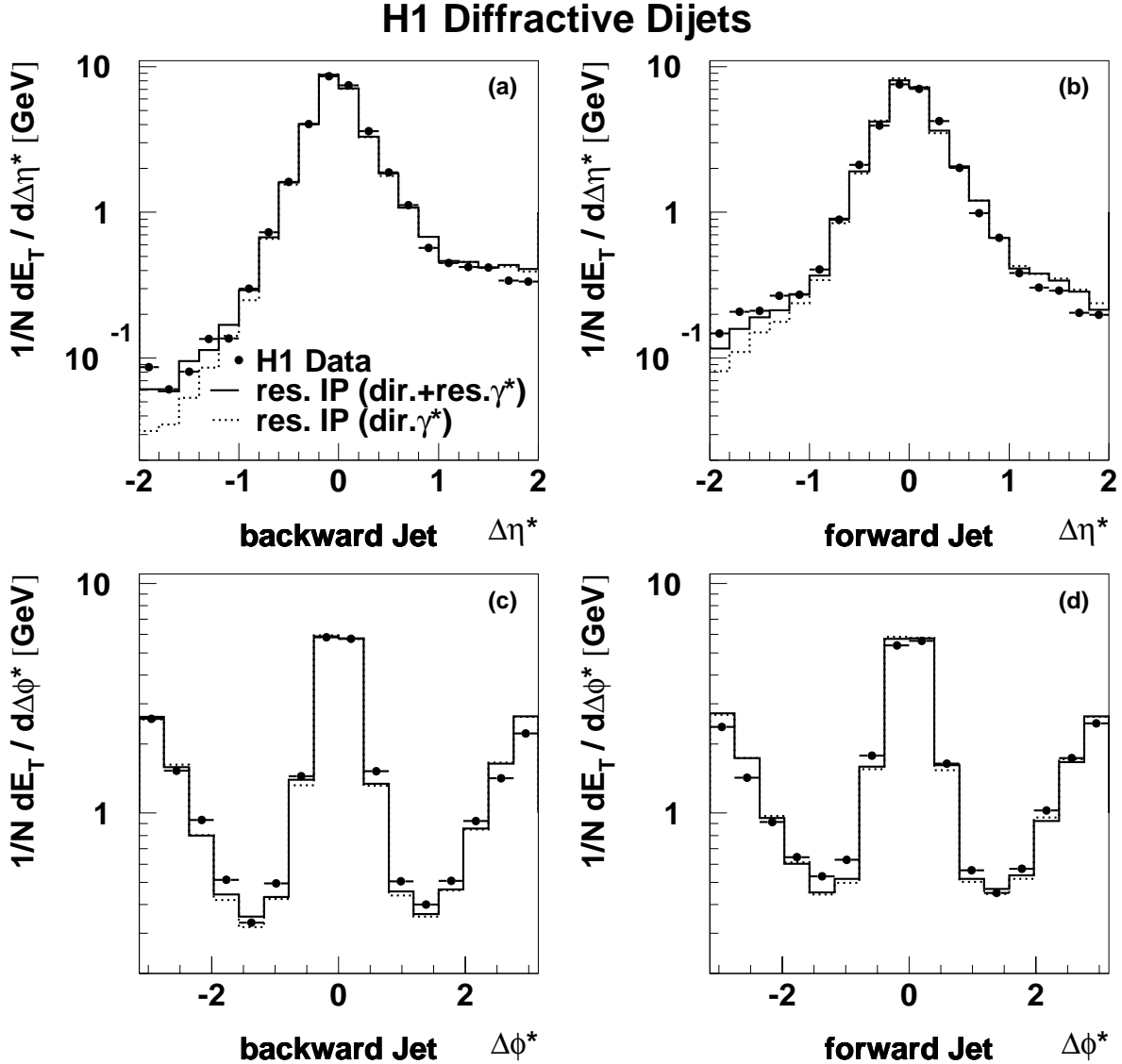
FIGURE 6.8: Observed distributions of the average transverse energy flow per event around the jet axes in the diffractive dijet sample. $\Delta\eta^*$ and $\Delta\phi^*$ are the distances from the jet axes in pseudorapidity and azimuthal angle in the hadronic centre-of-mass frame. The jet profiles in η^* and ϕ^* are integrated over ± 1 unit in ϕ^* and η^* respectively. *(a)* and *(c)* show the distributions for the backward jet in the laboratory frame, whereas *(b)* and *(d)* show those for the forward jet. The distributions for the simulated event samples as explained in the text are compared with the data. Here, the contributions from direct photons only *(dotted histograms)* and from the sum of direct and resolved photon contributions *(solid histograms)* are shown.

Phase Space for Jet Events

The phase space for dijet and 3-jet events is defined by means of the jet algorithm, as explained in section 5.4.1. The algorithm is applied to the hadrons contained in the X system, boosted into the $\gamma^* p$ centre-of-mass frame. Jets are only accepted if their transverse momentum with respect to the photon-proton collision axis satisfies

$$p^*_{T,jet} > 4 \text{ GeV} . \tag{6.13}$$

A cut on the pseudorapidities of the jets is made in the $\gamma^* p$ system which approximately matches the selection cut in the laboratory frame of $-1.0 < \eta^{lab}_{jet} < 2.2$:

$$-3 < \eta^*_{jet} < 0 . \tag{6.14}$$

Evidently, the following cuts are applied to select dijet and 3-jet events:

$$N_{\text{jets}} \geq 2 \quad \text{or} \quad N_{\text{jets}} = 3 . \tag{6.15}$$

Phase Space for Diffractive Events

As explained in section 3.2, diffractive events are defined at the hadron level in a model-independent manner by looking for the largest gap in η between any two hadronic final state particles and from that defining two systems X and Y. The phase space of the measured cross sections is then given in terms of the kinematic variables $x_{I\!P}$, M_Y and $|t|$, calculated from the 4-vectors p_X and p_Y. The cut on $x_{I\!P}$ matches the cut which is applied on detector level:

$$x_{I\!P} < 0.05 . \tag{6.16}$$

The cuts on M_Y and $|t|$ are chosen such that they roughly correspond to the upper end of the rapidity gap ($3.2 < \eta < 7.5$, given by the acceptance of the forward detectors) required for the measured events:

$$M_Y < 1.6 \text{ GeV} ; \qquad |t| < 1.0 \text{ GeV}^2 . \tag{6.17}$$

The motivation for choosing specifically these numbers is explained in section 6.4.5. The full definition of the hadron level cross sections is summarised in Tab. 6.1.

6.4   Corrections applied to the Data

In this section, it is explained how the corrected hadron level cross sections are obtained. The systematic uncertainties in the resulting cross sections are evaluated.

The procedure by which the hadron level cross sections are obtained comprises several steps: Firstly, a raw cross section is obtained by mainly correcting for trigger inefficiencies. Then, migrations into the measured region from events with high $x_{I\!P}$ or high M_Y are subtracted. The distributions are then corrected for detector effects using a bin-to-bin unfolding method. In addition, corrections have to be applied to take the noise in the FMD detector and the migrations over the $M_Y = 1.6$ GeV boundary into account. Finally, the cross sections are corrected for QED radiative effects, so that they are defined at the Born level.

Kinematic Range of Hadron Level Cross Sections
$4 < Q^2 < 80 \text{ GeV}^2$
$0.1 < y < 0.7$
$x_{I\!P} < 0.05$
$M_Y < 1.6 \text{ GeV}$
$|t| < 1.0 \text{ GeV}^2$
$N_{\text{jets}} \geq 2$ or $N_{\text{jets}} = 3$
$p^*_{T,jet} > 4 \text{ GeV}$
$-3 < \eta^*_{jet} < 0$

TABLE 6.1: The kinematic range to which the hadron level cross sections are corrected.

6.4.1   Raw Cross Section

In general, a cross section σ_i is defined experimentally as the number of accumulated events in interval i of a measured distribution as a function of the observable x, divided by the corresponding integrated luminosity:

$$\sigma_i(x) = \frac{N_{evt}(x_i)}{\mathcal{L}} \ . \tag{6.18}$$

As said in section 5.1, the integrated luminosity for the selected data sample corresponds to $\mathcal{L} = 17.96 \pm 0.36 \text{ pb}^{-1}$. In addition, the loss of events due to the trigger inefficiency has to be taken into account. This is achieved by dividing the number of selected events by the trigger efficiency $\epsilon_{trig,i}$, determined as explained in section 5.6. Furthermore, to obtain a *differential* cross section, σ_i is divided by the width Δ_i of the measurement interval or *bin*. The cross sections thus represent average values over the measurement intervals, which are quoted at the bin centre. The raw cross section is then given by:

$$\left(\frac{\mathrm{d}\sigma}{\mathrm{d}x}\right)_i = \frac{1}{\mathcal{L}} \ \frac{1}{\epsilon_{trig,i}} \ \frac{1}{\Delta_i} \ N_{evt}(x_i) \ . \tag{6.19}$$

6.4.2   Migrations from high $x_{I\!P}$ or high M_Y

Migrations of events into the measured sample which originate from the region of $x_{I\!P} > 0.2$ or $M_Y > 5.0 \text{ GeV}$ are taken into account by the simulation of standard DIS processes (RG-DIS, see section 3.3). This contribution is first subtracted from the data before in a second step the correction to the hadron level is performed by using only the colour singlet exchange simulation (RG-DIF).

For each measurement interval, the number of events to be subtracted is derived from the predicted number of standard DIS events N_{RG-DIS} which pass the selection cuts on detector level and fulfil

$$x_{I\!P} > 0.2 \ ; \qquad M_Y > 5.0 \text{ GeV} \tag{6.20}$$

at the hadron level. N_{RG-DIS} is scaled by the ratio of the integrated luminosities of the data $\mathcal{L}$ and the 'RG-DIS' simulation $\mathcal{L}_{RG-DIS}$:

$$N_{BKG,i} \;=\; \frac{\mathcal{L}}{C\,\mathcal{L}_{RG-DIS}} N_{RG-DIS}(x_i) \;. \tag{6.21}$$

C is a factor by which the prediction of the RG-DIS sample is scaled up (approximately 40% for dijet events) in order to give a good description of the inclusive (i.e. without diffractive cuts) jet cross section which is observed in the data. This discrepancy in normalisation which is observed when comparing jet cross sections with the predictions of leading order QCD Monte Carlo models is a well-known effect. It has been observed before [117] in a similar region of $p_{T,jet}$ and Q^2 and can be explained by the lack of full NLO QCD matrix elements for the calculation of the cross section within the simulation. The fraction of events which is subtracted corresponds to about 5% in total and is concentrated at large $x_{I\!P}$ values (see Figs. 6.5 and 6.6).

6.4.3 Correction to the Hadron Level

After the migrations from large $x_{I\!P}$ or M_Y have been subtracted, the corrections to be applied to the measured distributions to unfold the data to the hadron level can be performed with the simulation of colour singlet exchange events (RG-DIF) only.

The method employed for the unfolding of the hadron level cross sections is the so-called *bin-to-bin* correction method. It can be applied if it is a good approximation to unfolding with a matrix $\mathcal{M}$, defined as $\vec{n} = \mathcal{M} \cdot \vec{m}$, where $\vec{m}$ and $\vec{n}$ correspond to the measured and unfolded distributions, respectively. If the bin-to-bin migrations are small and therefore the matrix $\mathcal{M}$ is approximately diagonal, the bin-to-bin correction method is an adequate alternative to the matrix method.

Correction Factor   The so-called correction factor

$$C_{F,i} = \frac{\sigma_{rec,i}^{(rad)}}{\sigma_{had,i}^{(rad)}} \tag{6.22}$$

is calculated for every bin of the measured cross sections. It corresponds to a factor by which the raw cross section has to be divided to obtain the corresponding hadron level cross section. It is derived from calculating the following cross sections using the 'RG-DIF' sample of Monte Carlo events:

- $\sigma_{rec,i}^{(rad)}$, calculated at the level of measured detector observables from the sample of simulated events which pass all selection cuts which are applied to the data. The sample includes the effects of QED radiation and was passed through the full H1 detector simulation and reconstruction.

- $\sigma_{had,i}^{(rad)}$, calculated at the level of generated hadrons from all events which belong to the definition of the hadron level cross sections (Tab. 6.1). QED radiative effects are included.

It is noted that both samples include the effects of QED radiation. The correction to the Born level will be performed in a second step (section 6.4.6).

In the following, the migrations between measured cross section bins as well as *efficiencies* and *purities* are discussed. Every simulated event can be classified into one (and only one) of the following three sub-samples A, B or C:

- **A**: These are events which pass all cuts on detector level *and* belong to the definition of the hadron level cross sections. Taking the number of reconstructed jets as an example, sub-sample A corresponds to those events where two or more jets are found on detector level *and* on hadron level. It is noted that only for this sample the measured observables, such as e.g. the average transverse momentum of the jets, are well defined on both levels.

- **B**: This sub-sample corresponds to those events which belong to the hadron level cross section definition but do *not* pass all cuts applied to the events on detector level. These are events, for example, where two or more jets are found on hadron level, but only one jet is found on detector level.

- **C**: Events which do *not* fall into the hadron level definition of the cross sections but *do* pass all detector level selections fall into this sub-sample. This could be events for example, where only one jet is found on hadron level, but two jets are found on detector level.

Bin Purity and Stability   For sample **A**, the observable under study is well defined on hadron level and on detector level. The bin-to-bin migrations for this sample are studied by looking at the **bin purity** p and **bin stability** s, defined as:

$$p_i = \frac{N^A_{gen+rec,i}}{N^A_{rec,i}} \; ; \qquad s_i = \frac{N^A_{gen+rec,i}}{N^A_{gen,i}}. \qquad (6.23)$$

The bin purity is defined as the fraction of events reconstructed in a bin that are also generated in that bin. The bin stability is defined as the fraction of events generated in a bin that are also reconstructed in that bin. If both s and p are high, the correlation matrix $\mathcal{M}_{ij}$ between the hadron level and detector level quantities is dominated by the diagonal entries $\mathcal{M}_{ii}$, which is desirable in order to successfully apply a bin-to-bin correction method.

Global Efficiency and Background Fraction   From samples **A** and **B**, the selection efficiency can be studied in terms of the **global efficiency**, defined as

$$e_i = \frac{N^A_{gen,i}}{N^A_{gen,i} + N^B_{gen,i}} \; . \qquad (6.24)$$

In words, e_i corresponds to the fraction of generated events which belong to the cross section definition and are also reconstructed at the detector level, evaluated at bin i of

the hadron level distribution. Similarly, the **global background fraction** is defined for events which belong to sub-samples **A** or **C** as

$$b_i = \frac{N^C_{rec,i}}{N^A_{rec,i} + N^C_{rec,i}} \ .$$

(6.25)

This quantity measures the fraction of reconstructed events which are *not* generated within the hadron level cross section definition, evaluated at bin i of the detector level distribution.

The total correction factor $C_{F,i}$ for a measurement interval can be expressed in terms of e_i, b_i, s_i and p_i:

$$C_{F,i} = \frac{e_i \cdot s_i}{(1 - b_i) \cdot p_i} \ .$$

(6.26)

Distributions for e, s, b and p as well as for the combined factor C_F are shown in Fig. 6.9 for a selected number of cross sections. As a general rule, the binning of the cross sections was chosen such that the values of the bin purity and bin stability are well above 30%. Typical values are 50 to 60%. The correction factors C_F are typically in the range 0.5 to 0.8.

The integrated value of the global efficiency e is around 0.35. It shows a rising behaviour with the jet transverse momentum $p^*_{T,jets}$. The global efficiency is below average for the largest values of $x_{I\!\!P}$. These effects are caused by smearing over the measurement boundaries at $x_{I\!\!P} = 0.05$ and $p^*_{T,jet} = 4$ GeV.

The inverse behaviour with respect to the global efficiency is observed for the global background fraction b, which is about 45% on average. The value of b is above average at the largest $x_{I\!\!P}$ and smallest $p^*_{T,jets}$ values. For the 3-jet cross sections, the integrated values of global efficiency (background fraction) are smaller (larger) than for the dijet cross sections. This can be explained by the on average larger $x_{I\!\!P}$ value for 3-jet events[1] which leads to more smearing over the cut at $x_{I\!\!P} = 0.05$ and by more smearing about the minimum $p^*_{T,jet}$ if three jets are required.

The observed numbers for global efficiency (e) and global background fraction (b) result from the complicated selection of diffractive dijet and 3-jet events where many different cuts are applied in order to select DIS events, events with two or three jets and diffractive events all at the same time. The efficiency for example is thus the product of the DIS efficiency, the efficiency for jets and the efficiency for selecting diffractive events. All of these individual event signatures and corresponding selections are well understood individually. The dependence of the correction factors on the parameters of the physical model built into the simulation is studied in section 6.5.

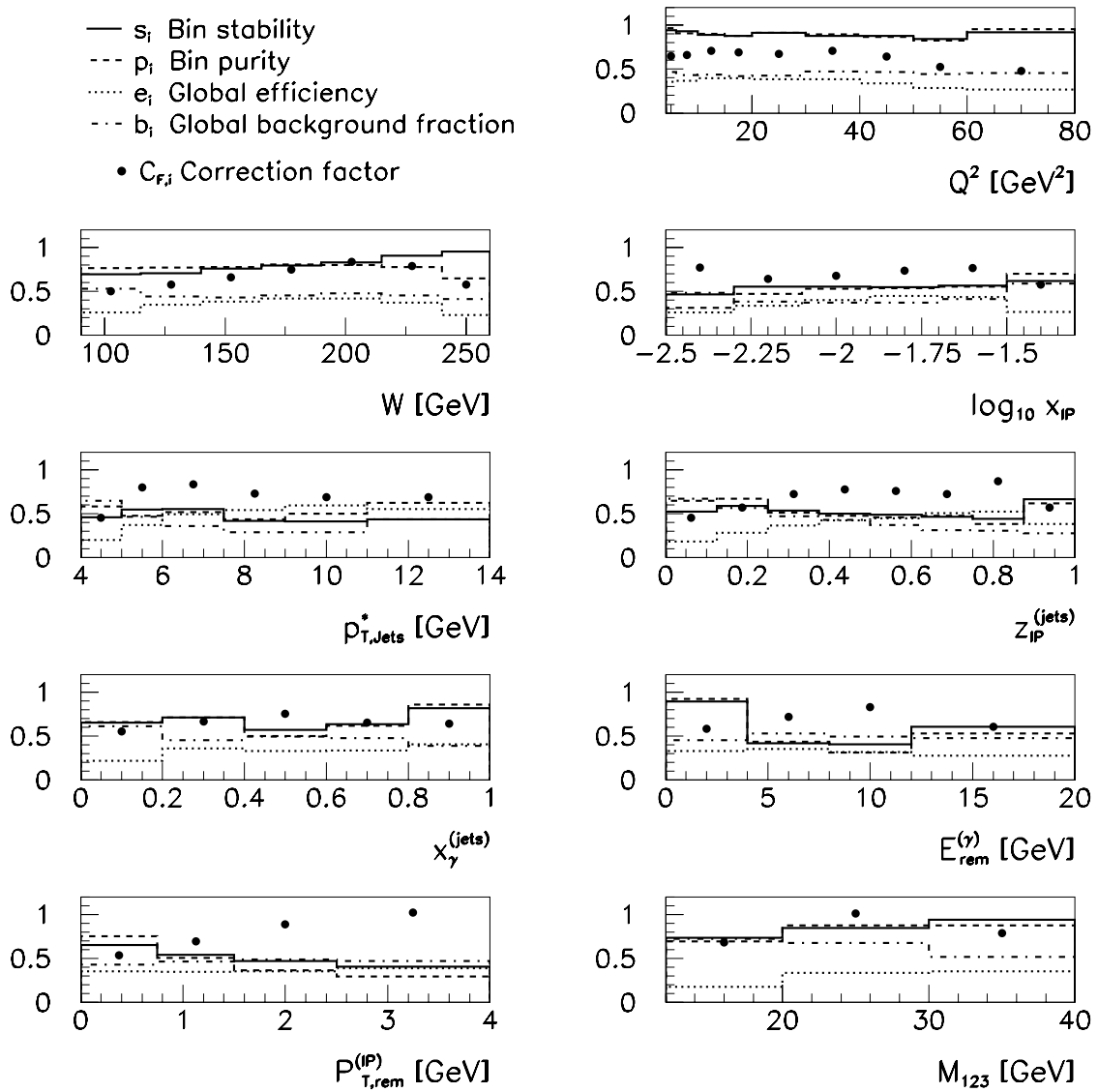[1]This is a kinematic effect due to the energy which is needed to produce three high-p_T jets.

FIGURE 6.9: Purities, efficiencies and correction factors. Shown are distributions for the bin stability s, the bin purity p, the global efficiency e, the global background fraction b and the combined correction factor C_F as defined in the text. The distributions are shown for a representative selection of the measured cross sections.

6.4.4   Correction for FMD Noise

As explained in section 5.5.2, diffractive events are rejected due to noise in the FMD detector which is misinterpreted as real hadronic activity in the outgoing proton region. Because this noise is not included in the Monte Carlo simulation, a correction has to be applied to the measured cross sections in order to compensate for the loss of events in the data. In section 5.5.2, the probability of reconstructing at least two hit pairs in the FMD due to noise, which leads to a rejection of the event, was estimated from a study of random trigger events as $5.5\% \pm 1.4\%$. To a very good approximation, this correction can be treated as a constant normalisation factor by which all of the extracted cross sections have to be increased:

$$C_{FMD} = +5.5\% \pm 1.4\% \ . \tag{6.27}$$

The uncertainty on the value of C_{FMD}, which is estimated as 25%, is included in the systematic error on the measured cross sections.

6.4.5   Smearing over $M_Y = 1.6$ GeV and $|t| = 1.0$ GeV^2

In this section, the smearing over the measurement boundaries at $M_Y = 1.6$ GeV and $|t| = 1.0$ GeV^2 is investigated. The additional correction which has to be applied to the measured cross sections because events with $M_Y > m_P$ (proton dissociation) are not included in the simulation (RG-DIF) is explained.

Fig. 6.10a shows the efficiency for detecting the proton dissociation system Y as a function of M_Y. The combined forward detector efficiency reaches $\sim 90\%$ for $M_Y \geq 5$ GeV. The individual detection efficiencies are:

- The PRT has a constant efficiency of around 45% because of its proximity to the beam pipe.

- The efficiency for detecting the Y system in the LAr is slowly increasing with M_Y and is comparable to the PRT efficiency above $M_Y \simeq 5$ GeV.

- The FMD is most efficient above $M_Y \simeq 2.5$ GeV because of secondary particle production.

For M_Y approaching the proton mass m_P, the efficiencies are quickly decreasing. This would lead to large corrections if cross sections were to be determined for elastically scattered protons only. This in turn would result in large systematic uncertainties. These uncertainties can be reduced if proton dissociation is included up to a finite value of M_Y in the cross section definition at the hadron level. As in previous H1 analyses, the value $M_Y = 1.6$ GeV is chosen here.

Figs. 6.10b,c show the efficiencies for detecting a proton dissociative system and an elastically scattered proton as a function of $|t|$, respectively. The combined detection efficiency for proton dissociation is approximately constant at the level of 85%. In the case of an elastic proton, the efficiency strongly increases with $|t|$ and reaches 30% at
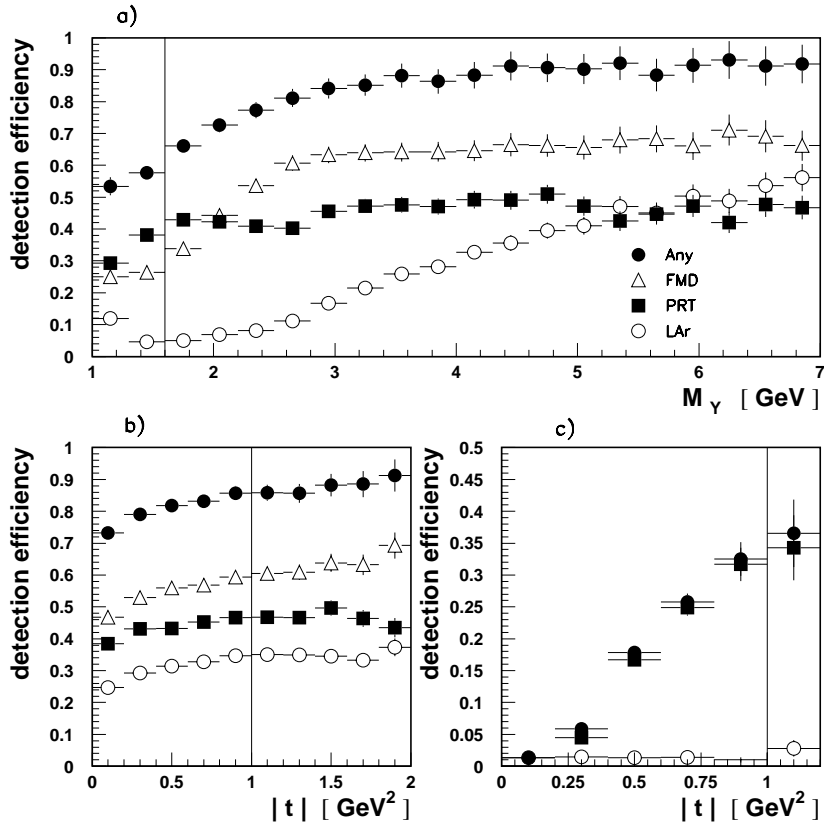
FIGURE 6.10: The efficiency for detecting the Y system as a function of M_Y and $|t|$, obtained using the DIFFVM [118] Monte Carlo simulation. Shown are efficiencies for detecting proton dissociation as a function of *(a)* M_Y and *(b)* and $|t|$ as well as the efficiency for detecting an elastic proton as a function of $|t|$ *(c)*. The efficiencies are shown for activity above noise thresholds in any forward detector *(full circles)* as well as for the FMD *(open triangles)*, the PRT *(full squares)* and the LAr *(open circles)* detectors individually (figure from [87]).

around 1.0 GeV^2. The measured hadron level cross sections are corrected to the range $|t| < 1.0$ GeV^2.

As said before, the basic acceptance corrections are performed with a simulation of colour singlet exchange events (RG-DIS). This procedure takes the migrations over $|t| = 1.0$ GeV^2 for elastically scattered protons into account. Proton dissociation is not included in the simulation. The high dissociation mass region of $M_Y > 5$ GeV is covered by the simulation of standard (i.e. non-diffractive) events (RG-DIS). The missing piece in the correction procedure is thus the treatment of the migrations over the $M_Y = 1.6$ GeV boundary for $M_Y < 5$ GeV. This correction, which is applied on top of the basic correction procedure, is determined using the DIFFVM [118] Monte Carlo model of proton disso-ciation in J/ψ production. The correction factor C_{M_Y} is determined from the following

formula:

$$C_{M_Y} = \frac{N_{gen}(M_Y < 1.6 \text{ GeV}, |t| < 1.0 \text{ GeV}^2) \ - \ N_{rec}}{N_{gen}(M_Y < 1.6 \text{ GeV}, |t| < 1.0 \text{ GeV}^2) \ + \ R \cdot N_{gen}(|t| < 1.0 \text{ GeV}^2)} \ . \tag{6.28}$$

Here, N_{gen} and N_{rec} are the number of hadron level and reconstructed detector level (i.e. passing forward cuts) proton dissociation events. R denotes the ratio of elastic to proton dissociation cross sections and is assumed as $R = 1$ for the determination of C_{M_Y}. The result for the correction is

$$C_{M_Y} = -6.5\% \pm 6.5\% \ . \tag{6.29}$$

The determination of the uncertainty in the value of C_{M_Y} is described in section 6.5. The correction leads to a global reduction of all measured cross sections. The number corresponds to the luminosity-weighted mean of the individual results for the 1996 and 1997 data taking periods which yield slightly different values individually, mainly because of the degrading PRT efficiency.

6.4.6 Correction to the Born Level

The Monte Carlo simulations used to correct the cross sections to the hadron level include various QED corrections to the bare Born term. These comprise initial and final state photon radiation from the electron as well as quark radiation and the corresponding virtual loop diagrams. Although it is possible to define the cross sections such that these QED effects are included, it is desirable to correct to the Born level. The reason is that model predictions which are to be compared with the data usually do not include these QED effects.

In consequence, a correction $C_{QED,i}$ factor is applied to the extracted cross sections. It is defined for every bin i of a measured distribution as

$$C_{QED,i} = \frac{\sigma_{had,i}^{(non-rad)}}{\sigma_{had,i}^{(rad)}} \ . \tag{6.30}$$

The values of $C_{QED,i}$ (Fig. 6.11), which on average are about 0.95, have been obtained from cross section predictions for colour singlet exchange events where the QED corrections to the cross sections were either switched on or off. Because for this task the generated Monte Carlo events need not be passed through the full time consuming detector simulation and reconstruction, high statistics event samples can be used to determine C_{QED}. In total, about 19M events each were generated for the two samples with and without QED effects, corresponding to integrated luminosities of more than 200 pb^{-1} each.

6.4.7 Summary of the Correction Procedure

The full correction procedure to the hadron level is summarised by the following formula:

$$\left(\frac{\mathrm{d}\sigma}{\mathrm{d}x}\right)_i = \left(\frac{N_{evt}(x_i)}{\epsilon_{trig,i}} - N_{BKG,i}\right) \ \frac{1}{\mathcal{L}} \ \frac{1}{\Delta_i} \ \frac{1}{C_{F,i}} \ C_{FMD} \ C_{M_Y} \ C_{QED,i} \ . \tag{6.31}$$

The values of $N_{evt}(x_i)$, $\epsilon_{trig,i}$, $N_{BKG,i}$, Δ_i, $C_{F,i}$ and $C_{QED,i}$ are determined individually for each measurement interval. By contrast, $\mathcal{L}$, C_{FMD} and C_{M_Y} are identical for all bins.
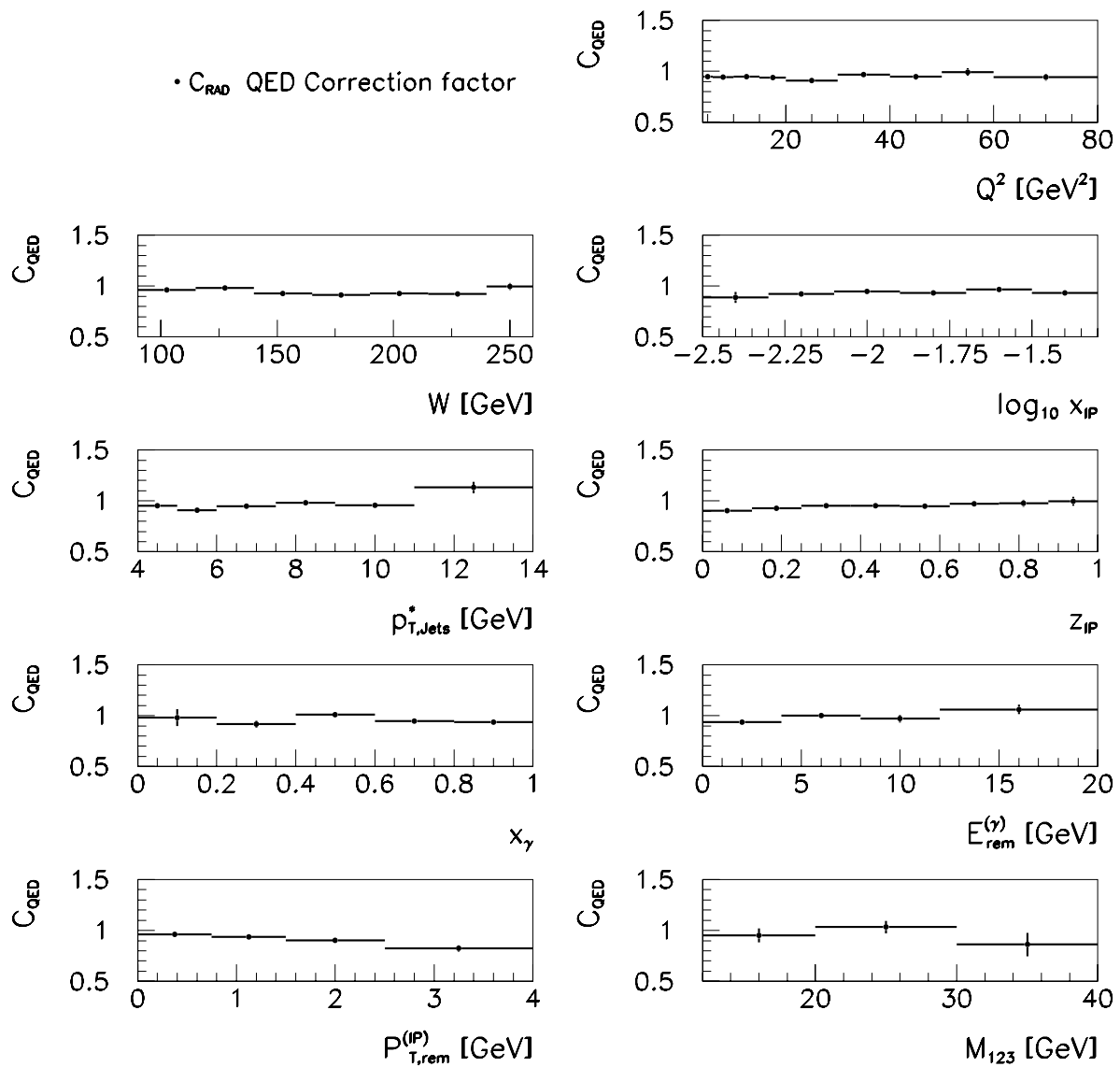
FIGURE 6.11: QED corrections applied to the measured cross sections. Shown are the values of $C_{QED} = \sigma_{had,i}^{(non-rad)}/\sigma_{had,i}^{(rad)}$ for several of the measured cross sections as obtained from simulations of colour singlet exchange events where QED radiative effects were either included or not.

6.5   Systematic Errors

The measurement of cross sections is always subject to systematic uncertainties. These uncertainties originate from an imperfect understanding of the detector, for example the knowledge of the absolute energy calibration of the calorimeters. In addition, uncertainties arise from the corrections applied to the data to correct them to the hadron level. These corrections generally depend on the physical model which was used in the Monte Carlo generator.

6.5.1   Detector Understanding

The uncertainties associated with detector understanding (see section 4.2) are as follows.

Calibration of Hadronic Energies

- The uncertainties in the hadronic calibrations of the LAr and SPACAL calorimeters are 4% and 7%, respectively. They mainly influence the measured values of $p^*_{T,jet}$ and M_X. The resulting uncertainties in the cross sections are up to 10% (with a mean value of 5%) for the LAr and 0.5% for the SPACAL.

- The uncertainty in the fraction of energy of the reconstructed hadronic objects carried by tracks is 3%. This leads to a systematic error in the range 1% to 5%.

Measurement of the Scattered Electron

The uncertainties in the measurements of the energy and polar angle of the scattered electron, E'_e and θ'_e, propagate into the reconstruction of Q^2, y and W and the definition of the γ^*p axis for the boost into the γ^*p frame.

- The uncertainty in θ'_e, which is 1 mrad, leads to a systematic error of 1% to 2%.

- The uncertainty in E'_e is estimated as 0.3% at the *kinematic peak* ($E'_e = 27.5$ GeV) and 2.0% at $E'_e = 8.0$ GeV [108]. It results in a systematic error between 1% and 5%, depending on the kinematics.

Trigger Efficiency and Luminosity

- The uncertainties in the determinations of the trigger efficiency and the ep luminosity affect the total normalisation by 5% and 2% respectively.

FMD Noise

- There is an uncertainty of 25% in the fraction of events lost due to noise in the FMD, which translates into a 1.4% normalisation error on the measured cross sections.

6.5.2   Modelling of the Data

The Monte Carlo modelling of the data gives rise to the following uncertainties.

Migrations from large $x_{I\!\!P}$, M_Y

- The uncertainty in the number of events migrating into the sample from $x_{I\!\!P} > 0.2$ or $M_Y > 5$ GeV, as obtained from the 'RG-DIS' sample of Monte Carlo events, is estimated as 25%. The result is a systematic error between 1% and 3%, with the biggest values at large $x_{I\!\!P}$.

Migrations about $M_Y = 1.6$ GeV

A 6.5% uncertainty arises from the M_Y smearing correction (section 6.4.5). It is estimated by variations of:

- The ratio of elastic proton to proton dissociation cross sections in DIFFVM, denoted R in Eq. 6.28, between 1:2 and 2:1;

- The generated M_Y distribution within $1/M_Y^{2.0 \pm 0.3}$;

- The t dependence in the proton dissociation simulation by changing the slope parameter by ± 1 GeV^{-2};

- The simulated efficiencies of the forward detectors FMD and PRT by $\pm 4\%$ and $\pm 25\%$ respectively.

QED Corrections

- The uncertainty arising from the correction of the cross sections to the Born level without QED radiative effects is typically 5%, originating from the finite statistical error on the cross section predictions.

Approximations for Higher Order QCD Effects

- The use of different approximations for higher order QCD diagrams, the parton shower (MEPS) model or the colour dipole approach (CDM), leads to a 3% uncertainty in the cross sections.

Model Dependence

The model dependence of the acceptance and migration corrections as obtained from the simulation is estimated by varying the shapes of kinematic distributions in the simulations beyond the limits imposed by previous measurements or the present data. This is done by reweighting

- The $z_{I\!\!P}$ distribution by $z_{I\!\!P}^{\pm 0.2}$ and $(1 - z_{I\!\!P})^{\pm 0.2}$;

- The p_T distribution by $(1/p_T)^{\pm 0.5}$;

- The $x_{I\!\!P}$ distribution by $(1/x_{I\!\!P})^{\pm 0.2}$;

- The t distribution by $e^{\pm 2t}$;

- The η_{jet}^{lab} distribution to that observed in the data.

The resulting systematic uncertainties range between 6% and 13%. The largest contributions originate from the assumed shapes of the $x_{I\!P}$ and η_{jet}^{lab} distributions.

Cut-Off to avoid Collinear Divergences

- The lower p_T^2 cut-off chosen to avoid collinear divergences in the leading order QCD matrix elements in the RAPGAP simulation is relatively high ($p_T^2 > 9$ GeV^2) with respect to the experimental cut $p_{T,jet}^{*2} > 16$ GeV^2 for technical reasons. Studying the dependence on the cut-off value results in an additional uncertainty of 5%.

Choice of the Jet Algorithm

In general, the measured jet cross sections depend on the jet algorithm which is used. For a sub-sample of the data, the effect of using a different jet algorithm, the so-called *inclusive k_T algorithm* [119], has been studied. The obtained cross sections, for the data as well as for the simulations, are smaller in normalisation by approximately 15%, but the shapes of the distributions are hardly affected. The conclusions drawn from the comparisons of different QCD models with the data do thus not significantly depend on the particular choice of the algorithm which has been made.

Most of the systematic uncertainties are not strongly correlated between data points. The total systematic error has been evaluated for each data point by adding all individual systematic errors in quadrature. It ranges between 15 and 30% and for most data points is significantly larger than the statistical uncertainty.

Chapter 7

Results and Interpretation

In this chapter, the measured differential cross sections at the hadron level are presented in the kinematic region specified in Tab. 6.1. The phenomenological models described in sections 1.2.5-1.2.7 are confronted with the measured data.

The cross sections are shown graphically in Figs. 7.2-7.9. In all figures, the inner error bars correspond to the statistical error, whilst the outer error bars represent the quadratic sum of the statistical and systematic errors. The numerical values of the measured cross sections can be found in appendix C in Tabs. C.1-C.6. The quoted differential cross sections are average values over the intervals specified in the tables.

7.1 General Properties of the Dijet Data

In this section, general features of the data are discussed, referring to Figs. 7.1-7.4. The model predictions which are also shown in these figures are discussed in sections 7.2 and 7.3.

7.1.1 Transverse Energy Flow and Correlation M_{12}^2-M_X^2

In Fig. 7.1a, the uncorrected average transverse energy flow per event for the dijet sample is shown as a function of the pseudorapidity $\eta^\dagger$ in the rest frame of the X system (see section 6.1). Positive values of $\eta^\dagger$ correspond to the pomeron hemisphere, negative values to the photon hemisphere. Both the total energy flow and the energy flow from particles outside the two leading jets are shown. The data exhibit considerable hadronic energy not associated with the jets. This additional energy is distributed in both hemispheres with some preference for the pomeron hemisphere.

In order to examine the sharing of energy within the X system on an event-by-event basis, Fig. 7.1b shows the uncorrected correlation between the squared dijet invariant mass M_{12}^2 and the squared total diffractive mass M_X^2 [57]. Except for a small subset of the events at low M_X, only a fraction of the available energy of the X system is contained in the dijet system, such that M_{12} is considerably smaller than M_X on average.
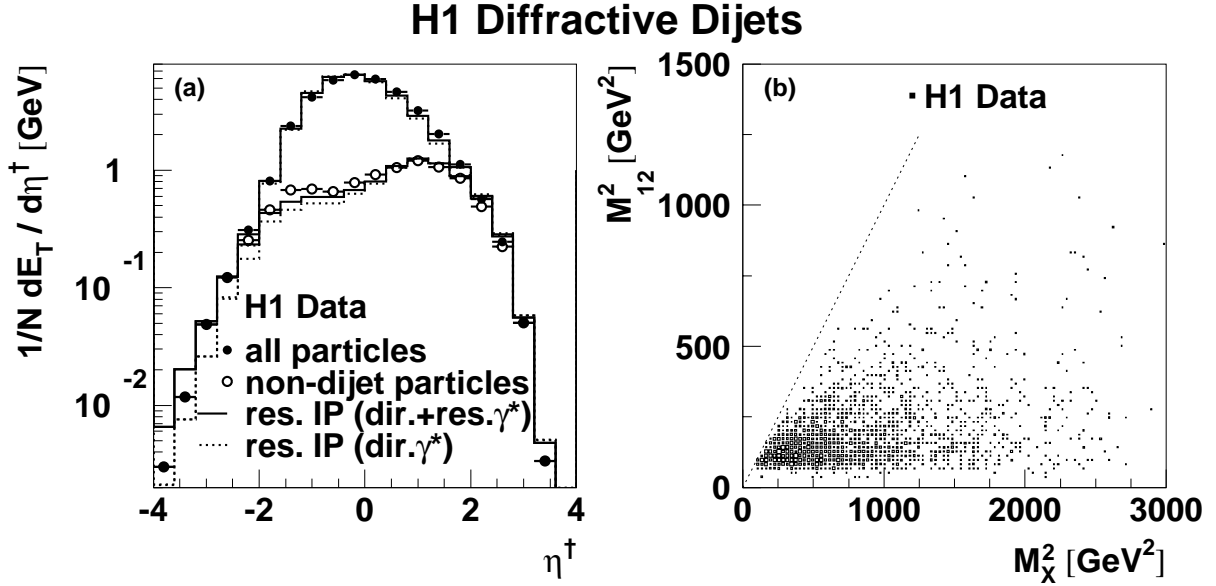
H1 Diffractive Dijets

FIGURE 7.1: *(a)* The uncorrected distribution of the average transverse energy per event for the diffractive dijet sample as a function of the pseudorapidity $\eta^\dagger$ in the centre-of-mass frame of the X system. Distributions are shown both for all final state particles *(solid points)* and for only those particles which do not belong to the two highest p_T jets *(open points)*. The prediction of the RAPGAP simulations for direct and for direct plus resolved virtual photon contributions are also shown. *(b)* The uncorrected correlation between the squared invariant mass of the X system M_X^2 and the squared dijet invariant mass M_{12}^2 for the diffractive dijet sample. The dotted line corresponds to $M_X^2 = M_{12}^2$.

7.1.2   Differential Cross Sections

Figs. 7.2 and 7.3 present differential dijet cross sections as functions of the following observables: the photon virtuality Q^2; the mean dijet transverse momentum

$$p_{T,jets}^* = \tfrac{1}{2} \left(p_{T,jet\,1}^* + p_{T,jet\,2}^* \right) \tag{7.1}$$

in the $\gamma^* p$ frame, the $\gamma^* p$ invariant mass W; the mean dijet pseudorapidity in the laboratory frame

$$\langle \eta \rangle_{jets}^{lab} = \tfrac{1}{2} \left(\eta_{jet\,1}^{lab} + \eta_{jet\,2}^{lab} \right) \tag{7.2}$$

and the logarithms of the $x_{I\!P}$ and β variables, which are calculated from

$$x_{I\!P} = \frac{Q^2 + M_X^2}{Q^2 + W^2} \; ; \qquad \beta = \frac{Q^2}{Q^2 + M_X^2} \; . \tag{7.3}$$

The Q^2, $p_{T,jets}^*$ and W Cross Sections

The Q^2 and $p_{T,jets}^*$ distributions are steeply falling (Fig. 7.2a,b). Due to the selection of events with $Q^2 > 4$ GeV^2 and $p_{T,jets}^{*\,2} > 16$ GeV^2, the relation $p_{T,jets}^{*\,2} > Q^2$ holds for
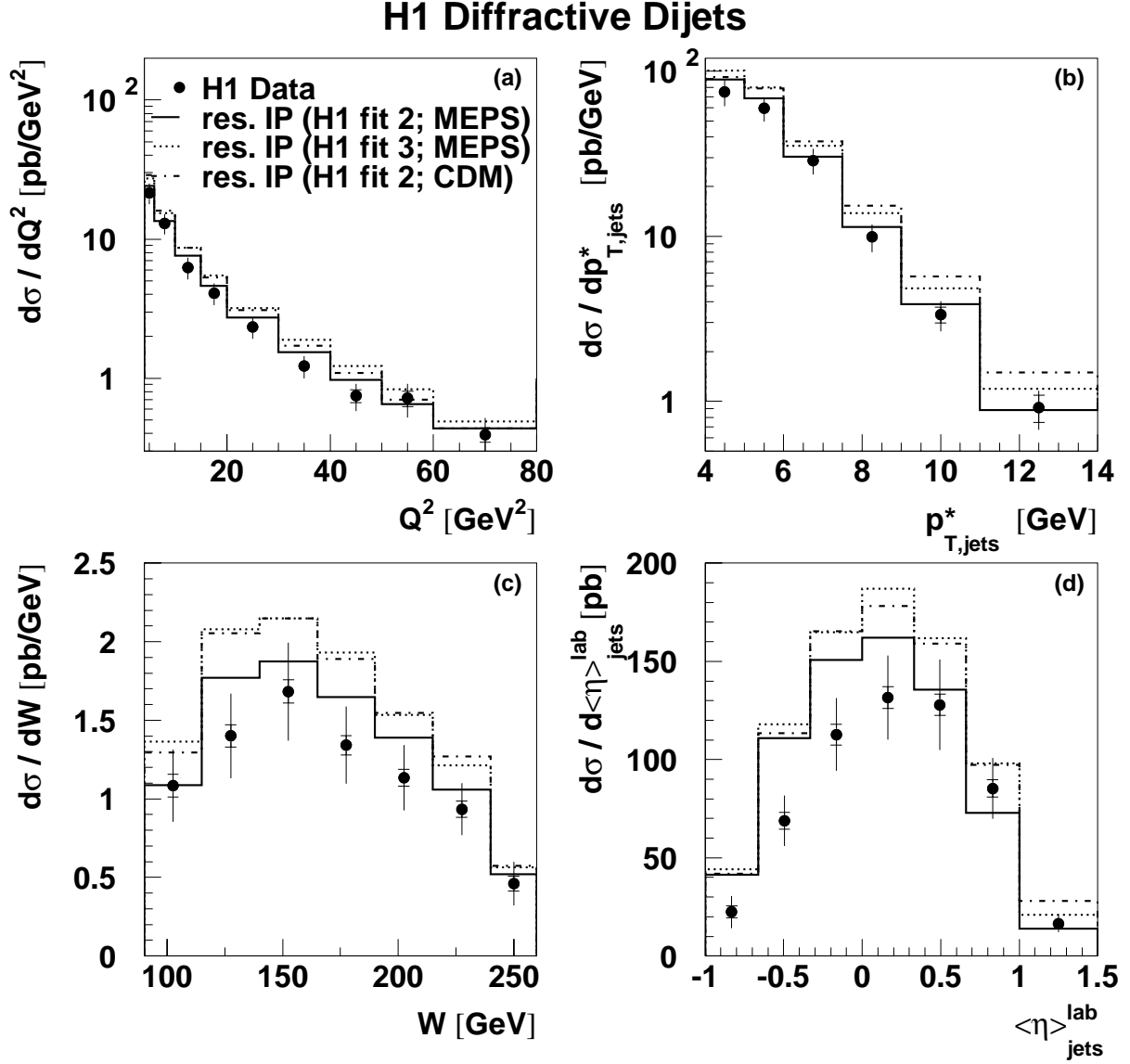
FIGURE 7.2: Diffractive dijet cross sections as a function of *(a)* the photon virtuality Q^2, *(b)* the mean transverse jet momentum $p^*_{T,jets}$ in the γ^*p centre-of-mass frame, *(c)* the γ^*p invariant mass W and *(d)* the mean jet pseudorapidity $\langle\eta\rangle^{lab}_{jets}$ in the laboratory frame. Also shown are the predictions from a resolved (partonic) pomeron model with gluon dominated pomeron parton distributions as obtained from the QCD analysis of $F_2^{D(3)}$ by H1 [3]. The results, using both the 'fit 2' ('flat gluon') and 'fit 3' ('peaked gluon') parton distributions for the pomeron, are shown evolved to a scale $\mu^2 = Q^2 + p_T^2$. Resolved virtual photon contributions are added according to the SaS-2D parameterisation [31]. The prediction based on 'fit 2' is also shown where the colour dipole approach (CDM) for higher order QCD effects is used in place of parton showers (MEPS).
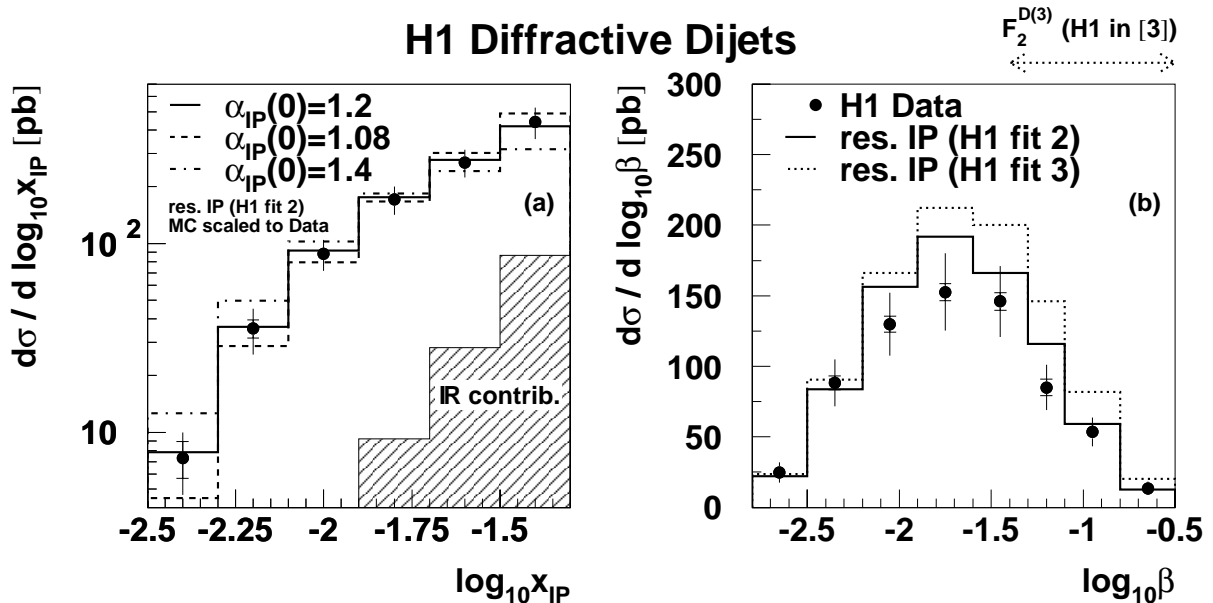
FIGURE 7.3: Differential diffractive dijet cross sections as functions of *(a)* $\log x_{I\!P}$ and *(b)* $\log \beta$. The solid curves represent the predictions of the resolved pomeron model ('fit 2') as described in the text with direct and resolved photon contributions. For the $\log x_{I\!P}$ distribution, the contribution from sub-leading reggeon exchange as obtained in [3] is indicated by the hatched area. The dashed and dashed-dotted histograms correspond to the cross section predictions where the value of the pomeron intercept $\alpha_{I\!P}(0)$ in the model was changed from the default value of 1.20 to 1.08 and 1.40 respectively. For this figure, all model predictions have been scaled to the integrated cross section in the data. For the $\log \beta$ distribution, the prediction using the 'fit 3' parton distributions is also shown and the range covered by the inclusive H1 measurement of $F_2^{D(3)}$ is indicated.

the bulk of the data. As can be seen in Fig. 7.2c, the W range of the selected events is approximately $90 < W < 260$ GeV.

The $\log x_{I\!P}$ and $\log \beta$ Cross Sections

The $x_{I\!P}$ distribution shows a rising behaviour from the lowest accessible values of ~ 0.003 up to the cut value of 0.05. For kinematic reasons, the dijet measurement is dominated by larger $x_{I\!P}$ values than is the case for inclusive diffractive measurements. The β range covered by the measurement extends down to almost 10^{-3}, lower than accessed so far in measurements of $F_2^{D(3)}$.

The shapes of the measured cross sections are generally well described by the RAPGAP simulation used to correct the data (solid histograms, see section 3.3). One exception is the $\langle \eta \rangle_{jets}^{lab}$ distribution, which shows that on average the measured jets have slightly larger pseudorapidities than is predicted by the simulations.
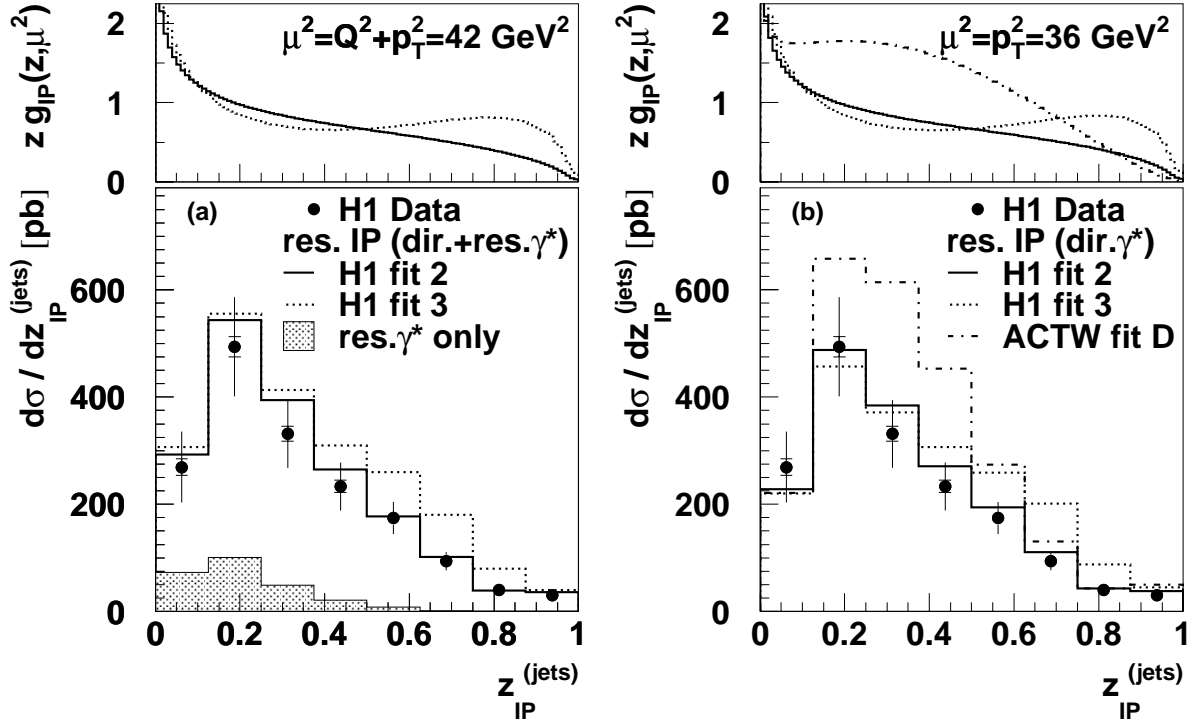
FIGURE 7.4: The diffractive dijet cross section as a function of $z_{I\!P}^{(jets)}$. The same data are compared to predictions of resolved pomeron models, where either *(a)* $\mu^2 = Q^2 + p_T^2$ or *(b)* $\mu^2 = p_T^2$ are used as renormalisation and factorisation scales. In *(a)*, the 'fit 2' (or 'flat gluon') and 'fit 3' (or 'peaked gluon') parameterisations based on the H1 leading order QCD fits to $F_2^{D(3)}$ [3] are shown. Direct and resolved γ^* contributions are both included. The size of the resolved γ^* contribution in 'fit 2' is indicated by the shaded histogram. In *(b)*, where only the direct γ^* contributions are shown, the preferred solution 'ACTW fit D' of the fits from [65] is shown in addition to the H1 fits. The corresponding gluon distributions, evolved to the mean value of the respective scale used and normalised such that the pomeron flux $f_{I\!P/p}(x_{I\!P} = 0.003, t = 0)$ is unity, are shown above the predictions.

The $z_{I\!P}^{(jets)}$ Cross Section

In Fig. 7.4, the cross section differential in $z_{I\!P}^{(jets)}$, calculated from

$$z_{I\!P}^{(jets)} = \frac{Q^2 + M_{12}^2}{Q^2 + M_X^2} \tag{7.4}$$

is shown. In loose terms, the $z_{I\!P}^{(jets)}$ observable measures the fraction of the hadronic final state energy of the X system which is contained in the two jets. The measured $z_{I\!P}^{(jets)}$ distribution is largest around 0.2 and thus confirms the observation from Fig. 7.1 that the total energy of the X system is typically much larger than that contained in the jets. Diffractively scattered $q\bar{q}$ photon fluctuations (see section 1.2.3) satisfy $z_{I\!P} \equiv 1$ at the

parton level, but can be smeared to $z_{I\!P}^{(jets)}$ values as low as 0.6 because of fragmentation and jet resolution effects. Even taking this smearing into account, the $z_{I\!P}^{(jets)}$ distribution implies the dominance of $q\bar{q}g$ over $q\bar{q}$ scattering in the proton rest frame picture.

7.2   Interpretation within a Partonic Pomeron Model

In this section, the data are compared with the Ingelman-Schlein model as introduced in section 1.2.5, using the RAPGAP Monte Carlo model with various sets of pomeron parton distributions. In all cases unless otherwise stated, the RAPGAP predictions shown use the parton shower approximation to higher order diagrams (MEPS) and a contribution from resolved virtual photons is included, as described in section 3.3. It has been shown in an H1 measurement of inclusive dijet production for similar ranges in Q^2 and $p_{T,jets}^*$ [36] that including resolved photon contributions improves the description of the data by leading order Monte Carlo Models in the region $p_{T,jets}^{*\,2} > Q^2$. It is thus reasonable to expect a similar contribution in diffraction.

7.2.1   Diffractive Gluon Distribution

Pomeron parton densities dominated by gluons have proved successful in describing not only inclusive measurements of the diffractive structure function [2, 3, 5], but also more exclusive hadronic final state analyses [10, 11, 85, 120]. By contrast, pomeron parton distributions dominated by quarks (e.g. 'fit 1' from [3]) do not describe the data [3, 11, 85]. In particular, they lead to significantly smaller predicted dijet electroproduction cross sections than were obtained in previous measurements [11] (see chapter 2 and appendix A.1). The free parameters of the Ingelman-Schlein model to which dijet production is most sensitive are the pomeron gluon distribution $g_{I\!P}(z, \mu^2)$ and the pomeron intercept $\alpha_{I\!P}(0)$. The sub-leading reggeon contribution and the pomeron quark distribution are better constrained by inclusive colour singlet exchange measurements [3, 121].

Predictions based on two sets of pomeron parton distributions obtained from the leading order DGLAP analysis of $F_2^{D(3)}$ from H1 in [3] are compared with the data in Figs. 7.2 and 7.3. The 'flat gluon' or 'fit 2' parameterisation gives a very good description of all differential distributions, except for $d\sigma/d\langle\eta\rangle_{jets}^{lab}$. Since $\langle\eta\rangle_{jets}^{lab}$ is correlated with all of $x_{I\!P}$, $z_{I\!P}^{(jets)}$, y and $x_\gamma^{(jets)}$, smaller deviations between the data and the simulation in these quantities may combine to give larger deviations in $\langle\eta\rangle_{jets}^{lab}$. The predictions based on the 'peaked gluon' or 'fit 3' parameterisation in Figs. 7.2 and 7.3 are also in fair agreement with the data, though the description is somewhat poorer than that from 'fit 2'. If the colour dipole approximation (CDM) to higher order QCD effects is used instead of parton showers (MEPS), the predicted dijet cross sections increase in normalisation by approximately 15% (Fig. 7.2). The shapes of the predicted distributions, including that of $z_{I\!P}^{(jets)}$, are not significantly affected.

The cross section differential in $z_{I\!P}^{(jets)}$ (Fig. 7.4) is also compared with predictions from different sets of pomeron parton distributions. As said before, in a resolved pomeron

model $z_{I\!\!P}^{(jets)}$ is an estimator for the longitudinal momentum fraction of the parton from the pomeron which enters the hard scattering process. Fig. 7.4a shows the predictions based on the partons extracted in 'fit 2' and 'fit 3' of [3]. The parton distributions are evaluated at a scale $\mu^2 = Q^2 + p_T^2$. Alternative reasonable choices of scale such as $Q^2 + 4p_T^2$ make only small differences to the Monte Carlo predictions (see appendix A.1). The contribution of quark induced processes in the predictions is small. The fraction of the cross section ascribed to resolved virtual photons, which is shown separately for 'fit 2' in Fig. 7.4a, is also small and is concentrated at low $z_{I\!\!P}^{(jets)}$. The same is true for the reggeon contribution (not shown). The predictions based on the 'flat gluon' or 'fit 2' parton densities are in very good agreement with the data. The 'peaked gluon' or 'fit 3' parameterisation leads to an overestimate of the dijet cross section at high values of $z_{I\!\!P}^{(jets)}$. The gluon distributions from which the predictions are derived are shown above the data at $\mu^2 = 42$ GeV^2, representing the mean value of $Q^2 + p_{T,jets}^{*\,2}$ for the selected events. The difference in shape between the gluon distributions and the hadron level predictions reflects the kinematic range of the measurement (Tab. 6.1). The dijet data are highly sensitive to the shape of the gluon distribution, which is poorly constrained by the $F_2^{D(3)}$ measurements. This is especially the case in the region of large momentum fractions ($z_{I\!\!P}$ or β), since data with $\beta > 0.65$ were excluded from the DGLAP analysis of $F_2^{D(3)}$ in [3].

In Fig. 7.4b, the same data are compared with the models where p_T^2 was chosen as the renormalisation and factorisation scale and only direct photon contributions are included. The level of agreement between the data and the simulations based on the H1 fits is similar to that in Fig. 7.4a. Also shown is a prediction based on the best combined fit in [65] to H1 and ZEUS $F_2^{D(3)}$ data and ZEUS diffractive dijet photoproduction data ('ACTW' parameterisation; section 1.2.5). In this parameterisation, the pomeron intercept is set to $\alpha_{I\!\!P}(0) = 1.19$. Due to the different shape and normalisation of the gluon distribution in this parameterisation, the agreement with the dijet data is significantly poorer than is the case for the two H1 fits.

In general, the close agreement between the 'fit 2' and 'fit 3' parameterisations and the data can be interpreted as support for factorisable pomeron parton distributions in DIS, strongly dominated by gluons with a momentum distribution relatively flat in $z_{I\!\!P}$.

In the following, some basic assumptions of the resolved pomeron model are tested, namely the evolution of the parton distributions with scale, Regge factorisation and the universality of the pomeron intercept.

7.2.2 Scale Dependence

Fig. 7.5a shows the cross section differential in $z_{I\!\!P}^{(jets)}$ in four intervals of the scale $\mu^2 = Q^2 + p_T^2$. Even in this double differential view, the 'fit 2' resolved pomeron model with parton densities evolving according to the DGLAP equations gives a very good description of the data. The 'peaked gluon' solution overestimates the cross section at high $z_{I\!\!P}^{(jets)}$ in all regions of μ^2.
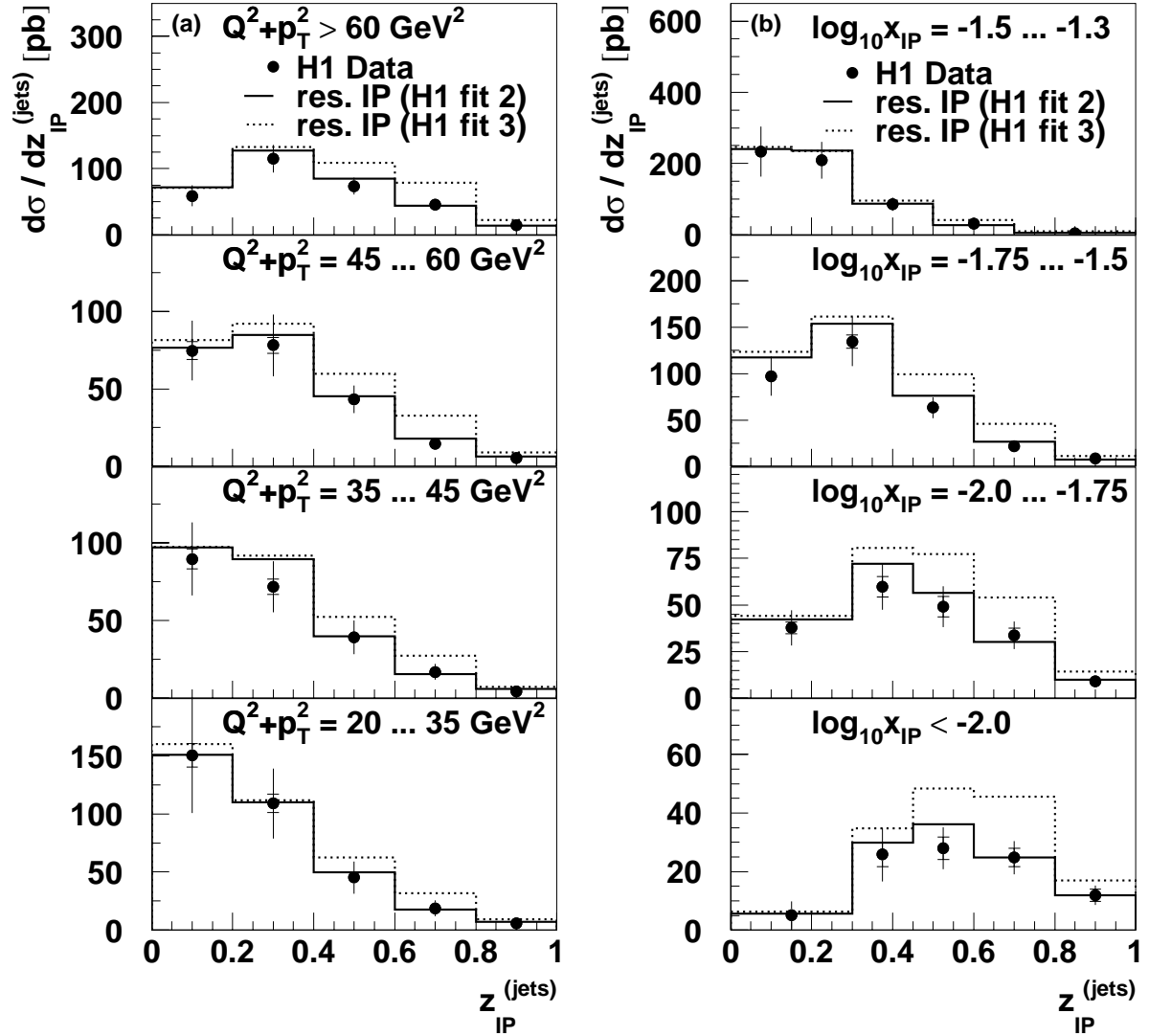
H1 Diffractive Dijets

FIGURE 7.5: Diffractive dijet cross sections as a function of $z_{I\!P}^{(jets)}$, shown in four intervals of (a) the scale $\mu^2 = Q^2 + p_T^2$ and (b) $\log x_{I\!P}$. The data are compared to the resolved pomeron model based on the two fits to $F_2^{D(3)}$ from H1, including both direct and resolved γ^* contributions.

7.2.3   Regge Factorisation

In Fig. 7.5b, the data are used to test Regge factorisation, i.e. the factorisation of the cross section into a pomeron probability distribution in the proton and a cross section for the interaction between the pomeron and the photon (Eq. 1.58). The cross section differential in $z_{I\!\!P}^{(jets)}$ is measured in four intervals of $x_{I\!\!P}$. A substantial dependence of the shape of the $z_{I\!\!P}^{(jets)}$ distribution on $x_{I\!\!P}$ is observed. This is dominantly a kinematic effect, since $x_{I\!\!P}$ and $z_{I\!\!P}^{(jets)}$ are connected via the relation

$$x_{I\!\!P} \cdot z_{I\!\!P}^{(jets)} = x_p^{(jets)} \ , \tag{7.5}$$

where $x_p^{(jets)}$ is the proton momentum fraction which enters the hard process. The range in $x_p^{(jets)}$ is approximately fixed by the kinematic range of the measurement.

Again, the factorising resolved pomeron model describes the distributions well. Thus, at the present level of precision, the data are compatible with Regge factorisation. There is little freedom to change the pomeron intercept $\alpha_{I\!\!P}(0)$ and compensate this by adjusting the gluon distribution. Fast variations of $\alpha_{I\!\!P}(0)$ with $z_{I\!\!P}$ are also incompatible with the data[1].

7.2.4   Pomeron Intercept

The value of $\alpha_{I\!\!P}(0)$ controls the energy or $x_{I\!\!P}$ dependence of the cross section. In the predictions of the resolved pomeron model shown in Figs. 7.2-7.5, a value of $\alpha_{I\!\!P}(0) = 1.2$ is used, as obtained in the H1 analysis of $F_2^{D(3)}$ [3]. Since this value of $\alpha_{I\!\!P}(0)$ is larger than that describing soft interactions, it is interesting to investigate whether further variation takes place with the additional hard scale introduced in the dijet sample. In Fig. 7.3a, the effect on the shape of the predicted cross section differential in $x_{I\!\!P}$ is investigated when $\alpha_{I\!\!P}(0)$ is varied. As examples, the predictions with $\alpha_{I\!\!P}(0) = 1.08$ ('soft pomeron') and $\alpha_{I\!\!P}(0) = 1.4$ (approximate leading order 'BFKL pomeron' [26], see sections 1.1.4,1.2.1) are shown. All predictions have been scaled to the total cross section in the data. The $x_{I\!\!P}$ dependence of the data requires a value for $\alpha_{I\!\!P}(0)$ close to 1.2. The values of 1.08 and 1.4 result in $x_{I\!\!P}$ dependences which are steeper or flatter than the data respectively.

Making a fit for $\alpha_{I\!\!P}(0)$ to the shape of the $x_{I\!\!P}$ cross section, assuming a flux of the form given in Eq. 1.62, yields a value of

$$\alpha_{I\!\!P}(0) = 1.17 \ \pm 0.03 \ (\text{stat.}) \ \pm 0.06 \ (\text{syst.}) \ ^{+0.03}_{-0.07} \ (\text{model}) \ .$$

The model dependence uncertainty is evaluated by varying:

- the resolved photon contribution by $\pm 50\%$;

- the reggeon contribution by $\pm 50\%$;

---

[1]In the analysis in [76] for example, the diffractive structure function $F_2^{D(3)}$ is parameterised as the sum of contributions from longitudinally and transversely polarised $q\bar{q}$ and $q\bar{q}g$ photon fluctuation cross sections which are dominant in different regions of β. The $x_{I\!\!P}$ dependences of the individual contributions are not assumed to be identical.

- the pomeron gluon distribution within the range allowed by the measured $z_{I\!\!P}^{(jets)}$ distribution;

- the assumed $\alpha'_{I\!\!P}$ by ± 0.26 GeV^{-2} and

- the slope parameter $b_{I\!\!P}$ within the range $b_{I\!\!P} = 2 \ldots 8$ GeV^{-2}.

The effects of NLO contributions and possible pomeron-reggeon interference have not been studied. The extracted value of $\alpha_{I\!\!P}(0)$ is compatible with that obtained from inclusive diffraction in a similar Q^2 region, despite the fact that the jets introduce an additional hard scale.

7.3 Energy Flow in the Photon Hemisphere and Resolved Virtual Photons

As can be seen from Figs. 7.2-7.5, the data are well described by the resolved pomeron model, where a contribution from resolved virtual photons is included as described in sections 1.1.6 and 3.3. In this section, two observables are studied which are particularly suited to the interpretation of the data in terms of direct and resolved photon contributions.

The $x_\gamma^{(jets)}$ Cross Section

The cross section differential in $x_\gamma^{(jets)}$, an estimator for the photon momentum fraction which enters the hard scattering process, is shown in Fig. 7.6a. $x_\gamma^{(jets)}$ is calculated from

$$x_\gamma^{(jets)} = \frac{\sum_i (E_i - p_{Z,i})_{jets}}{\sum_i (E_i - p_{Z,i})_X} \tag{7.6}$$

(see section 6.1). The distribution is peaked at values around 1 but there is also a sizeable cross section at lower $x_\gamma^{(jets)}$ values. The prediction of the resolved pomeron model with only direct photon contributions describes the high $x_\gamma^{(jets)}$ region, but lies significantly below the data at low values of $x_\gamma^{(jets)}$. The prediction is non-zero in this region only because of migrations from the true value of x_γ to the hadron level quantity $x_\gamma^{(jets)}$. If the contribution from resolved photons is included, a much improved description of the data is achieved. The total predicted dijet cross section then increases by 17%.

The $E_{rem}^{(\gamma)}$ Cross Section

The part of the hadronic final state not associated to the two highest p_T^* jets is best studied in the $\gamma^* I\!\!P$ centre-of-mass frame. Hadronic final state particle production outside the two highest p_T^* jets can originate from jet resolution effects, possible photon and pomeron remnants or from higher order QCD diagrams. In order to further investigate the energy in the photon hemisphere, the $E_{rem}^{(\gamma)}$ observable is studied, defined as the energy sum of
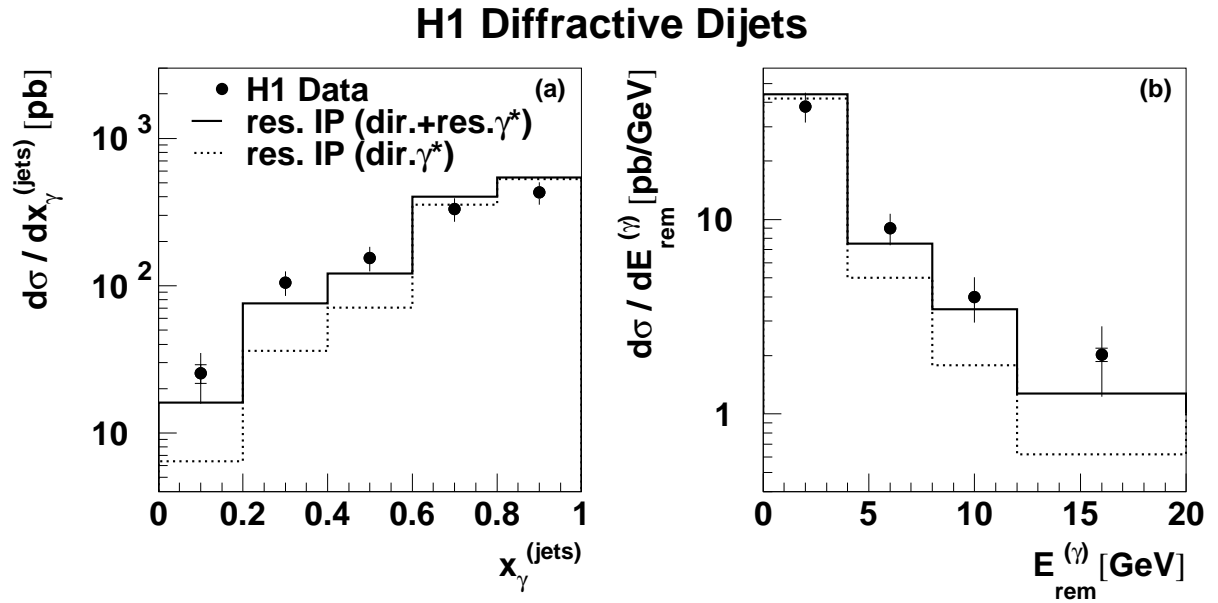
H1 Diffractive Dijets

FIGURE 7.6: Differential diffractive dijet cross sections as a function of (a) $x_\gamma^{(jets)}$, an estimator for the photon momentum fraction entering the hard scattering process, and (b) $E_{rem}^{(\gamma)}$, the summed hadronic final state energy not belonging to the two highest p_T^* jets in the photon hemisphere of the $\gamma^* I\!\!P$ centre-of-mass frame. The data are compared to the resolved pomeron model ('fit 2') with and without an additional contribution from resolved virtual photons, parameterised according to the SaS-2D photon parton distributions.

all hadronic final state particles of the X system not contained in the two highest p_T^* jets and located in the photon hemisphere of the $\gamma^* I\!\!P$ centre-of-mass frame (section 6.1):

$$E_{rem}^{(\gamma)} = \sum_i E_i^\dagger \quad (p_{z,i}^\dagger < 0; \ i \notin \text{Jets } 1, 2) \ . \tag{7.7}$$

The cross section is shown differentially in $E_{rem}^{(\gamma)}$ in Fig. 7.6b. The distribution falls quickly as $E_{rem}^{(\gamma)}$ increases, indicating the dominance of direct photon scattering. The description at high $E_{rem}^{(\gamma)}$ values (corresponding to $x_\gamma < 1$) is again much improved by adding the resolved γ^* contribution.

The presence of resolved virtual photon contributions is also suggested by the energy flow backward of the jets (corresponding to the photon direction) in the jet profiles (Fig. 6.8). Similarly, the transverse energy not associated with the jets in the $\eta^\dagger < 0$ hemisphere of the $\gamma^* I\!\!P$ system (Fig. 7.1a), is best described when the resolved photon contribution is added. Good descriptions of these distributions cannot be achieved by adjusting the diffractive gluon distribution.

The resolved virtual photon contributions can be viewed as an approximation to NLO QCD diagrams and/or contributions without strong k_T ordering. The possible presence of such effects will be investigated further in section 7.5.

7.4   Soft Colour Neutralisation Models

The Soft Colour Interactions (SCI) and semiclassical models (section 1.2.6) both give a reasonably good description of inclusive diffraction at HERA with a small number of free parameters. In Fig. 7.7, the predictions of these models are compared with the dijet cross sections as functions of $p_{T,jets}^*$, M_X, $\log x_{I\!P}$ and $z_{I\!P}^{(jets)}$. With the exception of the cross section differential in M_X, the data shown are identical to those in earlier figures.

7.4.1   Soft Colour Interactions

The original version of SCI gives a reasonable description of the shapes of the differential distributions of the dijet data, but the overall cross section is too low by a factor of about 2. The refined version of the SCI model, based on a generalised area law for string rearrangements, gives an improved description of $F_2^{D(3)}$ at low Q^2. It also reproduces the normalisation of the dijet cross sections much better than the original version. However, the shapes of the differential distributions are not described, with the exception of $p_{T,jets}^*$.

7.4.2   Semiclassical Model

The semiclassical model gives a good description of the shapes of the distributions, but the total predicted dijet cross section is only around half that measured. The free parameters of the semiclassical model were determined using only $F_2^{D(3)}$ data in the region $x_{I\!P} < 0.01$. Even at low $x_{I\!P}$, the predictions lie significantly below the dijet data (Fig. 7.7c). It is possible that the inclusion of NLO terms would improve the description of the data by the semiclassical model.

7.5   Colour Dipole and 2-Gluon Exchange Models

In this section, the saturation and BJLW models (section 1.2.7), based on the ideas of dipole cross sections and 2-gluon exchange, are compared with the dijet data. Because of the nature of the 2-gluon models, only final state parton showers are included in the simulations. A restricted data sample with the additional cut

$$x_{I\!P} < 0.01 \tag{7.8}$$

is studied, because the calculations were carried out under the assumption of low $x_{I\!P}$ to avoid contributions from secondary reggeon exchanges and ensure that the proton parton distributions are gluon dominated. Applying this additional restriction reduces the number of events in the data sample by a factor of approximately 4.
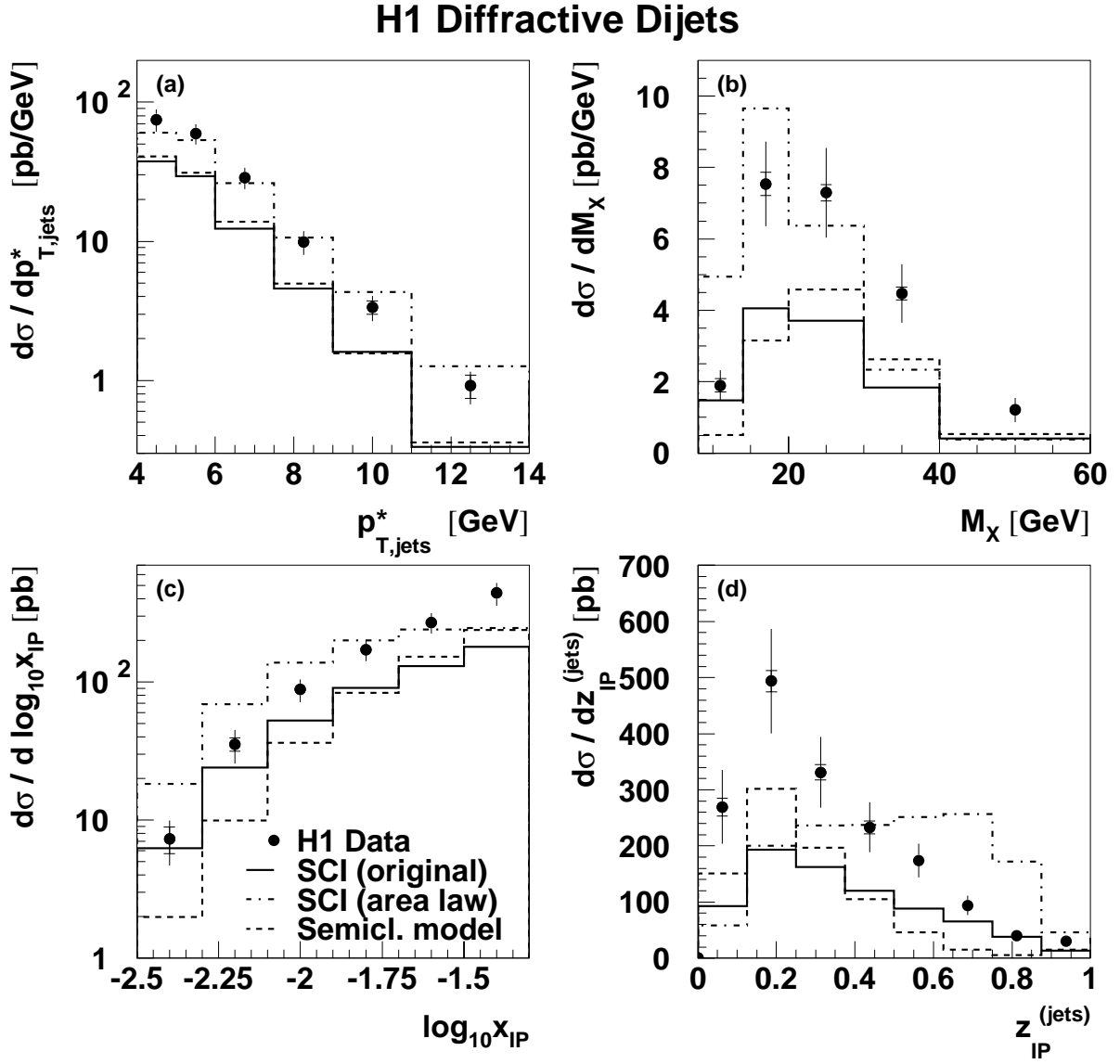
H1 Diffractive Dijets

FIGURE 7.7: Differential dijet cross sections as functions of (a) $p_{T,jets}^*$, (b) M_X, (c) $\log x_{I\!P}$ and (d) $z_{I\!P}^{(jets)}$. The data are compared to the original version of the Soft Colour Interaction (SCI) model, labelled 'SCI (original)', the prediction of the refined SCI version based on a generalised area law for string reconnections, labelled 'SCI (area law)', and to the semiclassical model.

The $p_{T,rem}^{(I\!\!P)}$ Cross Section

The resolved pomeron model implies the presence of a soft pomeron remnant. The same is true for $q\bar{q}g$ production within the saturation model where the gluon behaves in a 'remnant-like' manner, due to the k_T-ordering condition imposed in the calculations. By contrast, the $q\bar{q}g$ calculation within the BJLW model imposes high transverse momenta on all three partons and is not restricted to k_T-ordered configurations. Any 'remnant' system beyond the dijets in this model is thus expected to have relatively large p_T. To gain more insight into the properties of the part of the hadronic final state not belonging to the jets, the observable $p_{T,rem}^{(I\!\!P)}$ is studied, as defined in section 6.1:

$$p_{T,rem}^{(I\!\!P)} = \sqrt{(\textstyle\sum_i p_{x,i}^\dagger)^2 + (\sum_i p_{y,i}^\dagger)^2} \quad (p_{z,i}^\dagger > 0;\ i \notin \text{Jets } 1, 2) . \tag{7.9}$$

This variable measures the transverse momentum of all hadronic final state particles in the pomeron hemisphere of the $\gamma^* I\!\!P$ centre-of-mass frame ($\eta^\dagger > 0$) not belonging to the two highest p_T^* jets.

Dijet cross sections for the region $x_{I\!\!P} < 0.01$ differential in Q^2, $p_{T,jets}^*$, $z_{I\!\!P}^{(jets)}$ and $p_{T,rem}^{(I\!\!P)}$ are shown in Fig. 7.8. They are compared with the predictions of the saturation, BJLW and resolved pomeron ('fit 2') models.

7.5.1 Saturation Model

The saturation model is able to reproduce the shapes of the measured cross sections, though the overall predicted dijet rate is too low by a factor of approximately 2. The normalisation of the saturation model is fixed from the fit to inclusive F_2 data and by the assumed e^{6t} dependence for diffractive processes. The total predicted dijet cross section would increase whilst preserving a good description of $F_2^{D(3)}$ if the t dependence were found to be harder for dijet production than for inclusive diffraction (see appendix A.2).

7.5.2 BJLW Model

In the BJLW model, the contribution from $q\bar{q}$ states alone is negligibly small even at large values of $z_{I\!\!P}$. This is in accordance with the expectation for high p_T, high M_X diffractive final states. The predicted $q\bar{q}g$ contribution is much larger. The normalisation of the BJLW model for $q\bar{q}g$ production can be controlled by tuning the lower cut-off on the transverse momentum of the final state gluon $p_{T,g}^{cut}$ in the calculations. If this cut-off is set to 1.5 GeV, the total cross section for dijet production with $x_{I\!\!P} < 0.01$ is approximately correct in the model. Lowering $p_{T,g}^{cut}$ to 1.0 GeV leads to a prediction significantly above the measured cross section. The description of the shapes of the distributions is reasonable apart from small discrepancies in the $z_{I\!\!P}^{(jets)}$ distribution.

The differences between the predictions of the saturation and BJLW models may originate from the different parameterisations of the unintegrated gluon distribution of the proton $\mathcal{F}(x, k_T^2)$ (see appendix A.3), the different treatments of non-k_T-ordered configurations or from the assumed t dependence.
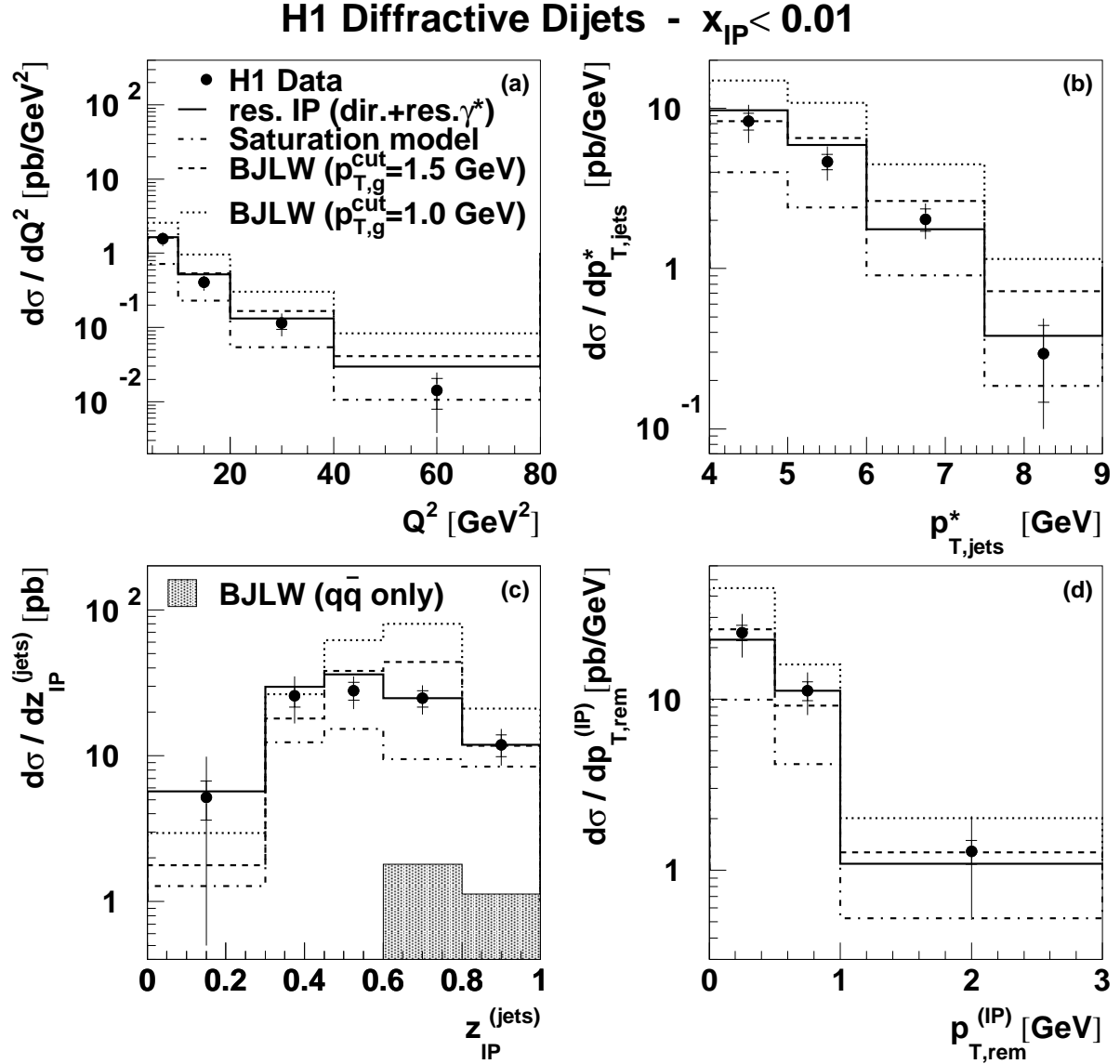
FIGURE 7.8: Diffractive dijet cross sections in the restricted kinematic range $x_{I\!P} < 0.01$, shown as functions of (a) Q^2, (b) $p^*_{T,jets}$, (c) $z^{(jets)}_{I\!P}$ and (d) $p^{(I\!P)}_{T,rem}$, the latter denoting the summed transverse momentum of the final state particles not belonging to the two highest p^*_T jets and located in the pomeron hemisphere of the $\gamma^* I\!P$ centre-of-mass frame. The data are compared to the saturation, BJLW and resolved pomeron ('fit 2', direct and resolved virtual photons) models. For the BLJW model, the contribution from $q\bar{q}$ states alone and the sum of the $q\bar{q}$ and $q\bar{q}g$ contributions for two different values of the p_T cut-off for the gluon $p^{cut}_{T,g}$ are shown.

The resolved pomeron model, in which the non-k_T-ordered resolved photon contributions are small in the low $x_{I\!P}$ region, continues to give the best description of all observables, including the $p_{T,rem}^{(I\!P)}$ distribution. The good description of the $p_{T,rem}^{(I\!P)}$ distribution by both the resolved pomeron and the BJLW models indicates that the present data are not easily able to discriminate between models with a soft 'remnant' and those with a third high-p_T parton.

7.6   3-Jet Production

In this section, cross sections for the diffractive production of three high-p_T jets as components of the X system are presented. Except for the requirement on the number of jets, the analysis is identical to the dijet analysis, such that no requirements are made on possible hadronic activity beyond the jets.

In Fig. 7.9, the measured 3-jet cross sections are presented as functions of the 3-jet invariant mass M_{123} and the $z_{I\!P}^{(3\ jets)}$ observable, as introduced in section 6.1:

$$z_{I\!P}^{(3\ jets)} = \frac{Q^2 + M_{123}^2}{Q^2 + M_X^2} \ . \tag{7.10}$$

Similarly to $z_{I\!P}^{(jets)}$ for dijet events, the $z_{I\!P}^{(3\ jets)}$ observable is a measure of the fraction of the energy of the X system which is contained in the jets. The $z_{I\!P}^{(3\ jets)}$ cross section is measured up to 0.8. With the present statistics, it is not possible to extract a cross section for the interesting region $0.8 < z_{I\!P}^{(3\ jets)} \leq 1.0$, which corresponds approximately to 'exclusive' 3-jet production. The measured $z_{I\!P}^{(3\ jets)}$ cross section demonstrates that additional hadronic activity beyond the jets is typically present even in the 3-jet sample.

7.6.1   Comparison with the Partonic Pomeron Model

The 3-jet data are compared with the resolved pomeron model ('fit 2'), with the hard interaction evaluated at a scale $\mu^2 = Q^2 + p_T^2$. Direct and resolved γ^* contributions are included. Because the leading order for 3-parton final states is $\mathcal{O}(\alpha_s^2)$, two different approximations for higher order QCD diagrams are considered here, the parton shower model (MEPS) and the colour dipole approach (CDM).

The measured cross sections are well described when using CDM. The MEPS simulation tends to lie below the data at low M_{123} or high $z_{I\!P}^{(3\ jets)}$.

7.6.2   Comparison with the BJLW Model

The BJLW calculation with $p_{T,g}^{cut} = 1.5$ GeV is not able to accommodate the observed rate of 3-jet events. The predicted cross section increases towards the high $z_{I\!P}^{(3\ jets)}$ regime of exclusive 3-jet production.

For kinematic reasons, the 3-jet sample originates from the region $x_{I\!P} > 0.01$, where contributions from the proton quark distributions and secondary exchanges, which are
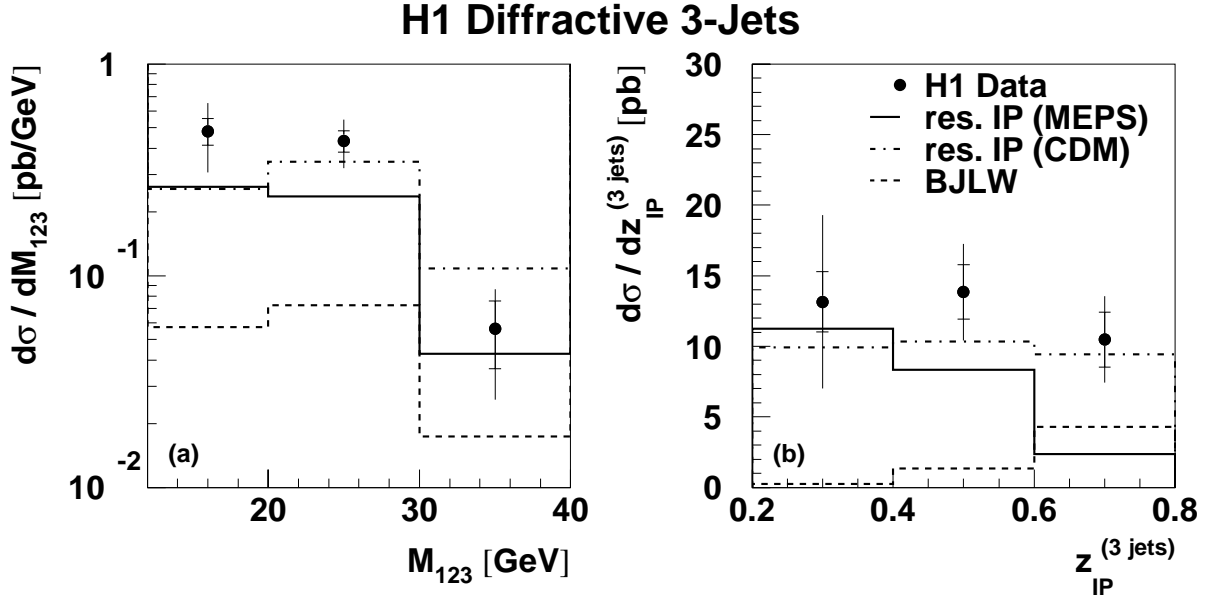
FIGURE 7.9: Differential cross sections for diffractive 3-jet production as functions of *(a)* the 3-jet invariant mass M_{123} and *(b)* the corresponding $z_{I\!P}$-variable $z_{I\!P}^{(3\ jets)}$, measuring the colourless exchange momentum fraction which enters the hard interaction. The data are compared with the resolved pomeron model with two different approaches for higher order QCD diagrams, the parton shower model (labelled 'MEPS') and the colour dipole approach (labelled 'CDM'). The 'H1 fit 2' parameterisation is used and direct and resolved virtual photon contributions are included. The BJLW model is also shown, including $q\bar{q}$ and $q\bar{q}g$ contributions, with the cut-off for the gluon $p_{T,g}^{cut}$ set to 1.5 GeV.

not included in the 2-gluon models, can no longer be neglected. An improvement in the predictions of dipole models may also come through the inclusion of higher multiplicity photon fluctuations such as $q\bar{q}gg$, which have not yet been calculated.

Summary and Conclusions

At the electron-proton collider HERA, colour singlet exchange interactions can be studied in deep-inelastic scattering, where the virtual photon introduces a hard scale Q^2 which probes the structure of the diffractive exchange. This thesis has been concerned with a measurement of diffractive jet production in deep-inelastic scattering. **The aim** of the measurement has been to illuminate the underlying dynamics of diffractive scattering in terms of Quantum Chromodynamics.

The analysis was performed using data corresponding to an integrated luminosity of $\mathcal{L} = 18.0 \text{ pb}^{-1}$ which were taken with the H1 detector at HERA. The kinematic range of the measurement was $4 < Q^2 < 80 \text{ GeV}^2$, $x_{I\!P} < 0.05$, $p_{T,jet}^* > 4 \text{ GeV}$, $M_Y < 1.6 \text{ GeV}$ and $|t| < 1.0 \text{ GeV}^2$. Compared with a previous measurement [11], the integrated luminosity was increased by one order of magnitude and the kinematic range was extended to lower Q^2 and $p_{T,jet}^*$ values. With these data, a high statistics measurement of diffractive dijet production in DIS was performed and the production of three high p_T jets was measured for the first time in diffraction.

The observed dijet events typically exhibit a structure where, in addition to the reconstructed jets, the photon dissociation system X contains hadronic energy with transverse momentum below the jet scale. The dijet invariant mass is thus generally smaller than the total mass M_X. Viewed in the proton rest frame, the data clearly require the dominance of higher multiplicity photon fluctuations (e.g. $q\overline{q}g$) over the simplest $q\overline{q}$ configuration. Considered in the proton infinite momentum frame, the data show that the diffractive gluon distribution is much larger than the quark distribution.

The data can be described by a **resolved partonic pomeron model**, with diffractive parton distributions extracted from $F_2^{D(3)}$ data [3]. The good description from this model strongly supports the validity of diffractive hard scattering factorisation in DIS [61]. The dominant contribution in the model arises from a diffractive exchange with factorising $x_{I\!P}$ dependence ('Regge' factorisation [63]). A value of

$$\alpha_{I\!P}(0) = 1.17 \ \pm 0.03 \text{ (stat.)} \ \pm 0.06 \text{ (syst.)} \ {}^{+0.03}_{-0.07} \text{ (model)}$$

is obtained for the intercept of the leading trajectory from fits to the dijet data. The compatibility of the data with QCD hard scattering and Regge factorisation contrasts with the observed strong factorisation breaking when diffractive ep and $p\overline{p}$ data are compared [8, 65] (see appendix B). The dijet data give the best constraints to date

on the pomeron gluon distribution. The data require a large fraction $(80 - 90\%$, as obtained in [3]) of the pomeron momentum to be carried by gluons with a momentum distribution which is comparatively flat in $z_{I\!P}$. Predictions derived from the 'flat gluon' (or 'fit 2') parameterisation in [3], with higher order QCD effects modelled using parton showers, are in remarkably good agreement with all aspects of the dijet data with the single exception of the $\langle\eta\rangle^{lab}_{jets}$ dependence. The level of agreement between the resolved pomeron model and the data is better than that obtained from leading order predictions for inclusive ep dijet data (e.g. [122]), where the NLO corrections are approximately 40% in a similar region of Q^2 and $p^*_{T,jets}$. A possible explanation for this observation is a reduced phase space (given by M_X compared with W) for higher order parton emissions in the case of diffraction.

The two versions of the **Soft Colour Interactions (SCI)** model [68, 69] are not able to reproduce the overall dijet rate and the shapes of the differential cross sections at the same time. The similarly motivated **semiclassical model** [54] in its present (leading order) form achieves a good description of the shapes of the cross sections but underestimates the total dijet cross section.

Models based on **colour dipole cross sections and 2-gluon exchange** have been compared with the dijet data in the restricted region $x_{I\!P} < 0.01$. The saturation model [80], which takes only k_T ordered configurations into account, describes the shapes of the jet distributions but underestimates the overall cross section. The normalisation of the BJLW model [81, 82], in which strong k_T ordering is not imposed, is close to the data if a cut-off for the gluon transverse momentum of $p^{cut}_{T,g} = 1.5$ GeV is chosen. The shapes of the differential distributions are reasonably well described.

From the **3-jet production** cross sections, strong conclusions cannot yet be drawn, because of the limited statistical accuracy and the kinematic restriction to large $x_{I\!P}$ implied by the requirement of three high p_T jets. At the present level of precision, the partonic pomeron predictions based on the 'fit 2' parameterisation in [3] are in good agreement with the 3-jet cross sections, provided the CDM model of higher order QCD effects is used. The BJLW model is unable to reproduce the rate of observed 3-jet events when $p^{cut}_{T,g}$ is kept fixed at 1.5 GeV.

Conclusions

Diffractive jet production has been shown to be a powerful tool to gain insight into the underlying QCD dynamics of diffraction, in particular the role of gluons. The jet cross sections are sensitive to differences between phenomenological models which all give a reasonable description of $F_2^{D(3)}$. Models based on fully factorisable diffractive parton distributions continue to be successful. Considerable progress has been made in calculations based on 2-gluon exchange.

Outlook

In the measurement which has been presented, the systematic uncertainties are the dominating sources of error on the measured cross section points. However, investigating diffractive jet production in DIS with higher statistical precision remains worthwhile for the following reasons:

- More data in restricted kinematic regions can be accumulated, especially at low $x_{I\!P}$ values, higher transverse momenta of the jets or near $z_{I\!P} \simeq 1$, the domain of *exclusive* dijet production. In these regions, perturbative calculations based on 2-gluon exchange claim to be applicable.

- A larger data sample would also allow to study diffractive 3-jet production in more detail, which currently suffers from limited precision.

A complementary experimental method to select diffractive final states in which an additional hard scale other than Q^2 is present is provided by diffractive open charm production. Clearly, much more precision is needed here to resolve the discrepancies which are observed when the results are compared with this analysis or inclusive $F_2^{D(3)}$ measurements.

New high precision measurements of the diffractive structure function $F_2^{D(3)}$ or preferentially $F_2^{D(4)}(x_{I\!P}, t, \beta, Q^2)$ are needed for a full extraction of diffractive parton distributions $f_i^D(x_{I\!P}, t, x, Q^2)$ and to investigate pomeron-reggeon interference and higher twist effects, for example.

Concerning the phenomenological models, the inclusion of higher order (NLO QCD) contributions is awaited. In the proton rest frame picture, contributions from higher multiplicity photon fluctuations such as $q\bar{q}gg$ are suggested by the present experimental data. The relationship between models based on dipole cross sections and those formulated in terms of diffractive parton distributions needs further clarification.

Appendix A

Additional Model Comparisons

In this appendix, additional comparisons of the resolved pomeron, saturation and BJLW models with the measured dijet cross sections are presented. It is demonstrated how the variation of certain parameters in these models affects the predicted cross sections.

A.1 Partonic Pomeron Model

In Fig. A.1, the measured diffractive dijet cross sections are again compared with the resolved pomeron model, based on the H1 fits to $F_2^{D(3)}$, as explained in section 1.2.5. In addition to the previously shown 'fit 2' and 'fit 3' parameterisations, in which a large fraction of the pomeron momentum $(80 - 90\%)$ is carried by gluons, the third parameterisation called 'fit 1' is compared with the data. This parameterisation assumes that only quarks contribute at the starting scale of the QCD evolution. It is not able to describe the observed scaling violations of $F_2^{D(3)}$. It also significantly underestimates the measured dijet cross sections. This observation was already made in the first H1 measurement of diffractive dijet production in DIS [11].

In Fig. A.2, the effect of varying the renormalisation and factorisation scales μ^2 is shown for the 'fit 2' and 'fit 3' parameterisations. A dependence on the choice of scale is introduced because the cross section calculations are performed at fixed (leading) order QCD. The differences in the predicted cross sections for the resolved pomeron model when choosing $\mu^2 = Q^2 + p_T^2$ or $\mu^2 = p_T^2$ as renormalisation and factorisation scales were shown to be small in Fig. 7.4. Fig. A.2 shows the variations in the cross sections if $\mu^2 = Q^2 + 4p_T^2$ is chosen instead of $\mu^2 = Q^2 + p_T^2$. Again, the effects on the predicted cross sections are small.

Because of the selection of events, all of these possible choices for the scale are such that the average values of μ^2 to which the parton distributions are evolved are rather large. For large values of μ^2, the dependence of the shapes of the parton distributions on the factorisation scale is weaker than for smaller μ^2. Cross section calculations performed at next-to-leading order QCD would further reduce the scale dependences.

A.2   Saturation Model

In Fig. A.3, the diffractive dijet cross sections for the restricted kinematic region $x_{I\!P} < 0.01$ are compared with the saturation model by Golec-Biernat and Wüsthoff (section 1.2.7). In this model, the diffractive cross section at $t = 0$ is extended to finite t via

$$\frac{\mathrm{d}\sigma}{\mathrm{d}t} = \left.\frac{\mathrm{d}\sigma}{\mathrm{d}t}\right|_{t=0} \cdot e^{Bt} \ . \tag{A.1}$$

The 'default' value for the slope parameter B in the model is set to $B = 6.0\ \mathrm{GeV}^{-2}$, which gives a reasonable description of the inclusive diffractive structure function $F_2^{D(3)}$. Fig. A.3 shows the effect of changing B to 4 or 8 GeV^{-2}. The normalisation of the predicted cross section increases by 50% for $B = 4.0\ \mathrm{GeV}^{-2}$, whereas it decreases by 25% for $B = 8.0\ \mathrm{GeV}^{-2}$. If $B = 4.0\ \mathrm{GeV}^{-2}$ is chosen, an improved description of the dijet cross section can be obtained. However, a good description of $F_2^{D(3)}$ can only be retained if the value of B would depend on a scale of the process other than Q^2, since the Q^2 ranges for the $F_2^{D(3)}$ and the dijet measurements are compatible.

A.3   BJLW Model

Fig. A.4 presents a comparison of the diffractive dijet cross sections for $x_{I\!P} < 0.01$ with the 2-gluon exchange model by Bartels et al. (BJLW, section 1.2.7). In this model, the cross section is proportional to the squared unintegrated gluon density $\mathcal{F}(x, k_T^2)$ in the proton. As default, the derivative of the GRV NLO [83] parameterisation of the gluon distribution is used for $\mathcal{F}(x, k_T^2)$. The figure shows how the predicted dijet cross section depends on this choice. As explained in section 1.2.7, the dipole cross section in the saturation model by Golec-Biernat and Wüsthoff, where the free parameters are fixed from a fit to the inclusive $F_2(x, Q^2)$, can be re-expressed in terms of $\mathcal{F}(x, k_T^2)$. If this parameterisation is used for the calculation of the diffractive dijet cross section in the BJLW model, the predicted cross section increases by approximately 50%, indicating large differences between the two parameterisations of $\mathcal{F}(x, k_T^2)$.
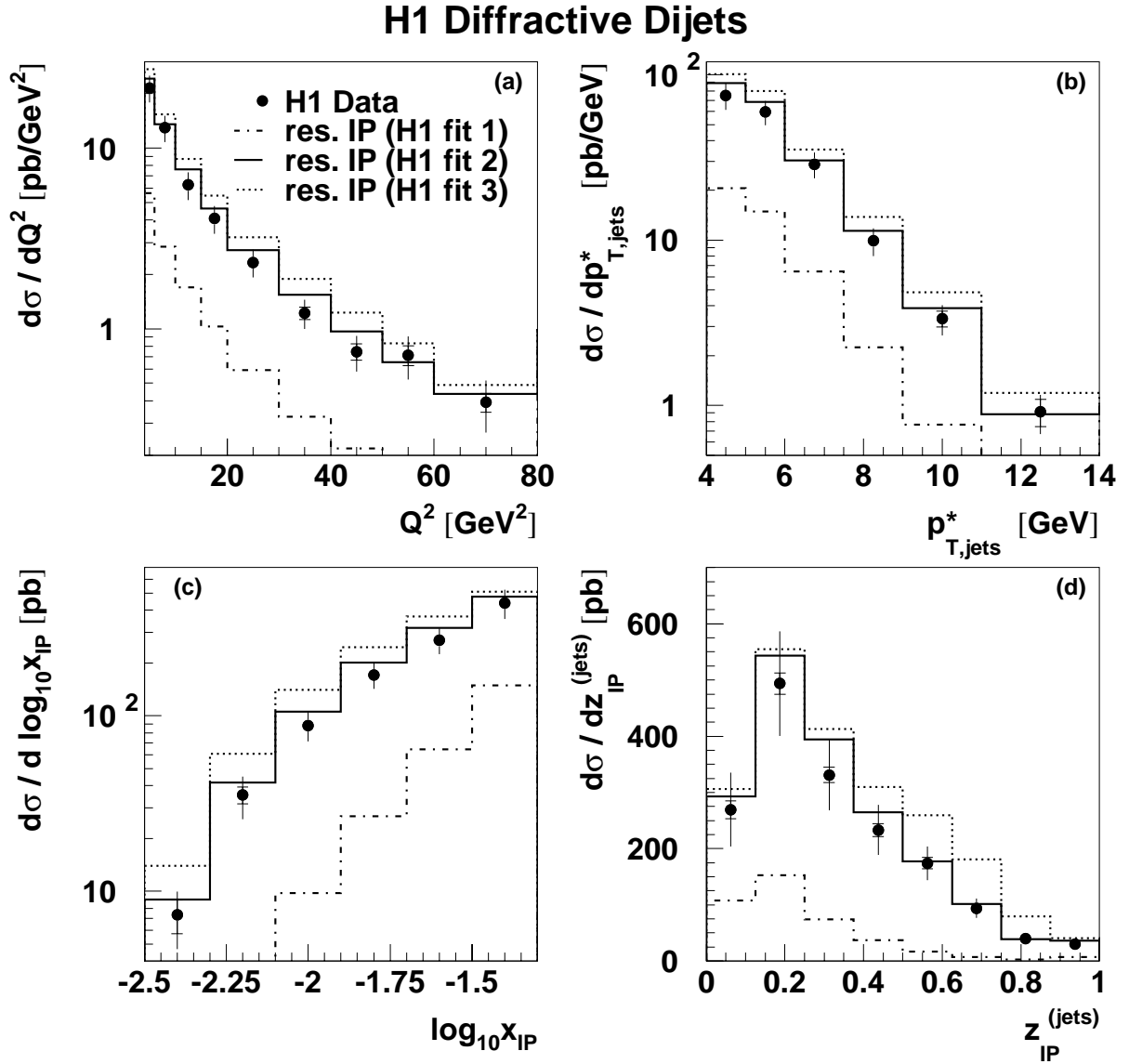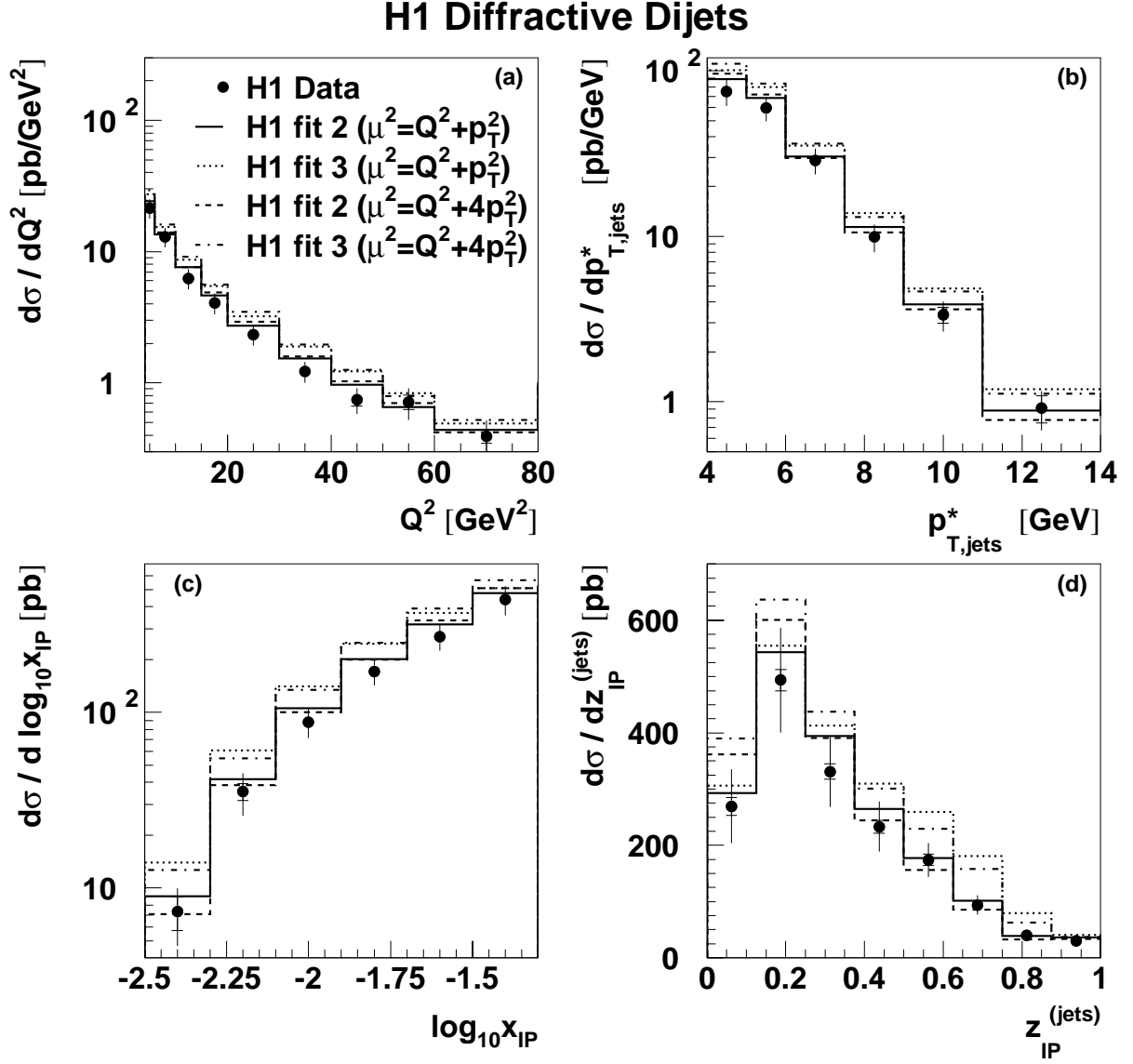
H1 Diffractive Dijets

FIGURE A.1: Diffractive dijet cross sections, compared with the predictions of the resolved pomeron model with pomeron parton densities obtained from the H1 QCD fits to $F_2^{D(3)}$ [3]. In addition to the two parameterisations where the majority of the colourless exchange momentum is carried by gluons, namely 'fit 2' *(solid histograms)* and 'fit 3' *(dotted histograms)*, the prediction for 'fit 1' *(dash-dotted histograms)* is shown, where only quarks contribute at the starting scale of the QCD evolution.

FIGURE A.2: Diffractive dijet cross sections, compared with the predictions of the resolved pomeron model with the 'flat gluon' (fit 2) and 'peaked gluon' (fit 3) pomeron parton densities, as obtained from the H1 QCD fits to $F_2^{D(3)}$ [3]. The parton distributions are evolved to either $\mu^2 = Q^2 + p_T^2$ (solid and dotted histograms) or $\mu^2 = Q^2 + 4p_T^2$ (dashed and dash-dotted histograms).
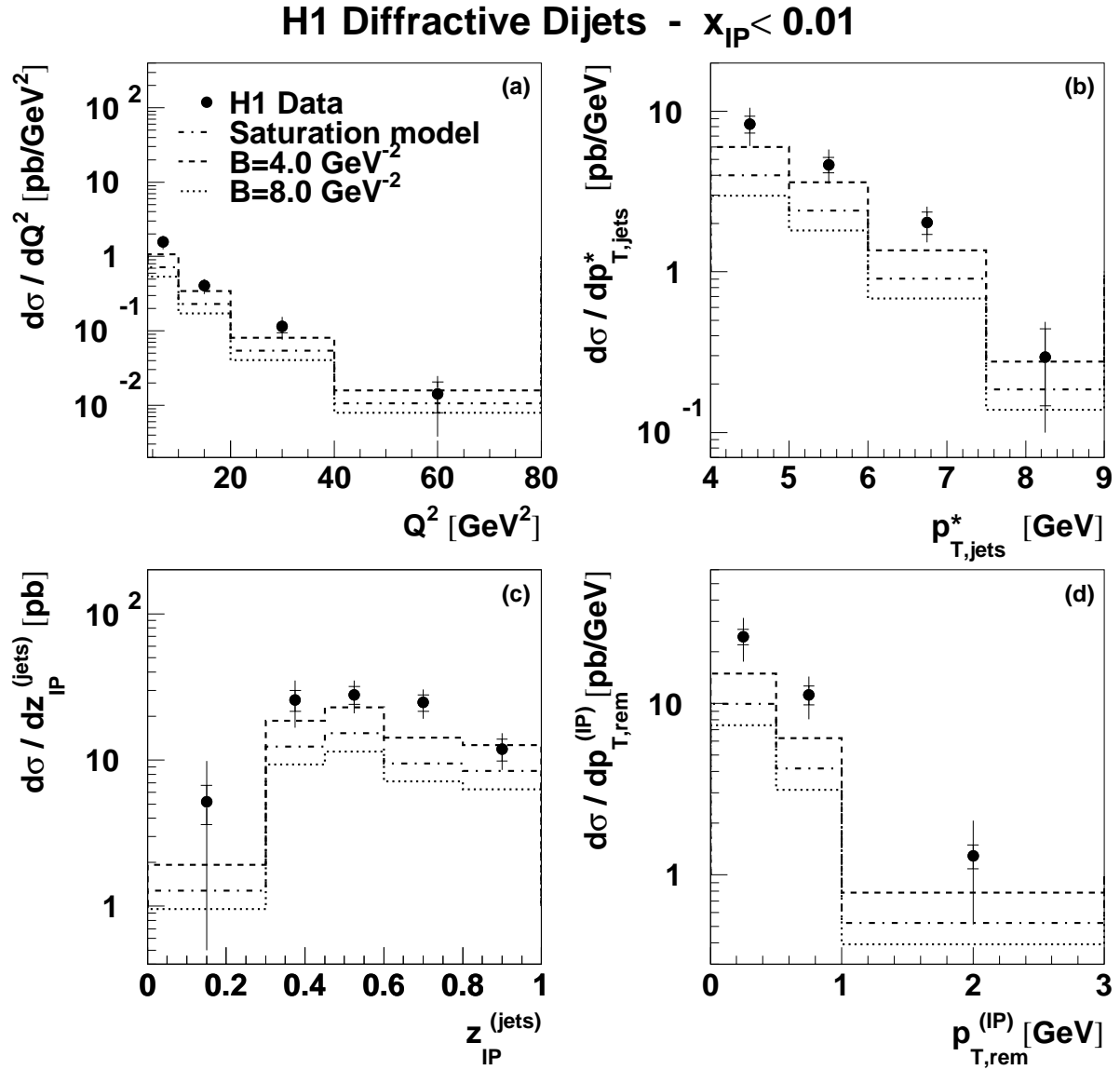
FIGURE A.3: Diffractive dijet cross sections for $x_{I\!P} < 0.01$. Overlaid are predictions of the saturation model by Golec-Biernat and Wüsthoff where the value of the t-slope parameter B is varied. Apart from the default value of $B = 6.0$ GeV^{-2} *(dash-dotted histograms)*, predictions for $B = 4.0$ GeV^{-2} *(dashed histograms)* and $B = 8.0$ GeV^{-2} *(dotted histograms)* are compared with the data.
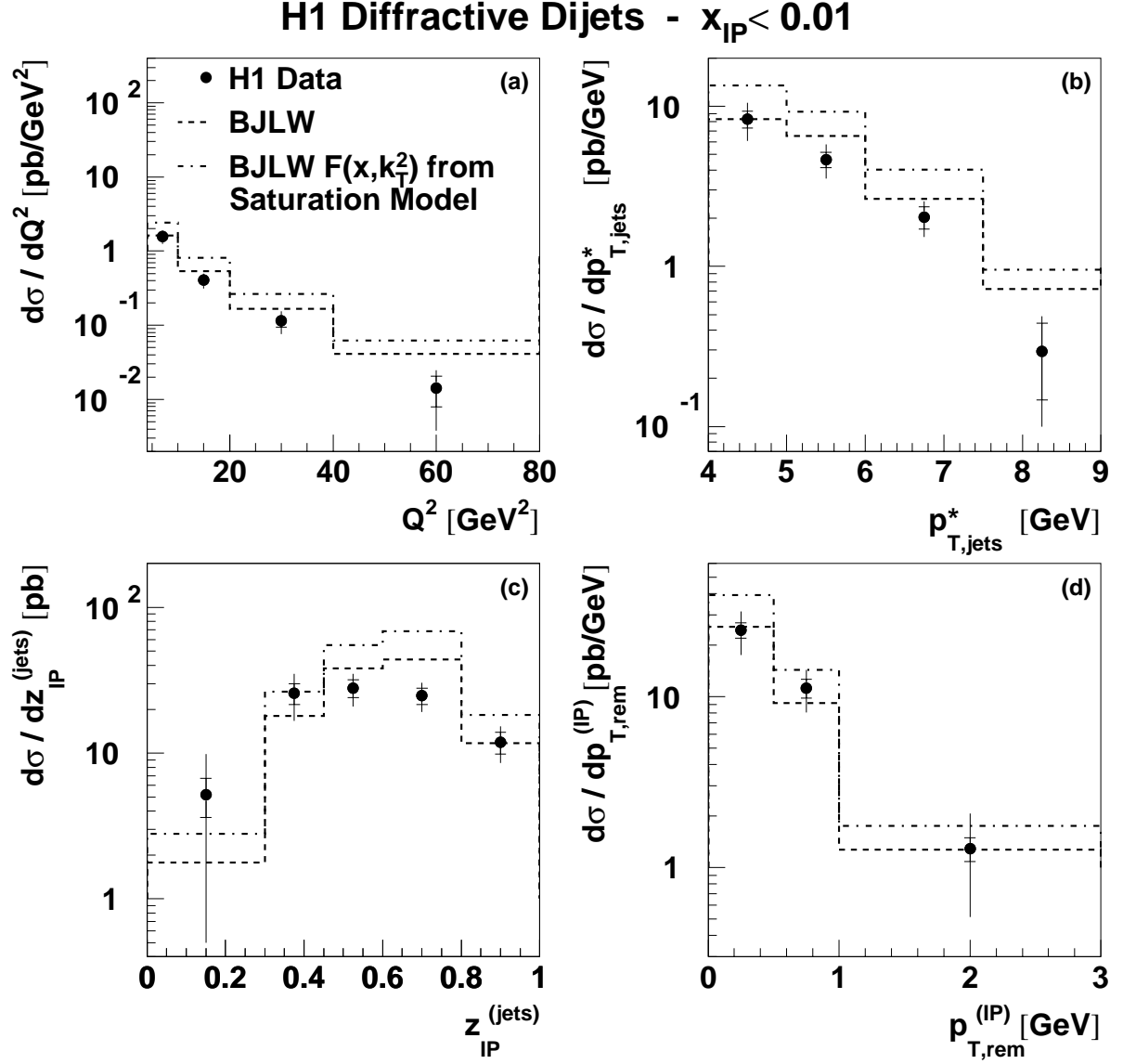
FIGURE A.4: Diffractive dijet cross sections for $x_{I\!P} < 0.01$. Overlaid are predictions of the BJLW 2-gluon exchange model, where either the derivative of the GRV NLO parameterisation of the proton gluon distribution is used for $\mathcal{F}(x, k_T^2)$ *(dashed histograms)* or the unintegrated gluon distribution as parameterised in the saturation model *(dash-dotted histograms)* is chosen.

Appendix B

Comparison with Tevatron Data

At the Fermilab Tevatron $\overline{p}p$ collider (Chicago, USA), a measurement of diffractive dijet production with a leading anti-proton was performed by the CDF collaboration [8]. The process under study is

$$\overline{p} + p \longrightarrow \overline{p} + \text{Jet } 1 + \text{Jet } 2 + X \ .$$

Diffractive events were selected by measuring the elastically scattered anti-proton in a forward *Roman pot* spectrometer 57m downstream from the interaction point. The basic selection cuts were $0.035 < x_{I\!\!P} < 0.095$, $|t| < 1.0$ GeV^2 and $E_{T,jet} > 7$ GeV. The longitudinal momentum fraction of the anti-proton carried by the struck parton, labelled x here, and the β variable are computed from

$$x = \frac{1}{\sqrt{s}} \sum_{i=1,2} E_{T,i} \ e^{-\eta_i} \ ; \qquad \beta = \frac{x}{x_{I\!\!P}} \ , \tag{B.1}$$

where $\sqrt{s} = 1.8$ TeV. The measured ratio $\tilde{R}(x)$ of diffractive to non-diffractive dijet events is shown as a function of x in Fig. B.1a. The ratio is evaluated in bins of $x_{I\!\!P} \equiv \xi$ and fitted to a function of the form

$$\tilde{R}(x) = R_0 \cdot (x/0.0065)^{-r} \ . \tag{B.2}$$

For the kinematic range under study, no significant dependence on $x_{I\!\!P} = \xi$ is observed and the extracted values for R_0 and r are $R_0 = (6.1 \pm 0.1) \cdot 10^{-3}$ and $r = 0.45 \pm 0.02$. From $\tilde{R}(x)$, an *effective diffractive structure function* $\tilde{F}_{jj}^D$ is extracted via

$$\tilde{F}_{jj}^D(\beta) = \tilde{R}(x = \beta x_{I\!\!P}) \cdot \tilde{F}_{jj}^{ND}(x \to \beta x_{I\!\!P}) \ , \tag{B.3}$$

where $\tilde{F}_{jj}^{ND}(x)$ corresponds to the non-diffractive effective structure function of the anti-proton. The $\tilde{F}_{jj}$ are defined as

$$\tilde{F}_{jj} = x[g(x,\mu^2) + \tfrac{4}{9}q(x,\mu^2)] \ . \tag{B.4}$$

The scale μ^2 is set to $\mu^2 = \langle E_{T,jet} \rangle^2 \simeq 75$ GeV^2. The non-diffractive anti-proton structure function is evaluated from the GRV98(LO) [123] parameterisation.
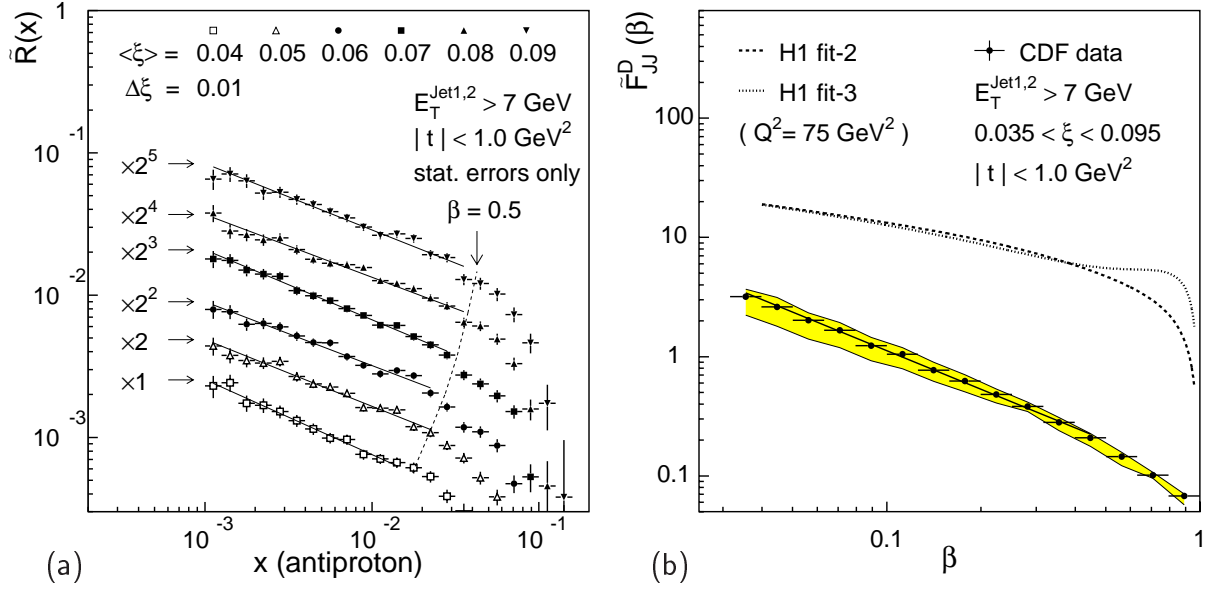
149

FIGURE B.1: Diffractive dijet production at the Tevatron [8]: *(a)* The ratio of diffractive to non-diffractive dijet events $\tilde{R}$ as a function of the anti-proton momentum fraction carried by the struck parton x, evaluated in bins of $\xi \equiv x_{I\!P}$. *(b)* The measured effective diffractive structure function $\tilde{F}_{jj}^{D}$ as a function of β. The data are compared with a prediction based on the two H1 fits to $F_{2}^{D(3)}$ data at HERA.

The obtained result for $\tilde{F}_{jj}^{D}(\beta)$ is shown in Fig. B.1b. The measurement is compared with the resolved pomeron model where the pomeron and meson flux factors and parton distributions are taken from the H1 fits to the diffractive structure function $F_{2}^{D(3)}$ in lepton-proton scattering [3]. The result is striking: Both the 'flat gluon' ('fit 2') and the 'peaked gluon' ('fit 3') parameterisations obtained in diffractive lepton-proton scattering clearly fail to describe the diffractive structure function which is obtained in $\overline{p}p$ collisions. It is recalled that the proof of diffractive hard scattering factorisation in [61] is only valid for lepton-hadron scattering, not for hadron-hadron interactions.

The result can be interpreted as strong evidence for a breakdown of Regge and diffractive hard scattering factorisation, when diffractive hadron-hadron and lepton-hadron scattering cross sections are compared.

Appendix C

Cross Section Tables

In this appendix, the numerical values of the measured cross sections, including the statistical and systematic errors, are summarised in a tabular form.

Bin	\multicolumn{3}{c}{Q^2 [GeV^2]}	σ [pb/GeV^2]	stat. err. [%]	syst. err. [%]	tot. err. [%]
\multicolumn{8}{l}{Dijet cross section as a function of Q^2.}
1	4.0	–	6.0	21.4	4.5	16.4	17.0
2	6.0	–	10.0	13.0	4.0	16.1	16.6
3	10.0	–	15.0	6.3	4.8	17.0	17.7
4	15.0	–	20.0	4.1	6.2	16.7	17.8
5	20.0	–	30.0	2.3	5.8	16.4	17.4
6	30.0	–	40.0	1.2	8.0	16.3	18.2
7	40.0	–	50.0	0.7	10.4	19.7	22.3
8	50.0	–	60.0	0.7	12.5	23.9	27.0
9	60.0	–	80.0	0.4	11.9	29.6	31.9

Dijet cross section as a function of Q^2.

Bin	Q^2 [GeV^2]			σ [pb/GeV^2]	stat. err. [%]	syst. err. [%]	tot. err. [%]
1	4.0	–	6.0	21.4	4.5	16.4	17.0
2	6.0	–	10.0	13.0	4.0	16.1	16.6
3	10.0	–	15.0	6.3	4.8	17.0	17.7
4	15.0	–	20.0	4.1	6.2	16.7	17.8
5	20.0	–	30.0	2.3	5.8	16.4	17.4
6	30.0	–	40.0	1.2	8.0	16.3	18.2
7	40.0	–	50.0	0.7	10.4	19.7	22.3
8	50.0	–	60.0	0.7	12.5	23.9	27.0
9	60.0	–	80.0	0.4	11.9	29.6	31.9

Dijet cross section as a function of $p^*_{T,jets}$.

Bin	$p^*_{T,jets}$ [GeV]			σ [pb/GeV]	stat. err. [%]	syst. err. [%]	tot. err. [%]
1	4.0	–	5.0	74.9	4.0	17.8	18.3
2	5.0	–	6.0	59.5	3.3	16.4	16.8
3	6.0	–	7.5	28.8	3.9	17.3	17.8
4	7.5	–	9.0	9.9	7.0	17.9	19.2
5	9.0	–	11.0	3.4	11.0	17.7	20.8
6	11.0	–	14.0	0.9	18.9	18.6	26.5

Dijet cross section as a function of $\langle\eta\rangle^{lab}_{jets}$.

Bin	$\langle\eta\rangle^{lab}_{jets}$			σ [pb]	stat. err. [%]	syst. err. [%]	tot. err. [%]
1	−1.00	–	−0.66	22.4	13.5	34.3	36.9
2	−0.66	–	−0.33	68.9	6.3	17.7	18.8
3	−0.33	–	0.00	112.8	4.7	15.7	16.4
4	0.00	–	0.33	131.6	4.2	15.7	16.3
5	0.33	–	0.66	127.9	4.3	17.5	18.0
6	0.66	–	1.00	85.3	5.1	17.4	18.2
7	1.00	–	1.50	16.4	6.8	25.6	26.5

Dijet cross section as a function of M_X.

Bin	M_X [GeV]			σ [pb/GeV]	stat. err. [%]	syst. err. [%]	tot. err. [%]
1	8.0	–	14.0	1.9	10.1	20.0	22.4
2	14.0	–	20.0	7.5	4.4	15.1	15.7
3	20.0	–	30.0	7.3	3.2	16.9	17.2
4	30.0	–	40.0	4.5	4.0	17.8	18.3
5	40.0	–	60.0	1.2	6.2	27.1	27.8

TABLE C.1: Differential hadron level dijet cross sections.

	Dijet cross section as a function of W.						
Bin	\multicolumn{3}{	c	}{W [GeV]}	σ [pb/GeV]	stat. err. [%]	syst. err. [%]	tot. err. [%]
1	90.0	–	115.0	1.1	6.6	20.3	21.3
2	115.0	–	140.0	1.4	5.1	18.5	19.2
3	140.0	–	165.0	1.7	4.4	18.0	18.5
4	165.0	–	190.0	1.3	4.5	17.7	18.3
5	190.0	–	215.0	1.1	4.7	17.7	18.3
6	215.0	–	240.0	0.9	5.4	17.0	17.8
7	240.0	–	260.0	0.5	10.3	28.5	30.3

	Dijet cross section as a function of $\log_{10} x_{I\!P}$.						
Bin	\multicolumn{3}{	c	}{$\log_{10} x_{I\!P}$}	σ [pb]	stat. err. [%]	syst. err. [%]	tot. err. [%]
1	−2.5	–	−2.3	7.3	21.8	28.8	36.1
2	−2.3	–	−2.1	35.4	10.8	25.1	27.4
3	−2.1	–	−1.9	88.2	6.8	17.5	18.8
4	−1.9	–	−1.7	171.2	4.7	16.3	17.0
5	−1.7	–	−1.5	269.3	3.6	16.3	16.7
6	−1.5	–	−1.3	440.7	3.2	18.6	18.8

	Dijet cross section as a function of $\log_{10} \beta$.						
Bin	\multicolumn{3}{	c	}{$\log_{10} \beta$}	σ [pb]	stat. err. [%]	syst. err. [%]	tot. err. [%]
1	−2.8	–	−2.5	24.9	11.3	26.4	28.7
2	−2.5	–	−2.2	88.3	5.6	18.1	19.0
3	−2.2	–	−1.9	129.9	4.3	16.7	17.2
4	−1.9	–	−1.6	152.7	3.9	17.4	17.9
5	−1.6	–	−1.3	145.9	4.3	16.8	17.3
6	−1.3	–	−1.1	85.0	7.0	17.5	18.8
7	−1.1	–	−0.8	53.4	7.8	17.4	19.0
8	−0.8	–	−0.5	13.5	17.7	29.8	34.6

	Dijet cross section as a function of $z_{I\!P}^{(jets)}$.						
Bin	\multicolumn{3}{	c	}{$z_{I\!P}^{(jets)}$}	σ [pb]	stat. err. [%]	syst. err. [%]	tot. err. [%]
1	0.000	–	0.125	269.4	5.8	23.7	24.4
2	0.125	–	0.250	493.9	3.8	18.4	18.8
3	0.250	–	0.375	331.3	4.2	18.6	19.1
4	0.375	–	0.500	233.2	4.9	18.5	19.2
5	0.500	–	0.625	174.2	5.9	16.1	17.2
6	0.625	–	0.750	94.0	8.1	16.3	18.2
7	0.750	–	0.875	39.8	11.7	16.3	20.0
8	0.875	–	1.000	30.0	16.7	24.5	29.7

	Dijet cross section as a function of $x_{\gamma}^{(jets)}$.						
Bin	\multicolumn{3}{	c	}{$x_{\gamma}^{(jets)}$}	σ [pb]	stat. err. [%]	syst. err. [%]	tot. err. [%]
1	0.0	–	0.2	25.4	14.3	35.1	37.9
2	0.2	–	0.4	104.8	6.5	17.7	18.9
3	0.4	–	0.6	153.8	5.0	18.1	18.8
4	0.6	–	0.8	331.5	3.6	18.0	18.3
5	0.8	–	1.0	428.3	3.1	16.7	17.0

	Dijet cross section as a function of $E_{rem}^{(\gamma)}$.						
Bin	\multicolumn{3}{	c	}{$E_{rem}^{(\gamma)}$ [GeV]}	σ [pb/GeV]	stat. err. [%]	syst. err. [%]	tot. err. [%]
1	0.0	–	4.0	38.1	2.5	17.2	17.3
2	4.0	–	8.0	9.0	4.7	17.6	18.2
3	8.0	–	12.0	4.0	6.7	25.4	26.3
4	12.0	–	20.0	2.0	8.0	38.6	39.4

Table C.2: Differential hadron level dijet cross sections (continued).

Dijet cross section as a function of $z_{I\!\!P}^{(jets)}$ for $-1.5 < \log_{10} x_{I\!\!P} < -1.3$.						
Bin	$z_{I\!\!P}^{(jets)}$		σ [pb]	stat. err. [%]	syst. err. [%]	tot. err. [%]
1	0.00 –	0.15	232.9	6.0	29.7	30.3
2	0.15 –	0.30	209.4	5.3	24.2	24.8
3	0.30 –	0.50	85.4	6.4	20.8	21.8
4	0.50 –	0.70	30.9	10.4	18.8	21.5
5	0.70 –	1.00	3.4	28.9	47.0	55.1

Dijet cross section as a function of $z_{I\!\!P}^{(jets)}$ for $-1.75 < \log_{10} x_{I\!\!P} < -1.5$.						
Bin	$z_{I\!\!P}^{(jets)}$		σ [pb]	stat. err. [%]	syst. err. [%]	tot. err. [%]
1	0.0 –	0.2	97.1	6.4	20.8	21.8
2	0.2 –	0.4	134.3	5.3	19.0	19.7
3	0.4 –	0.6	63.4	7.1	16.3	17.7
4	0.6 –	0.8	21.8	12.6	16.6	20.8
5	0.8 –	1.0	8.5	25.8	34.4	43.0

Dijet cross section as a function of $z_{I\!\!P}^{(jets)}$ for $-2.0 < \log_{10} x_{I\!\!P} < -1.75$.						
Bin	$z_{I\!\!P}^{(jets)}$		σ [pb]	stat. err. [%]	syst. err. [%]	tot. err. [%]
1	0.00 –	0.30	37.8	8.3	23.4	24.9
2	0.30 –	0.45	59.7	9.2	18.2	20.4
3	0.45 –	0.60	49.1	11.2	19.4	22.4
4	0.60 –	0.80	33.8	10.9	19.1	22.0
5	0.80 –	1.00	9.0	21.8	24.8	33.0

Dijet cross section as a function of $z_{I\!\!P}^{(jets)}$ for $\log_{10} x_{I\!\!P} < -2.0$.						
Bin	$z_{I\!\!P}^{(jets)}$		σ [pb]	stat. err. [%]	syst. err. [%]	tot. err. [%]
1	0.00 –	0.30	5.2	30.2	85.2	90.4
2	0.30 –	0.45	25.8	16.2	31.5	35.4
3	0.45 –	0.60	28.0	13.9	21.3	25.5
4	0.60 –	0.80	24.8	12.8	18.9	22.9
5	0.80 –	1.00	11.9	17.4	22.0	28.0

TABLE C.3: Differential hadron level dijet cross sections in four bins of $\log_{10} x_{I\!\!P}$.

Dijet cross section as a function of $z_{I\!\!P}^{(jets)}$ for 20 GeV$^2 < Q^2 + p_T^2 < 35$ GeV^2.						
Bin	$z_{I\!\!P}^{(jets)}$		σ [pb]	stat. err. [%]	syst. err. [%]	tot. err. [%]
1	0.0 –	0.2	150.5	6.7	32.4	33.1
2	0.2 –	0.4	109.0	7.3	26.6	27.6
3	0.4 –	0.6	45.2	10.8	28.8	30.8
4	0.6 –	0.8	18.7	16.2	31.6	35.5
5	0.8 –	1.0	5.9	31.6	54.4	63.0

Dijet cross section as a function of $z_{I\!\!P}^{(jets)}$ for 35 GeV$^2 < Q^2 + p_T^2 < 45$ GeV^2.						
Bin	$z_{I\!\!P}^{(jets)}$		σ [pb]	stat. err. [%]	syst. err. [%]	tot. err. [%]
1	0.0 –	0.2	89.7	7.1	25.2	26.2
2	0.2 –	0.4	71.8	6.9	21.8	22.9
3	0.4 –	0.6	39.3	9.0	26.1	27.6
4	0.6 –	0.8	16.9	14.4	26.3	30.0
5	0.8 –	1.0	4.3	27.7	26.2	38.1

Dijet cross section as a function of $z_{I\!\!P}^{(jets)}$ for 45 GeV$^2 < Q^2 + p_T^2 < 60$ GeV^2.						
Bin	$z_{I\!\!P}^{(jets)}$		σ [pb]	stat. err. [%]	syst. err. [%]	tot. err. [%]
1	0.0 –	0.2	74.6	7.7	24.6	25.8
2	0.2 –	0.4	78.0	6.7	24.5	25.4
3	0.4 –	0.6	43.2	8.6	18.6	20.5
4	0.6 –	0.8	14.7	14.7	20.1	25.0
5	0.8 –	1.0	5.5	23.6	28.7	37.2

Dijet cross section as a function of $z_{I\!\!P}^{(jets)}$ for $Q^2 + p_T^2 > 60$ GeV^2.						
Bin	$z_{I\!\!P}^{(jets)}$		σ [pb]	stat. err. [%]	syst. err. [%]	tot. err. [%]
1	0.0 –	0.2	58.7	9.2	25.2	26.9
2	0.2 –	0.4	114.6	5.8	17.4	18.4
3	0.4 –	0.6	73.4	6.8	15.6	17.0
4	0.6 –	0.8	45.3	9.4	15.3	18.0
5	0.8 –	1.0	14.4	18.3	22.3	28.8

TABLE C.4: Differential hadron level dijet cross sections in four bins of $Q^2 + p_T^2$.

Dijet cross section as a function of Q^2 for $x_{I\!P} < 0.01$.					
Bin	Q^2 [GeV^2]	σ [pb/GeV^2]	stat. err. [%]	syst. err. [%]	tot. err. [%]
1	4.0 — 10.0	1.58	9.7	18.5	20.9
2	10.0 — 20.0	0.40	13.9	18.4	23.1
3	20.0 — 40.0	0.12	17.7	29.2	34.1
4	40.0 — 80.0	0.01	44.7	58.3	73.5
Dijet cross section as a function of $p^*_{T,jets}$ for $x_{I\!P} < 0.01$.					
Bin	$p^*_{T,jets}$ [GeV]	σ [pb/GeV]	stat. err. [%]	syst. err. [%]	tot. err. [%]
1	4.0 — 5.0	8.3	12.0	23.9	26.8
2	5.0 — 6.0	4.7	11.0	21.3	24.0
3	6.0 — 7.5	2.0	16.0	19.1	24.9
4	7.5 — 9.0	0.3	50.0	43.2	66.1
Dijet cross section as a function of $z_{I\!P}^{(jets)}$ for $x_{I\!P} < 0.01$.					
Bin	$z_{I\!P}^{(jets)}$	σ [pb]	stat. err. [%]	syst. err. [%]	tot. err. [%]
1	0.00 — 0.30	5.2	30.2	85.2	90.4
2	0.30 — 0.45	25.8	16.2	31.5	35.4
3	0.45 — 0.60	28.0	13.9	21.3	25.5
4	0.60 — 0.80	24.8	12.8	18.9	22.9
5	0.80 — 1.00	11.9	17.4	22.0	28.0
Dijet cross section as a function of $p_{T,rem}^{(I\!P)}$ for $x_{I\!P} < 0.01$.					
Bin	$p_{T,rem}^{(I\!P)}$ [GeV]	σ [pb/GeV]	stat. err. [%]	syst. err. [%]	tot. err. [%]
1	0.0 — 0.5	24.5	10.3	26.8	28.8
2	0.5 — 1.0	11.2	12.7	24.8	27.9
3	1.0 — 3.0	1.3	16.0	58.1	60.3

TABLE C.5: Differential hadron level dijet cross sections for $x_{I\!P} < 0.01$.

3-jet cross section as a function of M_{123}.					
Bin	M_{123} [GeV]	σ [pb/GeV]	stat. err. [%]	syst. err. [%]	tot. err. [%]
1	12.0 — 20.0	0.48	14.4	33.0	36.1
2	20.0 — 30.0	0.43	11.6	23.0	25.7
3	30.0 — 40.0	0.06	35.3	40.5	53.7
3-jet cross section as a function of $z_{I\!P}^{(3\ jets)}$.					
Bin	$z_{I\!P}^{(3\ jets)}$	σ [pb]	stat. err. [%]	syst. err. [%]	tot. err. [%]
1	0.2 — 0.4	13.1	16.2	43.8	46.7
2	0.4 — 0.6	13.9	13.9	20.5	24.7
3	0.6 — 0.8	10.5	18.6	22.6	29.2

TABLE C.6: Differential hadron level 3-Jet cross sections.

References

[1] ZEUS Collaboration, M. Derrick *et al.*, *Phys. Lett.* **B 315** (1993) 481.
H1 Collaboration, T. Ahmed *et al.*, *Nucl. Phys.* **B 429** (1994) 477.

[2] H1 Collaboration, T. Ahmed *et al.*, *Phys. Lett.* **B 348** (1995) 681.

[3] H1 Collaboration, C. Adloff *et al.*, *Z. Phys.* **C 76** (1997) 613.

[4] ZEUS Collaboration, J. Breitweg *et al.*, *Eur. Phys. J.* **C 1** (1998) 81.

[5] ZEUS Collaboration, J. Breitweg *et al.*, *Eur. Phys. J.* **C 6** (1999) 43.

[6] UA8 Collaboration, R. Bonino *et al.*, *Phys. Lett.* **B 211** (1988) 239;
UA8 Collaboration, A. Brandt *et al.*, *Phys. Lett.* **B 297** (1992) 417.

[7] CDF Collaboration, F. Abe *et al.*, *Phys. Rev. Lett.* **80** (1998) 1156;
CDF Collaboration, F. Abe *et al.*, *Phys. Rev. Lett.* **79** (1998) 2636.

[8] CDF Collaboration, T. Affolder *et al.*, *Phys. Rev. Lett.* **84** (2000) 5043.

[9] D0 Collaboration, B. Abbott *et al.*: *Hard Single Diffraction in $p\bar{p}$ Collisions at 630 and 1800 GeV*, hep-ex/9912061, subm. to *Phys. Rev. Lett.*

[10] ZEUS Collaboration, J. Breitweg *et al.*, *Eur. Phys. J.* **C 5** (1998) 41.

[11] H1 Collaboration, C. Adloff *et al.*, *Eur. Phys. J.* **C 6** (1999) 421.

[12] H1 Collaboration, *Diffractive Dijet Electroproduction at HERA*, paper **157ae** subm. to the Intl. Europhysics Conference on High Energy Physics (EPS-HEP 99), Tampere, Finland (1999).

[13] F.-P. Schilling, *Diffractive Dijet and 3-Jet Electroproduction at HERA* in J. Gracey and T. Greenshaw (eds.), Proc. of the 8th Intl. Workshop on Deep-Inelastic Scattering (DIS2000), Liverpool, Great Britain (2000), hep-ex/0012065, to be published.

[14] H1 Collaboration, *Diffractive Jet-Production in Deep-Inelastic e^+p Collisions at HERA*, paper **960** subm. to the 30th Intl. Conference on High Energy Physics (ICHEP 2000), Osaka, Japan (2000).

[15] H1 Collaboration, C. Adloff *et al.*, *Diffractive Jet Production in Deep-Inelastic e^+p Collisions at HERA*, **DESY 00-174**, hep-ex/0012051, to appear in *Eur. Phys. J. C*.

155

[16] R. Ellis, W. Stirling, B. Webber, *QCD and Collider Physics*, Cambridge University Press (1996).

[17] D. Groom *et al.* (Particle Data Group), *Eur. Phys. J.* **C 15** (2000) 1.

[18] M. Breidenbach *et al.*, *Phys. Rev. Lett.* **23** (1969) 935.

[19] J. Bjorken, *Phys. Rev.* **179** (1969) 1547.

[20] R. Feynman, *Phys. Rev. Lett.* **23** (1969) 1415.

[21] M. Gell-Mann, *Phys. Lett.* **8** (1964) 214.

[22] M. Klein, *Structure functions in deep inelastic lepton nucleon scattering*, in J. Jaros, M. Peskin (eds.), Proc. of the 19th Intl. Symposium on Lepton and Photon Interactions at High Energies (LP 99), Stanford, USA (1999).

[23] F. Eisele, *Nucleon structure functions* in S. Bianco, A. Calcaterra, P. De Simone, F. Fabbri (eds.), Proc. of the 18th Intl. Conference on Physics in Collision, Frascati, Italy (1998).

[24] V. Gribov, L. Lipatov, *Sov. J. Nucl. Phys.* **15** (1972) 438 and 675;
Y. Dokshitzer, *Sov. Phys. JETP* **46** (1977) 641;
G. Altarelli, G. Parisi, *Nucl. Phys.* **B 126** (1977) 298.

[25] F. Zomer (for the H1 Collaboration), *Deep-Inelastic Inclusive ep Scattering at Low x and a Measurement of* α_s, talk at the 30th Intl. Conference on High Energy Physics (ICHEP 2000), Osaka, Japan (2000).

[26] V. Fadin, E. Kuraev, L. Lipatov, *Phys. Lett.* **B 60** (1975) 50;
L. Lipatov, *Sov. J. Nucl. Phys.* **23** (1976) 338;
V. Fadin, E. Kuraev, L. Lipatov, *Sov. Phys. JETP* **44** (1976) 443;
V. Fadin, E. Kuraev, L. Lipatov, *Sov. Phys. JETP* **45** (1977) 199;
Y. Balitzkii, L. Lipatov, *Sov. J. Nucl. Phys.* **28** (1978) 822.

[27] V. Fadin, L. Lipatov, *Phys. Lett.* **B 429** (1998) 127;
G. Camici, M. Ciafaloni, *Phys. Lett.* **B 430** (1998) 349.

[28] H1 Collaboration, C. Adloff *et al.*, *Phys. Lett.* **B 462** (1999) 440.

[29] T. Wengler, Ph.D. Thesis, University of Heidelberg, Germany (1999).

[30] M. Erdmann, *The Partonic Structure of the Photon*, Springer Tracts in Modern Physics **138**, Berlin and Heidelberg (1997).

[31] G. Schuler, T. Sjöstrand, *Z. Phys.* **C 68** (1995) 607;
G. Schuler, T. Sjöstrand, *Phys. Lett.* **B 376** (1996) 193.

[32] W. Bardeen, A. Buras, D. Duke, T. Muta, *Phys. Rev.* **D 18** (1978) 3998.

[33] M. Drees, R. Godbole, *Phys. Rev.* **D 50** (1994) 3124.

[34] F. Borzumati, G. Schuler, *Z. Phys.* **C 58** (1993) 139.

[35] M. Glück, E. Reya, A. Vogt, *Phys. Rev.* **D 45** (1992) 3986.

[36] H1 Collaboration, C. Adloff *et al.*, *Eur. Phys. J.* **C 13** (2000) 397.

[37] H. Jung, L. Jönsson, H. Küster, *Eur. Phys. J.* **C 9** (1999) 383.

[38] A. Hebecker, *Phys. Rept.* **331** (2000) 1.

[39] W. Buchmüller, *Towards the theory of diffractive DIS*, hep-ph/9906546.

[40] A. Hebecker, T. Teubner, *High-Energy Scattering and Diffraction: Theory Summary*
in J. Gracey and T. Greenshaw (eds.), Proc. of the 8th Intl. Workshop on Deep-
Inelastic Scattering (DIS 2000), Liverpool, Great Britain (2000), hep-ph/0006234.

[41] T. Regge, *Nuovo Cim.* **14** (1959) 951;
T. Regge, *Nuovo Cim.* **18** (1960) 947.

[42] J. Jackson, *Rev. Mod. Phys.* **37** (1965) 484.

[43] A. Barnes *et al.*, *Phys. Rev. Lett.* **37** (1976) 76.

[44] A. Donnachie, P. Landshoff, *Phys. Lett.* **B 296** (1992) 227.

[45] H1 Collaboration, S. Aid *et al.*, *Z. Phys.* **C 69** (1995) 27.

[46] V. Gribov, *Sov. Phys. JETP* **41** (1961) 667;
G. Chew, S. Frautschi, S. Mandelstam, *Phys. Rev.* **126** (1962) 1202.

[47] A. Donnachie, P. Landshoff, *Nucl. Phys.* **B 231** (1983) 189.

[48] L. Lukaszuk, B. Nicolescu, *Nuovo Cim. Lett.* **8** (1973) 405;
D. Joynson, E. Leader, C. Lopez, B. Nicolescu, *Nuovo Cim.* **30A** (1975) 345.

[49] A. Schäfer, L. Mankiewicz, O. Nachtmann, *Diffractive η_c, η, η', J/Ψ and Ψ' produc-
tion in electron-proton collisions at HERA energies* in W. Buchmüller, G. Ingelman
(eds.): *Physics at HERA*, Proc. of the Workshop, DESY (1992) 243;
W. Kilian, O. Nachtmann, *Eur. Phys. J.* **C 5** (1998) 317.

[50] H1 Collaboration, C. Adloff *et al.*, *Phys. Lett.* **B 483** (2000) 23.

[51] P. Merkel, Ph.D. Thesis, University of Hamburg, Germany (2000).

[52] S. Brodsky, G. Lepage, P. Mackenzie, *Phys. Rev.* **D 28** (1983) 228.

[53] A. Donnachie, P. Landshoff, *Phys. Lett.* **B 437** (1998) 408.

[54] W. Buchmüller, T. Gehrmann, A. Hebecker, *Nucl. Phys.* **B 537** (1999) 477.

[55] J. Bjorken, J. Kogut, *Phys. Rev.* **D 8** (1973) 1341.
G. Bertsch, S. Brodsky, A. Goldhaber, J. Gunion, *Phys. Rev. Lett.* **47** (1981) 297.

[56] M. Ryskin, *Sov. J. Nucl. Phys.* **52** (1990) 529;
N. Nikolaev, B. Zakharov, *Z. Phys.* **C 53** (1992) 331.

[57] W. Buchmüller, A. Hebecker, M. McDermott, *Phys. Lett.* **B 410** (1997) 304.

[58] L. Trentadue, G. Veneziano, *Phys. Lett.* **B 323** (1994) 201.

[59] A. Berera, D. Soper, *Phys. Rev.* **D 50** (1994) 4328.

[60] M. Grazzini, L. Trentadue, G. Veneziano, *Nucl. Phys.* **B 519** (1998) 394.

[61] J. Collins, *Phys. Rev.* **D 57** (1998) 3051 and erratum-ibid. **D 61** (2000) 019902.

[62] F. Hautmann, Z. Kunszt, D. Soper, *Phys. Rev. Lett.* **81** (1998) 3333.

[63] G. Ingelman, P. Schlein, *Phys. Lett.* **B 152** (1985) 256.

[64] J. Cudell, K. Kang, S. Kim, *Phys. Lett.* **B 395** (1997) 311.

[65] L. Alvero, J. Collins, J. Terron J. Whitmore, *Phys. Rev.* **D 59** (1999) 074022;
L. Alvero, J. Collins, J. Whitmore: *Tests of Factorisation in Diffractive Charm Production and Double Pomeron Exchange*, hep-ph/9806340.

[66] ZEUS Collaboration, M. Derrick *et al.*, *Z. Phys.* **C 68** (1995) 569;
ZEUS Collaboration, M. Derrick *et al.*, *Z. Phys.* **C 70** (1996) 391.

[67] ZEUS Collaboration, M. Derrick *et al.*, *Phys. Lett.* **B 356** (1995) 129.

[68] A. Edin, G. Ingelman, J. Rathsman, *Phys. Lett.* **B 366** (1996) 371;
A. Edin, G. Ingelman, J. Rathsman, *Z. Phys.* **C 75** (1997) 57.

[69] J. Rathsman, *Phys. Lett.* **B 452** (1999) 364.

[70] T. Sjöstrand, *Comp. Phys. Commun.* **39** (1986) 347;
T. Sjöstrand, M. Bengtsson, *Comp. Phys. Commun.* **43** (1987) 367.

[71] A. Hebecker, *Nucl. Phys.* **B 505** (1997) 349.

[72] M. Wüsthoff, A. Martin, *J. Phys.* **G 25** (1999) R309.

[73] N. Nikolaev, B. Zakharov, *Z. Phys.* **C 49** (1990) 607.

[74] J. Forshaw, D. Ross, *QCD and the Pomeron*, Cambridge University Press (1996).

[75] M. Wüsthoff, *Phys. Rev.* **D 56** (1997) 4311.

[76] J. Bartels, J. Ellis, H. Kowalski, M. Wüsthoff, *Eur. Phys. J.* **C 7** (1999) 443.

[77] F. Low, *Phys. Rev.* **D 12** (1975) 163;
S. Nussinov, *Phys. Rev. Lett.* **34** (1975) 1286.

[78] A. Mueller, *Nucl. Phys.* **B 335** (1990) 115;
M. Diehl, *Z. Phys.* **C 66** (1995) 181.

[79] J. Forshaw, G. Kerley, G. Shaw, *Phys. Rev.* **D 60** (1999) 074012;
L. Frankfurt, V. Guzey, M. McDermott, M. Strikman: *Unitarity and the QCD-improved dipole picture*, hep-ph/9912547.

[80] K. Golec-Biernat, M. Wüsthoff, *Phys. Rev.* **D 59** (1999) 014017;
K. Golec-Biernat, M. Wüsthoff, *Phys. Rev.* **D 60** (1999) 114023.

[81] J. Bartels, H. Lotter, M. Wüsthoff, *Phys. Lett.* **B 379** (1996) 239 and erratum-ibid.
B 382 (1996) 449;
J. Bartels, C. Ewerz, H. Lotter, M. Wüsthoff, *Phys. Lett.* **B 386** (1996) 389;
H. Lotter, *Phys. Lett.* **B 406** (1997) 171.

[82] J. Bartels, H. Jung, M. Wüsthoff, *Eur. Phys. J.* **C 11** (1999) 111;
J. Bartels, H. Jung, A. Kyrieleis: *Massive c̄cg-Production in Diffractive DIS*, hep-ph/0010300.

[83] M. Glück, E. Reya, A. Vogt, *Z. Phys.* **C 67** (1995) 433.

[84] A. Donnachie, P. Landshoff, *Nucl. Phys.* **B 244** (1984) 322.

[85] H1 Collaboration, C. Adloff *et al.*, *Eur. Phys. J.* **C 1** (1998) 495;
H1 Collaboration, C. Adloff *et al.*, *Phys. Lett.* **B 428** (1998) 206;
H1 Collaboration, C. Adloff *et al.*, *Eur. Phys. J.* **C 5** (1998) 439.

[86] H1 Collaboration, *Measurement of the Production of D* Mesons in Deep-inelastic Diffractive Interactions at HERA*, paper **157ag** subm. to the Intl. Europhysics Conference on High Energy Physics (EPS-HEP 99), Tampere, Finland (1999).

[87] P. Thompson, Ph.D. Thesis, University of Birmingham, Great Britain (1999).

[88] S. Hengstmann, Ph.D. Thesis, University of Zürich, Switzerland (2000).

[89] M. Bengtsson, T. Sjöstrand, *Z. Phys.* **C 37** (1988) 465.

[90] G. Gustafson, *Phys. Lett.* **B 175** (1986) 453;
G. Gustafson, U. Petterson, *Nucl. Phys.* **B 306** (1988) 746;
B. Andersson, G. Gustafson, L. Lönnblad, U. Petterson, *Z. Phys.* **C 43** (1989) 625;
B. Andersson, G. Gustafson, L. Lönnblad, *Nucl. Phys.* **B 339** (1990) 393.

[91] B. Webber, *Nucl. Phys.* **B 238** (1984) 492.

[92] H. Jung, *Comp. Phys. Commun.* **86** (1995) 147.
(see also http://www.desy.de/∼jung/rapgap.html)

[93] J. Owens, *Phys. Rev.* **D 30** (1984) 943.

[94] N. Nikolaev: *Intrinsic $k_\perp$ in the Pomeron* in A. Doyle, G. Grindhammer, G. Ingelman, H. Jung (eds.): *Monte Carlo Generators for HERA Physics*, **DESY-PROC-1999-02** (1999) 377.

[95] L. Lönnblad, *Comp. Phys. Commun.* **71** (1992) 15.

[96] T. Sjöstrand, *Comp. Phys. Commun.* **82** (1994) 74.

[97] A. Kwiatkowski, H. Spiesberger, H. Möhring, *Comp. Phys. Commun.* **69** (1992) 155.

[98] J. Bromley *et al.*: *HzTool: A Package for Monte Carlo - Data Comparison at HERA* in G. Ingelman, A. De Roeck, R. Klanner (eds.): *Future Physics at HERA*, Proc. of the Workshop, DESY (1996), 611.
(see also http://www.desy.de/∼h01rtc/hztool.html)

[99] A. Edin, G. Ingelman, J. Rathsman, *Comp. Phys. Commun.* **101** (1997) 108.

[100] U. Amaldi (ed.), *Proc. of the study for an ep facility for Europe*, **DESY 79-48** (1979).

[101] H1 Collaboration, I. Abt *et al.*, *Nucl. Instrum. Methods* **A 386** (1997) 310 and 348.

[102] H1 CST group, D. Pitzl *et al.*, *Nucl. Instrum. Methods* **A 454** (2000) 334.

[103] H1 BST group, W. Eick *et al.*, *Nucl. Instrum. Methods* **A 386** (1997) 81.

[104] B. Schwab, Ph.D. Thesis, University of Heidelberg, Germany (1996).

[105] A. Glazov, Ph.D. Thesis, Humboldt University of Berlin, Germany (1998).

[106] P. Sievers, Diploma Thesis, University of Heidelberg, Germany (1999).

[107] H1 SPACAL group, R. Appuhn *et al.*, *Nucl. Instrum. Methods* **A 374** (1996) 149 and *Nucl. Instrum. Methods* **A 386** (1997) 397.

[108] H1 Collaboration, ELAN working group, internal communication (2000).

[109] H1 Collaboration, *Guide to the Simulation program H1SIM*, *H1 Software Note* **3** (1989).

[110] R. Brun, F. Carminati, *GEANT Detector description and Simulation Tool*, *CERN Program Library* **W5013** (1993).

[111] H1 Collaboration, *H1REC User Guide*, unpublished.

[112] T. Carli, private communication (1999).

[113] H1 Collaboration, C. Adloff *et al.*, *Z. Phys.* **C 74** (1997) 221.

[114] CDF Collaboration, F. Abe *et al.*, *Phys. Rev.* **D 45** (1992) 1448.

[115] V. Blobel, *LOOK - A system for data analysis*, *H1 Software Note* **4** (1990).

[116] H1 Collaboration, C. Adloff *et al.*, *Phys. Lett.* **B 483** (2000) 36;
ZEUS Collaboration, J. Breitweg *et al.*, *Eur. Phys. J.* **C 11** (1999) 35.

[117] H1 Collaboration, C. Adloff *et al.*, *Eur. Phys. J.* **C 13** (2000) 415.

[118] B. List, Diploma Thesis, Tech. Univ. Berlin, Germany (1993);
B. List, A. Mastroberardino: *DIFFVM: A Monte Carlo Generator for diffractive processes in ep scattering* in A. Doyle, G. Grindhammer, G. Ingelman, H. Jung (eds.): *Monte Carlo Generators for HERA Physics*, **DESY-PROC-1999-02** (1999) 396.

[119] S. Ellis, D. Soper, *Phys. Rev.* **D 48** (1993) 3160;
S. Catani, Y. Dokshitzer, M. Seymour, B. Webber, *Nucl. Phys.* **B 406** (1993) 187.

[120] ZEUS Collaboration, J. Breitweg *et al.*, *Phys. Lett.* **B 421** (1998) 368.

[121] H1 Collaboration, C. Adloff *et al.*, *Eur. Phys. J.* **C 6** (1999) 587.

[122] H1 Collaboration, C. Adloff *et al.*, *Eur. Phys. J.* **C 13** (2000) 415.

[123] M. Glück, E. Reya, A. Vogt, *Eur. Phys. J.* **C 5** (1998) 461.

List of Figures

163

List of Tables

Acknowledgements

At this point I want to express my sincere gratitude to all those I was working together with and I could profit from during the past almost three years. I enjoyed the friendly and professional atmosphere in the H1 collaboration. In my opinion, working in such an environment is a real experience for a lifetime. My special thanks go to:

- Prof. Franz Eisele (Heidelberg), for being the supervisor of this thesis. His guidance, support and commitment were very valuable to me;

- Prof. Otto Nachtmann (Heidelberg), for his friendly willingness to act as the second referee of this thesis;

- Dr. habil. Peter Schleper (DESY), for his very motivating guidance and support;

- Dr. Paul Richard Newman (Birmingham). I could not have profited more from his extensive knowledge of diffractive scattering. His cooperation in the course of the publication of the results from this thesis was invaluable;

- Dr. Hannes Jung (Lund). This analysis benefited a lot from his fast response and help concerning Monte Carlo aspects at all times. He also contributed a lot to my understanding of the phenomenology of diffractive DIS and to the interpretation of the data;

- All members of the H1 collaboration and the H1 diffraction physics working group who contributed with their expertise to this work. Among many others, I especially want to thank Dr. Paul Thompson (Birmingham);

- From the 'theory side' I want to thank Prof. Jochen Bartels (Hamburg), Dr. habil. Arthur Hebecker (Heidelberg and CERN) and Dr. Martin McDermott (Liverpool). I could profit a lot from discussions and their suggestions;

- All technicians and engineers who run and maintain the HERA accelerator and the H1 detector, especially the technicians from Heidelberg Rudi Eitel, Rudi Hotz and Christian Rummel for their work and the good collaboration concerning the BDC;

- All colleagues from the H1 group of the physics institute at the University of Heidelberg for the good collaboration;

- Last, but certainly not least, I want to thank my parents and Karin for their understanding and support at all times.